



**Deployable S-Band helix antenna compatible  
with the CubeSat standard**

BY

**Robert Christopher Daniels**

DISSERTATION SUBMITTED IN PARTIAL FULFILMENT OF  
THE REQUIREMENTS FOR THE DEGREE  
MASTER OF ENGINEERING: SATELLITE SYSTEMS AND  
APPLICATIONS

IN THE FACULTY OF ENGINEERING & THE BUILT  
ENVIRONMENT

AT THE CAPE PENINSULA UNIVERSITY OF TECHNOLOGY

SUPERVISOR: APROF RR VAN ZYL

CO-SUPERVISOR: M PETERSEN

BELLVILLE

DECEMBER 2022

CPUT COPYRIGHT INFORMATION

The dissertation may not be published either in part (in scholarly, scientific or technical journals), or as a whole (as a monograph), unless permission has been obtained from the University.

# DECLARATION

I, Robert Daniels, declare that the contents of this dissertation represents my own unaided work, and that the dissertation has not previously been submitted for academic examination towards any qualification. Furthermore, it represents my own opinions and not necessarily those of the Cape Peninsula University of Technology.



09/03/2023

---

Robert Daniels

---

Date

# ABSTRACT

CubeSats are becoming fundamental aspects of communications across the world. Currently, limited antenna configurations are utilised, mainly due to CubeSat size restrictions present on available CubeSat form factors. These limited antenna configurations often lead to the exclusion of the extra volume known as the "tuna-can", which forms part of the CubeSat costs.

To combat this trend an S-band Quadrifilar Helix Antenna is proposed. The proposed antenna is mechanically designed by exploring shape memory alloys and traditional spring approaches, to create an antenna deployment system, which is safe and reliable, while meeting CubeSat platform communication needs.

The initial research showed that both the traditional spring and SMA approach provided reliable antenna deployment solutions, however, due to material availability and the lack of ability of the thinner SMA wire to retain its shape, the traditional spring approach was successfully developed. The developed spring QHA reliably deploys, however vibrational tests are recommended.

The antenna successfully deploys and therefore offers alternative means for communication on the CubeSat platform. This allows the available CubeSat platform volume and surface area to be utilised more efficiently, thus creating the opportunity for additional payloads or technology demonstration to commence.

# ACKNOWLEDGEMENTS

I wish to thank:

- Prof Van Zyl and Mr. Petersen for their guidance and exceptional supervision throughout the course of my Masters.
- Mr. S. Martin and Mr. D. Cogan for their tireless support and willingness to assist.
- J.G. Naidoo for his support and advice.
- Dr Wiid for his help with the electrical designs.
- Mr. Maqina for his help and support with electrical testing.
- Mr. Louw for the PCB manufacturing.
- K. Ross for her love, support, guidance and compassion. For being the rock in my life in times of uneasiness.
- My parents and family members for their love and support throughout the years.

The financial assistance of the National Research Fund (NRF) towards this research is acknowledged. Opinions expressed in this thesis and the conclusions arrived at, are those of the author, and are not necessarily to be attributed to the National Research Foundation.

# Nomenclature

$\sigma_f$	Detwinning Finish Stress
$\sigma_s$	Detwinning Start Stress
$\sigma_{A_f}$	Austenite Finish Stress
$\sigma_{M_f}$	Martensite Finish Stress
$\sigma_{M_s}$	Martensite Start Stress
$A_f$	Austenite Finish Temperature
$A_s$	Austenite Start Temperature
$M_f$	Martensite Finish Temperature
$M_s$	Martensite Start Temperature
CDS	CubeSat Design Specification
CoG	Centre of Gravity
COTS	Commercially-off-the-shelf
CPU	Central Processing Unit
CVCM	Collected Volatile Condensable Material
DAS	Debris Assessment Software
DSC	Differential Scanning Calorimetry
ECSS	European Cooperation for Space Standardisation
FEA	Finite Element Analysis
FEM	Finite Element Method
FOS	Factor of Safety
GEVS	General Environmental Verification Standard
GPU	Graphics Processing Unit
IADC	Inter-Agency Space Debris Coordination Committee

LEO Low Earth Orbit  
LTAN Local Time at Ascending Node  
NiTi Nitinol  
NOL Naval Ordnance Laboratory  
P-POD Poly Picosatellite Orbital Deployer  
PLMCC Product Lifecycle Management Competency Centre  
PSD Power Spectral Density  
QHA Quadrifilar Helix Antenna  
RBE Rigid Body Elements  
SIM Stress Induced Martensite  
SMA Shape Memory Alloy  
SME Shape Memory Alloy  
SSDL Space Systems Development Laboratory  
TML Total Mass Loss  
VNA Vector Network Analyser

# Contents

<b>List of Tables</b>	<b>xii</b>
<b>List of Figures</b>	<b>xiii</b>
<b>1 Introduction</b>	<b>1</b>
1.1 Background . . . . .	1
1.2 Statement of the Research Problem . . . . .	2
1.3 Research Questions . . . . .	3
1.4 Research Objectives . . . . .	3
1.5 Methodology . . . . .	4
1.6 Delineation . . . . .	6
1.7 Significance of Research . . . . .	7
1.8 Expected Outcomes . . . . .	8
1.9 Dissertation Preview . . . . .	8
<b>2 Literature Review</b>	<b>9</b>
2.1 CubeSat Design Specification . . . . .	9
2.1.1 Historical Background of CubeSats . . . . .	9
2.1.2 General and Mechanical Requirements . . . . .	9
2.1.3 “Tuna can” Dimensions . . . . .	10
2.1.4 CubeSat Standards . . . . .	11

2.1.4.1	CDS Testing for Space and Launch . . . . .	11
2.1.4.2	ECSS Standards and Methodology . . . . .	11
2.1.4.3	IADC Guidelines . . . . .	13
2.2	Shape Memory Alloys . . . . .	13
2.2.1	History Of Shape Memory Alloys . . . . .	14
2.2.2	General Properties of SMAs . . . . .	14
2.2.3	Phenomenology of Phase Transformation in SMA . . . . .	15
2.2.4	Pseudoelasticity . . . . .	20
2.2.5	Shape Memory Effect . . . . .	22
2.2.6	Limitations of NiTi Shape Memory and Superelastic Behaviour	23
2.2.7	Composition of NiTi SMAs and its Effects . . . . .	24
2.2.8	Properties of NiTi Alloy . . . . .	25
2.2.9	Shape Setting . . . . .	26
2.3	Theory . . . . .	27
2.3.1	Helical Spring Theory . . . . .	27
2.3.2	SMA Spring Theory . . . . .	31
2.3.3	Thermal Balance Theory . . . . .	33
2.3.3.1	Solar Radiation . . . . .	34
2.3.3.2	Planetary Albedo . . . . .	34
2.3.3.3	Planetary Radiation . . . . .	38
2.3.3.4	Thermal Balance . . . . .	38
2.4	Manufacturing for the Space Environment . . . . .	41
2.4.1	Material Sourcing and Selection . . . . .	41
2.4.2	Manufacturing Techniques . . . . .	42
2.4.2.1	Additive Manufacturing . . . . .	42



2.4.2.2	Multiple Axis CNC Machine Centre . . . . .	43
2.4.2.3	Injection Moulding . . . . .	43
2.5	Quadrifilar Helix Antenna . . . . .	44
2.6	Finite Element Analysis . . . . .	47
2.6.1	FEM Versus Classical Method . . . . .	49
2.6.2	CPUT Simulation Computer Specification . . . . .	50
<b>3</b>	<b>Design and Testing Methodology</b>	<b>52</b>
3.1	Design Methodology . . . . .	52
3.1.1	Initial Design Phase: Open Helical and SMA Spring Design	53
3.1.1.1	Nitinol Properties Characterisation . . . . .	54
3.1.1.2	Shape Setting Procedure . . . . .	55
3.1.1.3	Start and Finish Activation Temperature Procedure	58
3.1.2	Simulation Phase . . . . .	62
3.1.2.1	Launch Environment and Loading Methodology . .	62
3.1.3	Thermal Environment Methodology . . . . .	65
3.2	Test Methodology . . . . .	66
3.2.1	Deployment Testing . . . . .	66
3.2.2	Electrical Testing . . . . .	68
3.2.3	Environment Testing . . . . .	68
<b>4</b>	<b>Antenna Mechanical Design, Specification and Analysis</b>	<b>69</b>
4.1	Design Requirements, Constraints and Criteria . . . . .	69
4.1.1	Design Requirements . . . . .	69
4.1.2	Design Constraints . . . . .	70
4.1.3	Design Criteria . . . . .	70

4.2	Antenna Spring Design . . . . .	71
4.2.1	SMA Spring Design . . . . .	71
4.2.2	Traditional Spring Design . . . . .	74
4.2.2.1	Iteration 1 . . . . .	74
4.2.2.2	Iteration 2 . . . . .	79
4.2.3	Spring Design Outcome . . . . .	83
4.3	Concepts . . . . .	85
4.3.1	Concept A . . . . .	85
4.3.2	Concept B: . . . . .	86
4.3.3	Concept C: . . . . .	87
4.3.4	Concept D: . . . . .	89
4.3.5	Concept E: . . . . .	91
4.3.6	Design Matrix . . . . .	92
4.4	Material Selection . . . . .	92
4.4.1	Spring Material Selection . . . . .	93
4.4.2	Antenna Housing Material Selection . . . . .	93
4.5	Thermal Balance Calculation . . . . .	94
4.5.1	Design Parameters . . . . .	95
4.5.2	Assumptions . . . . .	95
4.5.3	Calculations . . . . .	96
<b>5</b>	<b>Analysis</b>	<b>100</b>
5.1	Finite Element Analysis . . . . .	100
5.1.1	Simulation Setup . . . . .	100
5.1.1.1	Antenna Spring Model Simulation . . . . .	101

5.1.1.2	Thermal Cycling Simulation . . . . .	111
5.1.1.3	Thermal Expansion and Contraction Simulations . . . . .	124
5.1.2	Launch Simulations . . . . .	132
5.1.2.1	Modal Simulation . . . . .	132
5.1.2.2	Quasi Static Simulation . . . . .	138
5.1.2.3	Sine Wave Sweep Simulation . . . . .	145
5.1.2.4	Random Vibration Simulation . . . . .	157
5.1.2.5	Shock Simulation . . . . .	165
5.2	Debris Assessment . . . . .	166
<b>6</b>	<b>Testing</b>	<b>170</b>
6.1	Deployment Test . . . . .	170
6.1.1	Pre-Deployment Test Checks . . . . .	170
6.1.2	Deployment Test . . . . .	174
6.1.3	Deployment Test with Decreased Antenna Wire Diameter . . . . .	177
6.1.3.1	Deployment Test with Staged Deployment . . . . .	180
6.2	Thermal Cycling Test . . . . .	182
6.2.1	Chamber Setup and Thermal Cycling Test . . . . .	182
6.2.2	Thermal Cycling Results . . . . .	184
6.3	Electrical Test . . . . .	187
6.4	Sine Wave Sweep and Random Vibration Test . . . . .	190
<b>7</b>	<b>Conclusion and Recommendations</b>	<b>192</b>
7.1	Conclusion . . . . .	192
7.2	Recommendations . . . . .	195

**A Antenna Dimensions and Simulations**

**B Nitinol Specimen Testing**

**C Material Data**

**D Engineering Drawings**

**E Modal Frequencies**

**F Calculations**

F.1 Thermal Balance Calculations . . . . .

F.2 Traditional Spring Calculations . . . . .

**G Top Brace Iterations**

**H Deployment Test Results**

# List of Tables

2.1	Simulation Computer Specifications . . . . .	50
4.1	Shape Training Results 425 °C . . . . .	72
4.2	Shape Training Results 475 °C . . . . .	72
4.3	Shape Training Results 525 °C . . . . .	73
4.4	Estimated Wire Temperature . . . . .	74
4.5	SMA versus Helical Design Approach . . . . .	84
4.6	Concept Design Matrix . . . . .	92
4.7	Spring Material Design Matrix . . . . .	93
4.8	Antenna Housing Material Design Matrix . . . . .	94
4.9	Calculation Parameters . . . . .	95
5.1	Solver Solutions Used for Analysis . . . . .	101
6.1	1.91 mm Deployment Reliability Assessment . . . . .	176
6.2	1.6 mm Deployment Reliability Assessment . . . . .	179
6.3	1.1 mm Deployment Reliability Assessment . . . . .	179
6.4	1.91 mm Staged Deployment Reliability Assessment . . . . .	181

# List of Figures

1.1	Given Electrical Design of Antenna Iteration 1 . . . . .	6
1.2	Given Electrical Design of Antenna Iteration 2 . . . . .	7
2.1	“Tuna can” Dimensions 1 (Munakata et al., 2009) . . . . .	10
2.2	“Tuna can” Dimensions 2 (Munakata et al., 2009) . . . . .	10
2.3	Temperature Induced Phase Change Under No Mechanical Loading (Lagoudas et al., 2008) . . . . .	16
2.4	Depiction of SME Showing Detwinning of Material Under an Applied Stress (Lagoudas et al., 2008) . . . . .	17
2.5	Depiction of SME Showing Unloading and Heating to Austenite Un- der No Load (Lagoudas et al., 2008) . . . . .	17
2.6	Temperature Induced Transformation Under an Applied Load (Lagoudas et al., 2008) . . . . .	18
2.7	Typical Pseudoelastic Loading Path (Lagoudas et al., 2008) . . . . .	19
2.8	Typical Pseudoelastic Stress-Strain Diagram(Lagoudas et al., 2008).	19
2.9	Typical Stress-Temperature Diagram for an SMA (Lagoudas et al., 2008). . . . .	20
2.10	Loading Paths Phase Diagram of the Pseudoelastic Effect (Lagoudas et al., 2008). . . . .	20
2.11	Loading Path of a Typical SMA (Lagoudas et al., 2008). . . . .	21
2.12	Stress-Strain-Temperature Phase Diagram Depicting the SME of a Typical NiTi Specimen (Lagoudas et al., 2008). . . . .	23
2.13	Nitinol Transformation Properties (Johnson-Matthey, 2015) . . . . .	25

2.14 Nitinol Physical Properties (Johnson-Matthey, 2015) . . . . .	26
2.15 Electrical and Magnetic Nitinol Properties (Johnson-Matthey, 2015)	26
2.16 Nitinol Mechanical Properties (Johnson-Matthey, 2015) . . . . .	26
2.17 Types of Ends for Helical Spring (Shigley and Mischke, 1996) . . . .	28
2.18 Buckling Curves Shigley and Mischke (1996) . . . . .	30
2.19 Maximum Allowable Torsional Stress (Shigley and Mischke, 1996) .	31
2.20 Albedo and Planetary Radiation Cold Case (Gilmore and Donabedian, 2002) . . . . .	35
2.21 Albedo and Planetary Radiation Hot Case (Gilmore and Donabedian, 2002) . . . . .	36
2.22 Albedo Correction (Gilmore and Donabedian, 2002) . . . . .	36
2.23 Beta Angle (Gilmore and Donabedian, 2002) . . . . .	37
2.24 Visibility Factor (Fortescue et al., 2011) . . . . .	37
2.25 Quadrifilar Helix Antenna (Olsen et al., 2018) . . . . .	44
2.26 QHA 8 Helix Pantograph Deployer(Olsen et al., 2018) . . . . .	45
2.27 QHA 3D Link Deployer(Olsen et al., 2018). . . . .	45
2.28 QHA Dilator Cell Deployer (Olsen et al., 2018). . . . .	46
2.29 QHA Dilator Cell Deployer 2 (Olsen et al., 2018). . . . .	46
2.30 Stowed QHA (HCT, 2020) . . . . .	47
2.31 Deployed QHA (HCT, 2020) . . . . .	47
3.1 Antenna Design Methodology Algorithm . . . . .	52
3.2 Initial Spring Design Methodology . . . . .	53
3.3 Nitinol Wire Specimen . . . . .	54
3.4 Shape Setting Procedure . . . . .	55
3.5 Constrained Wire Specimen . . . . .	55

3.6	CPUT Kiln . . . . .	56
3.7	Open CPUT Kiln . . . . .	56
3.8	Test Sample Placed in Kiln . . . . .	57
3.9	Test Sample Duration . . . . .	57
3.10	Trained Specimen Left to Air Cool . . . . .	58
3.11	Start and Finish Activation Temperature Procedure . . . . .	59
3.12	Tray and Transparent Dish with Specimen . . . . .	59
3.13	Probe Thermometer . . . . .	60
3.14	Remembered Shape at Austenite Finish Temperature . . . . .	61
3.15	Remembered Shape of Specimen at Room Temperature . . . . .	61
3.16	Antenna Design Simulation Methodology . . . . .	62
3.17	Load Cycle Design Loop (ECSS, 2013) . . . . .	63
3.18	Soyuz Launcher Quasi Static (Arianespace, 2011) . . . . .	64
3.19	Soyuz Launcher Sine Vibration Equivalent (Arianespace, 2011) . . . . .	64
3.20	Soyuz Launcher Random Vibration (Arianespace, 2011) . . . . .	64
3.21	Thermal Margin (ECSS, 2013) . . . . .	65
3.22	Antenna Stowing Jig View 1 . . . . .	67
3.23	Antenna Stowing Jig View 2 . . . . .	67
3.24	Antenna Stowing Jig View 3 . . . . .	68
4.1	NiTi Activation Start and Finish Temperature Graph . . . . .	73
4.2	Buckling Curves (Shigley and Mischke, 1996) . . . . .	77
4.3	Maximum Allowable Torsional Stress (Shigley and Mischke, 1996) . . . . .	78
4.4	Buckling Curves Shigley and Mischke (1996) . . . . .	81
4.5	Maximum Allowable Torsional Stress Shigley and Mischke (1996) . . . . .	82



4.6	Concept A . . . . .	85
4.7	Concept A Stowed . . . . .	86
4.8	Concept C . . . . .	87
4.9	Concept C Stage 2 . . . . .	88
4.10	Concept C Stage 3 . . . . .	88
4.11	Concept C Stage 4 . . . . .	89
4.12	Concept D . . . . .	90
4.13	Concept D Cross-Section . . . . .	90
4.14	Concept E . . . . .	91
4.15	Concept E Cross-Section . . . . .	91
4.16	Antenna Thermal Equilibrium Temperatures . . . . .	98
5.1	Simulation Setup . . . . .	102
5.2	Simulation Setup Wall Contact . . . . .	103
5.3	Simulation Setup Filar Contact . . . . .	103
5.4	Fixed Filar Constraint . . . . .	104
5.5	Fixed Cylinder Constraint . . . . .	104
5.6	Filar Mesh . . . . .	105
5.7	Enforced Displacement Constraint . . . . .	106
5.8	Simulation Results . . . . .	107
5.9	Simulated Displacement . . . . .	108
5.10	Model Cross-Section Von-Mises Stress . . . . .	109
5.11	Model Cross-Section Shear Stress . . . . .	110
5.12	Shear Stress Manipulated Legend . . . . .	111
5.13	Thermal Cycling 1D Mesh . . . . .	112

5.14	Thermal Cycling 1D Solid Mesh . . . . .	113
5.15	Thermal Mesh Collector . . . . .	113
5.16	Thermo-optical Properties . . . . .	114
5.17	Thermal Cycling Transient Setup . . . . .	115
5.18	Thermal Cycling Ambient Conditions Setup . . . . .	115
5.19	Thermal Cycling Orbital Heating Setup . . . . .	116
5.20	Thermal Cycling Orbital Parameters Setup . . . . .	117
5.21	Thermal Cycling Sun-planet Characteristics . . . . .	118
5.22	Maximum and Minimum Flux Cold Case Temperature Range . . . . .	119
5.23	Maximum and Minimum Flux Hot Case Temperature Range . . . . .	120
5.24	Thermal Load . . . . .	121
5.25	Maximum and Minimum Flux Cold Case Temperature Range with Power . . . . .	122
5.26	Maximum and Minimum Flux Hot Case Temperature Range with Power . . . . .	123
5.27	Simulated QHA Thermal Range . . . . .	124
5.28	SOL 153 Thermal Expansion Simulation . . . . .	125
5.29	SOL 153 Thermal Heating Constraint . . . . .	126
5.30	SOL 153 Thermal Environment (Hot Case) . . . . .	127
5.31	SOL 101 Thermal Expansion Simulation . . . . .	128
5.32	Initial Temperature Input . . . . .	128
5.33	Solution 101 Thermal Expansion Subcase . . . . .	129
5.34	Thermal Expansion Displacement Results . . . . .	129
5.35	Thermal Expansion Stress Results . . . . .	130
5.36	Thermal Contraction Displacement Results . . . . .	130
5.37	Thermal Contraction Stress Results . . . . .	131

5.38	Modal Model . . . . .	133
5.39	Modal Model Side View . . . . .	133
5.40	Solution 103 Real Eigenvalue Simulation Setup . . . . .	134
5.41	Residual Vectors Turned On . . . . .	134
5.42	All Modes Turned On . . . . .	135
5.43	Model Fixed Constraint . . . . .	135
5.44	Tapped Bolt Connection . . . . .	136
5.45	Effective Mass Movement . . . . .	137
5.46	Solution 402 Time Step . . . . .	138
5.47	Axial Gravitational Load . . . . .	139
5.48	Lateral Gravity Load . . . . .	139
5.49	SOL101 Static Axial Displacement Results . . . . .	140
5.50	SOL101 Static Axial Stress Results . . . . .	140
5.51	SOL101 Static Lateral Displacement Results . . . . .	141
5.52	SOL101 Static Lateral Stress Results . . . . .	141
5.53	SOL402 Quasi-Static Axial Displacement Results . . . . .	142
5.54	SOL402 Quasi-Static Axial Stress Results . . . . .	143
5.55	SOL402 Quasi-Static Lateral Displacement Results . . . . .	144
5.56	SOL402 Quasi-Static Lateral Stress Results . . . . .	144
5.57	Sine Wave Sweep Solutions . . . . .	146
5.58	Sine Sweep Setup Case Control . . . . .	147
5.59	Structural Damping Input . . . . .	148
5.60	Logarithmic Sweep Input (FREQ2) . . . . .	148
5.61	Spread Around Natural Frequencies Input (FREQ4) . . . . .	149
5.62	Sine Sweep Subcase . . . . .	149

5.63	Excitation Input . . . . .	150
5.64	Soyuz Excitation Profile . . . . .	150
5.65	Enforced Motion Load . . . . .	151
5.66	X-Axis Acceleration Versus Frequency Graph . . . . .	151
5.67	Y-Axis Acceleration Versus Frequency Graph . . . . .	152
5.68	Z-Axis Acceleration Versus Frequency Graph . . . . .	152
5.69	Sine Wave Sweep X-Axis Acceleration Results . . . . .	153
5.70	Sine Wave Sweep X-Axis Stress Results . . . . .	154
5.71	Sine Wave Sweep Y-Axis Acceleration Results . . . . .	155
5.72	Sine Wave Sweep Y-Axis Stress Results . . . . .	155
5.73	Sine Wave Sweep Z-Axis Acceleration Results . . . . .	156
5.74	Sine Wave Sweep Z-Axis Stress Results . . . . .	156
5.75	Random Vibration Setup . . . . .	158
5.76	Soyuz Power Spectral Density Specification Input . . . . .	159
5.77	RANFRF(524) Parameter Input . . . . .	160
5.78	Gaussian Bell-Shaped Distribution . . . . .	161
5.79	X-axis RMS Acceleration Results . . . . .	162
5.80	X-axis RMS Stress Results . . . . .	162
5.81	Y-axis RMS Acceleration Results . . . . .	163
5.82	Y-axis RMS Stress Results . . . . .	163
5.83	Z-axis RMS Acceleration Results . . . . .	164
5.84	Z-axis RMS Stress Results . . . . .	164
5.85	X-RMS Standard Deviation Stress . . . . .	165
5.86	Y-RMS Standard Deviation Stress . . . . .	165
5.87	Z-RMS Standard Deviation Stress . . . . .	165

5.88	DAS Payload Input 1 . . . . .	166
5.89	DAS Payload Input 2 . . . . .	167
5.90	DAS Mission-Related Debris . . . . .	167
5.91	DAS Requirement Assessments . . . . .	168
5.92	Human Casualty Requirements Input . . . . .	168
5.93	Antenna System Side View . . . . .	169
6.1	Antenna System Side View . . . . .	171
6.2	Antenna System Top View . . . . .	171
6.3	Bifilar Antenna Test Setup . . . . .	172
6.4	Optimised Antenna Top Brace . . . . .	173
6.5	Compressed Antenna With Optimised Top Brace . . . . .	173
6.6	QHA Test Model . . . . .	174
6.7	Antenna Mounted to Deployment Jig . . . . .	175
6.8	Antenna Deployment Test 1 Result . . . . .	176
6.9	1.1 mm Wire Diameter Antenna Configuration . . . . .	178
6.10	1.6 mm Wire Diameter Antenna Configuration . . . . .	178
6.11	1.91 mm Staged Deployment Stage 1 (Stowed) . . . . .	181
6.12	1.91 mm Staged Deployment Stage 2 . . . . .	181
6.13	1.91 mm Staged Deployment Stage 2 (Deployed) . . . . .	181
6.14	Binder MKT115 Thermal Chamber . . . . .	182
6.15	QHA Thermal Test Input . . . . .	183
6.16	QHA Placed in Thermal Chamber . . . . .	183
6.17	QHA Placed in Thermal Chamber Close Up . . . . .	184
6.18	Antenna System In Test Check Up . . . . .	185

6.19	Antenna System Post Thermal Test . . . . .	186
6.20	Thermal Test Antenna Deformation . . . . .	187
6.21	Antenna PCB . . . . .	188
6.22	Antenna Mounted PCB . . . . .	189
6.23	VNA S11 Reflection Coefficient Actual Versus Simulation Results .	190

# Chapter 1

## Introduction

### 1.1 Background

The use of CubeSats in data-intensive applications is becoming more prolific. This poses engineering challenges for deploying advanced communications systems on small satellite platforms, such as CubeSats. As the demand for higher data rates increases, higher frequency bands are being exploited.

The small platform of CubeSats poses engineering challenges that require antennas to be compact and in some instances deployable. Patch antennas are regularly used; however, they suffer from narrowband performance if applications require circular polarisation (Imbriale et al., 2008).

An alternative to these antennas is the quadrifilar helix antenna (QHA). These antennas have high gain, in certain instances an ‘isoflux’ radiation pattern, and wideband circular polarisation performance (Imbriale et al., 2008).

Building on existing work of CubeSat design and antenna implementation, the project looks into how shape memory alloys (SMAs) such as Nitinol (NiTi), and traditional spring materials, may be used in the construction, as well as how a suitable and compact antenna deployment system may be designed and implemented. The structure will undergo rigorous environmental testing to validate the design for deployment on future missions.

Overall, the project aims to deliver an S-band helix antenna centred around 2.2 GHz and a deployment system that has been deemed mechanically suitable and cost-effective for deployment from the ‘tuna can’ volume of a CubeSat.

For the research project, a reliable S-band QHA that has high gain and an isoflux radiation pattern or wide beamwidth is required for deployment on a CubeSat. A higher antenna gain and wideband circular polarisation allow for wider bandwidth communications and an improved link budget. This allows for a better quality com-

munication link between the ground station and the satellite. An isoflux radiation pattern or wide beamwidth is required, as satellites point nadir and therefore need more gain on the horizons.

Low Earth orbit (LEO) satellites rely on an isoflux radiation pattern to communicate with ground stations because the beam pattern is shaped so that the received signal remains constant (ESA, 2018). Circular polarisation must also be considered and is required. It provides a higher probability of a successful link because it is transmitting on all planes (Weik, 2000). The ground plane is required as it helps propagate the signal from the antenna in the transmitting direction, therefore improving the communications link with the ground station.

An S-band alternative to VHF and UHF band communications for telemetry, tracking, and command is required. This is due to that VHF and UHF bands are becoming congested or overly used. Congestion causes packet loss, and signal delays and can result in connections being blocked (Raiesh et al., 2017). This can be detrimental to a space mission, especially one built for communications. Therefore, an S-band solution, where there is less congestion, is required. The S-band also allows for higher data rates, meaning more data can be transferred at a faster rate. The frequency is less susceptible to rain fading compared to higher frequencies, which is the attenuation of an electromagnetic wave caused by weather, such as rain, and results in signal path losses (Ippolito, 2008).

The advantages of the helix versus patch antennas need to be considered. Currently, patch antennas are popular choices for space missions, due to their relatively low cost, high gain, and a large variety of sizes. Helix antennas give wideband circular polarisation, which might be difficult to achieve with compact patch antennas. Helix antennas offer comparable gain and demonstrate low sensitivity when compared to a patch antenna of the same size, helix antennas are also omnidirectional and robust, which may be characteristically difficult to achieve with a patch antenna (Imbriale et al., 2008).

## 1.2 Statement of the Research Problem

CubeSats are becoming fundamental aspects of communications across the world. Currently, limited antenna configurations are utilised, mainly due to CubeSat size restrictions present on available CubeSat form factors. Antenna gain is generally associated with electrically large antennas; hence, the CubeSat size restrictions essentially lead to lower gain antennas and the associated lower data rates.

CubeSats require circularly polarised antennas to promote successful link budgets between the ground station and the CubeSat, which is characteristically difficult to achieve with widely-used compact patch antennas. According to Imbriale et al. (2008), compact patch antennas suffer from narrowband performance, which contributes to lower data rates.



These compact patch antennas lead to a lack of design freedom and available surface area on the CubeSat structure, which often leads to the exclusion of the extra volume, known as the “tuna can”. The “tuna can” of the CubeSat forms part of the associated costs of constructing a CubeSat. Exclusion of the “tuna can” leads to the non-optimal use of the CubeSat surface area and is essentially a waste of financial resources.

An alternative to the patch antenna is the helix antenna, which provides wide-band circular polarisation, high gain, and is robust, however, requires additional space compared to compact patch antennas (Imbriale et al., 2008).

Therefore, to fully optimise the CubeSat space and increase antenna gain to support higher data rates, a compatible S-band (2.2 GHz) helix antenna is proposed that deploys from the ‘tuna can’ space of the CubeSat. The research project looks into how the proposed electrical designs can be mechanically manufactured and stowed within the confines of the “tuna can”, using the traditional theory of springs and shape memory alloys.

### 1.3 Research Questions

The following research questions can be asked to better define the fundamental aspects of the research. These questions provide a guideline for this research:

- How may an S-band QHA be deployed and mechanically tested for use on a CubeSat, while following CubeSat standards?
- What are the advantages of a QHA?
- What materials will be used or considered?
- How will the prototype/design be tested?
- What CubeSat design philosophy will be considered?
- To what extent must the antenna be reliably deployed?
- What design limits need to be considered?

With the above questions in mind, the research project can be better focused and the most workable or suitable solution(s) can be brought forward and validated.

### 1.4 Research Objectives

The aims or objectives of the research will help to focus the research. These are the key or fundamental aspects of the research, based on the research questions,

which will help develop the outcomes of the research. The objectives are divided into main and subsidiary objectives. The objectives are as follows:

- The design and testing of a mechanically sound S-band antenna that conforms to CubeSat standards (main objective), and can be split into smaller objectives such as:
  - Determining through simulations whether the antenna can survive the launch and space environment.
  - Determine through tests if the antenna can survive the launch and space environment.
  - The construction of a functional prototype (from a mechanical perspective).
  - Determine if the antenna can be deployed from the tuna can.
- Reliability assessment for deployment.
- The validation and test process for the antenna and deployment system.

With the above objectives stated, the project can better focus on and determine the research design and methodologies that need to be followed, so that a mechanically sound device can be constructed and validated.

## 1.5 Methodology

The research design and methodology serve as the cornerstone of the research. It includes the theory, processes, and method of investigation that will be used to conduct the research. The research design and methodology are as follows:

The engineering process is a key cornerstone in any engineering design. The research project will follow the traditional engineering process, to identify a need, which forms a research problem, where solutions are developed, the most promising solution is selected, a prototype is constructed, which is then tested, and validated and the final working design communicated.

To optimise CubeSat space and increase antenna gain to support higher data rates, a compatible S-band helix antenna that deploys from the “tuna can” of a CubeSat is proposed. The primary research method for the research project is a literature review. Using information gathered from journals, articles, websites, videos, and theses, the relevant topics have been researched.

Research questions formed help define fundamental aspects of the research. The research questions formed contribute to the objectives set for the research, as previously mentioned. Steps to achieve these objectives must be characterised.

Stated objectives will be achieved through the use of theory, research, simulation, conceptual modelling, and the construction of a prototype, which can be physically tested. The design of the QHA is the first objective of the research.

Different iterations and methods will be reviewed to construct the QHA, ranging from the use of simple springs to SMA's. The methods for QHA deployment mentioned will be evaluated through the use of relevant theoretical groundwork. Of which, it is important to note the shape memory effect (SME) of SMA's and how classical spring theory can be modified for such an effect, as is mentioned in the literature review.

Through the use of simulations, finite element analysis (FEA) will be conducted upon the QHA structure. The finite element method (FEM) will be used to structurally analyse the QHA, determining stress present in the materials used, as well as defining harmful harmonics (frequencies) which need to be avoided, thus limiting the number of prototypes that need to be constructed. An aspect of the QHA that can't be ignored is instances where SMA's are used. Procured material will be physically tested to determine the martensite to austenite phase change of the SMA. If physical testing shows that the procured material can remember its shape once cooled (after a thermo-mechanical load has been induced), FEA will be used to simulate stresses present in the material. By characterising the phase change of the SMA used through the FEA simulation, a better understanding of the behaviour of an SMA QHA design can be realised. The use of the FEM allows simulated models to be tested and validated. Three-dimensional simulation software such as Siemens NX and FEA software such as Nastran NX will be used for modelling components of the design.

Once the theoretical design and simulations have been completed, validation of the design is required. The design must be validated to determine its viability. Design concepts will be subjected to a design matrix. The best scoring concept will be manufactured for use as a prototype. Rigorous testing of the prototype is needed to validate both the electrical and mechanical aspects of the deployment system. A test methodology will be implemented covering the fundamental tests required for CubeSat launch clearance, to their relevant specifications. The prototype will be subjected to the test methodology. Testing of the prototype is limited by available funds.

The last objective is a reliability assessment for the deployment of the prototype. The reliability assessment is required to determine the validity of the prototype, encompassing how well the prototype meets the overall objective of deploying the QHA. The assessment will take into account deployment repeatability, ease of deployment, ease of stowing, deployment height and the antenna form factor once deployed. The study will quantify the degree to which the prototype delivers stable and consistent results. The reliability assessment will also be used to determine any variability encountered when deploying the prototype. The assessment will determine if the prototype conforms to the aims and objectives of the research. Overall, the research aims to produce a functional validated prototype that conforms to CubeSat standards.

## 1.6 Delineation

Having examined the methodologies that will be implemented, the research needs to be delineated, so that the project becomes more focused. The electrical design of the antenna will be given. Therefore, the research project will not look into electrically designing the antenna, however, the mechanical implementation and deployment of the antenna will be covered. The antenna and deployment system will be limited to the area of the “tuna can” of the CubeSat structure. The project will be limited to a prototype; a flight-qualified model is not required. Commercially-off-the-shelf (COTS) parts will be used where applicable. The design will be limited to LEO applications and use similar orbital parameters compared to ZACube-1 and ZACube-2 missions. Therefore, orbital parameters of 550 km (orbital height), with an inclination of  $99.7^\circ$ , with orbital sunlit periods of approximately 60 minutes and darkness periods of approximately 34 minutes.

Nitinol wire was sourced from the CPUT mechatronics workshop. Nitinol is not manufactured locally in South Africa. The 0.5 mm Nitinol wire provided will be used to determine the feasibility of an SMA deployable antenna.

For the research project, two electrically designed S-band antennas have been proposed. Figures 1.1 and 1.2, depict the two electrically designed iterations of the antenna. Both antennas have a  $100\text{ mm} \times 100\text{ mm} \times 1\text{ mm}$  ground plane used to increase the directivity of the antenna.

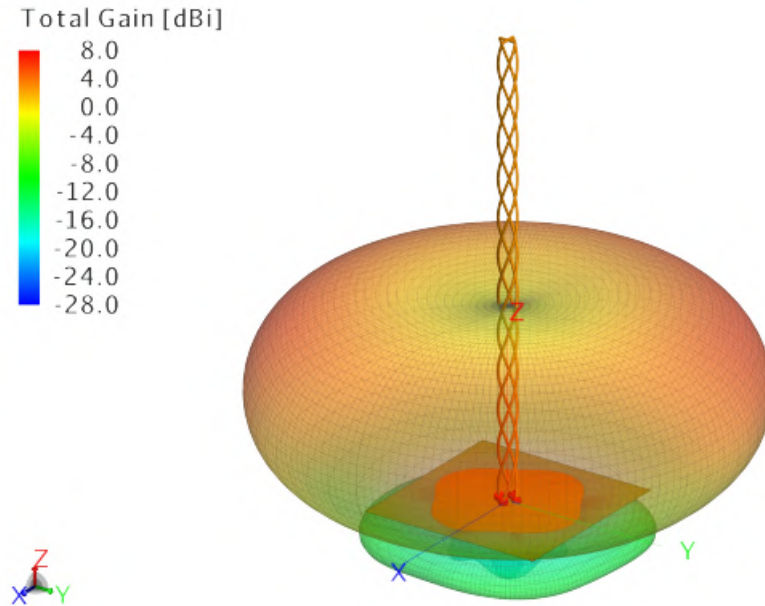


Figure 1.1: Given Electrical Design of Antenna Iteration 1

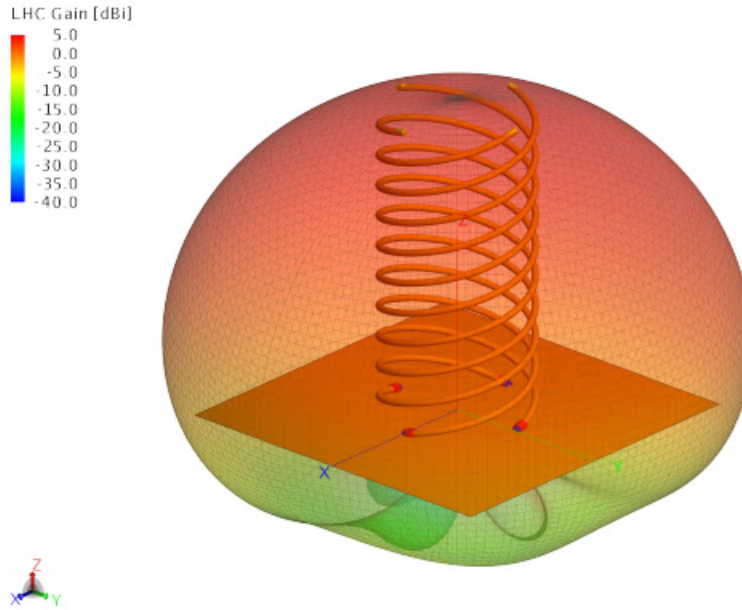


Figure 1.2: Given Electrical Design of Antenna Iteration 2

Antenna iteration one consists of a dimensionally long quadrifilar S-band antenna that displays circular polarisation, an isoflux radiation pattern and operates within the required S-band limitations. The antenna consists of 3 turns, is approximately 250 mm long, has a mean diameter of 9.3 mm and is constructed from 0.5 mm wire.

Antenna iteration two consists of a dimensionally wide quadrifilar S-band antenna that displays circular polarisation. The antenna does not exhibit an isoflux radiation pattern due to its shorter length, however, has a wide beamwidth. The antenna consists of 2.5 turns, is approximately 88.7 mm long, has a mean diameter of 42 mm and is constructed from 1.91 mm wire. Full dimensions and electrical simulations of both antennas are given in Appendix A.

Antenna iteration one represents the first choice and the most ideal scenario for successful CubeSat-to-ground communications. However, due to its large length, may present difficulties in characterising the antenna as a traditional spring or SMA spring. In a scenario where the research shows that iteration one is not possible, antenna iteration two will be considered as the best design.

## 1.7 Significance of Research

The project is significant in the sense that a unique antenna implementation and deployment system is required, which is confined to the “tuna can” of a CubeSat. This allows for the optimisation of the available surface area of the CubeSat, which allows for design freedom. For example, ZACube-2 has an S-band patch antenna, which requires the side with the antenna on it to be nadir pointing towards the

Earth. While the S-band QHA will also require pointing, it will free up space for an additional payload or subsystem. Overall, this will benefit the CubeSat and space industry, by looking at how large objects, relative to a CubeSat, may be compacted, stored, and reliably deployed, allowing for greater design freedom and optimal use of available space on a CubeSat.

## **1.8 Expected Outcomes**

The expected outcomes of the research include a test methodology for the mechanical antenna implementation and mechanical antenna deployment system, as well as a reliability assessment, which can be used to produce a validated prototype that conforms to CubeSat standards. The validated prototype allows for greater design freedom of antenna positioning on CubeSat platforms, as well as more optimal use of the available surface area.

## **1.9 Dissertation Preview**

The dissertation follows a simple layout where the background of the research is initially explored, followed by a literature review, covering key aspects of interest. Following the literature review, the design and testing methodologies are explored. After the design and test methodology have been established, antenna design is explored. The highest scoring antenna design is then subjected to simulations, after which simulations are validated through tests, where applicable. Lastly, the research project conclusion is given, followed by recommendations.

# Chapter 2

## Literature Review

### 2.1 CubeSat Design Specification

#### 2.1.1 Historical Background of CubeSats

The historical background of CubeSats is required, as it is important to understand where and why the CubeSat project was started, as well as the purpose of CubeSats. The CubeSat Project started off as a collaboration between two universities and professors, namely Prof. Jordi Puig-Suari at California Polytechnic State University (Cal Poly), and Prof. Bob Twiggs at Stanford University's Space Systems Development Laboratory (SSDL) , in 1999 (Munakata et al., 2009).

The intention of the project was to provide a design standard for miniaturised satellites so that costs and developments could be reduced and to increase accessibility to space, as well as sustain frequent launches (Munakata et al., 2009). The CubeSat Project's main objective was to provide access to space for small payloads.

#### 2.1.2 General and Mechanical Requirements

CubeSats follow a set of regulations called a CubeSat Design Specification (CDS) (Munakata et al., 2009). The CDS looks into the CubeSat standards that need to be followed, as well as the general, mechanical, electrical, and operational requirements, which must be adhered to.

All CDS requirements must be adhered to, except when overruled by launch provider requirements. Important general requirements which apply to the research include that all parts of a CubeSat must remain attached to the CubeSat during launch, ejection, and operation (general requirement 3.1.2). This ensures that no additional space debris is ejected, but limits the overall design (Munakata et al.,

2009).

All mechanical requirements are important and must be adhered to. An important mechanical requirement to heed is the mass limit set per ‘U’ form factor. According to the CDS, CubeSat mass limits for 1U, 2U and 3U Cubesats are 1.33 kg, 2.66 kg and 4 kg, respectively. Therefore, the antenna system must be as lightweight as possible.

### 2.1.3 “Tuna can” Dimensions

The research project specifically investigates how an antenna can be mechanically stowed and deployed from the “tuna can” or extra volume of a CubeSat. The general dimensions of the “tuna can” are defined in the CDS. Figures 2.1 and 2.2 depict the general dimensions of the “tuna can”.

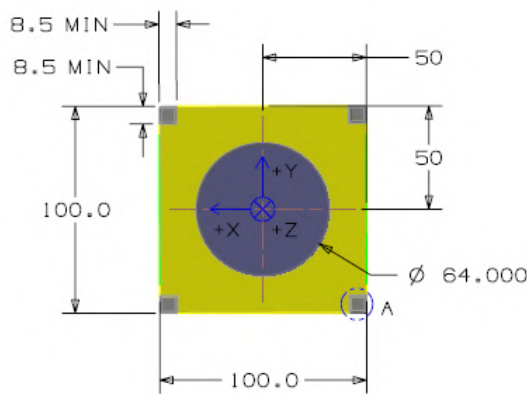


Figure 2.1: “Tuna can” Dimensions 1 (Munakata et al., 2009)

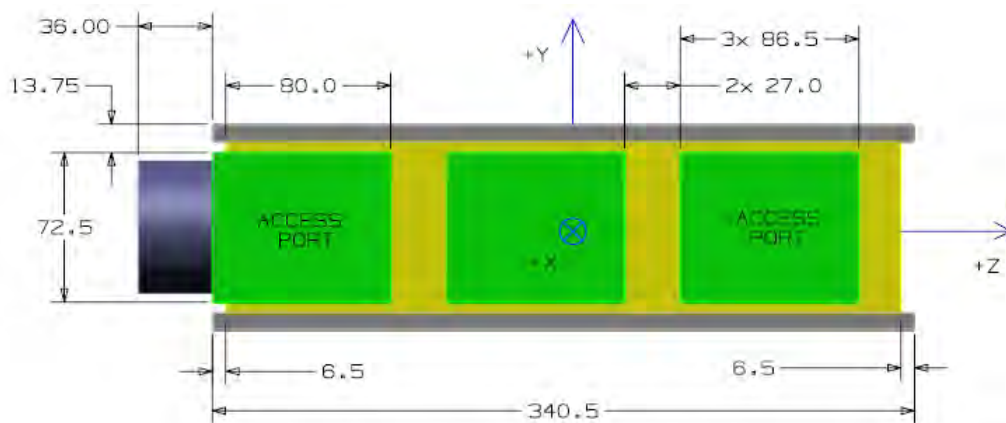


Figure 2.2: “Tuna can” Dimensions 2 (Munakata et al., 2009)

The “tuna can” has an outer diameter of 64 mm and a depth of 36 mm. It is important that the antenna design fits inside the mentioned dimensions, otherwise, the design is deemed unsuitable.



## 2.1.4 CubeSat Standards

CubeSats must adhere to the relevant design and test standards so that they can be subjected to qualification and acceptance testing so that flight readiness can be determined. The CDS, as mentioned previously, is a good starting point for developing a CubeSat. While the CDS provides a guideline for the construction of CubeSats, it does not cover specific test qualification and acceptance guidelines, test parameters and design methodologies. For these crucial parameters, NASA's General Environmental Verification Standard (GEVS) and ESA's European Cooperation for Space Standardisation (ECSS) must be considered.

In regard to CubeSats, NASA's GEVS and ESA's ECSS are fairly similar, however, have their key differences in methodology. Within CPUT the standards and methodologies presented by the ECSS are adhered to. To keep in line with CPUT, ECSS guidelines and methodologies will be followed. The following sections will cover the relevant required tests and design standards which must be adhered to in accordance with the CDS and ECSS.

### 2.1.4.1 CDS Testing for Space and Launch

Space is a harsh environment, however, the trip to space is just as harsh. The research project prototype must be subjected to various tests to ensure its survivability during a mission and launch. According to the CDS, the tests to perform include vibration and shock testing, thermal cycling (within a vacuum), visual inspection, and thermal vacuum bake out, which is conducted for the outgassing of components (Munakata et al., 2009).

A test methodology will need to be established (measured against design specifications, as described by ECSS) so that the durability of the design can be measured. Failure to pass the above-mentioned tests (whether simulated or tested) will result in an unsuitable design. Electrical testing will be conducted to determine if the QHA and ground plane work from an electrical standpoint and will be handled by the CPUT engineering team. The tests required can be very expensive and are subject to the availability of funds.

### 2.1.4.2 ECSS Standards and Methodology

According to Kriedte and El Gammal (1995), the ECSS is an initiative established by the ESA to help develop a set of coherent and comprehensible standards for use in all European space activities. The standards provide initial test parameters that must be adhered to for both analysis by simulation and analysis by testing. Tests are conducted to validate the simulations performed.

The ECSS standards and handbooks for satellite design and testing are usually

used for designing larger, more robust satellites, as opposed to CubeSats. However, due to CubeSats becoming more prolific and widely utilised, documents such as the “Tailored ECSS Engineering Standards for In-Orbit Demonstration CubeSat Projects” have been developed. The document was created to outline the relevant ECSS standards which apply to CubeSat projects. According to the document, the following general standards must be followed within the mechanical field for CubeSat component and payload design;

- ECSS-E-ST-31C Thermal control general requirements
- ECSS-E-ST-32C Rev.1 Structural general requirements
- ECSS-E-ST-32-08C Materials
- ECSS-E-ST-33-01C Mechanisms

The above general standards provide guidelines and methodologies for sound design meant for space programmes. The mentioned standards are also accompanied by ECSS handbooks providing detailed methodologies and test parameters to adhere to. For the design project, the test parameters and methodologies described in the ECSS-E-HB-32-26A handbook will be used in the design of the antenna. The mentioned handbook covers spacecraft mechanical loads and analysis. The handbook coincides with the tests that need to be run in accordance with the CDS. However, more in-depth explanations and test parameters are given. According to the handbook ECSS (2013), the following simulations and tests must be accomplished to characterise the flight environment for verification of space hardware:

- Quasi-static loads:  
Defined as a combination of static and dynamic loads, which are combined to form an equivalent static load specifically for design purposes. The load is generally expressed as an equivalent acceleration at the centre of gravity (CoG).
- Sine Vibration:  
The objective of sine vibration simulations and testing is to verify the strength of the spacecraft structure (whether primary or secondary). Sine wave sweep consists of a periodic sweep specified to a particular space launcher manual, usually conducted in the range of 10  $Hz$  to 100  $Hz$ .
- Random Vibration:  
Random vibration testing and simulations help exhibit that the hardware is capable of surviving the high frequency environment that may be experienced during the launch phase of a mission. Tests are usually performed on a 'shaker' to a specified vibration level, depending on the launcher service used.
- Shock Testing: Shocks are described as transient mechanical loading that results from launcher stage separations, launcher separation and other events. They are mainly caused by the actuation of release mechanisms and deployable

mechanisms. The main objective of shock testing is to prove the hardware is capable of withstanding the shock loads specified by space launcher manuals.

The ECSS guidelines also outlines factors of safety (FOS) that payloads or system design should adhere to, depending on the application. According to the handbook, mission payloads FOS can be determined via simulation, physical testing or preferably both. According to ECSS guidelines, in instances where designed systems do not meet required FOS values, the design must be tested to show that it is both reliable and safe. According to ECSS (2013), the antenna design should incorporate a FOS of 1.5. Therefore, ECSS methodologies as described in the ECSS-E-HB-32-26A (ECSS, 2013) handbook will be followed.

Another important aspect of the design is the creation of space debris. The following section covers the guidelines set out for the reduction of space debris.

### **2.1.4.3 IADC Guidelines**

Following Inter-Agency Space Debris Coordination Committee (IADC) guidelines, the satellite and its parts must be disposed of properly. According to the guidelines of the IADC set in 2002, satellites passing through the LEO region or have the potential to interfere in the region should be de-orbited or be moved into a reduced lifetime orbit or be retrieved (Mejía-Kaiser, 2020).

A program such as the debris assessment software (DAS) will be used to assess possible re-entry threats. DAS is distributed by the NASA Orbital Debris Program Office as a means of evaluating a space mission's compliance with NASA's requirements for the reduction of orbital debris (Lips and Fritsche, 2005).

## **2.2 Shape Memory Alloys**

SMA's are metallic alloys, which can experience reversible martensitic phase transformation as a result of heat. When heated above a transition temperature, they are able to recover strain (Sanusi et al., 2014).

SMA's are a special order of materials, which are able to recover strain when an increase in thermal load is applied. When the thermal load is increased, shape recovery from specimens subjected to high applied loads is possible. Under certain conditions, where SMAs are under the influence of applied mechanical cyclic loading, they are able to store and release mechanical energy by experiencing a reversible hysteretic shape change (Lagoudas et al., 2008).

SMAs have peculiar characteristics, which make them excellent for many applications including, sensing, actuation, impact absorption and vibration damping,

among others. Applications of SMAs are wide and varied; they are used in industrial sectors such as the automotive, biomedical, oil exploration, and aerospace industries.

### 2.2.1 History Of Shape Memory Alloys

The history of SMAs starts off in the 1890s with the discovery of the martensite phase in steels by Adolf Martens (Lagoudas et al., 2008). During the 1900s, martensitic transformations are stated to perhaps be the most widely studied metallurgical phenomenon, which helped contribute to the discovery of SMAs. In 1949, the concept of thermoelastic martensitic transformations was established, which explained the reversible transformation changes, associated with the martensite phase. This was based on observations of the reversible transformation of martensitic structure, found in CuZn and CuAl alloys under applied thermal loads. However, even documented alloys that exhibited these reversible martensitic transformation traits remained unutilised until 1963 (Lagoudas et al., 2008).

A breakthrough for SMAs with regard to engineering applications came about with the discovery of NiTi by W. J. Buehler (Buehler et al., 1963). The material displayed good mechanical properties and shape recovery capabilities. Following its discovery, the material was named “NiTiNOL”, coined for the material consisting of equal parts Ti and Ni, as well as being discovered at the Naval Ordnance Laboratory (NOL). The shape recovery behaviour or nature of the materials was termed the Shape Memory Effect (SME). The discovery of the materials resulted in a surge of active research regarding SMAs. As a result of this breakthrough, the previously unknown effects of composition, heat treatment and material microstructure were studied.

Many and varied commercial applications have been developed, since the discovery of NiTi in 1963. In the 1970s biomedical applications of NiTi were developed, however, it was only in the 1990s that the well-known NiTi stent made its commercial debut (Lagoudas et al., 2008). Thanks to the active research conducted, SMAs found many additional applications from air conditioning and electronic cable connectors to many other products.

### 2.2.2 General Properties of SMAs

SMAs exist in two crystal phases, the austenite and martensite phases. The austenite phase is the parent phase and is stable at high temperatures. It consists of an ordered body-centred cubic structure that has only one variant or true form (Sanusi et al., 2014). The martensite phase is softer and stable at low temperatures. NiTi SMAs in the martensite phase can be easily distorted due to their relative softness. The martensite can exist in multiple variations, depending on the phase transformation (Sanusi et al., 2014).

Among commercially available SMAs, NiTi (nickel-titanium) alloys are widely used for their shape-memory characteristics, mechanical properties, machinability, corrosion resistance, temperature cycle stability and wear resistance (Sanusi et al., 2014). NiTi generally consists of equal parts Nickel and Titanium, however other compositions are available. Reducing the amount of Titanium present reduces the activation temperature of the alloy.

Copper-based SMAs are preferred for high-temperature applications due to their ability to handle higher temperatures, compared to other SMAs (Najah Saud Al-Humairi, 2019).

Due to Nitinol's extensive use in aerospace applications, proven space heritage, and lower activation temperatures, Nitinol will be considered for the research.

### 2.2.3 Phenomenology of Phase Transformation in SMA

A metallurgical phase diagram of a metallic alloy is a representation of the equilibrium conditions between set distinguishable phases (Lagoudas et al., 2008). These diagrams separate distinct phases from each other with the use of phase boundaries or equilibrium lines. For alloys consisting of at least 2 elements, the concentration of elements becomes an important measurable variable. Temperature is also a common variable that is represented along the ordinate axis.

Phase diagrams can have different control variables, which help represent the equilibrium phases. Such control variables include stress, temperature, the concentration of electric field, etc. Within an operating temperature range, SMAs depict two phases consisting of different crystalline structures, with different properties (Lagoudas et al., 2008).

One phase is the austenite phase (parent phase), which occurs at high temperatures, while the martensite phase (product phase), occurs at low temperatures. According to Lagoudas et al. (2008), the austenite phase consists of a cubic crystal structure and differs from the martensite phase, which consists of either a tetragonal, orthorhombic, or monoclinic crystal structure.

The transformation from one crystal structure to another takes place through martensitic transformation, also called shear lattice distortion (Lagoudas et al., 2008). Martensitic crystal structures formed may exhibit a different orientation, which is known as a variant. Martensitic variants are found in two forms, twinned and detwinned martensite (Lagoudas et al., 2008). Through a combination of self-accommodating martensitic variants (i.e., no set form), detwinned, also known as reorientated martensite is formed where a specific variant is usually found to be dominant. The reversible phase change from austenite to martensite is the foundation for the unique behaviour SMAs exhibit.

When an SMA specimen is cooled under no applied load, the crystal structure

transforms from austenite to martensite, which is termed the forward transformation. As a result of the transformation, several martensitic variants can be formed. For Nitinol, up to 24 martensitic variants have been recorded (Lagoudas et al., 2008). The arrangement of these variants exists in a way that the average observable change in shape can be deemed as negligible, which results in twinned martensite. When heated, the crystal structure transforms from the martensitic to the austenite phase. The transition is referred to as the reverse transformation. The reverse transformation has no associated material shape change.

Figure 2.3 depicts the associated crystal structures of twinned martensite and austenite for a typical SMA (such as Niti) as well as the temperatures experienced with the various stages of phase transformation. When the material is cooled, the austenite phase (under no loading) initiates its transformation, where twinned martensite at the martensitic start temperature ( $M_s$ ) is formed and finalises the forward transformation at the martensitic finish temperature ( $M_f$ ). The SMA now exists in the twinned martensitic phase.

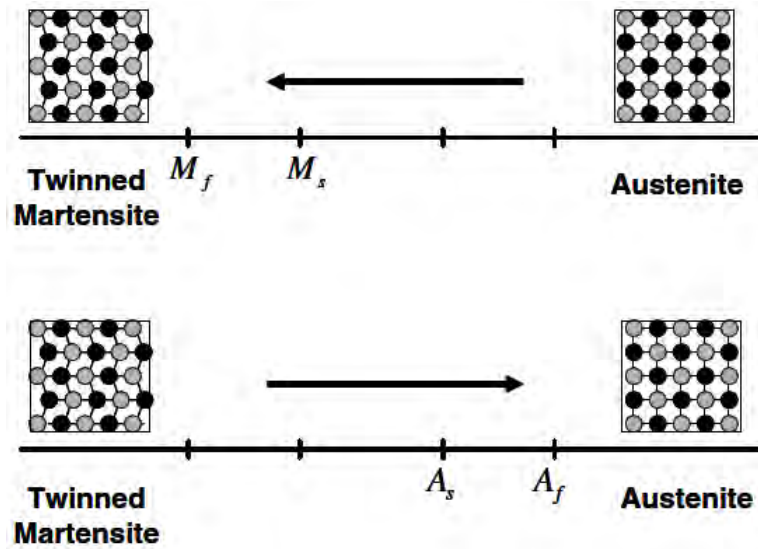


Figure 2.3: Temperature Induced Phase Change Under No Mechanical Loading (Lagoudas et al., 2008)

Under an increase in temperature, the reverse transformation commences at the austenite start temperature ( $A_s$ ) and is finalised at the austenite finish temperature ( $A_f$ ). Figure 2.4 shows that when a mechanical load is applied to the SMA, while in the twinned martensitic phase, detwinning of the martensite is possible by reorientating a certain number of variants. When the load is released, the deformed shape of the material is retained, because of the macroscopic shape change associated with the detwinning process (Lagoudas et al., 2008).

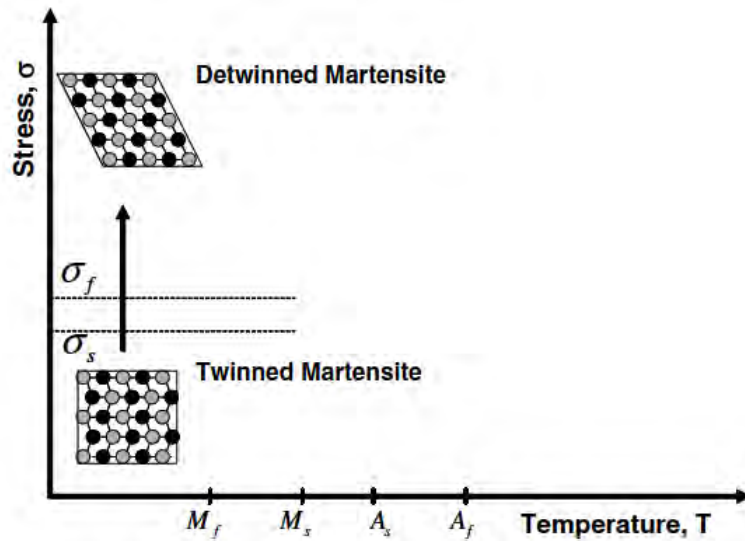


Figure 2.4: Depiction of SME Showing Detwinning of Material Under an Applied Stress (Lagoudas et al., 2008)

Heating of the SMA to the austenite finish temperature will result in the reverse transformation, causing the material to reorientate to its austenite phase configuration and resulting in complete shape recovery. If the material is cooled again to a temperature equal to or below  $M_f$ , twinned martensite is once again formed with no shape change observed. This process is termed the Shape Memory Effect (SME) and is depicted in Figure 2.5.

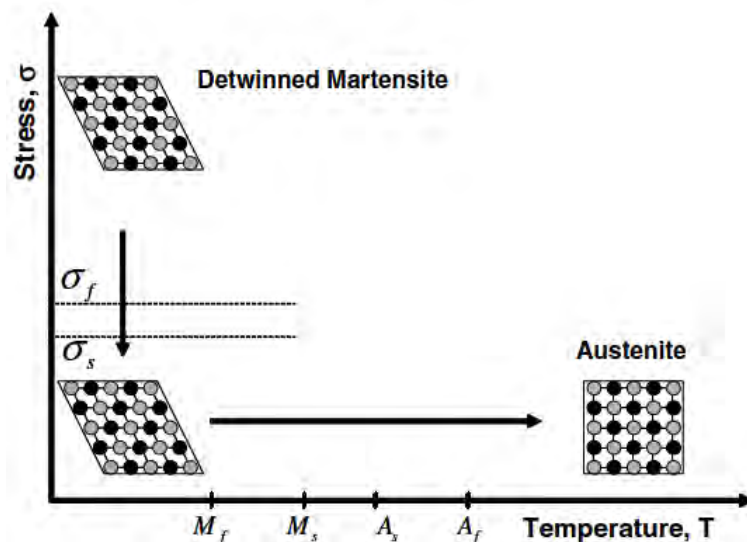


Figure 2.5: Depiction of SME Showing Unloading and Heating to Austenite Under No Load (Lagoudas et al., 2008)

For the detwinning process to start, a load bigger than the detwinning start stress  $\sigma_s$  is required. High stresses will result in the material completely detwinning, which occurs at the detwinning finish stress  $\sigma_f$ . When a material is cooled under

a load greater than the  $\sigma_s$ , while in the austenite phase, detwinned martensite will be formed. If the material is heated again while still under the load, the material will recover its shape. The thermomechanical transformations occur over varying temperatures (as stated) allowing for any SMA to be graphed within the stress-temperature space, as shown in Figure 2.6.

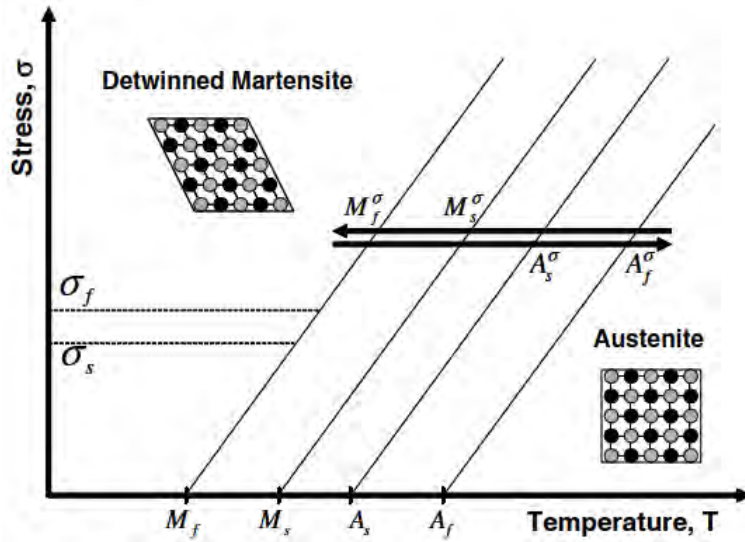


Figure 2.6: Temperature Induced Transformation Under an Applied Load (Lagoudas et al., 2008)

An alternative use of SMA's involves applying a load to the material while within the austenite phase. If the material is subjected to a temperature above  $A_f$ , full shape recovery is observed when the specimen is unloaded. This behaviour is termed the pseudoelastic effect, or otherwise known as superelasticity (Lagoudas et al., 2008). Figure 2.7 shows the typical macroscopic shape change associated with the effect, while Figure 2.8 depicts the typical loading Path of the effect. It is important to note that should the material specimen be subjected to a temperature above  $M_s$ , but below  $A_f$ , only partial shape recovery will be experienced.



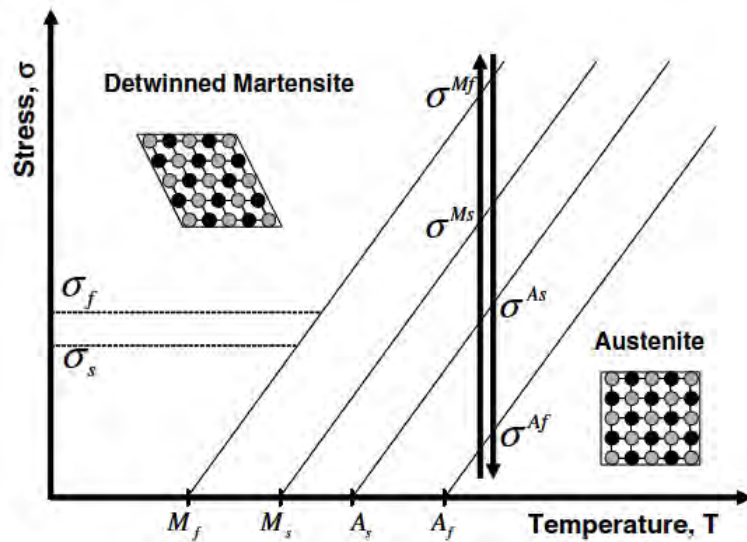


Figure 2.7: Typical Pseudoelastic Loading Path (Lagoudas et al., 2008)

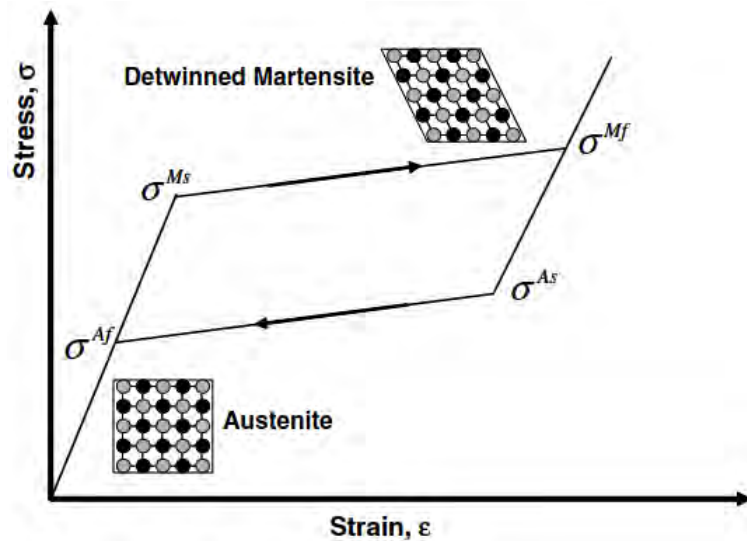


Figure 2.8: Typical Pseudoelastic Stress-Strain Diagram(Lagoudas et al., 2008).

Figure 2.9 depicts the phase diagram. The phase diagram shows the relationship between the distinct phases of the material, at their respective temperature and where applicable, stresses. The diagram interprets the material response of the SMA when exposed to thermomechanical loading, causing a thermal response (under or without load) and pseudoelastic behaviour. The SME and pseudoelastic effect will be explained further in the next sections.

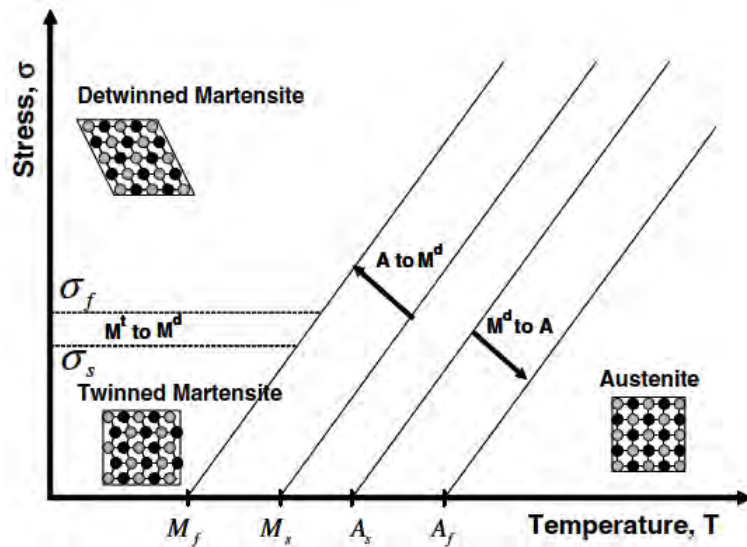


Figure 2.9: Typical Stress-Temperature Diagram for an SMA (Lagoudas et al., 2008).

## 2.2.4 Pseudoelasticity

The superelastic phenomenon associated with SMA's is a result of a stress-induced transformation resulting in strain generation while a specimen is loaded and then strain recovery when unloaded at temperatures above  $A_f$ , as described by (Lagoudas et al., 2008). The thermomechanical loading Path associated with the superelastic behaviour starts at temperatures where stable austenite exists, under a load detwinned martensite is formed and then returns to the zero-stress state where austenite phase is stable, once the applied is removed. An example of this is shown in Figure 2.10 at Path 1. A pseudoelastic test is usually used at a constant temperature above  $A_f$  to characterise the superelastic behaviour of the specimen.

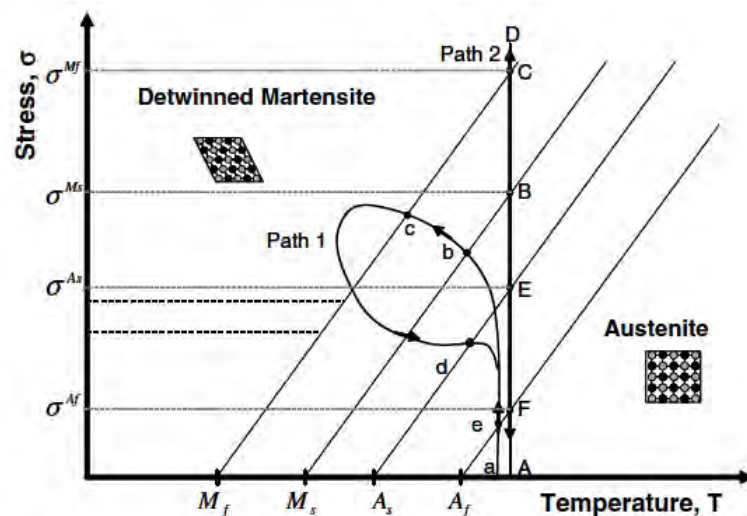


Figure 2.10: Loading Paths Phase Diagram of the Pseudoelastic Effect (Lagoudas et al., 2008).

The pseudoelastic behaviour can be explained in greater detail by observing Path 2 in Figure 2.10 and comparing the Path with its corresponding experimental data as depicted in Figure 2.11. The graph starts at a zero-stress level at a temperature above  $A_f$ . When a specimen is loaded, the austenite phase is subjected to elastic loading, characterised as points A to B. The loading Path crosses the starting point of the martensitic transformation at a specific load level. This stress level ( $\sigma_{M_s}$ ) marks the start of the transformation of austenite into detwinned martensite. The stress-induced transformation results in the generation of inelastic strain. From point B to C, the stress level increases to ( $\sigma_{M_f}$ ) where the loading Path intercedes the  $M_f$  transformation limit, ending the transformation. The

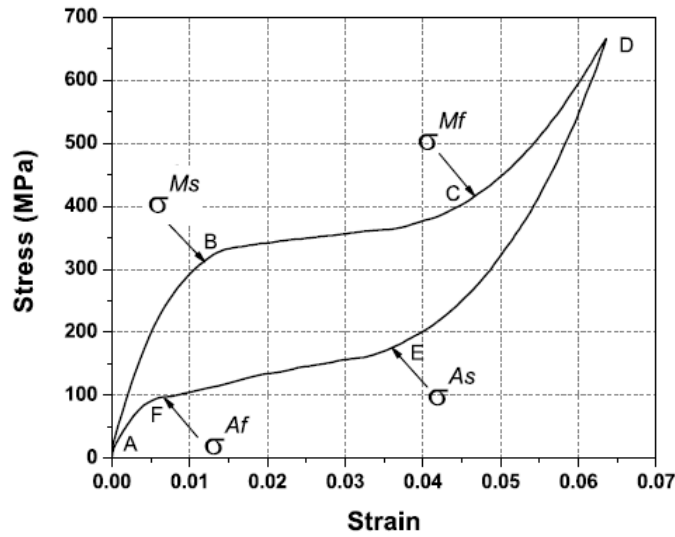


Figure 2.11: Loading Path of a Typical SMA (Lagoudas et al., 2008).

The martensitic transformation is recorded. due to the change in slope of the  $\sigma - \varepsilon$  diagram that is related to the elastic loading of the martensitic phase. Increasing the stress from this point causes no further transformation. Only the elastic deformation of detwinned martensite is experienced, seen between points C and D. When the specimen is unloaded the martensite is unloaded, along the Path created by points D to E. At point E, the unloaded specimen crosses the austenite start surface, which results in the transformation of martensite to austenite. Therefore, the strain is recovered at the end of unloading as a result of phase transformation.

The end of the transformation occurs at point F, where the unloading curve joins the elastic phase of the austenite ( $\sigma_{A_f}$ ). The material then further unloads to point A in an elastic manner. The reverse and forward transformations during a full pseudoelastic cycle results in a hysteresis, where the area encapsulated by the stress-strain diagram represents the dissipated heat by the transformation cycle (Lagoudas et al., 2008). The stress levels and size of the hysteresis associated with SMAs vary depending on the material specimen used, as well as the test conditions.

Detwinned martensite that is formed under an applied load from the austenite phase (either through Path 1 or 2) is called stress-induced martensite (SIM).

Pseudoelasticity is used to describe the superelastic effect as well as the rubber-like effect associated with SMAs (Otsuka and Wayman, 1999). However, the reversible phase transformation caused by an applied load is strictly known as superelastic behaviour. The rubber-like effect while similar to the superelastic effect is an exclusive behaviour, which is attributed to the martensite phase only and occurs due to the reversible reorientation of martensite. However, falls outside the project scope.

## 2.2.5 Shape Memory Effect

The shape memory effect (SME) is an occurrence whereby an SMA that has been deformed can revert to its trained shape after being heated above a certain temperature. The SME phenomenon is the result of the reversible martensitic transformation of an SMA between austenitic and martensitic phases through applications of heat or stress (Sanusi et al., 2014).

There are two types of SMEs; one-way and two-way SMEs. One-way SME starts from the highly symmetric austenitic phase. After cooling to the martensite phase, the material can be subjected to permanent deformations and changes to its original state when heated above the specimen's specified transition temperature. Two-way SMEs are able to remember two shapes; one at a low temperature and another at a high temperature (Sanusi et al., 2014).

For the research project, two-way SMEs might cause design issues or antenna deployment failures, due to the temperature cycling experienced in space; therefore one-way SMEs will be considered. The one-way SME is explained in further detail below.

The shape memory effect associated with SMAs occurs when any SMA is deformed (loaded) within the twinned martensite phase and is then unloaded while the specimen is below the austenite start temperature. Upon heating the specimen to the austenite finish temperature, the SMA will transform (through reverse transformation) back to the original parent shape (austenite phase).

The transitory character of the SME is depicted in Figure 2.12 and can be perceived by looking at the loading Path of the combined stress, strain, and temperature relationship of the SME. The figure below depicts typical experimental data for a NiTi specimen subjected to uniaxial loading. The strain ( $\epsilon$ ) is described as the change in length recorded due to loading, divided by the original length of the specimen.

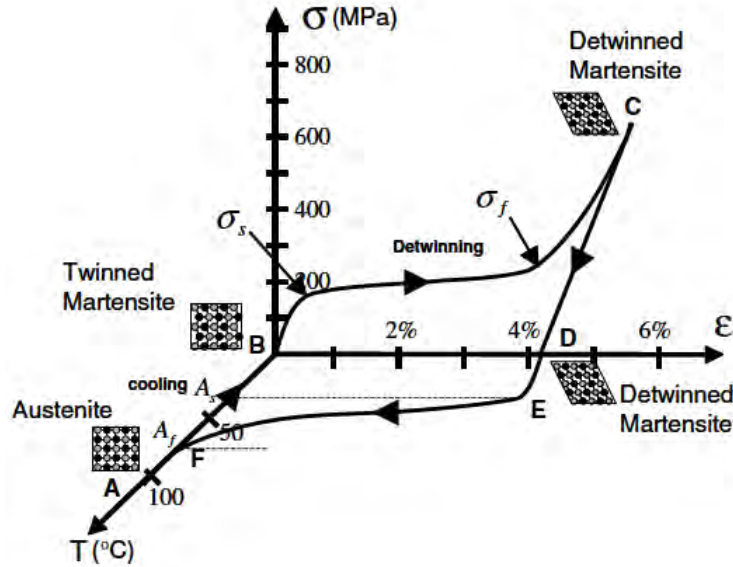


Figure 2.12: Stress-Strain-Temperature Phase Diagram Depicting the SME of a Typical NiTi Specimen (Lagoudas et al., 2008).

Looking at Figure 2.12, according to Lagoudas et al. (2008), point A is the parent phase (austenite). Cooling of the austenite under no load, to temperatures below that of the forward reaction ( $T < M_f$  and  $M_s$ ), results in twinned martensite found at point B. Under an applied load (when stressed) that surpasses the  $\sigma_s$ , the reorientation of twinned to detwinned martensite begins. This process results in the formation of favourably oriented martensite at the cost of the less favourable variants. The detwinning culminates at the finish stress ( $\sigma_f$ ), which is characterised by the end of the plateau like line in the  $\sigma - \varepsilon$  diagram.

At point C, the material is unloaded elastically to point D, where the detwinned martensitic phase is retained. Under no load, if the material is heated to  $A_s$  at point E, the reverse transformation is initiated. At point F, the transformation of the material is complete. At this temperature and beyond, only the austenitic parent phase exists. If no plastic strain is formed during the detwinning process, the original shape of the SMA is recovered (point A).

The strain that is recovered as a result of the phase transformation between the distinct phases is known as the transformation strain ( $\varepsilon^t$ ). The whole SME (Shape Memory Effect) cycle can be repeated. This type of SME is known as the one-way shape memory effect.

## 2.2.6 Limitations of NiTi Shape Memory and Superelastic Behaviour

Nitinol shape memory alloy specimens have recorded a recoverable strain of up to 8% upon unloading and heating. Any strain that exceeds this limit will remain

as permanent plastic deformation. An important aspect to keep in mind when using SMAs is that they must not stray too far away from their recommended use conditions, especially with regard to temperature. Using SMAs in operating conditions that are vastly different from the activation temperatures may result in the shape memory characteristics being altered (Longela, 2013).

### 2.2.7 Composition of NiTi SMAs and its Effects

From the initial investigation of SMAs in the 1930s, a vast variety of SMAs have been researched, of those Nitinol is the most researched. Various compositions were created by combining varying alloying elements with known alloys, creating a catalogue of SMAs with different properties to select from. This provides engineers with a variety of SMA properties to select for their particular constraints and design needs. SMAs are categorised based on their primary/main alloying elements, mode of actuation, activation temperature and behaviour. The following section looks into NiTi SMAs, some of their properties and some effects of alloying.

The Nitinol alloy composition is the most studied SMA and is also used in a vast variety of commercial applications (Lagoudas et al., 2008). Nitinol exhibits a strong SME and pseudoelastic behaviour, making it the ideal material for many applications. It has high corrosion resistance and is biocompatible. The crystallography, as well as the thermomechanical response of the material, are well known and documented compared to less widely used alloys, as well as the effects of heat treatment and activation temperature found with a change of material composition.

The effects of the change in the composition of NiTi based alloys can be quite vast depending on the ternary alloy used. The equiatomic composition of NiTi exhibits a maximum  $A_f$  temperature of  $120\text{ }^\circ\text{C}$  of all studied NiTi compositions (Lagoudas et al., 2008). A decrease in the Ni percentage of the alloy does not lead to a change in the activation temperature of the alloy. However, if the percentage of the Nickel present in the specimen is increased above 50%, the activation temperature of the specimen decreases. An activation temperature of as low as  $-40\text{ }^\circ\text{C}$  has been recorded for NiTi with a 51% Nickel composition (Lagoudas et al., 2008). It is important to note that this change in composition from the standard base causes the room temperature ( $23\text{ }^\circ\text{C}$ ) characteristics of NiTi to change from SME to pseudoelasticity.

NiTi alloys display transformation strain recovery of up to 8% and are commercially available in many forms. More recent studies have shown that a NiTi composition of 55% Nickel consists of a chemically multiphased alloy that exhibits activation temperatures in the range of  $-10\text{ }^\circ\text{C}$  and  $60\text{ }^\circ\text{C}$ . However, this particular composition exhibits low transformation strain (Hartl and Lagoudas, 2007).

The addition of Copper, preferably replacing Nickel, forms NiTiCu alloys. Adding copper reduces the hysteresis of the SMA response, but also decreases the transformation strain. The addition of copper also greatly affects the sensitivity of

the martensitic start temperature, depending on the composition (Lagoudas et al., 2008).

In situations where the engineering design requires an SMA that shows little response to wide temperature ranges, Niobium can be added to the NiTi alloy to form NiTiNb. However, the addition of the material leads to a broader thermal hysteresis. The addition of Nb as a ternary alloy also results in only partial strain recovery due to the formation of pure Nb precipitates, which are soft.

Lastly, the addition of alloying materials such as Pd, Pt, Hf or Zr results in high temperature SMAs. These alloys exhibit high transformation temperatures, which can withstand and be used in scenarios where high operating temperatures are experienced (Lagoudas et al., 2008).

## 2.2.8 Properties of NiTi Alloy

Properties of NiTi can be very hard to find without experimentation of a particular sample. This is due to that SMA properties can be modified by changing the composition, mechanical working, and heat treatment of the material. Figures 2.13 to 2.16, display the properties of NiTi as described by Nitinol medical components manufacturing company Johnson Matthey. All values expressed in the figures below are for the full transformation of martensite to austenite.

Transformation temperature		-200 to 110 deg. C
Latent heat of transformation		5.78 cal/g
Transformation strain (for polycrystalline material)	for a single cycle	max 8%
	for 100 cycles	6%
	for 100,000 cycles	4%
Hysteresis		30 to 50 deg. C

Figure 2.13: Nitinol Transformation Properties (Johnson-Matthey, 2015)

The hysteresis of the material specimen can be reduced by the addition of a ternary alloy such as previously mentioned or by partial transformation of the material.

Melting point		1300 deg. C (2370 deg. F)
Density		6.45 g/cu.cm (0.233 lb/cu.in)
Thermal conductivity	austenite	0.18 W/cm * deg. C (10.4 BTU/ft * hr * deg. F)
	martensite	0.086 W/cm * deg. C (5.0 BTU/ft * hr * deg. F)
Coefficient of thermal expansion	austenite	11.0E-6/deg. C (6.11E-6/deg. F)
	martensite	6.6E-6/deg. C (3.67E-6/deg. F)
Specific heat		0.20 cal/g * deg. C (0.20 BTU/lb * deg. F)
Corrosion performance		excellent

Figure 2.14: Nitinol Physical Properties (Johnson-Matthey, 2015)

Resistivity [resistance = resistivity * length / cross-sectional area]	austenite	approx. 100 micro-ohms * cm (39 micro-ohms * in)
	martensite	approx. 80 micro-ohms * cm (32 micro-ohms * in)
Magnetic permeability		< 1.002
Magnetic susceptibility		3.0E6 emu/g

Figure 2.15: Electrical and Magnetic Nitinol Properties (Johnson-Matthey, 2015)

Young's modulus****	austenite	approx. 83 GPa (12E6 psi)
	martensite	approx. 28 to 41 GPa (4E6 to 6E6 psi)
Yield strength	austenite	195 to 690 MPa (28 to 100 ksi)
	martensite	70 to 140 MPa (10 to 20 ksi)
Ultimate tensile strength	fully annealed	895 MPa (130 ksi)
	work hardened	1900 MPa (275 ksi)
	Poisson's ratio	0.33
Elongation at failure	fully annealed	25 to 50%
	work hardened	5 to 10%
Hot workability		quite good
Cold workability		difficult due to rapid work hardening
Machinability		difficult, abrasive techniques preferred

Figure 2.16: Nitinol Mechanical Properties (Johnson-Matthey, 2015)

The modulus of elasticity,  $E$  or young's modulus, is highly nonlinear with temperature.

### 2.2.9 Shape Setting

Training, or shape setting, is the process used to form SMAs, into a new “memory” shape. This is accomplished by using a fixture or mandrel, to fix a material specimen



in the desired configuration and performing a heat treatment. The temperature required for heat treatment is in the range of 500-550 °C. However, some sources suggest that temperatures as low as 400 °C can be used (Johnson Matthey, 2021). The specimen should be cooled rapidly to avoid ageing effects; a water quench or air cooling is suggested. The duration of the heat treatment should allow the cross-section of the specimen to heat up evenly (Herring, 2010). The training times and parameters used for shape setting are usually determined experimentally per a specimen (Johnson Matthey, 2021).

Alternatively, the wire could be re-trained using resistive heating (Case, 2004). By using currents in the range of 3-5 A (greater wire thickness may require higher amperes). However, this method does not always yield favourable results. According to Case (2004), an estimation of the wire temperature can be deduced from the following equation:

$$T_{max} = 16.383\frac{I}{d} + 3.987\left(\frac{I}{d}\right)^2 \quad (2.1)$$

Where;  $T$  is the wire temperature,  $I$  is the current and  $d$  is the wire diameter in  $mm$ .

Once trained the SMA  $A_s$  and  $A_f$ , can be determined using Differential Scanning Calorimetry (DSC). DSC is a technique where a specimen is tested to discover the difference in the amount of heat required to increase the temperature of a sample and reference and is recorded as a function of temperature (Lagoudas et al., 2008). Alternatively, should the technique/equipment required not be available, the activation temperatures can be determined through the use of an oven or, if the activation temperatures are low enough, varying degrees of hot water.

## 2.3 Theory

### 2.3.1 Helical Spring Theory

Helical compression springs are open-pitch springs, which are designed to resist compression or to store energy. Many configurations and wire shapes can be used to form the desired spring depending on the application. Wire shapes such as rectangular and circular cross-sections are of particular interest. However, for simplicity and adherence to the electrical design, only wires of a circular cross-section will be considered for the research project.

Round high-carbon steel is usually used for spring design and manufacturing (Shigley and Mischke, 1996). However, a wide range of shapes and other materials can be used depending on the application and environment. The springs usually consist of a uniform coil diameter, also known as the mean diameter. However,

conical, barrel and hourglass shapes, among others, are also available. The antenna design consists of a uniform coil diameter. Therefore, only a uniform coil diameter spring design approach will be considered.

Helical compression springs experience stress in the torsional mode, where stress within the elastic range is not uniform about the cross-section of the wire. According to, (Shigley and Mischke, 1996) the maximum stress induced in such a spring is found on the inner surface of the coil, otherwise known as the inner diameter,  $ID$ .

The outside diameter of a helical compression spring must be taken into account where a small clearance tolerance is required, such as is present with the "tuna can". As the spring is compressed, the coil diameter increases. The following equation is used to calculate the expected increase in diameter as the spring is compressed to its solid height (Shigley and Mischke, 1996);

$$OD_{at\ solid} = \sqrt{D^2 + \frac{p^2 - d^2}{\pi^2}} + d \quad (2.2)$$

Where  $D$  is the mean coil diameter of the spring,  $p$  is the pitch of the spring and  $d$  is the wire diameter.

The solid height of the spring will play a key factor in the design of the antenna. The solid height refers to the height of the spring where it is loaded so that all coils of the spring are compressed on top of one another. Different ends play a role in how the solid height of the spring is calculated. Figure 2.17 depicts the possible spring ends that could be used for the antenna.

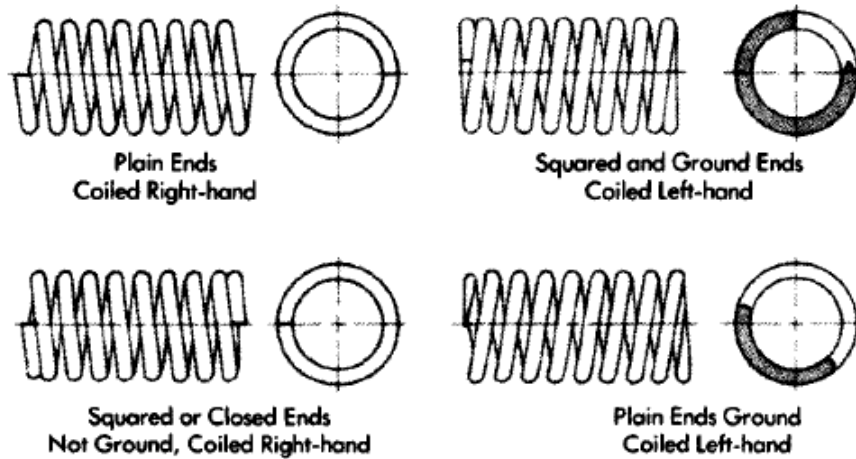


Figure 2.17: Types of Ends for Helical Spring (Shigley and Mischke, 1996)

The solid height for ground springs can be calculated using equation (2.3), while plain spring ends are calculated using equation (2.4), where  $N_t$  is the total number of coils or turns of the spring (Shigley and Mischke, 1996);

$$L_s = (N_t + 1)d \quad (2.3)$$

$$L_s = N_t d \quad (2.4)$$

According to Shigley and Mischke (1996), the spring rate or stiffness of the spring is the change in load per unit deflection and is given by equation (2.5);

$$k = \frac{P}{f} = \frac{Gd^4}{8D^3 N_a} \quad (2.5)$$

Where  $G$  is the shear modulus or modulus of rigidity.  $N_a$  refers to the number of active turns (the number of compressed coil turns). Due to the limited space of the "tuna can" the number of active coils, is taken as the total number of coils.

The torsional or shear stress present in the spring is calculated using equation (2.6)(Shigley and Mischke, 1996);

$$S = \frac{8K_w P D}{\pi d^3} \quad (2.6)$$

When the spring is exposed to elastic conditions, the torsional stress present is diverse about the cross-section of the wire, due to coil curvature and direct shear loading. The maximum shear stress occurs at the surface of the inner diameter of the spring. To account for the effects of direct shear and change due to coil curvature, the Wahl correction factor or stress concentration factor is used to compute the maximum stress present in the spring (Shigley and Mischke, 1996). In most cases, it is given by equation (2.7);

$$K_{w1} = \frac{4C - 1}{4c - 4} + \frac{0.615}{C} \quad (2.7)$$

Where  $C$  is the spring index and is given by  $C = D/d$

The concentration factor changes to equation (2.8), after the spring, has been set out. Set out is a process whereby a spring is manufactured to be slightly longer than its design requirements. It is then compressed to its solid height, where plastic deformation occurs. Thus, changing the free height of the spring. Equation (2.8) is used because the stress present in the spring becomes more uniformly distributed due to plastic flow experienced during the set out (Shigley and Mischke, 1996);

$$K_{w2} = 1 + \frac{0.5}{C} \quad (2.8)$$

According to the local spring manufacturer, Springman, set out is not recommended as it more often than not damages the spring.

The buckling of a spring is also a key factor that needs to be accounted for in spring design. According to Shigley and Mischke (1996), compression springs with a free length that is 4 or more times greater than the mean coil diameter ( $D$ ) could experience buckling when compressed. Buckling can be minimised by using a guide rod, tube or cylinder; however, this can result in additional friction. Buckling conditions of a particular spring can be determined from Figure 2.18. The figure depicts a graph consisting of two curves. Curve A is used for springs that are only fixed at one end, while curve B is used for springs fixed on both ends.

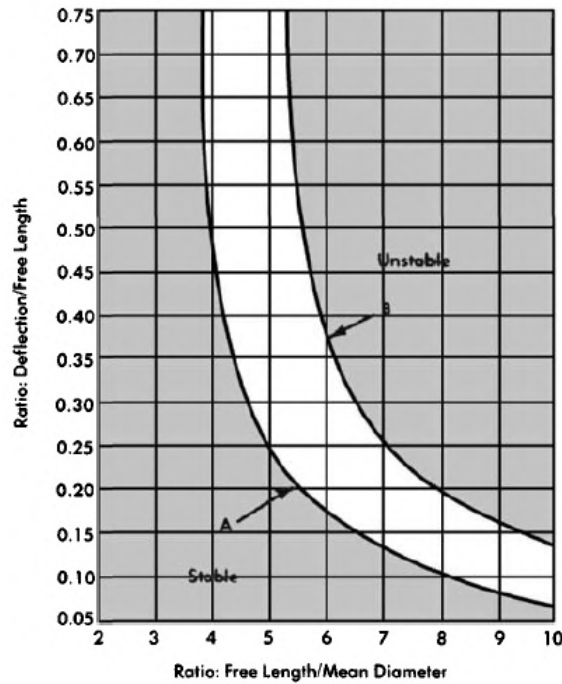


Figure 2.18: Buckling Curves Shigley and Mischke (1996)

Figure 2.18 shows that for any particular spring whose ratio of free length over mean diameter, compared to its deflection over the free length is below curves A and B (depending on constraints), then the spring should not be exposed to critical buckling and therefore will not buckle.

Lastly, the maximum allowable torsional stress for a helical compression spring in static applications is determined by the selected material. It is calculated based on a maximum percentage of the tensile strength of a material. Figure 2.19 shows the percentage of tensile strength utilised.

<b>Materials</b>	<b>Maximum % of Tensile Strength</b>	
	<b>Before Set Removed (<math>K_{W1}</math>)</b>	<b>After Set Removed (<math>K_{W2}</math>)</b>
<b>Patented and cold drawn carbon steel</b>	45%	65–75%
<b>Hardened and tempered carbon and low alloy steel</b>	50%	
<b>Austenitic stainless steels</b>	35%	
<b>Nonferrous alloys</b>	35%	

Figure 2.19: Maximum Allowable Torsional Stress (Shigley and Mischke, 1996)

The antenna design will consist of four helices 90 degrees out of phase with one another. Therefore, four springs would exist in parallel with one another, each of equal length. According to Drotsky (1984), the following equations apply to springs in parallel conditions:

The total force required to compress the springs is taken as the sum of the forces, assuming that all springs are the same length;

$$W = W_1 + W_2 \quad (2.9)$$

As a result, the displacement of one spring is equal to that of all other springs in the parallel system;

$$\delta_1 = \delta_2 = \delta_{total} \quad (2.10)$$

Lastly, the total torsional stress in the system is equal to the sum of torsional stresses in each individual spring;

$$S = S_1 + S_2 \quad (2.11)$$

### 2.3.2 SMA Spring Theory

The QHA poses a few obstacles in terms of characterising how external and internal forces affect an SMA while stowed and deployed. SMAs are smart metals, which as previously stated are manufactured to undergo deliberate phase changes. This poses a challenge of trying to characterise the phase change of stowed to deployed via the strength of material calculations. For simple springs, the classical strength of material theory will be adhered to.

Therefore, the behaviour of SMA helical springs must be characterised. Research into SMA spring actuators showed that the properties, output force, and output displacement of SMA helical springs can be found, according to (Ma et al., 2013). These properties are required as they provide a basis for the initial design and characterisation of an SMA spring.

SMA springs work on the same principles as traditional helical springs, however, SMAs depict a dependence on temperature for the given material's shear modulus. According to Ma et al. (2013), the following equations can be used to characterise an SMA spring. For an SMA, the relationship between temperature and shear modulus is given by;

$$G = \begin{cases} G_M & \text{when } T < M_f < A_s \\ G(\gamma, T) & \text{when } M_f \leq T \leq A_f \\ G_A & \text{when } > A_f \text{ and } T > M_s \end{cases} \quad (2.12)$$

Where  $G$ , represents the shear modulus of the SMA.  $T$  represents the temperature and  $M_s, M_f, A_s$  and  $A_f$  represent the start and finish temperatures of the martensite and austenite phases, respectively.  $G_M$  and  $G_A$  represent the shear modulus for the martensite and austenite phases, respectively, while  $M_f \leq T \leq A_f$ , in the absence of stress. The shear modulus of the SMA can approximately be expressed as;

$$G(T) = G_M + \frac{G_A - G_M}{2} [1 + \sin\varnothing(T - T_m)] \quad (2.13)$$

When the SMA is heated;  $T_m = \frac{(A_s + A_f)}{2}$  and  $\varnothing = \frac{\pi}{A_f - A_s}$ .

When the SMA experiences cooling;  $T_m = \frac{(M_s + M_f)}{2}$  and  $\varnothing = \frac{\pi}{A_s - A_f}$ .

The SMA QHA will experience a moderated increase in temperature (either through supplied current or an element), therefore while the QHA is in the process of being deployed, and while it is operational, it will only experience heating. When the antenna is not operational (such as when it's not in sight of the ground station), the QHA may experience cooling due to the cycling of temperature in space.

Shear stress in an SMA spring can be expressed as;

$$\tau = k \frac{FD}{\pi d^3} = k \frac{FC}{\pi d^2} \quad (2.14)$$

Where  $D$  is the average diameter of the spring,  $d$  represents the wire diameter and  $F$ , is the axial load.  $C$  is the spring index,  $C = D/d$  and  $k$  is termed as the Wahl correction factor, as previously described.

The Wahl correction factor is used to take into account the effect of direct shear and the change in coil curvature present in the SMA spring.

Therefore, when  $M_f \leq T \leq A_f$ , the output force at temperature  $T$  exerted by the spring is given by;

$$F(T) = \frac{G(T)d^4}{8D^3n} \delta_L \quad (2.15)$$

Where the compressed length of the stowed SMA is  $\delta_L$ .

The output displacement of the SMA spring is given by;

$$\Delta\delta = \frac{\pi D^2 n}{d} \left(1 - \frac{G_L}{G}\right) \gamma_{max} \quad (2.16)$$

Where  $G_L$  is the modulus of rigidity of the compressed SMA spring.

### 2.3.3 Thermal Balance Theory

All spacecraft equipment has a range of temperatures, at which they function best. Making sure that all temperatures within the satellite balance is important. This ensures that temperatures of and within the satellite are not too high or too low.

Components only operate efficiently and reliably within specific temperature ranges. Components tend to run hot because there is no convection in space. Space is "cold", however, this coldness cannot be experienced as known on Earth, due to the lack of convection within space. Objects out of view of the sun will radiate their heat away until the object reaches the background temperature of space, which is approximately 3K (Fortescue et al., 2011). Without the protection of the atmosphere, the sun exerts vast amounts of radiative energy, which is harmful to space equipment.

To sum up the problem, electronics and mechanical equipment only operate efficiently and reliably within certain temperature ranges. Therefore, thermal distortion due to different thermal expansion coefficients between materials can lead to distortion of optical and radio instruments, which may break within structural components. Material selection is essential for any mission. According to Fortescue et al. (2011), a spacecraft can only interact with its environment by radiation, which is characterised by an exchange of energy, by the following aspects:

1. Direct solar radiation
2. Albedo radiation (solar radiation reflected from nearby planets)

3. Planetary radiation (thermal energy radiation from nearby plants)
4. Radiation from satellite to deep space

### 2.3.3.1 Solar Radiation

Solar radiation is experienced by spacecraft via the energy radiated by the sun; it is mostly in the visible range, as we can see it. The value for solar intensity is calculated with the solar radiation intensity equation  $J_s$  for a particular planet. The solar intensity is dependent on the total output power of the sun and the distance between a celestial body and the sun. For planets, the average distances are used, therefore set values are usually recorded and used for the solar radiation intensity. The antenna and satellite will be orbiting around Earth, therefore  $J_s$  of Earth will be used. The solar intensity between the Earth and the Sun (extending 1AU) is about  $1371 \text{ W/m}^2$  (Fortescue et al., 2011). However, the solar radiation intensity of the sun fluctuates between solar cycles. According to Gilmore and Donabedian (2002), the maximum solar flux is measured as  $1414 \text{ W/m}^2$  and the minimum as  $1332 \text{ W/m}^2$ .

The solar radiation intensity at any distance from the sun can be found from equation 2.17 (Fortescue et al., 2011):

$$J_s = \frac{P}{4\pi d^2} \quad (2.17)$$

Where:

$J_s$  = Solar radiation intensity ( $\text{W/m}^2$ )

$P$  = Total power output from the Sun ( $3.856 \times 10^{26}$ )

$d$  = Distance from the sun ( $m$ )

The antenna will operate within Earth's influence at an LEO altitude similar to ZACube-1 and ZACube-2 ( $\pm 550 \text{ km}$ ). Therefore, to account for the worst case heating and cooling scenarios, the maximum and minimum solar radiation intensities will be used within calculations.

### 2.3.3.2 Planetary Albedo

Planetary albedo is the amount of Sun energy that is reflected by a planet's surface and or the atmosphere. The value is not necessarily constant over a full orbit or mission. For example, during the winter on a continent such as Europe, a spacecraft/satellite will receive more albedo radiation due to the high reflectance of snow on large portions of land. The average orbital albedo of the Earth ranges from 0.31



to 0.39, according to Fortescue et al. (2011). However, while this assumption provides a good starting point for defining the planetary albedo, it is not as accurate as the method described by Gilmore and Donabedian (2002) in Spacecraft Thermal Control Handbook. According to Gilmore and Donabedian (2002), the albedo and planetary radiation can be interpreted from Figures 2.20 and 2.21 for a hot and cold case.

The values selected from the table depend on the sensitivity of the surface exposed to the radiation effect. For example, a surface finish where emittance and absorptance consist of similar values ( $\frac{\epsilon}{\alpha} \approx 1$ ) then the last row of the table designated as "Both albedo and IR" is used. The inclination of the satellite orbit and the time period of study is then selected to determine the albedo and planetary radiation of the satellite. According to Gilmore and Donabedian (2002), time periods greater than 24 hours do not change the albedo and planetary radiation values significantly. Gilmore and Donabedian (2002) further states that the recommended values depicted in the tables will only be exceeded 0.04% of the time, making them very accurate readings.

Surface Sensitivity	Time Period	Inclination (deg)					
		0-30		30-60		60-90	
		Albedo	IR (W/m <sup>2</sup> )	Albedo	IR (W/m <sup>2</sup> )	Albedo	IR (W/m <sup>2</sup> )
Albedo	16 sec	0.06	273	0.06	273	0.06	273
	128 sec	0.06	273	0.06	273	0.06	273
	896 sec	0.07	265	0.08	262	0.09	264
	30 min	0.08	261	0.12	246	0.13	246
	90 min	0.11	258	0.16	239	0.16	231
	6 h	0.14	245	0.18	238	0.18	231
	24 h	0.16	240	0.19	233	0.18	231
IR	16 sec	0.40	150	0.40	151	0.40	108
	128 sec	0.38	154	0.38	155	0.38	111
	896 sec	0.33	173	0.34	163	0.33	148
	30 min	0.30	188	0.27	176	0.31	175
	90 min	0.25	206	0.30	200	0.26	193
	6 h	0.19	224	0.31	207	0.27	202
	24 h	0.18	230	0.25	210	0.24	205
Both albedo and IR	16 sec	0.13	225	0.15	213	0.16	212
	128 sec	0.13	226	0.15	213	0.16	212
	896 sec	0.14	227	0.17	217	0.17	218
	30 min	0.14	228	0.18	217	0.18	218
	90 min	0.14	228	0.19	218	0.19	218
	6 h	0.16	232	0.19	221	0.20	224
	24 h	0.16	235	0.20	223	0.20	224

Figure 2.20: Albedo and Planetary Radiation Cold Case (Gilmore and Donabedian, 2002)

Surface Sensitivity	Time Period	Inclination (deg)					
		0–30		30–60		60–90	
		Albedo	IR (W/m <sup>2</sup> )	Albedo	IR (W/m <sup>2</sup> )	Albedo	IR (W/m <sup>2</sup> )
Albedo	16 sec	0.43	182	0.48	180	0.50	180
	128 sec	0.42	181	0.47	180	0.49	184
	896 sec	0.37	219	0.36	192	0.35	202
	30 min	0.33	219	0.34	205	0.33	204
	90 min	0.28	237	0.31	204	0.28	214
	6 h	0.23	248	0.31	212	0.27	218
	24 h	0.22	251	0.28	224	0.24	224
IR	16 sec	0.22	331	0.21	332	0.22	332
	128 sec	0.22	326	0.22	331	0.22	331
	896 sec	0.22	318	0.22	297	0.20	294
	30 min	0.17	297	0.21	282	0.20	284
	90 min	0.20	285	0.22	274	0.22	250
	6 h	0.19	269	0.21	249	0.22	221 <sup>c</sup>
	24 h	0.19	262	0.21	245	0.20	217 <sup>c</sup>
Both albedo and IR	16 sec	0.30	298	0.31	267	0.32	263
	128 sec	0.29	295	0.30	265	0.31	262
	896 sec	0.28	291	0.28	258	0.28	259
	30 min	0.26	284	0.28	261	0.27	260
	90 min	0.24	275	0.26	257	0.26	244
	6 h	0.21	264	0.24	248	0.24	233
	24 h	0.20	260	0.24	247	0.23	232

Figure 2.21: Albedo and Planetary Radiation Hot Case (Gilmore and Donabedian, 2002)

According to Gilmore and Donabedian (2002), the albedo values shown in the figures must be corrected (added to values from the above tables) to account for non-Lambertian reflection near the day/night terminator (the moving point at which day becomes night). This can be accomplished using Figure 2.22 below.

Short-Term Albedo Correction		Orbit-Average Albedo Correction	
Position from Subsolar Point (deg)	Add Correction	Orbit $\beta$ angle (deg)	Add Correction
0	none	0	0.04
20	0.02	20	0.05
40	0.04	40	0.07
50	0.05	50	0.09
60	0.08	60	0.12
70	0.13	70	0.16
80	0.20	80	0.22
90	0.31	90	0.31

Figure 2.22: Albedo Correction (Gilmore and Donabedian, 2002)

Two types of albedo correction are explored, one for short term and one for orbit average. If the orbit average is used, the correction is based on the orbit  $\beta$  angle. If the short term correction is used, the correction is determined based on the angle from the sub-solar point. Only one type of correction can be used at a time. For the antenna, the orbit average albedo correction will be used.

The  $\beta$  angle is the minimum angle between the orbit plane of the satellite and solar vector, as shown in Figure 2.23. It ranges between  $-90^\circ$  and  $+90^\circ$ .

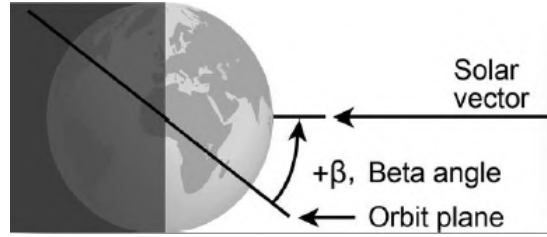


Figure 2.23: Beta Angle (Gilmore and Donabedian, 2002)

Due to that satellites are usually "close" to the planetary body, a visibility factor also needs to be taken into account to characterise the radiative heat exchange. The visibility factor can be interpreted from Figure 2.24 and is dependent on the satellite altitude and  $\beta$  angle between the local vertical and the Sun's rays.

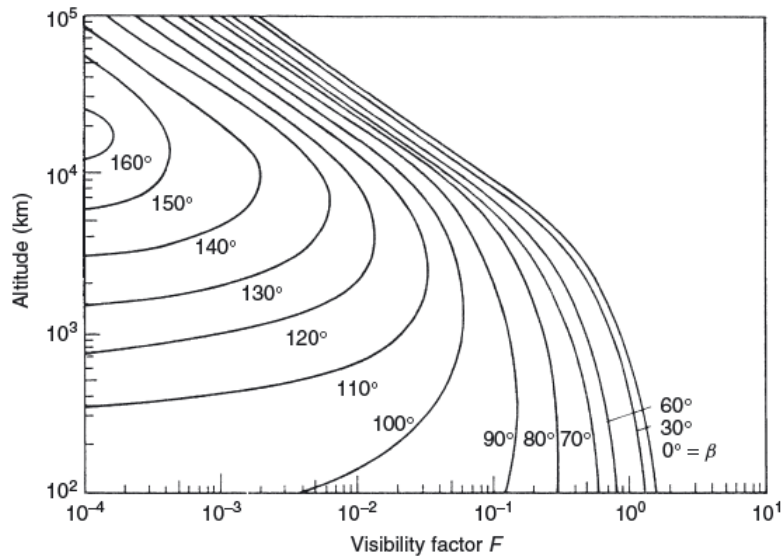


Figure 2.24: Visibility Factor (Fortescue et al., 2011)

The albedo radiation intensity is given by equation 2.18, (Fortescue et al., 2011).

$$J_a = J_s a F \quad (2.18)$$

Where:

$J_a$  = Albedo radiation intensity ( $W/m^2$ )

$J_s$  = Solar radiation intensity ( $W/m^2$ )

$F$  = Visibility factor, interpreted from Figure 2.24

$a$  = Orbital average albedo

### 2.3.3.3 Planetary Radiation

Due to that a planet and other objects in space have a temperature above 0 K, they will radiate energy. The radiated energy received by the satellite/antenna is a complex function of the energy radiated by the planet itself, the energy radiated by the atmosphere and the energy of the planet absorbed by the atmosphere. Therefore, planetary radiation is the thermal radiation emission from a planet, as a result of exposure to solar radiation (Fortescue et al., 2011).

According to (Gilmore and Donabedian, 2002) Planetary radiation or Earth infrared (Earth IR) can be interpreted from Figures 2.20 and 2.21 for hot and cold cases, depending on the designed satellite orbit inclination and time period to be examined.

Due to the complexity of satellites, the antenna will be treated as a black body ( $\frac{\varepsilon}{\alpha} \approx 1$ ). Therefore, only the albedo and IR section of Figures 2.20 and 2.21, will be used.

### 2.3.3.4 Thermal Balance

The temperature of a satellite or its components depends on how much heat is transferred from internal components and external sources, as well as the heat that is radiated out to the space environment. To control a satellite's temperature, the heat absorbed and radiated needs to be controlled. If spacecraft were treated as black bodies and, therefore absorbed all the radiation that interacted with them, they would only need to acquire a specific temperature. As a result, however, thermal control would be impossible, except for instances where internal heat dissipation could be controlled (by varying heat dissipation) (Fortescue et al., 2011).

Spacecraft are not black bodies and, therefore only receive a fraction of the incident energy  $\alpha$  (absorptance). They also radiate a fraction of the radiation they receive back of a black body at the same temperature  $\varepsilon$  (emittance). According to Fortescue et al. (2011), this relationship can be expressed as;

$$J_{absorbed} = \alpha J_{incident} \quad (2.19)$$

$$J_{radiated} = \varepsilon \sigma T^4 \quad (2.20)$$

Where:

$\alpha$  = Absorptance

$\varepsilon$  = Emittance

$\sigma =$  Stefan-Boltzmann constant ( $5.67 \times 10^{-8} W m^{-2} K^{-4}$ )

In instances where satellites have no internal heat dissipation, an effective absorbing area  $A_\alpha$  and emitting area  $A_\varepsilon$ , the thermal equilibrium is achieved when (Fortescue et al., 2011);

$$A_\alpha J_{absorbed} = A_\varepsilon J_{radiated} \quad (2.21)$$

Which from equations 2.19 and 2.20 gives;

$$A_\alpha \alpha J_{incident} = A_\varepsilon \varepsilon \sigma T^4 \quad (2.22)$$

So that the temperature equilibrium  $T$  is given by;

$$T^4 = \frac{A_\alpha}{A_\varepsilon} \frac{J_{incident}}{\sigma} \left( \frac{\alpha}{\varepsilon} \right) \quad (2.23)$$

Therefore, since the area values and  $\sigma$  are constant for a given value of  $J_{incident}$ , the equilibrium temperature  $T$ , can be controlled by manipulating the value of  $\alpha/\varepsilon$ . Considering a simple spacecraft in LEO that has a polar orbit that does not suffer from eclipses and assuming that the spacecraft has high isothermal thermal inertia, we have (Fortescue et al., 2011);

$J_s \alpha A_{solar} =$  heat received directly from the Sun

$J_a \alpha A_{albedo} =$  albedo contribution

$J_p \varepsilon A_{planetary} =$  planetary radiation contribution

$\sigma T^4 \varepsilon A_{surface} =$  heat radiated to space

$Q =$  internally dissipated power

Where  $A_{solar}$ ,  $A_{albedo}$  and  $A_{planetary}$  are the projected areas and  $A_{surface}$  is the total surface area of the spacecraft, respectively. Assuming that  $J_s$ ,  $J_a$ ,  $J_p$  and  $Q$  are constant, the spacecraft will reach an equilibrium temperature  $T$  when (Fortescue et al., 2011);

$$(A_{solar} J_s + A_{albedo} J_a) \alpha + A_{planetary} J_p \varepsilon + Q = A_{surface} \sigma T^4 \varepsilon \quad (2.24)$$

Therefore, with  $T$  as the subject;

$$T^4 = \frac{A_{planetary}J_p}{A_{surface}\sigma} + \frac{Q}{A_{surface}\sigma\varepsilon} + \frac{A_{solar}J_s + A_{albedo}J_a}{A_{surface}\sigma} \left(\frac{\alpha}{\varepsilon}\right) \quad (2.25)$$

If the satellite moves within the Earth's shadow, the heat absorbed from the Sun will be less than that received under full sunlight. As a result, a different equilibrium temperature will be calculated. During an eclipse, albedo radiation (radiation received from the Earth) is zero. Therefore, under these circumstances the new equilibrium temperature can be found from (Fortescue et al., 2011);

$$T^4 = \frac{A_{planetary}J_p}{A_{surface}\sigma} + \frac{Q}{A_{surface}\sigma\varepsilon} + \frac{A_{solar}J_s + A_{albedo}J_a}{A_{surface}\sigma} \left(\frac{\alpha}{\varepsilon}\right)(f) \quad (2.26)$$

Where:

$f$  = fraction of the orbit that is illuminated by the Sun.

According to (Gilmore and Donabedian, 2002), the fraction of the orbit exposed to the eclipse is related to the  $\beta$  angle of the orbit and can be calculated using the following equation;

$$f_E = \frac{1}{180^\circ} \cos^{-1} \left[ \frac{(h^2 + 2Rh)^{1/2}}{(R + h)\cos\beta} \right] \text{ if } |\beta| < \beta^* \\ = 0 \text{ if } |\beta| \geq \beta^* \quad (2.27)$$

Where:

$R$  = The Earth's radius (6738 km)

$h$  = The orbit altitude (km)

$\beta^*$  = The angle at which the eclipse begins, given by:

$$\beta^* = \sin^{-1} \left[ \frac{R}{R + h} \right] \quad 0^\circ \leq \beta^* \leq 90^\circ \quad (2.28)$$

Therefore, the fraction of the orbit exposed to sunlight is given as;

$$f = 1 - f_E \quad (2.29)$$

These calculated temperatures will display the point at which heat radiated out of the antenna system, equals heat being absorbed and therefore, provides temperature averages of what could be expected of the antenna while in the thermal

environment. Therefore, using the thermal balance equation, an initial basis for establishing the expected temperatures of the antenna can be determined. These temperatures can then be compared to simulated values so that the antenna can be tested in a thermal chamber to determine, how well the design handles the thermal environment.

## 2.4 Manufacturing for the Space Environment

Manufacturing for the space environment needs to be considered. The space environment exhibits harsh conditions, including radiation, temperature variations or spikes, and other factors.

The Sun's substantial features affect the near-Earth environment in the form of solar radiation. Solar radiation occurs as a result of the Sun essentially being a thermonuclear fusion reactor, the Sun also emits enhanced ultraviolet emissions (Fortescue et al., 2011). During solar maximum or high energy output from the sun, enhanced radiation emissions occur at radio wavelengths, X-ray and Gamma-ray energies. Solar winds are also present, which is an outward flux from the Sun, consisting of plasma expelled at high velocity.

The absorption of UV radiation in the upper atmosphere leads to the separation of oxygen into its atomic particles, which can cause atomic oxygen erosion. Cosmic radiation, resulting from high energy cosmic ray particles, can have permanent effects on the materials they pass through. Space debris, including man-made and naturally occurring micrometeoroid debris, is also present (Fortescue et al., 2011).

Another important factor to consider is the cold welding of materials in the space environment. Cold welding or cold pressure welding occurs between two similar materials under high pressure conditions, especially within a vacuum, where oxide layers formed on materials no longer exist. To prevent cold welding, structures in contact with one another should be made of dissimilar materials (Munakata et al., 2009).

Materials that can survive the space environment need to be considered, such as certain shape memory alloys, steels, aluminium and space approved plastics. CubeSats are unique in that commercially-off-the-shelf (COTS) parts are used, therefore materials that are readily available must be considered.

### 2.4.1 Material Sourcing and Selection

Space-graded materials are required for the overall design of the research project. Materials used for the construction of the antenna and its housing structure must be made of space-approved materials. Space-approved materials can be found using the Space Materials Database or SPACEMATDB (<https://www.spacematdb.com/>).

The database contains lists of metallic and plastic materials that can be used for space missions. Outgassing data for plastics and composites are also available.

Material properties of components must also be considered. For the research project, NiTi, spring materials and space approved plastics will be considered. Material properties for these materials will be sourced from online material databases, such as MatWeb.

Metallic materials can be sourced locally from stores such as CMC Hobbies for metallic rods (for springs), while 3D Printing Store and Gartech Engineering Plastics, can be considered for sourcing of plastics.

## 2.4.2 Manufacturing Techniques

In any project, manufacturing considerations must be taken into account should the design need to be manufactured, such as the structural housing of the antenna.

Research into the manufacturing process of tools and procedures showed that various forms of manufacturing are used to produce structures and components used on CubeSats. Such manufacturing techniques include:

1. Plastic/metal additive manufacturing
2. Multi-axis CNC machine centres
3. Injection moulding

The following section briefly explores the manufacturing methods that can be utilised for designing the antenna housing system.

### 2.4.2.1 Additive Manufacturing

According to Chen (2018), the structure of a CubeSat can be manufactured using different materials and 3D-Printing techniques (additive manufacturing). Some of the materials that can be used include space-graded plastics and composites, aluminium, gray cast iron, and copper. The material used mainly depends on the design requirements specified by the mission and what the launch provider specifications allow.

The additive manufacturing technique (whether metal or plastic) provides many advantages such as fast implementation, production accuracy and low cost. Regarding the construction of small satellite parts, as is the case with CubeSats, this manufacturing technique is very useful as great amounts of accuracy can be achieved, which can be difficult and costly to accomplish with machine tools (Chen, 2018).



Compared to traditional manufacturing techniques, additive manufacturing can produce complex shapes that are often nearly impossible to achieve in the form of low cost and short production cycles compared to traditional methods. Another advantage of additive manufacturing is that material is deposited layer by layer, as opposed to traditional manufacturing where the material is removed from the metal base. According to Chen (2018), this is advantageous due to that material wastage is eliminated, parts are produced at the same time, and the product is produced as a whole as opposed to in parts.

The advantages provided by additive manufacturing helps to reduce the total number of parts, fasteners, adhesives, and simplifies the assembly process, and increase the structural reliability of the product. Therefore, low cost products are produced faster, can be mass manufactured, and allow for COTS parts to be made.

#### **2.4.2.2 Multiple Axis CNC Machine Centre**

Multiple-axis CNC machining is a manufacturing process where tools within a CNC (computer numerical control) machine can move in multiple ways or directions (usually 4 or more) to manufacture parts that require precision machining, such as the complex geometry associated with CubeSat structures and parts. Multi-axis CNC machines can deliver accurate components and offers greater flexibility and innovative machining technology as multiple sides of a part can be processed in a single setup.

Multiple-axis CNC machining is used to complete the entire machining operation in a single set-up. Therefore, the lead times associated with manufacturing are reduced, as various operations are performed in the same machine. Multiple-axis CNC machines are widely used in the aerospace industry, due to the complex geometry of required parts (Kumar et al., 2020).

#### **2.4.2.3 Injection Moulding**

One of the most common processes for the manufacturing of plastic parts is injection moulding. Injection moulding is a cyclic process where components are made by filling a mould, followed by cooling and the ejection of the part. Many different materials can be used for injection moulding, ranging from plastic to non-plastic material, as long as the machine is configured for the desired material (Goodship, 2004).

The selected material is plasticised in an injection unit, where it is injected into a clamped mould under high pressure, and the part is then cooled and ejected. The main advantage of the process is that parts can be economically mass-produced. Parts that require tight tolerances can be easily produced in one step (Goodship, 2004).

With the above-mentioned processes in mind, CPUT possesses multiple 3D printers in the rapid prototype lab, along with varying colours and different types of filament, such as PLA and PETG. Therefore, additive manufacturing will be used for rapid prototyping and the design of the antenna system.

## 2.5 Quadrifilar Helix Antenna

For the research project, a suitable antenna design must be chosen. The antenna required must be circularly polarised, have an isoflux radiation pattern or wide beamwidth, and must operate at the S-band frequencies (2.2 GHz). With the above requirements in mind, a QHA was selected and electrically designed for the research project. To avoid antenna radiation being directed towards the satellite, a ground plane needs to be deployed directly underneath the antenna (Costantine et al., 2016). The required antenna ground plane has the same dimensions as the CubeSat top and bottom panel. Therefore, the panels can be used as the ground plane and no deployment of the ground plane is required.

A QHA consists of 4 filars (conducting wires) wound about each other. The QHA can either be left open or closed at the top. Each filar of the QHA, must be fed  $90^\circ$  out of phase with that before it. A QHA can be described by the total amount of revolutions each helix (filar) of the QHA makes, the distance between the same point on consecutive turns of one element, which is known as the pitch and by the radius, which refers to the circular area enclosed by the QHA (Fraser, 2010). Figure 2.25 depicts a commercially available QHA.



Figure 2.25: Quadrifilar Helix Antenna (Olsen et al., 2018)

Methods for deploying QHAs are varied. A simple spring solution could offer an

easy to deploy option, however, the stresses present due to axial compression, will need to be considered. An alternative solution utilizes helical pantograph linkages using S-2 glass composite helices (for support) and Beryllium Copper helices (as conductors) that have a total of 8 helices (Olsen et al., 2018). The eight helix pantograph can be compacted as seen in Figure 2.26.

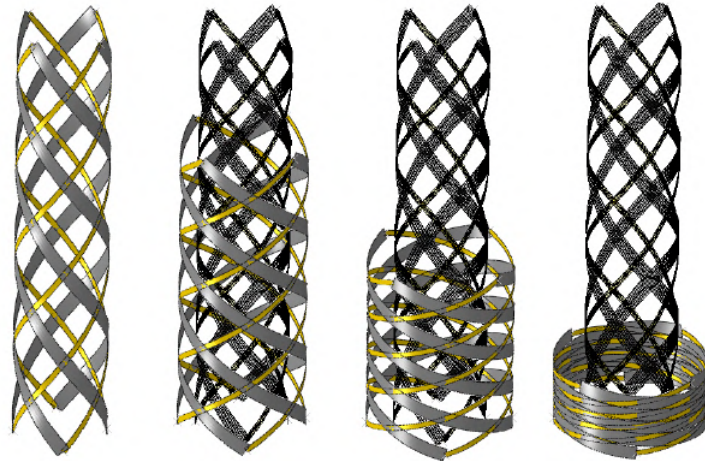


Figure 2.26: QHA 8 Helix Pantograph Deployer(Olsen et al., 2018)

One deployment option for the pantograph utilizes the three-dimensional expansion of a structure consisting of four identical links, shown in Figure 2.27 below.

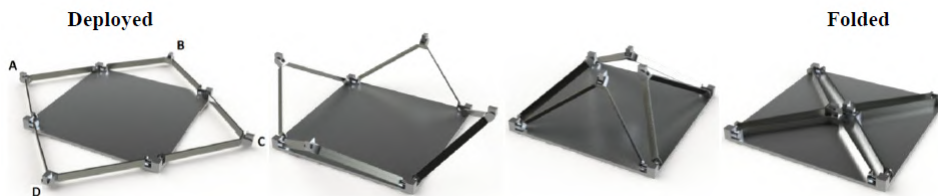


Figure 2.27: QHA 3D Link Deployer(Olsen et al., 2018).

The four links can be secured to a square plate using revolute joints. This allows for a clearance of 2 mm. This design supports an antenna diameter of up to 7.4 cm after axial compaction (Olsen et al., 2018).

The second concept incorporates a dilator cell-like mechanism, shown in Figure 2.28. The dilator cell consists of a planar mechanism that has four identical right triangles, connected to the corner of a square. The cell has one degree of freedom, which allows the cell to rotate and, in doing so, uses the stored strain energy of the helices to deploy the antenna (Olsen et al., 2018).

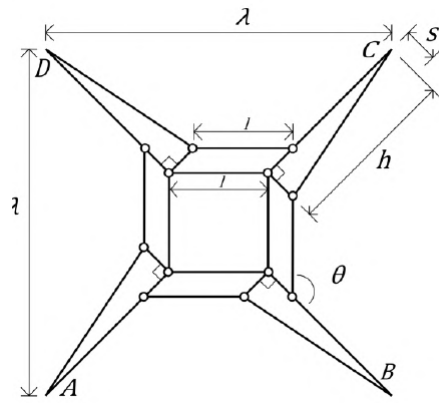


Figure 2.28: QHA Dilator Cell Deployer (Olsen et al., 2018).



Figure 2.29: QHA Dilator Cell Deployer 2 (Olsen et al., 2018).

Other alternatives include the use of shape memory wire or shape memory alloy (SMA). An example of such a deployment system can be seen in Figures 2.30 and 2.31. Prior to QHA deployment, the filars are held in place by a heated holding system. During deployment, an element is heated, which heats up resistors until they are sufficiently hot enough to sever the holding line, which holds the components in place. A deployment sensor tracks this process. Once triggered the sensor indicates to the system that the antenna has been deployed. Therefore, this system uses the heat and the stored strain and elastic energy of the SMA to reliably deploy the antenna (HCT, 2020).

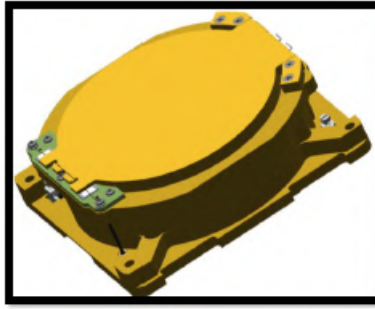


Figure 2.30: Stowed QHA (HCT, 2020)



Figure 2.31: Deployed QHA (HCT, 2020)

## 2.6 Finite Element Analysis

The QHA design will need to undergo structural analysis, in the form of Finite Element Analysis (FEA). According to Bhavikatti (2005), FEA is a numerical technique used to analyse structural complexities of various engineering problems such as varying shape of an object, boundary conditions and loads. This analysis tool is versatile and can be used to analyse many and varied complex structures, either in static, quasi-static or dynamic environments, using the FEM. Due to the complexity of parts and model assemblies within the shipping, aerospace, aeronautical, and automotive industries, FEA is used extensively for analysis. There are various popular finite element analysis packages available on the market, such as Ansys, Nastran, Abaqus, and many others. Each has their own subtle differences which affects how the software package works and its capabilities.

Due to that, the SMAs will be considered in the construction of the QHA, FEA software packages, which can characterise the unique superelastic and SME behaviours of SMA's undergoing martensite to austenite phase changes, due to temperature variations are required. At the CPUT Belleville Campus', Product Lifecycle Management Competency Centre (PLMCC) , Siemens NX and Abaqus FEA software packages are available. According to the Siemens NX user manual, the unique Nastran solver utilised by the program is capable of analysing complex SMA and superelastic structures using FEA. Abaqus on the other hand has the

material model, which is capable of modelling shape memory alloys, however the license is not as easily accessible at the PLMCC as Siemens NX. Therefore, Siemens NX will be used to conduct FEA on all QHA parts.

The FEA simulations, whether for traditional springs or SMAs, will produce information that validates the QHA design, by showing the effects that environmental and structural loading has on the QHA. These loading profiles will account for the vibration experienced by the QHA during launch, temperature cycling experienced in space and any harmful harmonics which could cause irreversible damage to the structure. The simulations will validate the reliable deployment of the QHA and characterise the phase change of martensite to austenite under the influence of heat.

Using FEA, the behaviour of entire complex and non-complex structures can be analysed and predicted. Engineering problems consist of unknown variables such as displacement, velocities, and temperature among others. Using the FEM, these unknowns can be reduced to a finite number, by partitioning these unknowns into smaller parts, called elements. The unknown variables within an element are expressed as an approximate function and is assumed within each element. According to (Bhavikatti, 2005), these approximate functions are expressed as variables of specific points called nodes, therefore the unknown variable within FEA are the nodes or nodal points. Once the unknown variables are found at these nodal points, field variables can be found for any point using interpolating functions.

Once elements and nodes have been selected, element properties for each element must be assigned. In solid mechanics, the stiffness characteristics of each element is required. This relationship can be mathematically expressed as (Bhavikatti, 2005);

$$[k]_e \{\delta\}_e = \{F\}_e \quad (2.30)$$

where  $[k]_e$  is element stiffness matrix,  $\{\delta\}_e$  is the nodal displacement vector of the element and  $\{F\}_e$  is the nodal force vector.

According to Bhavikatti (2005), four methods are utilised for determining element properties. These four methods include the direct approach, variational approach, weighted residual approach and energy balance approach. Any of the above methods can be used for formulating element properties, however, in mechanics, the variational approach is more commonly used.

The  $[k]_e$  and  $\{F\}_e$  element properties are utilised to form the global structural properties from which the system equations are formed. Once the system equations are formed, boundary conditions of the system are imposed, thus creating a range of simultaneous equations, from which the nodal unknowns of the system can be found (Bhavikatti, 2005). Utilising the nodal values of the system, additional calculations can be performed to determine the stresses, moments, etc. present in the system.

FEA simulation packages, such as those mentioned previously, are able to compute complex structures consisting of thousands of nodes and simultaneous equa-

tions, which can determine the unknown variables of the system and determine the resulting stresses, displacements, moments and reaction forces present within the examined structure.

### 2.6.1 FEM Versus Classical Method

The research project requires precise and accurate simulation, calculation and testing data to validate the QHA system for deployment on future missions. To determine the benefits of FEM, the FEM compared to classical methods must be considered.

According to Bhavikatti (2005), the classical method utilises an exact set of equations to form an exact solution, this slightly differs compared to the FEM, where exact equations are devised, however, only approximate solutions are output. In the case of the classical methods, solutions are acquired for a few standardised cases, whereas solutions for all problems can be obtained using FEA.

The classical method utilises assumptions in cases where solutions require calculations based on shape, boundary conditions and loading. Using the classical method, these cases are solved by assuming rectangular shapes, the same boundary condition along a side and regular equivalent loads (Bhavikatti, 2005). When utilising the FEM, these drastic assumptions are not required and the problem can be solved as is.

In cases where materials properties are not isotropic, obtaining solutions using the classical method can be extremely difficult to achieve. According to Bhavikatti (2005), only a few simple cases have been successfully tried by researchers, where favourable solutions were achieved. However, when using the FEM, structures with anisotropic material properties can be solved with relative ease.

Classical methods struggle to account for scenarios where multiple materials are used. However, the FEM handles these situations without difficulty. In scenarios, where material and geometric non-linearities are present, only the FEM can be used to determine the solutions to such problems, such as those experienced by the QHA system (Bhavikatti, 2005).

Therefore, in scenarios where complexities are experienced, the FEM is vastly superior to the classical method. However, for all regular problems, solutions obtained through the classical method offer the best solution. According to Bhavikatti (2005), to check the validity of FEM programs, the FEM solutions are often compared with the solutions by classical methods for standard problems. Therefore, a good practice to maintain is to compare solutions obtained by the classical method to those obtained from the FEM and look for where discrepancies lie.

## 2.6.2 CPUT Simulation Computer Specification

Any simulation conducted using FEA is ultimately limited by the processing power of the workstation used to conduct such simulations. In the case of the antenna system, the sine wave sweeps, random vibration and shock simulations are expected to use vast amounts of processing power, as well as primary drive storage space.

Siemens NX user guide states that the greater the frequency range being inspected, the more computational power and storage space are required. The table below depicts the specification of the simulation computer based at the PLMCC in CPUT's lab.

Table 2.1: Simulation Computer Specifications

Simulation Computer Specifications		
Component Type:	Name and Specification:	Release Date:
Processor	Intel(R) Xeon(R) CPU E5-2670 0 @ 2.60 Hz (2 processors)	March 6, 2012
Installed memory	RAM 128 GB	N/A
Operating System	Windows 10 Pro; 64-bit operating system	Jul 29, 2015
Primary Storage	Solid State Drive (SSD) 250 GB	N/A
Secondary Storage	Hard Drive 1 TB	N/A
Graphics Processing Unit	NVIDIA QUADRO K5000 4 GB GDDR5	August 17, 2012

Two of the main components responsible for processing the simulations are the graphics processing unit and the central processing unit. The processor and the GPU on the simulation computer are a decade old, however, are still able to conduct and keep up with more modern simulation packages, such as NX 12.

The biggest problem and limiting factor encountered with the simulation computer is the primary storage, which only consists of 250 GB. When a simulation is conducted in Siemens NX, a scratch folder is created, which contains the workings out and processes of the simulation conducted. In scenarios where a vast number of frequencies are examined, this folder can become very large.

In the case of random vibration (100 Hz - 2000 Hz), the scratch folder can be in excess of 90 GB for one axis (3 axes needed to be examined). In the case where there isn't enough space on the primary drive, such as for shock simulations, which cover a range of 2000 Hz - 10000 Hz, the simulation crashes and no results are exported. This combined with the excessive simulation time experienced, due to the large frequency range being examined and older equipment, limited the examinable frequency range, which could be simulated. In the case of shock simulations, due to their extreme complexity, especially over a wide frequency range and the complexity



of the QHA system, this simulation could be considered a researchable entity of its own. Budgetary requirements and procurement times also limited the procurement of simulation computer upgrades. Therefore, shock simulations were not conducted due to the limited simulation computer hardware, extremely vast frequency range and overall complexity of the simulation.

Therefore, with the literature review complete gaps in knowledge have been identified, which includes the following areas;

- The use and characterisation of SMA material, specifically Nitinol for space bound QHA solutions.
- Deployment of QHA solutions for space bound applications.
- Characterisation of the thermal environment of QHA solutions.
- Shape setting and activation temperature characterisation of the procured Nitinol specimen.
- Characterisation of the launch environment the QHA system will be exposed to.
- The limitations of spring materials and Nitinol for deployment purposes.

To investigate these gaps of knowledge, the research will follow a methodological approach based on ECSS standards, which will assist in characterising the QHA system. Gaps in knowledge relating to Nitinol, specifically, will be addressed through rigorous testing following a methodological approach, which is described in depth within Chapter 3. Deployment solutions will be assessed through simulations, testing and will be compared through a design matrix. The launch environment will be characterised through the use of simulations and testing (should time and budget allow it), with the use of Soyuz launch provider load profiles. Characterisation of the thermal environment will be accomplished through simulations, testing and calculations. Deployment of spring like filars will be characterised through spring calculations, simulations and testing.

# Chapter 3

## Design and Testing Methodology

### 3.1 Design Methodology

The antenna design process will follow two approaches. One approach will cover the mechanical spring design of open-coil helical compression springs, while the second approach will cover the SMA spring design. Design approaches and concepts will be compared with one another and the most suitable design will be chosen. Figure 3.1 depicts the overall design algorithm, that will be used to design the antenna system.

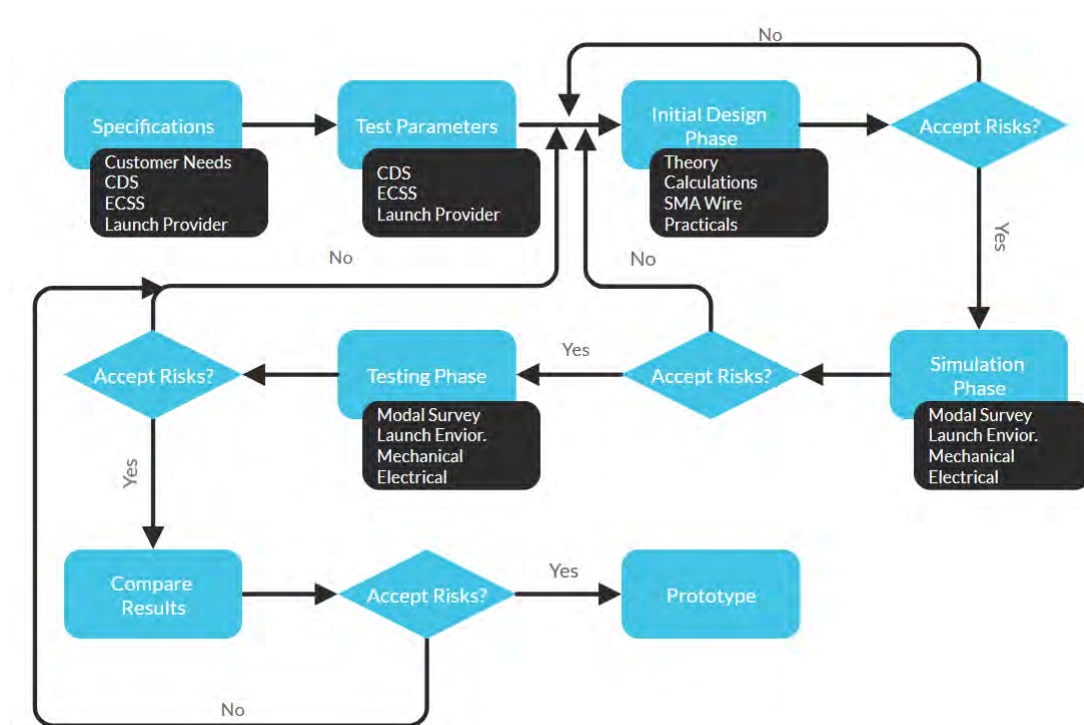


Figure 3.1: Antenna Design Methodology Algorithm

The methodology algorithm describes an iterative method tailored so that risks are analysed after each step of the design process. If the design presents risks, which cannot be accepted, such as those that could be detrimental to a space mission, then the design is rendered unacceptable, and the design process starts over. This continues until a set of acceptable designs, which meets mission specifications, with minimal or no risks is accomplished. Designs which meet specifications are then compared with one another and the best design is developed into a prototype.

The following sections describe in greater detail the design steps of the process.

### 3.1.1 Initial Design Phase: Open Helical and SMA Spring Design

The initial design phase of the antenna system follows a simple process, as shown in Figure 3.2.

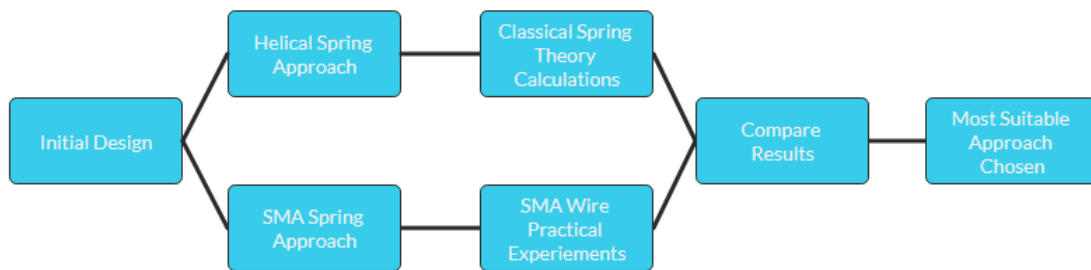


Figure 3.2: Initial Spring Design Methodology

The methodology shows that two design approaches will be considered, namely the classical and SMA spring design approaches. Classical spring theory will be used to design the antenna system as an open-coil helical spring. The classical spring theory will be used to design both iterations 1 and 2 of the given electrical antenna designs. Therefore, calculations will be used to determine the feasibility of an open coil helical spring being used as a QHA.

For the SMA spring design approach, the procured Nitinol SMA must first be characterised to determine how well the material remembers a particular shape, and to determine the activation/transformation temperature of the wire specimen. If the wire is able to retain its shape after cooling, it will be considered as a feasible approach for antenna deployment and will be validated through simulations using the FEM.

The methodological process used for the open coil helical spring is more concise than the SMA approach, due to the various unknowns associated with the procured SMA wire, which need to be physically tested. Both approaches will be compared to one another and the most feasible approach will be selected via a design matrix. The

following sections describe the experimental setup used to determine the feasibility of the approach.

### 3.1.1.1 Nitinol Properties Characterisation

The procured Nitinol wire will undergo thermal tests to determine the activation, start and finish temperatures of the SMA. The material will also be subjected to heat treatment within a kiln, to determine its feasibility for the development of a QHA deployable antenna. The kiln is situated at the CPUT Belleville campus in the mechanical labs. The material will be heat treated to determine how well the Nitinol wire retains its shape, after shape setting, and whether the material has enough strain energy to keep its shape once cooled to room temperature. Figure 3.3 below depicts the procured 0.5 mm Nitinol wire.

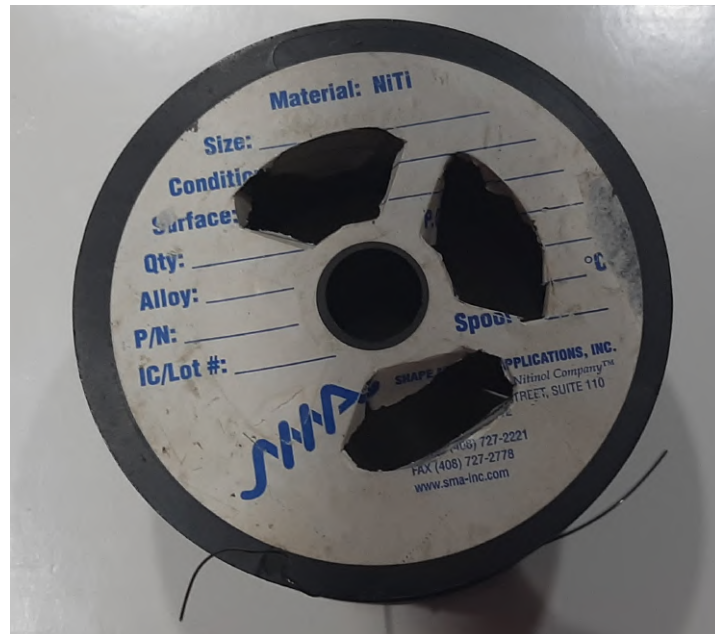


Figure 3.3: Nitinol Wire Specimen

The length of procured wire was measured to be 10 m. While this may seem like a lot, many tests need to be conducted to properly characterise the start and finish temperature of the wire at different shape setting temperatures. The wire must be characterised, because the material data sheets of this particular specimen had been unavailable. The company who manufactured this material also no longer exists, making it impossible to procure the required data sheets. Spectroscopy was considered for determining the material composition of the Nitinol specimen, however, the wire was too small for the equipment available in the CPUT mechanical labs. Wire training was conducted over a range of temperatures at different times. The following section covers the test procedures used to characterise the material.

### 3.1.1.2 Shape Setting Procedure

The shape setting process is essential for imparting a shape on the wire specimen. To create an SMA antenna that can be reliably deployed, the material must be able to remember its shape once heated and retain its shape once cooled. If the material changes shape as a result of cooling (lack of strain energy) then the material cannot be used to construct the antenna.

The antenna's electrical capabilities are directly linked to the number of turns, mean diameter of the helix, and wire diameter. A change in the mean helix diameter or shortening of the antenna will lead to deterioration of its radiative capabilities. Therefore, to determine how well the Nitinol wire remembers its shape and whether the supplied material has enough strain energy to remember its shape once cooled, the shape setting process must be performed. The basic shape setting procedure is shown in Figure 3.4.

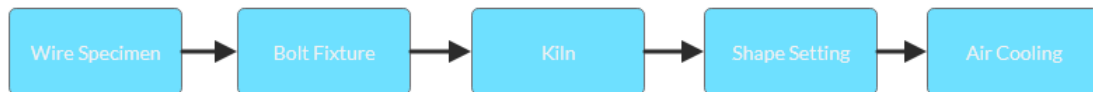


Figure 3.4: Shape Setting Procedure

To conduct the shape setting process, key components and apparatus are required. Firstly, a wire specimen is required. The procured Nitinol wire will be used as the wire specimen throughout the testing processes. In order for the specimen to remember a shape, it needs to be sufficiently constrained into the shape via a mandrel.

The easiest way to accomplish this for multiple tests is to constrain the wire to the threading of a bolt, using a nut and galvanised binding wire. Stainless steel nuts and bolts were selected as opposed to galvanised alternatives, due to that galvanised parts oxidise at high temperatures. Therefore, in order to limit any adverse effects due to the oxidising of galvanised parts, stainless steel was used where possible. Figure 3.5 depicts the constrained wire specimen.



Figure 3.5: Constrained Wire Specimen

Once the wire specimen is firmly constrained to the desired shape, it needs to be heat treated. As mentioned in the literature review, shape setting for Nitinol is usually performed between 500 and 550 °C. However, temperatures as low as 400 °C can be used. Due to the very small cross-section of the wire, tests were conducted at temperatures of 425, 475, and 525 °C, respectively. Heat treating of the specimen was performed in the kiln situated within the CPUT mechanical labs. Figures 3.6 and 3.7 depict the kiln.



Figure 3.6: CPUT Kiln



Figure 3.7: Open CPUT Kiln

The kiln is capable of reaching 1000 °C, making it more than capable of performing the experiments. Once the specimen is placed in the oven, it is heat treated over varying periods of time. Figure 3.8 depicts the specimen placed in the kiln. For each temperature setting, four tests were conducted on the Nitinol specimens. Therefore, four test samples were recorded for each temperature setting. The tests were conducted to determine the best temperature and training duration for the heat treatment of the Nitinol, which would best allow the material to remember the desired shape.



Figure 3.8: Test Sample Placed in Kiln

Figure 3.9 depicts the testing duration per sample. Sample test 1 allowed the material to heat up in the kiln. Once at the desired temperature, the specimen was kept in the oven for 10 minutes. The rest of the experiments allowed the kiln to heat up to the desired temperature and once at the desired temperature the specimen was placed in the kiln for the allocated time period.



Figure 3.9: Test Sample Duration

Once the specimen has been trained for the designated amount of time, it is removed from the oven and left to air cool. Figure 3.10 depicts a specimen removed from the kiln and left to rapidly air cool.



Figure 3.10: Trained Specimen Left to Air Cool

This concludes the shape training procedure. Following the shape setting process, specimens were subjected to further testing to determine their activation temperatures.

### 3.1.1.3 Start and Finish Activation Temperature Procedure

The  $A_s$  and  $A_f$  temperatures of the Nitinol wire specimen are of particular interest. The activation temperatures dictate the point at which the SME starts to occur as part of the reverse reaction under a thermo-mechanical load. Without knowing the activation temperatures of the material before and after shape setting, the material cannot be used for designing either of the electrically proposed antenna designs.

To determine the activation temperature of the wire specimens, a test procedure is required. The literature suggests in section 2.2.9 that DSC, can be used to determine the activation temperature, however the mechanical workshop does not have the required apparatus. Therefore, a different method to assess the activation temperature was required. The test needed to determine these critical temperatures must allow the observer to witness how the specimen transforms from a deformed shape to its trained shape, and allow the temperature at which this transformation occurs to be recorded. The best way to do this is with an oven or a kiln. The kiln housed within the CPUT mechanical labs would be a good candidate for this test. However, due to that the shape change needs to be observed, it would require the kiln door to constantly be open, which exposes the user to potential risks.

Therefore, to allow for observation, a conventional house oven was used to determine the activation temperatures. As mentioned previously, Nitinol SMAs usually have maximum activation temperatures of approximately  $110\text{ }^{\circ}\text{C}$ , making the conventional house oven a suitable candidate for the required tests. However, something that needs to be accounted for is the inaccuracy associated with conventional house oven thermometers. This can, however, be mitigated with a probe thermometer.



Figure 3.11 depicts the test procedure for determining the activation temperatures of the specimens.



Figure 3.11: Start and Finish Activation Temperature Procedure

The first step of the procedure is to remove the shape set specimen from its constrained mandrel, unwind it, and place it on a tray within a transparent oven dish, as shown in Figure 3.12.



Figure 3.12: Tray and Transparent Dish with Specimen

The transparent dish allows for the specimen to be contained. Unrestrained Nitinol wire can become excited during the reverse transformation, causing it to move around. The transparency of the dish also allows the material specimen to be observed during the reverse transformation.

To increase the accuracy of recorded temperature results, a probe thermometer, as seen in Figure 3.13, was used alongside the oven thermometer. The probe thermometer is calibrated to within  $1\text{ }^{\circ}\text{C}$ , making it much more accurate than that of a conventional oven.



Figure 3.13: Probe Thermometer

The probe of the thermometer is placed within the transparent dish, while the thermometer is kept outside the oven. The probe must be within the dish to determine the environmental temperature the specimen is directly exposed to. The dish, tray, probe, and specimen are then placed in the oven. The oven is initially set to  $70\text{ }^{\circ}\text{C}$  (lowest setting) and the temperature of the oven as it warms up is monitored via the probe thermometer.

The material specimen is observed during this time to look for the temperature at which the specimen starts to react. If no reaction occurs at  $70\text{ }^{\circ}\text{C}$ , the oven temperature is increased in increments of  $10\text{ }^{\circ}\text{C}$ , until a reaction is observed.

The temperature at which the specimen starts to react is the austenite start temperature. Therefore, once the material begins to react, the oven temperature is increased until the specimen stops reacting. Figure 3.14 depicts the SMA specimen at the austenite finish temperature.



Figure 3.14: Remembered Shape at Austenite Finish Temperature

Once the austenite finish temperature has been determined, the oven is turned off. The specimen and test apparatus are then removed from the oven. The transparent dish is removed, and the material is allowed to cool to room temperature. This step is very important. Allowing the material to cool to room temperature helps determine if the material is able to remember its shape at lower temperatures. As previously mentioned, space is a harsh environment and is cold. The material needs to have enough strain energy to keep its shape once cooled, otherwise it will not be able to function as one of the antenna designs. Figure 3.15 depicts the results of the cooling process.

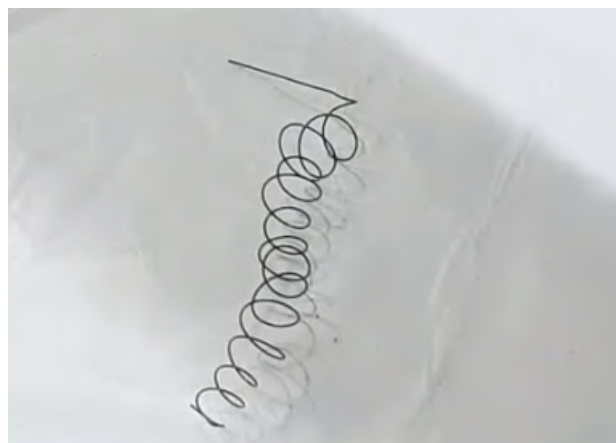


Figure 3.15: Remembered Shape of Specimen at Room Temperature

Once at room temperature, the specimen is visually observed and measured. A vernier calliper is used to determine the helix diameter of the specimen after

cooling. The helix diameter at room temperature will be compared to the helix diameter of the Nitinol wire fixed to the bolt before shape setting. The percentage increase in diameter is recorded. Appendix B lists the extensive test outcomes.

### 3.1.2 Simulation Phase

After the initial design phase, the most suitable antenna system design will be compared to a simulation of the model using the FEM. Figure 3.16, depicts the process that will be followed to validate the most suitable approach found in the initial design phase.

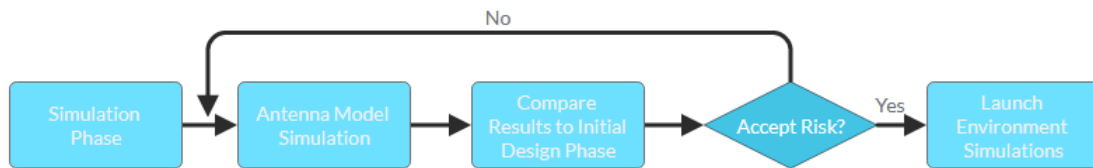


Figure 3.16: Antenna Design Simulation Methodology

Thus, the calculated design parameters of the antenna will be validated by means of a simulation using the FEM. The simulation model will be compared to the results found in the initial design phase. If the simulation model validates the initial design results, the model will then be subjected to launch environment simulations.

#### 3.1.2.1 Launch Environment and Loading Methodology

The project follows the design philosophy described by ECSS guidelines for design loads and safety factors (ECSS-E-HB-32-26A). Load analysis using ECSS methodologies will be adhered to as per the ECSS-E-HB-32-26A handbook on spacecraft mechanical loads analysis. Load analysis encompasses establishing appropriate loads or design environments for design and testing. The ultimate goal of load analysis is to support the efficacy of the design.

The life of a spacecraft is subjected to multiple events, each having their own structural loads. The challenge of these events are to identify critical loads, predict loads that may be caused by load sources and combine the predicted loads so that they may be deemed suitable for design. Usually, the launch of a spacecraft generates the highest loads. In the case of the antenna, the highest loads will most likely occur for the compression of the antenna into the "tuna can", as well as the actual launch into space.

For the initial design, major uncertainties are present, in the case of a space mission, these uncertainties may arise from transient forcing functions, launch environment, and mathematical representative models used for load analysis. To

combat these uncertainties, design or uncertainty factors are applied to calculated loads.

Load analysis is a crucial step in the design of a space structure including payloads, such as the antenna. Any mistake in load analysis could lead to the structure being designed and tested with wrong loads, where either an under or over design is present. To combat this, ECSS iterative design methodology as shown in Figure 3.17 will be used to design the antenna system. Often, the design of a spacecraft system is dependent on both structural loads and the inherent structural properties of the material used. Sizing is often controlled by the need to withstand loads, therefore structural design and loads analysis are usually an iterative process. The process is known as a load cycle. The antenna dimensions are fixed, therefore the iterative process will only include SMA and normal spring variations.

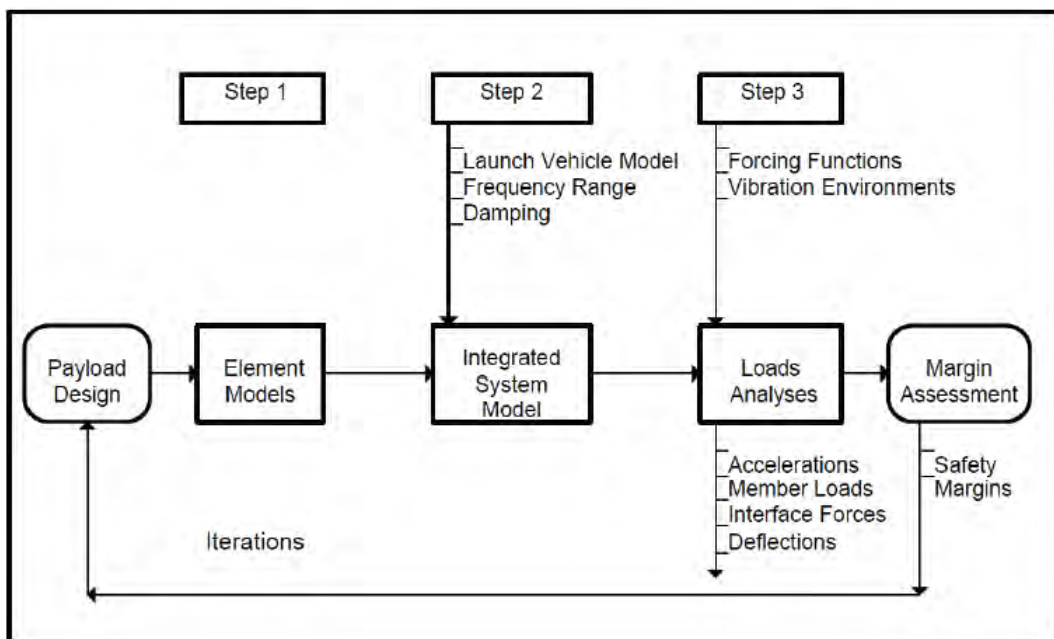


Figure 3.17: Load Cycle Design Loop (ECSS, 2013)

The process includes generating and combining mathematical models for either a proposed or developed design, distinguishing forcing functions and load factors to describe critical loading events, calculation of design load displacements for all significant events, assessing of results to identify potential modifications or risks and lastly modifying the design or accepting risks.

In some cases, mechanisms are constructed with very small factors of safety due to size restrictions and other limitations and therefore do not meet the required factor of safety set by the ECSS standards (1.5 in this case). In instances where the factor of safety present in the design (possibly the spring like antenna) is less than the required value, according to the methodology described, then the design must be proven through testing and simulation to be reliable and safe.

The antenna will be tested according to Arianespace Soyuz user manual and

specifications for quasi-static loading, sine vibration, random vibration and shock testing. Loading profiles are seen below for the relevant tests.

Characteristic		Qualification	Acceptance
Test		Recommended	Not required
Directions	Body Reference Frame (BRF)	X, Y, Z	
Acceleration axis	Axial (Launch Vehicle Reference Frame [LRF]) or flight axis	+ 10 [g]	
	Lateral (LRF)	+ 9 [g]	
Duration		10 [min]	

Figure 3.18: Soyuz Launcher Quasi Static (Arianespace, 2011)

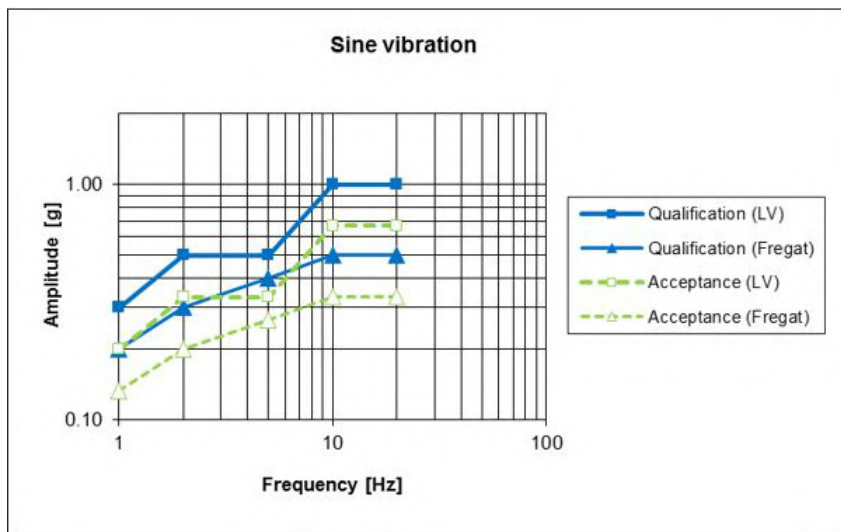


Figure 3.19: Soyuz Launcher Sine Vibration Equivalent (Arianespace, 2011)

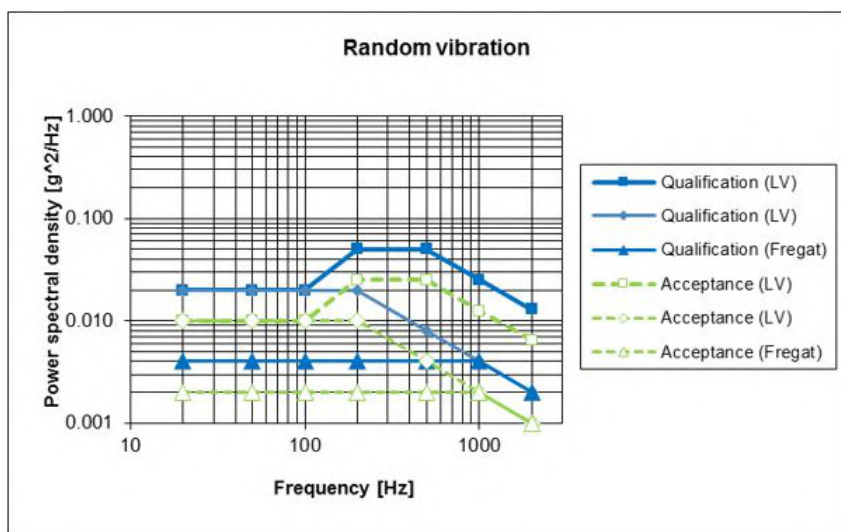


Figure 3.20: Soyuz Launcher Random Vibration (Arianespace, 2011)

### 3.1.3 Thermal Environment Methodology

Classifying the thermal environment of any space mission is essential. Temperature cycling in space can have dramatic effects on materials. Figure 3.21 depicts the basic methodology used by ECSS standards for charting the thermal environment of a space mission.

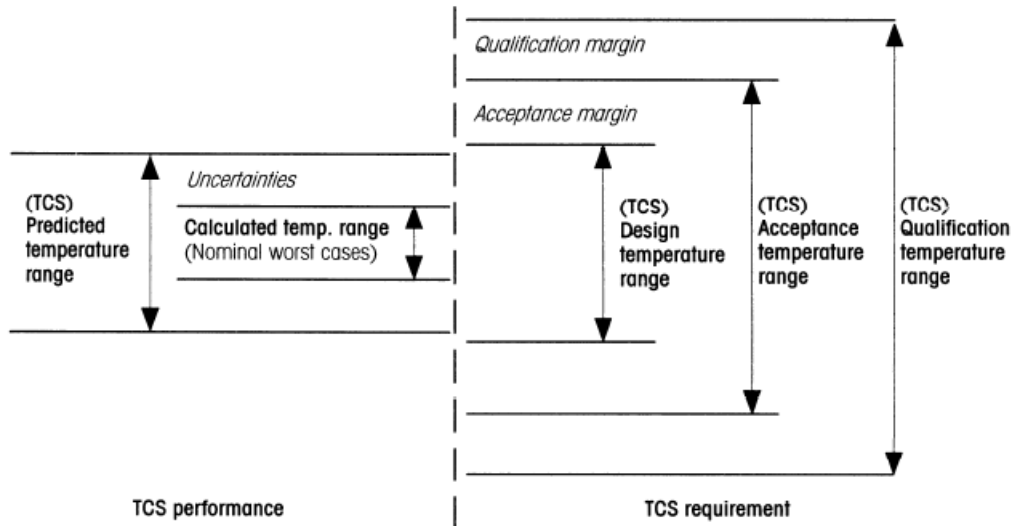


Figure 3.21: Thermal Margin (ECSS, 2013)

Initially, a predicted or expected temperature range is selected for the mission. For the project, orbit altitude and conditions similar to ZACube-1 and ZACube-2 missions will be used to characterise the thermal environment. Initial conditions will be calculated with the thermal balance equations and worst case sun-synchronous thermal cycling simulations.

Once the initial temperature range has been established, the acceptance and qualification margins will be set. Acceptance margins will have a temperature range of  $\pm 5\text{ }^{\circ}\text{C}$ , while a qualification margins will have a temperature range of  $\pm 10\text{ }^{\circ}\text{C}$ .

Once the design temperature margins are established, the antenna deployment system will be subjected to thermal cycling tests, using the acceptance and qualification margins.

## 3.2 Test Methodology

### 3.2.1 Deployment Testing

The deployment of the designed antenna will need to be tested. The tests need to be conducted to determine the reliability of the antenna deployment system and to determine other unseen problems or alternative considerations that need to be accounted for or optimised.

Deployment testing will be accomplished with a reliability assessment. The assessment will determine the ease of deployment as well as the deployed height and form factor of the antenna. For the antenna to be deemed feasible, it must show exact or similar dimensional characteristics compared to the given electrical design (depending on which design is mechanically feasible). The test setup is as follows.

The antenna will consist of either a Nitinol spring or open-coil helical spring. Springs, whether traditional or SMA, are made to store energy when loaded and dissipate the stored energy when unloaded. Therefore, a safe test jig is required. The test jig consists of a platform on which the antenna system will rest. A hole is drilled in the centre of the platform for burn wires to pass through. Burn wires are then able to pass through a wooden shaft, which is able to rotate and when doing so, stows the antenna system. In instances where staged deployment is tested, the jig has hooks on which burn wire can be secured.

To help with the stowing process, a bolt is used as a pin to stop the antenna from releasing its stored energy. The jig can then be clamped to a table or work surface to secure it in place. A ruler is placed at the end of the system to record the deployed height of the antenna system, after deployment has commenced. The deployment of the antenna is recorded through the use of smartphone video camera and tripod setup. Figures 3.22 to 3.24, depicts the jig setup.





Figure 3.22: Antenna Stowing Jig View 1



Figure 3.23: Antenna Stowing Jig View 2



Figure 3.24: Antenna Stowing Jig View 3

### 3.2.2 Electrical Testing

The final design of the antenna and deployment system will be subjected to electrical testing. The tests will be conducted in-house at the CPUT/F'SATI labs to determine whether the antenna works electrically, this will be accomplished through an S11 reflection coefficient test, to determine if the antenna mechanically implemented system operates at the required frequency. Once the electrical parameters have been determined, the tested results will be compared with the electrically designed antenna simulation in Appendix A, to determine the feasibility of the overall mechanical implementation of the electrical design.

### 3.2.3 Environment Testing

Environment testing will be conducted to determine temperature cycling in space. With the thermal environment of the antenna system being determined via calculations and simulations, the antenna will be subjected to thermal cycling within the thermal chamber at the CPUT/F'SATI labs. The test will determine how well the antenna deployment system handles the thermal environment as if it were in space orbiting Earth.

Should time and budget constraints allow it, the antenna system will be subject to sine sweep and random vibration tests on a shaker table. This will be conducted to determine whether test results coincide with simulation results and to prove that the antenna system will survive the launch environment.

# Chapter 4

## Antenna Mechanical Design, Specification and Analysis

This section of the report covers initial design aspects that include the design requirements, constraints and criteria to be adhered to during the design process. The section also includes preliminary designs for selection of the best antenna solution, which cover SMA material characterisation, spring design, thermal calculations, concept determination and material selection.

### 4.1 Design Requirements, Constraints and Criteria

An important aspect to any design is defining the requirements, constraints and criteria that the design must adhere to. These factors help guide the design and are based on CDS and ECSS requirements, as discussed in sections 2.1.4.1 and 2.1.4.2. The following section lists design requirements, constraints and criteria that must be adhered to for the design of the antenna deployment system.

#### 4.1.1 Design Requirements

- The antenna design must have an isoflux radiation pattern or wide beamwidth, high gain and circular polarisation performance;
- The QHA must operate within the specified S-band frequency;
- The design must survive the harsh space environment as well as launch phase;
- The device will adhere to CDS and ECSS guidelines and standards, where applicable;

- Safety procedures and protocols outlined by the OHS Act, and laboratory safety guides will be followed;
- The device must disintegrate upon atmospheric re-entry;
- All components must remain attached to the antenna deployment system, to ensure that no additional space debris will be created;
- The antenna must be fed by 4 points, 90° out of phase from one another (1 for each filar);
- All deployables, must wait a minimum of 30 minutes after the CubeSat’s deployment switch(es) are activated to deploy, once ejected from the P-POD ejection;
- The antenna system’s first mode must be above 40 Hz, as per Soyuz launcher requirements;
- The antenna must be safely deployed from the ”tuna can” of a CubeSat; and
- The deployment mechanism must be structurally sound and be able to allow the antenna to send and receive signals at the specified S-band frequency.

#### 4.1.2 Design Constraints

- Only locally sourced materials will be used;
- The antenna system cannot exceed the “tuna can” dimensions as specified in the CDS;
  - 64 mm diameter
  - 36 mm depth
- Only materials outlined by ECSS guidelines and space materials database can be used;
- COTS parts must be used where applicable; and
- Readily available and well documented space approved materials must be used;

#### 4.1.3 Design Criteria

- Concepts will be compared and rated based on a design matrix, which will compare cost, design complexity, ease of manufacturing, mass and reliability;
- Reliability and test methodology, based on CDS and ECSS guidelines, will be followed so that the design requirements can be measured and tested against industry standards;

- Materials must satisfy proper outgassing criterion:
  - Total Mass Loss (TML) < 1.0%
  - Collected Volatile Condensable Material (CVCM) < 0.1%
- The final design will be validated through Siemens NX simulation software for rapid prototyping;
- The QHA design and deployment system must be rigorously tested to determine its functionality and whether the design will survive the launch phase and the space environment. Mechanical tests will include thermal cycling, deployment testing and vibration testing (should time and budget constraints allow it). Electrical testing will include S11 reflection coefficient test; and
- The antenna system shall be designed in accordance with NPR 8715.6 2.1.4.1 to limit orbital debris.

With the important design requirements, constraints and criteria defined, the design and testing process of the antenna can commence.

## 4.2 Antenna Spring Design

The antenna design presents a unique set of challenges, requiring a large antenna to be stowed within the "tuna can", where space is limited. As mentioned previously, two design approaches will be discussed; one for traditional spring design and one for SMA spring design. Traditional spring design will follow the traditional calculations used for helical compression spring characterisation, while SMA spring design will look at the characterisation of the procured Nitinol wire, if the wire provides satisfactory results, the adapted spring theory for SMA spring design will be used. The following sections look into the design process of a traditional spring-like antenna and SMA spring antenna for both electrical configurations presented. The most feasible antenna solution will be used to design antenna deployment concepts.

### 4.2.1 SMA Spring Design

For the SMA spring design, 0.5 mm Nitinol wire was procured. Before SMA spring design can commence, the transformation and structural feasibility of the procured 0.5 mm Nitinol wire needed to be characterised. The Nitinol specimen had no data sheets regarding activation temperatures. A way to determine the activation temperatures of the Nitinol specimen is to use a thermodynamic technique called DSC; however, CPUT mechanical workshops do not have the required equipment for the tests. Therefore, a way to determine the activation temperatures of the specimen needed to be characterised. With the methodology described in section 3.11, a method for determining the activation temperatures through observation

was established. Tests performed using the methodology showed that the Nitinol specimen had an initial activation start temperature of  $\pm 80$  °C and an activation finish temperature of  $\pm 90$  °C.

While the experiment does not present the most accurate procedure for determining the activation temperatures of the specimen, it does provide a good basis for the initial design.

Another key aspect of the design is how well the Nitinol specimen can remember a trained shape and keep its shape once cooled. Using the methodology described in section 3.4, multiple tests were conducted over a range of shape setting temperatures and times. These tests were completed to determine the best shape setting parameters for the Nitinol wire specimen. Once trained, the specimens were tested using the activation temperature characterisation methodology to record any shift in activation temperature as a result of the shape setting process. Appendix B depicts a complete list of testing outcomes in accordance with the methodologies described.

Tables 4.1 to 4.3 exhibit the recorded data for the NiTi specimens. The tables depict the activation temperatures of each sample, as well as the percentage increase in diameter recorded for each specimen as a result of cooling to room temperature.

Table 4.1: Shape Training Results 425 °C

Shape Training Recording @ 425 °C					
Parameter:	Unit:	Sample Number:			
		1	2	3	4
A_s	°C	90	70	73	82
A_f	°C	100	95	100	108
Original dimension	mm	8,61	8,61	8,61	8,61
Dimension @ room temp.	mm	10,79	9,44	10,21	10,17
% Dimension increase	%	25,3194	9,63995	18,583	18,1185

Table 4.2: Shape Training Results 475 °C

Shape Training Recording @ 475 °C					
Parameter:	Unit:	Sample Number:			
		1	2	3	4
A_s	°C	90	91	93	104
A_f	°C	100	100	109	115
Original dimension	mm	8,61	8,61	8,61	8,61
Dimension @ room temp.	mm	10,48	10,82	10,53	10,39
% Dimension increase	%	21,7189	25,6678	22,2997	20,6736

Table 4.3: Shape Training Results 525 °C

Shape Training Recording @ 525 °C					
Parameter:	Unit:	Sample Number:			
		1	2	3	4
A <sub>s</sub>	°C	104	95	94	99
A <sub>f</sub>	°C	121	111	112	116
Original dimension	mm	8,61	8,61	8,61	8,61
Dimension @ room temp.	mm	14,52	14,48	13,02	14,67
% Dimension increase	%	68,6411	68,1765	51,2195	70,3833

Outcomes of the shape setting procedure were mixed. However, one key feature that kept appearing was the inability of the wire specimen to completely remember its shape once cooled. This has massive implications for the SMA design approach. As the antenna would be exposed to a cycling of temperature in space, the antenna would inevitably cool down, resulting in the antenna not conforming to the form factor of the given electrical design; thus, affecting the electrical characteristics of the antenna.

The activation temperature of the wire specimen also needs to be scrutinised. Figure 4.1 depicts the activation temperatures of the samples based on training time and temperature. The graph shows that temperatures as high as 121°C, could be required to heat the wire to its austenite finish temperature, with the best case scenario of 95°C. This is worrying, as the activation temperatures, before shape setting, were already high.

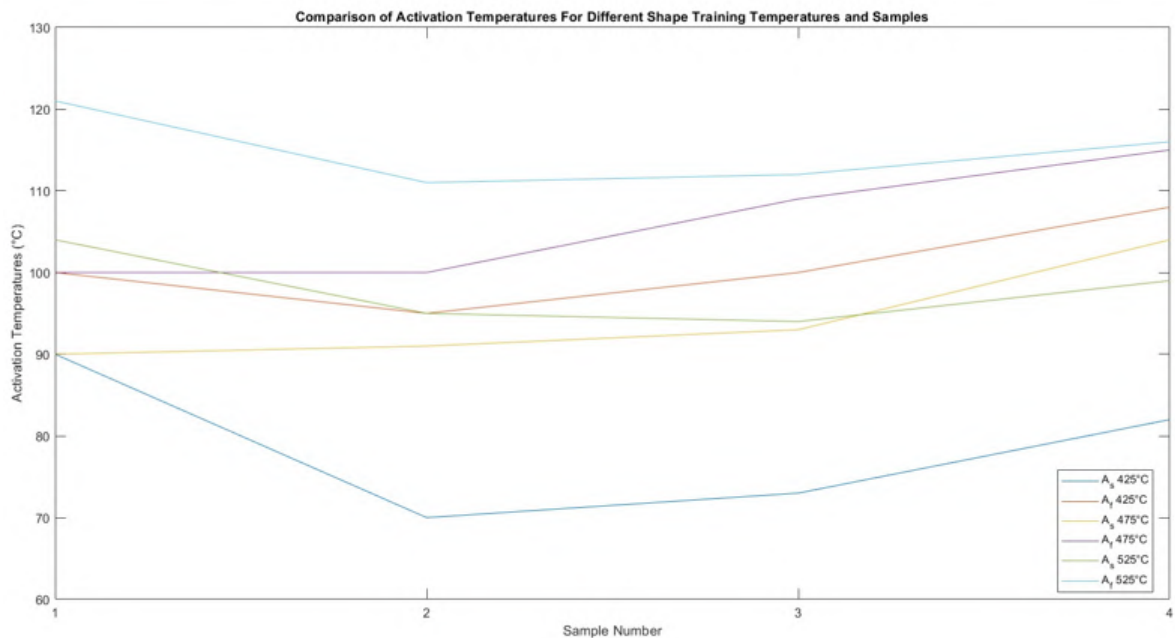


Figure 4.1: NiTi Activation Start and Finish Temperature Graph

As a result of the high activation temperature, another issue is encountered, which is the heating source requirements to get the Nitinol wire to the required ac-

tivation temperatures. The Nitinol wire would require a heat source to activate the reverse transformation from martensite to austenite to deploy the antenna in space. From a design and power budget perspective, this is worrying. The CubeSat would have limited power available to supply the SMA antenna with the heat necessary for the reverse transformation. Using equation (2.1) as described in the literature review, an estimation of the amperage required to heat the Nitinol specimen in space can be determined. Table 4.4 shows the temperature of the 0.5 mm Nitinol wire at different electrical currents.

Table 4.4: Estimated Wire Temperature

Estimated Wire Temperature				
Current (amps)	1	1,5	2	2,5
Wire diameter (mm)	0,5	0,5	0,5	0,5
Wire Temperature (°C)	48,714	85,032	129,324	181,59

The table shows that relatively high electrical currents are required to heat the Nitinol wire to its required temperature, which would be difficult to achieve on a CubeSat platform with a limited power budget.

## 4.2.2 Traditional Spring Design

Treating the antenna as a helical spring presents an easy and effective way of stowing the antenna and deploying the antenna with the use of its stored strain energy. Using the equations listed in the literature review for helical compression springs, the antenna can be characterised in a mechanical manner. Below are the calculations for the first and second antenna iterations.

### 4.2.2.1 Iteration 1

As the spring is compressed, the outer diameter,  $OD$ , changes. The outer diameter is calculated for the solid height of the spring. Therefore, when all coils of the spring are active, the outer diameter will be as calculated below. The outer diameter is dependent on the wire diameter,  $d$ , mean diameter of the spring,  $D$ , and the pitch of the spring,  $p$ . Looking at Appendix A, the dimensions of the first antenna iteration can be found. The antenna has a mean diameter of  $0.0093\text{ m}$ , a wire diameter of  $0.0005\text{ m}$  and a pitch of  $0.08333\text{ m}$ . Using the values presented, the outer diameter of the spring as it is compressed to its solid height can be calculated;

$$\begin{aligned}
 OD_{at\ solid} &= \sqrt{0.0093^2 + \frac{0.08333^2 - 0.0005^2}{\pi^2}} + 0.0005 \\
 &= 0.02861\text{ m}
 \end{aligned}$$



The *OD* of the first antenna iteration was calculated as 0.02861 m. This is a big change in the diameter of the spring. The initial *OD* of the spring would be  $0.0093 + 0.0005 = 0.0098$ ; this results in a difference of 0.01881 m. Therefore, compression to the solid height of the spring causes the outer diameter to become almost 3 times bigger.

The spring will have plain ends; as such, equation (2.4) can be used to determine the solid height of the spring when fully compressed;

$$\begin{aligned} L_s &= 3 \times 0.0005 \\ &= 0.0015 \text{ m} \times 4 \\ &= 0.006 \text{ m} \end{aligned}$$

When fully compressed using plain ends, the spring will have a solid height of 0.0015 m. The antenna consists of four springs, interwoven 90° out of phase with one another. The solid height of the spring would therefore be four times the height of one spring. Therefore, the solid height of the spring system is 0.006 m, which fits within the confines of the tuna can.

The next calculation to perform is the stiffness of the spring. The stiffness of the spring is closely related to the material selected for the spring. Section 4.4.1 covers the material design matrix, where the most suitable material for this application was selected. The material design matrix shows that music wire (ASTM A228) presented the best overall properties for the application. Appendix C depicts the material properties for the spring material used, as taken from the MatWeb material database. Music wire has a shear modulus  $G$  of 80 *GPa*. Using equation (2.5), the stiffness of the spring and the four springs in parallel can be calculated as;

$$\begin{aligned} k &= \frac{P}{f} \\ &= \frac{80000000 \times 0.0005^4}{8 \times 0.0093^3 \times 0.0015} \\ &= 259 \text{ N/m} \times 4 \\ &= 1036 \text{ N/m} \end{aligned}$$

The stiffness of the four parallel springs is calculated as 1036 *N/m*. With the overall stiffness of the 4 parallel springs known, the force required to compress the springs to its solid height can be calculated, using equation (2.5);

$$\begin{aligned}
P &= \frac{k}{f} \\
&= k \times (\text{spring height} - \text{solid height}) \\
&= 1036 \times (0.250 - 0.012) \\
&= 250.72 \text{ N}/4 = 62.6 \text{ N per spring}
\end{aligned}$$

The spring would require 250.72 N of force to completely be compressed to its solid height. The solid height of the spring is less than that of the depth of the "tuna can" (36 mm). Therefore, the force required to compress the spring to a height where it just fits inside the "tuna-can", can be calculated. If a clearance of 1 mm is assumed from the top of the tuna can and PCB height of 2 mm, the spring could be compressed to a height of 33 mm. Therefore;

$$\begin{aligned}
P &= \frac{k}{f} \\
&= k \times (\text{spring height} - \text{solid height}) \\
&= 1036 \times (0.250 - 0.033) \\
&= 224.812 \text{ N}/4 = 56.2 \text{ N per spring}
\end{aligned}$$

As seen from the calculations, whether the spring is compressed to its solid height or to 33 mm, a substantial force is required to compress the spring. This is something that needs careful consideration for both iterations of the eclectically designed antennas. An important factor, which also needs to be considered, is whether the spring will buckle. As described in section 2.3.1 of the literature review, for a spring to be considered stable it must fall below curve A, where one end of the spring is fixed, or alternatively must fall below curve B, for when both ends of the spring are fixed. The graph shows that the ratio of the free length and the mean diameter of the spring are compared to the ratio of deflection and free length of the spring. The free length,  $F_L$ , of the spring is 0.250 m, while the mean diameter is 0.0093 m. Assuming in the worst case scenario that the spring is compressed to its solid height, the deflection of the spring is 0.242 m. Therefore;

$$\begin{aligned}
\frac{F_L}{D} &= \frac{0.250}{0.0093} \\
&= 26.88
\end{aligned}$$

$$\begin{aligned}
\frac{f}{F_L} &= \frac{0.242}{0.250} \\
&= 0.968
\end{aligned}$$

Comparing the calculated ratios to the graph shows that the values lie far off the graph and the spring will definitely buckle. Should the spring be made, it will need to be guided by a rod or cylinder.

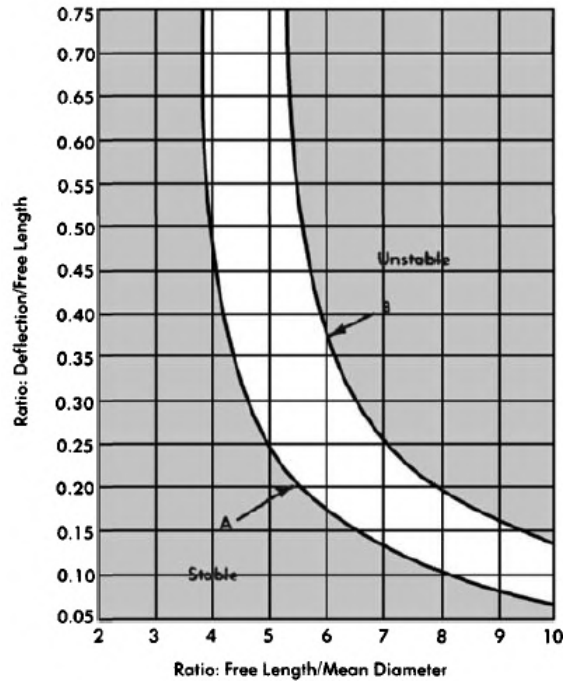


Figure 4.2: Buckling Curves (Shigley and Mischke, 1996)

To determine the torsional stress present in the spring, the Wahl correction factor needs to be calculated. The factor helps account for the direct shear and change in coil curvature of the spring. Using equation (2.7), the factor can be calculated. If a spring has been successfully set out, (2.8) is used instead;

$$K_{w1} = \frac{4\left(\frac{0.0093}{0.0005}\right) - 1}{4\left(\frac{0.0093}{0.0005}\right) - 4} + \frac{0.615}{\left(\frac{0.0093}{0.0005}\right)}$$

$$= 1.076$$

$$K_{w2} = 1 + \frac{0.5}{\frac{0.0093}{0.0005}}$$

$$= 1.027$$

Using the calculated Wahl correction factor, the torsional stress present in the spring at solid height can be calculated using equation (2.6);

$$S = \frac{8 \times 1.076 \times 0.0093}{\pi 0.0005^3}$$

$$= 12.773 \text{ GPa}$$

The torsional stress for the first antenna iteration is calculated as 12.773 GPa. The torsional stress is compared to a percentage of the maximum tensile strength of the material used. Figure 4.3 shows, that different types of material use different percentages of the maximum tensile strength. ASTM A228 falls under the patented and cold drawn carbon steel material category.

Materials	Maximum % of Tensile Strength	
	Before Set Removed ( $K_{W1}$ )	After Set Removed ( $K_{W2}$ )
Patented and cold drawn carbon steel	45%	65–75%
Hardened and tempered carbon and low alloy steel	50%	
Austenitic stainless steels	35%	
Nonferrous alloys	35%	

Figure 4.3: Maximum Allowable Torsional Stress (Shigley and Mischke, 1996)

Therefore, 45 % of the maximum tensile strength of the material is used. Using mechanical properties from the MatWeb material database found in Appendix C, the maximum tensile strength of 0.5 mm wire can be interpolated as between 2425 MPa and 2680 MPa. For a conservative design approach and worst case scenario, the lower end of the material’s strength was used. Taking 45 % of the tensile stress, the maximum torsional stress the material can be exposed to is 1.09 GPa. Comparing the maximum allowable torsional stress of the material with the calculated torsional stress of the spring shows that the torsional stress of the spring greatly exceeds the maximum of the material. However, if the spring were successfully set out, the  $K_{W2}$  correction factor can be used instead of  $K_{W1}$ , as well as a greater percentage of the maximum tensile strength for the maximum allowable torsional stress. Using  $K_{W2}$ , the torsional stress calculated in the spring is;

$$\begin{aligned}
 S &= \frac{8 \times 1.027 \times 0.0093}{\pi 0.0005^3} \\
 &= 12.19 \text{ GPa}
 \end{aligned}$$

The torsional stress for the first antenna iteration after the spring has been set out is calculated as 12.19 GPa. Using Figure 4.3, the maximum percentage of tensile strength can be taken as between 65 % and 75 % of the tensile strength. Using the set out percentage values, the maximum torsional stress that the material can withstand is between 1.5 GPa and 1.82 GPa. Therefore, in a situation where the spring is set out, the spring would still not be manufacturable due to the excessive torsional force present in the material.

Iteration 1, will therefore not be able to be stowed within "tuna can" space safely, without causing permanent damage to the spring/antenna.

#### 4.2.2.2 Iteration 2

Iteration 2 follows the same design sequence. Dimensions for iteration 2 consist of a mean diameter,  $D$ , of 42 mm, wire diameter,  $d$ , of 1.91 mm, pitch,  $p$ , of 35.48 mm, and a number of turns equal to 2.5. Using the given dimensions, the outer diameter  $OD$  of the spring compressed to its solid height is determined as;

$$\begin{aligned} OD_{at\ solid} &= \sqrt{0.042^2 + \frac{0.03548^2 - 0.00191^2}{\pi^2}} + 0.00191 \\ &= 0.0454\ m \end{aligned}$$

The  $OD$  of the second antenna iteration was calculated as 0.0454 m when fully compressed. The initial  $OD$  of the spring would be  $0.042 + 0.00191 = 0.04391\ m$ ; this results in a difference of  $0.00149\ m$ . Therefore, the second iteration is more realistic in terms of the change in diameter as the spring is compressed.

The spring will have plain ends; as such, equation (2.4) can be used to determine the solid height of the spring when fully compressed;

$$\begin{aligned} L_s &= 2.5 \times 0.00191 \\ &= 0.0044775\ m \times 4 \\ &= 0.0191\ m \end{aligned}$$

When fully compressed using plain ends, the spring will have a solid height of  $0.0044775\ m$ , with four springs interwoven  $90^\circ$  out of phase with one another, the solid height of the spring would be four times the height of one spring. Therefore, the solid height of the spring system is  $0.0191\ m$ , which fits within the confines of the tuna can.

The next calculation to perform is the stiffness of the spring. Using equation (2.5), the stiffness of the spring and the four springs in parallel can be calculated as;

$$\begin{aligned} k &= \frac{P}{f} \\ &= \frac{80000000 \times 0.00191^4}{8 \times 0.042^3 \times 2.5} \\ &= 718.5\ N/m \times 4 \\ &= 2874.12\ N/m \end{aligned}$$

The stiffness of the four parallel springs is calculated as 2874.12  $N/m$ . With the overall stiffness of the 4 parallel springs known, the force required to compress the springs to its solid height can be calculated using equation (2.5);

$$\begin{aligned}
 P &= \frac{k}{f} \\
 &= k \times (\text{spring height} - \text{solid height}) \\
 &= 2874.12 \times (0.0887 - 0.0191) \\
 &= 200.04 \text{ N}/4 = 50 \text{ N per spring}
 \end{aligned}$$

The spring would require 200 N worth of force to completely be compressed to its solid height. The solid height of the spring is less than that of the depth of "tuna can" (36 mm). Therefore, the force required to compress the spring to a height, where it just fits inside the "tuna can", can be calculated. If a clearance of 1 mm is assumed from the top of the tuna can and PCB height of 2 mm, the spring could be compressed to a height of 33 mm. Therefore;

$$\begin{aligned}
 P &= \frac{k}{f} \\
 &= k \times (\text{spring height} - \text{solid height}) \\
 &= 2874.12 \times (0.0887 - 0.033) \\
 &= 160.08 \text{ N}/4 \\
 &= 40.02 \text{ N per spring}
 \end{aligned}$$

As seen from the calculations, whether the spring is compressed to its solid height or to 33 mm, a fairly substantial force is required to compress the spring. An important factor, which also needs to be considered, is whether the spring will buckle. The spring will be fixed on one end, therefore curve A will be used. The graph shows that the ratio of the free length and the mean diameter of the spring is compared to the ratio of deflection and free length of the spring. The free length,  $F_L$  of the spring is 0.0887 m, while the mean diameter is 0.042 m. Assuming in the worst case scenario the spring is compressed to its solid height, the deflection of the spring is 0.0696 m. Therefore;

$$\begin{aligned}
 \frac{F_L}{D} &= \frac{0.0887}{0.042} \\
 &= 2.11
 \end{aligned}$$

$$\begin{aligned}
 \frac{f}{F_L} &= \frac{0.0696}{0.0887} \\
 &= 0.785
 \end{aligned}$$

Comparing the calculated ratios to the graph shows that the values lie within the boundaries applicable to curve A, as a result the spring should not buckle.

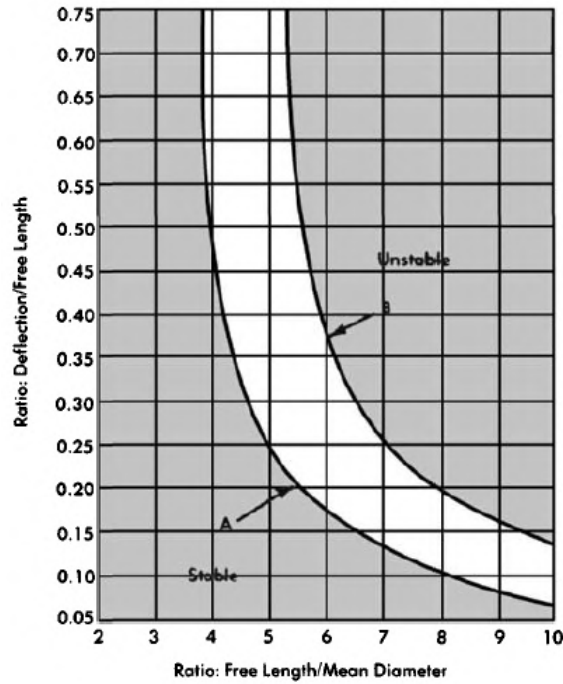


Figure 4.4: Buckling Curves Shigley and Mischke (1996)

The correction factors of antenna iteration 2 are calculated as;

$$K_{w_1} = \frac{4\left(\frac{0.042}{0.00191}\right) - 1}{4\left(\frac{0.042}{0.00191}\right) - 4} + \frac{0.615}{\left(\frac{0.042}{0.00191}\right)}$$

$$= 1.064$$

$$K_{w_2} = 1 + \frac{0.5}{\frac{0.042}{0.00191}}$$

$$= 1.023$$

Using the calculated Wahl correction factor, the torsional stress present in the spring at solid height can be calculated using equation (2.6).

$$S = \frac{8 \times 1.064 \times 0.042}{\pi 0.00191^3}$$

$$= 816.51 \text{ MPa}$$

The torsional stress for the first antenna iteration is calculated as 816.51 MPa. The torsional stress is compared to a percentage of the maximum tensile strength of the material used. Figure 4.5 shows that different types of material use different percentages of the maximum tensile strength. ASTM A228 falls under the patented and cold drawn carbon steel material category.

Materials	Maximum % of Tensile Strength	
	Before Set Removed ( $K_{W1}$ )	After Set Removed ( $K_{W2}$ )
Patented and cold drawn carbon steel	45%	65–75%
Hardened and tempered carbon and low alloy steel	50%	
Austenitic stainless steels	35%	
Nonferrous alloys	35%	

Figure 4.5: Maximum Allowable Torsional Stress Shigley and Mischke (1996)

Therefore, 45 % of the maximum tensile strength of the material is used. Using the mechanical properties from the MatWeb material database found in Appendix C, the maximum tensile strength of 1.91 mm wire can be interpolated as between 1970 MPa and 2180 MPa. For a conservative design approach, the lower end of the material's strength was used. Taking 45 % of the tensile stress, the maximum torsional stress the material can be exposed to is 886.5 MPa. Comparing the maximum allowable torsional stress of the material with the calculated torsional stress of the spring shows, that the torsional stress of the spring lies within the maximum allowed by the material. However, if the spring were successfully set out, the  $K_{W2}$  correction factor can be used instead of  $K_{W1}$ , as well as a greater percentage of the maximum tensile strength. Using  $K_{W2}$  the torsional stress calculated in the spring is;

$$\begin{aligned}
 S &= \frac{8 \times 1.027 \times 0.0093}{\pi 0.0005^3} \\
 &= 785.07 MPa
 \end{aligned}$$

The torsional stress for the second antenna iteration after set has been removed is calculated as 785.07 MPa. Using Figure 4.3, the maximum percentage of tensile strength can be taken as between 65 % and 75 % of the tensile strength. Using the set out percentage values, the maximum torsional stress the material can withstand is between 1.280 GPa and 1.477 GPa. Therefore, in both situations the spring can be manufactured. Ideally, setting out the spring would yield more favourable results as the factor of safety would increase. The factor of safety for  $K_{W1}$  and  $K_{W2}$  are shown below.



$$\begin{aligned}
FOS_{K_{w_1}} &= \frac{\textit{Max. Allowable Stress}}{\textit{Calculated Stress}} \\
&= \frac{886.5 \textit{ MPa}}{816.51 \textit{ MPa}} \\
&= 1.085
\end{aligned}$$

$$\begin{aligned}
FOS_{K_{w_2}} &= \frac{\textit{Max. Allowable Stress}}{\textit{Calculated Stress}} \\
&= \frac{1280 \textit{ MPa}}{785.07 \textit{ MPa}} \\
&= 1.63
\end{aligned}$$

As calculated, a set-out spring would result in a higher factor of safety. However, removing set from a spring can be a difficult process that does not always yield favourable results. As mentioned in the literature review, local spring manufacturer Springman advised against the process as it can also break the spring. Therefore, antenna iteration 2 using the first Wahl correction factor, presents the most promising spring prospect of the 2 antenna configurations. However, the factor of safety is still less than 1.5 and therefore as described in section 2.1.4.2 of the literature review would need to be validated. Therefore, should the design be chosen, the spring system must be proven without a doubt to be safe and workable.

### 4.2.3 Spring Design Outcome

The spring design approaches need to be analysed to determine, overall, which design approach presents the most favourable and workable solution. The advantages and disadvantages of the design approaches are shown in the table 4.5.

Table 4.5: SMA versus Helical Design Approach

SMA Spring Design Approach	
Advantages:	Disadvantages:
Easily stowed No additional mechanisms required	Requires heat source Doesn't completely retain shape when cooled Requires more amperage than might be available on small CubeSat platform Requires constant power supply Requires specialised software to model Uncertainties concerning design Only works for antenna iteration 1 (based on procured material)
Helical Compression Spring Design Approach	
Advantages:	Disadvantages:
Easy to manufacture Keeps shape when stowed and deployed Uses stored strain energy to deploy Easier to model Not heat dependant Low material costs Well documented design approach	Large compression and stored force May require mechanism Low factor of safety Only works for antenna iteration 2 (iteration 1 is subject to extreme amounts of stress)

Table 4.5 shows that both design approaches have their own merits. The SMA design approach offers a solution where the spring can be easily stowed, without any additional mechanisms. However, requires a constant heat supply in order for the material to keep its shape. If the heat supply falls below the required activation temperatures and is subjected to temperature cycling within the space environment, the antenna could lose its shape, which will affect the electrically designed parameters. This can be detrimental to a space mission, as it affects how the antenna communicates with the ground station and could limit data transmission. Due to the wire size procured, the approach only caters to antenna iteration 1.

The helical compression spring design approach offers a simple solution that uses the stored strain energy in the spring to deploy. However, additional mechanisms may need to be added to limit the deployment forces of the spring. The spring will keep its shape once deployed and is not dependent on a heat source. The spring is also easy to manufacture. The approach only caters to antenna iteration 2, as iteration 1 is subjected to extreme torsional stresses. The design also has a low factor of safety and will need to be validated through simulation and testing to ultimately prove its feasibility.

Comparing the design approaches shows that the helical compression spring design approach is more feasible than the SMA approach. This is based off of the inability of the SMA to completely retain its trained shape, if it is subjected to cooling. This is possibly the single most important electrical design factor which must be adhered. The communication band the QHA operates in is dependent on the mean diameter of the helix, if the helix diameter were to change, while in the deployed position, the communication band could change and mismatch

the frequency of the onboard software defined radio rendering the antenna useless. Therefore, the helical design approach for the second antenna iteration will be taken as the best antenna design.

## 4.3 Concepts

In this section of the report, antenna deployment concepts which adhere to the design requirements are discussed and rated based on a design matrix. The design of the antenna needs to be robust, but not overly complicated. The concepts will be scored based on ease of manufacturing, possible cost, complexity, mass, and reliability criterion. Each criterion has its own weighting which will influence the overall score of the design concepts. The concepts are as follows.

### 4.3.1 Concept A

The first concept proposed for the antenna deployment system is very simple. The concept uses the stored strain energy of the QHA springs to deploy itself, once a burn wire mechanism has been activated (shown in green). The antenna is guided by an inner and outer boundary, depicted as two walls designated by the colours yellow and orange respectively, as seen in Figure 4.6.

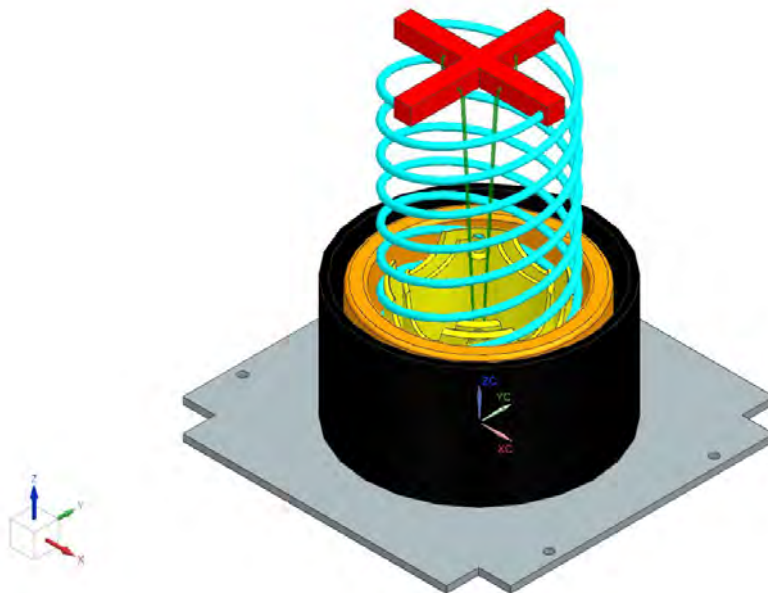


Figure 4.6: Concept A

The walls help guide the spring-like antenna when it is being stowed and deployed. The function of the walls is to also limit the lateral travel of the spring,

which could change the overall mean diameter of the springs and affect the electrical performance. Figure 4.7 depicts the stowed antenna. The filars of the antenna are kept in place with the use of the inner boundary layer. Inserts are used to secure the system walls to the antenna plate.

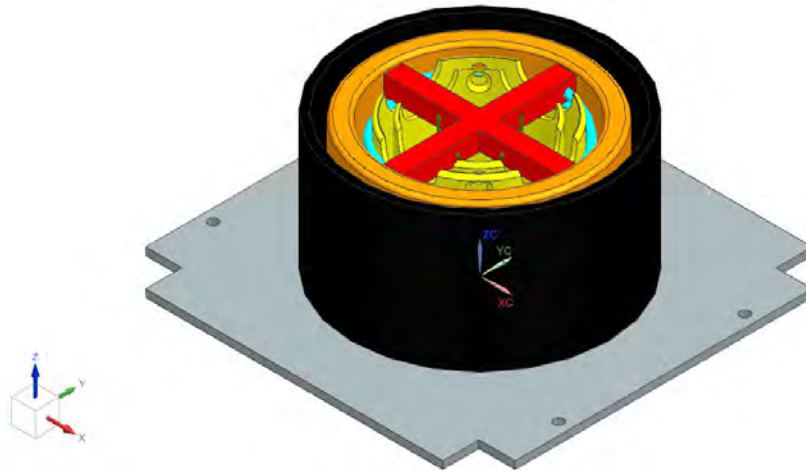


Figure 4.7: Concept A Stowed

Overall, the design of concept A is quite simple. In terms of reliability, due to the simple design, the concept should have greater success compared to a more complex option. The structure doesn't consist of too many components and uses less space than the "tuna can" (depicted in black) provides. The simplicity of the design will also make it much easier to manufacture, which would reduce the overall cost of the design. The only downside of the concept is the possible reactive force the antenna exhibits, while it is being deployed.

### 4.3.2 Concept B:

Concept B is identical to concept A. However, the antenna is designed to be slightly longer than the given electrical design. This way the burn wire limits the travel of the spring antenna as it deploys, to the dimensions of the given electrical design. Therefore, limiting the reactive force of the antenna as it deploys with the use of its stored strain energy.

Therefore, as the antenna is deployed, the coiled burn wire reacts against the pull of the antenna. This leads to a more controlled deployment. The design is very similar to concept B in terms of cost, complexity, and ease of manufacturing. However, with a longer antenna comes additional mass.

### 4.3.3 Concept C:

Concept C is similar to concepts A, however has added complexity. The concept also consists of boundary walls used for limiting the movement of the antenna. The concept makes use of multiple burn wires to deploy the antenna in stages, thus mitigating the full force of the antenna could experience during deployment.

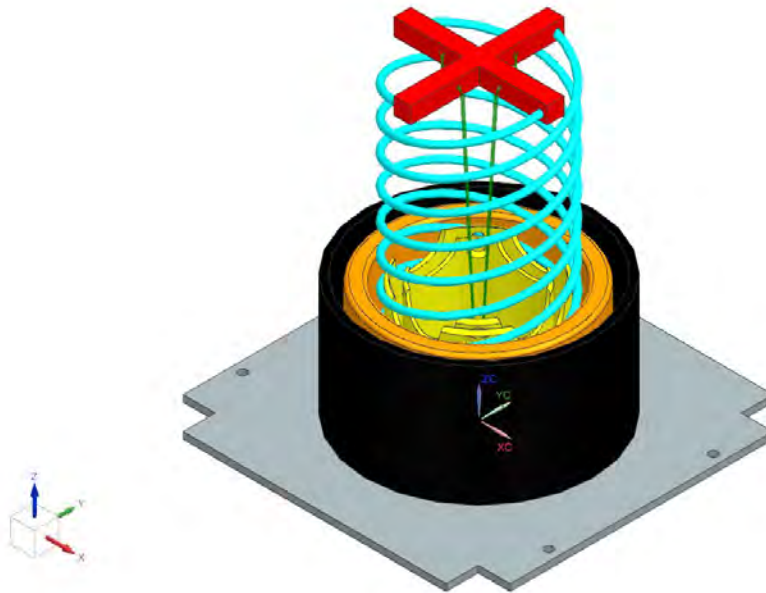


Figure 4.8: Concept C

Burn wires are attached to the top brace of the antenna (indicated as holes on the red top brace). As the antenna is stowed, burn wire is secured at varying height as shown in Figures 4.9 to 4.11. This helps to mitigate the deployment force of the antenna. The concept effectively spreads the deployment force over multiple burn wire strands as opposed to one, potentially greatly reducing the reactive force.

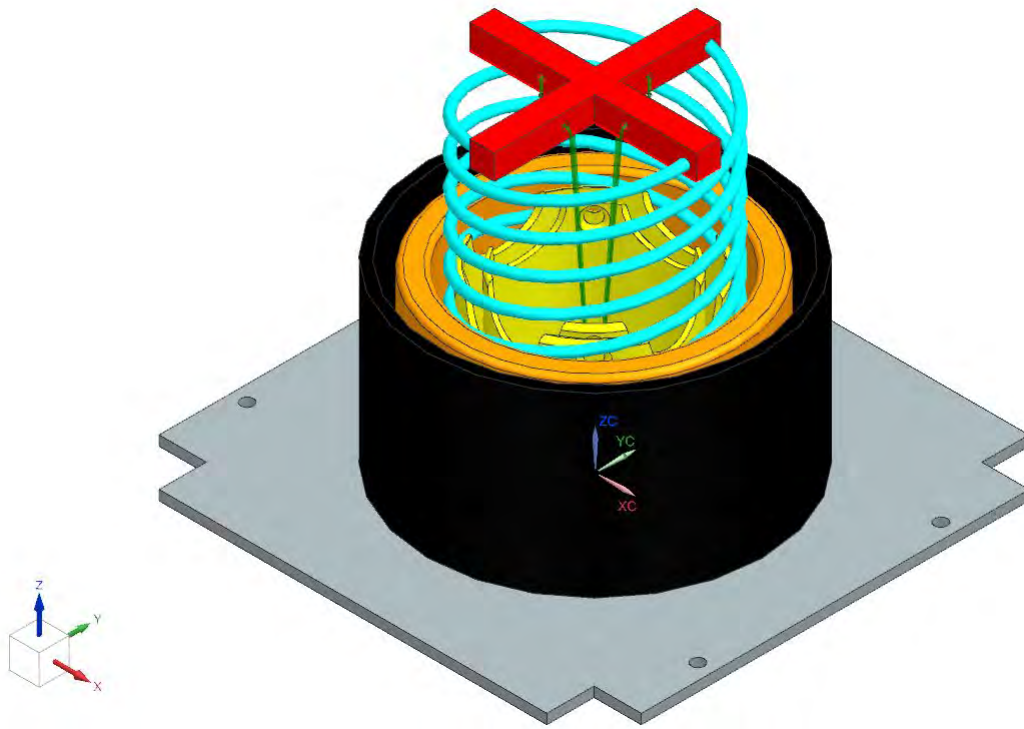


Figure 4.9: Concept C Stage 2

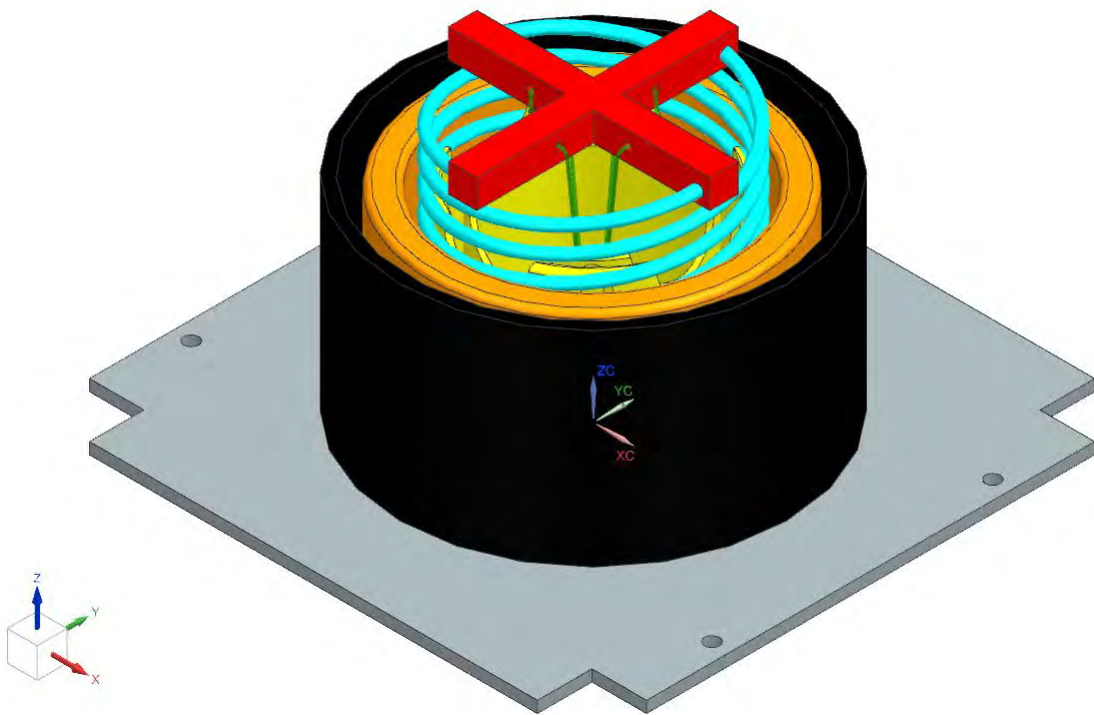


Figure 4.10: Concept C Stage 3

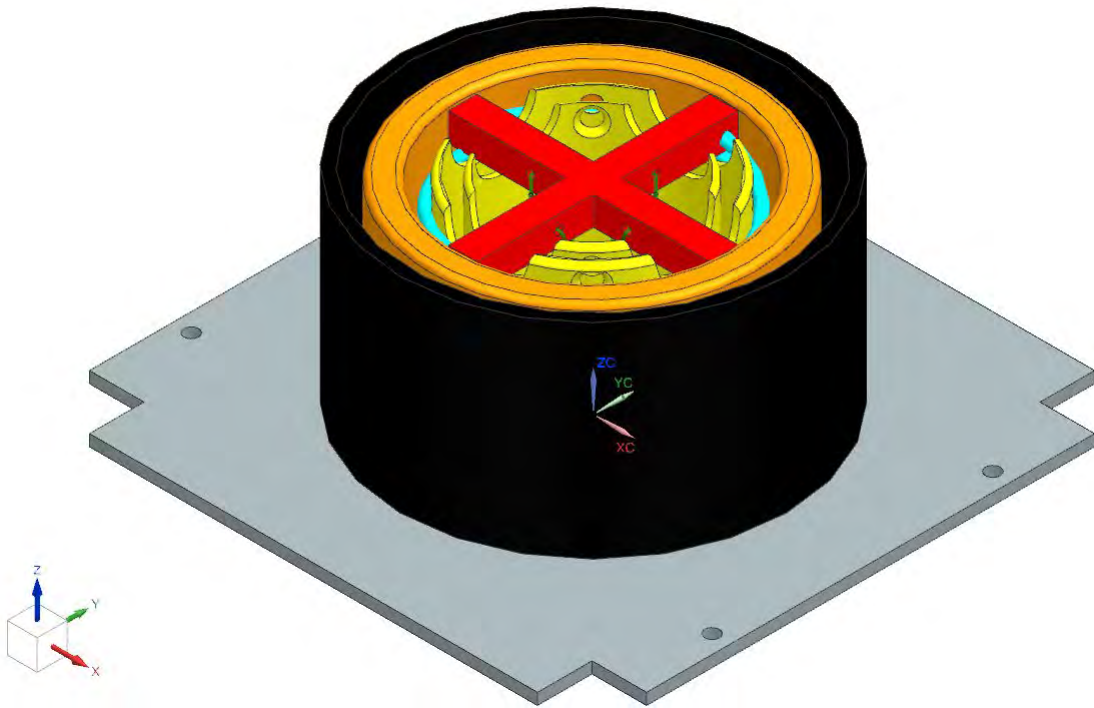


Figure 4.11: Concept C Stage 4

Overall, the concept is slightly more complicated than concept A. The design doesn't require additional structures and therefore in terms of mass should be similar to concept A. However, the design is potentially more reliable in that the deployment of the antenna is controlled better than concept A. With the design being slightly more complicated, stowing of the antenna may be slightly more difficult to achieve, due to multiple burn wires.

#### 4.3.4 Concept D:

Concept D consists of a simple design where the antenna is held in series with a spring of greater stiffness, as shown in Figure 4.12. The design uses an outer boundary wall to limit the lateral travel of the spring when it is stowed and deployed.

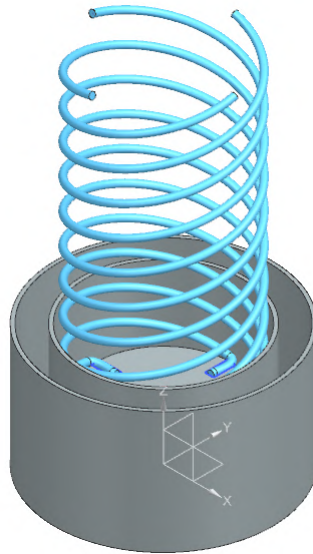


Figure 4.12: Concept D

Figure 4.13 depicts the cross-section of concept D. A stiff extension spring is used to limit the reaction of the deployment force generated by the QHA as it is deployed. The design is simple, however has a few drawbacks. The use of multiple springs in the design could lead to unwanted oscillations that could generate harmful frequency responses. The design also would weight more compared to the previously mentioned concepts, due to the mass of the extension spring. The cost to manufacture the concept could be high due to the second spring.

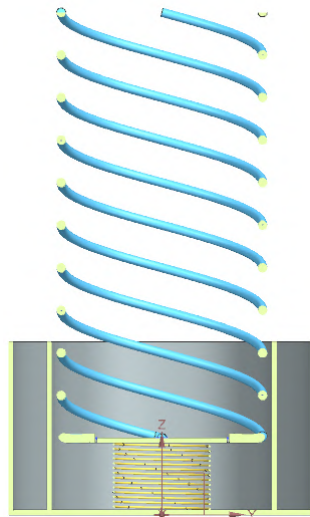


Figure 4.13: Concept D Cross-Section

Overall, the design is simple, however not very reliable and could potentially have a higher cost than other concepts. The stiffness required and dimensions required for the extension spring may also be difficult to achieve from a manufacturing perspective.



### 4.3.5 Concept E:

Concept E is a very complex design. The design uses a spring in parallel with the QHA to deploy, as shown in Figure 4.14. The idea of the concept is to help guide the QHA as much as possible, while also limiting the deployment force of the antenna as it moves from its stowed to its deployed position.

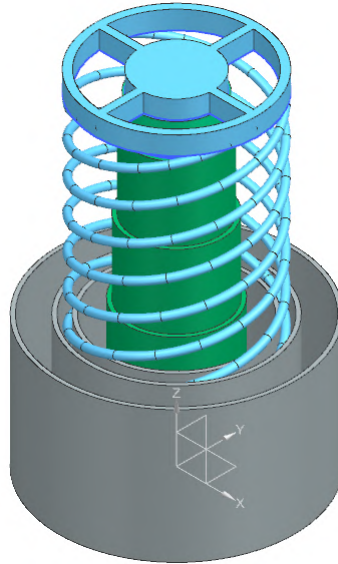


Figure 4.14: Concept E

Figure 4.13 depicts the cross-section of concept E. A smaller spring is housed within concentric cylinders that collapse upon one another as the antenna is stowed. As the antenna is deployed, the central spring limits the deployment force of the QHA and helps limit its travel.

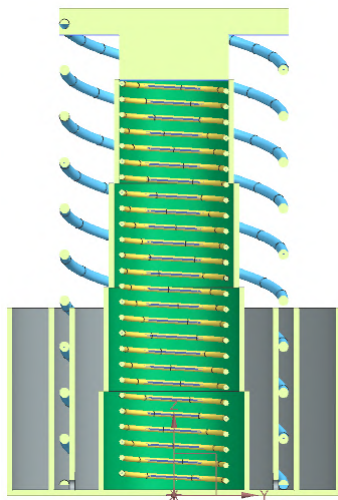


Figure 4.15: Concept E Cross-Section

The design is quite complex and could lead to the development of unwanted

harmonics due to the addition of the central spring in parallel with the QHA. This could create a situation where large loads are required to compress the QHA, as the stiffness of the springs in parallel are taken as the sum of the springs used. The design could also be very expensive to make due to the concentric cylinders and central spring required. The weight of the structure may also be an issue, due to the number of components required. Overall, the design is very complex and may not be reliable due to resonance issues.

### 4.3.6 Design Matrix

Concepts A to E, provide alternative methods for deploying the QHA, however only one that meets all the project specifications can be selected for the simulation and testing phase. Table 4.6 depicts the design matrix of antenna deployment system concepts.

Table 4.6: Concept Design Matrix

		Concepts Score (1 - 5)				
Criterion	Weight	A	B	C	D	E
Cost	0,2	5	4	2	3	1
Complexity	0,1	5	3	2	4	1
Ease of Manufacturing	0,2	2	1	4	3	5
Mass	0,2	3	2	5	1	4
Reliability	0,3	4	5	3	1	2
<b>Total Score</b>						
	-	3,7	3,2	3,3	2,1	2,7
<b>Concept Rank</b>						
	-	1	3	2	5	4

The design matrix shows that concepts A, B, and C show the most promise and have similar scores. Therefore, concept A will be tested first and concept B and C will be tested should concept A fail to provide satisfactory results. Appendix D, depicts the engineering drawings of concept A. Concept A consist of 5 components, being the spring filars, top brace, inner wall, outer wall and deployment base.

## 4.4 Material Selection

An important aspect of any design is selecting the right material for the application. In this section, material selection for a spring-like antenna as well as the housing of the antenna will be discussed, compared, and rated via design matrices. In accordance with the design requirements, only space approved materials can be considered for the final design. However, similar materials can be used to develop a prototype. Appendix C depicts a condensed table of material properties studied as part of the design matrix, as taken from the MatWeb material database.

### 4.4.1 Spring Material Selection

According to the space materials database, both stainless steel and carbon steel spring materials can be considered for the spring-like antenna. According to (Shigley and Mischke, 1996), ASTM A228 (music wire) and ASTM A227 are commonly used carbon steel spring grades, while ASTM A313 (302) and ASTM A313 (631) are commonly used stainless steel spring grades. It is important to note that stainless steel grades offer more corrosion resistance, however have lower tensile strength. This is an extremely important consideration, as the maximum torsional stress of the antenna is dependent on the maximum tensile strength of the material.

Table 4.7 displays the spring material design matrix used for selecting the spring material. Each criterion has a weighting, where more important material factors contribute higher scores, compared to less required criterion. Criteria such as material availability, thermal expansion coefficient, stress corrosion status, material cost, material density, service temperature and tensile strength are assessed.

Table 4.7: Spring Material Design Matrix

		Spring Material Score (1-5)			
Criterion	Weight	ASTM A228	ASTM A227	ASTM A313 (302)	ASTM A313 (631)
Availability	0,15	4	4	2	1
Coefficient of Thermal Expansion	0,1	3	4	2	5
Corrosion Status (Stress)	0,1	4	3	4	4
Cost	0,15	5	4	3	2
Density/Weight	0,15	3	3	2	3
Service Temperature	0,1	3	3	4	5
Tensile Strength	0,25	5	2	2	3
<b>Total Score</b>	-	<b>4,05</b>	<b>3,15</b>	<b>2,55</b>	<b>3,05</b>
<b>Material Rank</b>	-	<b>1</b>	<b>2</b>	<b>4</b>	<b>3</b>

The material design matrix shows that ASTM A228 is the best suited material for the spring design. The material is readily available and quite cost-effective. It has a service temperature of  $120^{\circ}C$ , which is adequate. The material has a typical density associated with steel which is  $7800\text{ kg/m}$ . In terms of tensile strength, the material exhibits a much higher average and maximum tensile strength compared to the alternatives. The material has the second-lowest thermal expansion coefficient of the considered materials and has been tested to possess high resistance to stress-corrosion cracking. ASTM A228 will therefore be considered the preferred spring material for the antenna design.

### 4.4.2 Antenna Housing Material Selection

As per design requirements only locally sourced materials and where applicable, COTS parts should be considered for the design. For the housing structure of

the antenna, suitable space approved plastics that can be locally sourced must be considered. As mentioned in the literature review, Gartech Engineering Plastics is a local supplier of plastic materials, which could be considered. Gartech offers a wide range of materials as mentioned. Other materials which will be considered are those available at the CPUT/F'SATI workshop, such as PETG and PLA.

An important consideration when selecting plastics for space missions are their outgassing and insulator properties. As per design requirements, the selected material must have a TML < 1.0% and a CVCM < 0.1%. Therefore, materials that can be locally sourced will be compared to NASA's outgassing data as acquired from the space material database. Materials that fail to reach a particular requirement will be given a zero score for the assessed criteria. The dielectric constant of a plastic shows how good of an insulator a plastic is. The higher the constant, the less likely an electric current can be conducted through the material. If a current is able to pass through the material, it could change the electrical characteristics of the antenna, which could be detrimental to a communications payload.

Therefore, outgassing and dielectric constant of the materials has the highest weighting among the criteria, as they are the two most important properties. Table 4.8 depicts the design matrix of the antenna housing material.

Table 4.8: Antenna Housing Material Design Matrix

Criterion	Weight	Material Score (1-5)										
		Acetal	Nylon 6	Cast Nylon	PETP	HDPE	PE500	UHMWPE	PVC	PTFE	PETG	PLA
Cost	0,15	4	4	4	5	5	4	4	5	2	2	2
Density/Weight	0,1	3	4	4	3	5	5	5	3	2	3,5	2,5
Dielectric Constant	0,25	4	5	5	4	3	2	2	3	1	3	1
Durability/Strength	0,15	4,5	5	5	3	1	2	2,5	2	1	3	4
Ougassing Data	0,25	4	1	1	0	5	5	5	0	2,5	4	0
Service Temperature	0,1	3	2,5	2,5	2,5	3	4	4,5	1	5	2,5	1
<b>Total Score</b>	-	3,875	3,5	3,5	2,75	3,7	3,55	3,675	2,2	2,025	3,1	1,5
<b>Material Rank</b>	-	1	5	5	7	2	4	3	8	9	6	10

The design matrix shows that Acetal is the best option for the final design of the housing structure. However, the CPUT/F'SATI labs have PETG in stock, which can be used to 3D print the prototype for testing. PETG and Acetal have similar dielectric constants, density, outgassing, and somewhat similar durability/strength. Therefore, for the prototype, 3D printed parts will be used to test the antenna deployment system.

## 4.5 Thermal Balance Calculation

Antenna design showed that antenna iteration 2 proposed the best workable solution for the project. With the dimensions of the antenna known, the initial thermal equilibrium temperature of the antenna as it is exposed to space-like conditions

can be determined. Using the equations as presented in the literature review in section 2.3.3, thermal equilibrium temperatures for the worst case scenarios can be determined for the antenna. The following sections depict the design calculations for determining worst case thermal conditions.

### 4.5.1 Design Parameters

The following parameters will be used to determine the worst case temperature scenario of the antenna as it orbits in space.

Table 4.9: Calculation Parameters

Calculation Parameters		
Parameter	Value	Unit
Orbit altitude	550	km
$\beta$ angle	0 - 90	$^{\circ}$
Fraction of orbit exposed to sunlight ( $f$ )	Varies	
Internal heat dissipation of components (Q)	0 - 1	W
Black paint finish		
(a) absorptance, $\alpha$	0.95	
(b) emittance, $\varepsilon$	0.8	

### 4.5.2 Assumptions

Planetary albedo and planetary radiation (Earth IR) will be interpreted from tables 2.21 and 2.20 for an orbit inclination of  $- + 90^{\circ}$ , over a 24-hour period, where both albedo and planetary radiation are equally dominant. The albedo correction will be accomplished using orbit average albedo.

Earth's radius will be used at 6378 km. The solar radiation intensity will be used at the minimum ( $1332 W/m^2$ ) and maximum ( $1414 W/m^2$ ) value for each iteration as a hot and cold case.

The antenna is nadir pointing, one face/surface of the antenna will always be facing the Earth. Therefore, since the planetary and albedo areas used for calculating equilibrium ( $A_{albedo}$  and  $A_{planetary}$ ) are based off surface area in contact with the radiation effect, only the surface of area of the top helix of the antenna will be used. Therefore,  $A_{albedo}$  will be equal to  $A_{planetary}$  ( $A_{albedo} = A_{planetary}$ ).

The total surface area of the antenna will be the sum of all areas. Due to that the antenna rotates around the Earth, the surface area affected by solar radiation constantly changes. To simplify this effect for calculation purposes, the average surface areas of the broadside, top, and bottom sides of the antenna were taken. While not being completely accurate, this assumption does provide an acceptable basis for simple, meaningful calculations.

### 4.5.3 Calculations

A sample calculation is seen below. The calculated thermal equilibrium temperatures were programmed into an Excel spreadsheet and calculated for  $\beta$  angles  $0^\circ$  to  $90^\circ$  and can be seen in Appendix F. To start off, the albedo radiation intensity  $J_a$ , can be calculated. To calculate  $J_a$ , the visibility factor is required. Knowing the altitude of the orbit (550 km) and the  $\beta$  angle required ( $0^\circ C$ ). The visibility factor can be interpreted off Figure 2.24 in the literature review. Using the defined parameters and reading off the graph, a visibility factor of 1.5 will be used for an  $\beta$  angle of zero.

For a hot case scenario, the maximum solar radiation intensity is given as  $1414 W/m^2$ . Using table 2.21, the hot case albedo for an  $90^\circ$  orbit inclination is given as 0.23 for 24-hour time period. With the addition of the orbit-average albedo correction in table 2.22, the albedo is taken as 0.27.

Using the albedo radiation intensity formula as mentioned in equation 2.18, the albedo radiation intensity is calculated as;

$$J_a = (1414)(0.27)(1.5)$$

$$J_a = 572.67W/m^2$$

Next is to determine the planetary radiation intensity experienced by the antenna at its orbital altitude. Using table 2.21, the hot case planetary radiation intensity for an  $90^\circ$  orbit inclination is given as  $232 W/m^2$  for 24-hour time period.

Using the previously stated area assumptions, the respective areas required for the temperature equilibrium are found as;

$$\begin{aligned} A_{albedo} &= A_{planetary} = A_{OD} - A_{ID} \\ &= \frac{\pi 0.043.91}{4} - \frac{\pi 0.04009}{4} \\ &= 0.003 m^2 \end{aligned}$$

$$\begin{aligned} A_{surface} &= ((2\pi 0.000955)^2 + (0.03548^2))^2 = 0.03598 m \\ &= 0.03598 \times 2.5 = 0.08996 m \\ &= 0.08996 \times \pi \times 0.04391 = 0.01241 m^2 \\ &= 0.01241 \times 4 = 0.04964 m^2 \end{aligned}$$

$$\begin{aligned}
A_{solar} &= \frac{A_{planetary} + A_{surface}}{2} \\
&= \frac{0.04964 + 0.003}{2} \\
&= 0.01316 m^2
\end{aligned}$$

The fraction of orbit subjected to sunlight for an  $\beta$  angle of  $0^\circ$  can be calculated, using equations 2.27 to 2.29.

$$\begin{aligned}
f_E &= \frac{1}{180^\circ} \cos^{-1} \left[ \frac{(h^2 + 2Rh)^{1/2}}{(R + h)\cos\beta} \right] \text{ if } |\beta| < \beta^* \\
&= 0 \text{ if } |\beta| \geq \beta^*
\end{aligned}$$

$$\begin{aligned}
\beta^* &= \sin^{-1} \left[ \frac{6378}{6378 + 550} \right] \quad 0^\circ \leq \beta^* \leq 90^\circ \\
&= 67.015^\circ
\end{aligned}$$

$$|\beta| < \beta^*$$

$$0^\circ < 67.015^\circ$$

$$\begin{aligned}
f_E &= \frac{1}{180^\circ} \cos^{-1} \left[ \frac{(550^2 + 2 \times 6378 \times 550)^{1/2}}{(6378 + 550)\cos 0^\circ} \right] \\
&= 0.3723
\end{aligned}$$

Therefore, the fraction of the orbit exposed to sunlight is;

$$\begin{aligned}
f &= 1 - 0.3723 \\
&= 0.628
\end{aligned}$$

Having all the required parameters, the equilibrium temperature of the CubeSat can be calculated as;

$$\begin{aligned}
T^4 &= \frac{(0.003)(232)}{(0.04964)(5.67 \times 10^{-8})} + 0 \\
&\quad + \frac{(0.01316)(1414) + (0.003)(572.67)}{(0.04964)(5.67 \times 10^{-8})} \left( \frac{0.95}{0.8} \right) (0.628)
\end{aligned}$$

$$T = 270.16^{\circ}K$$

$$T = -2.99^{\circ}C$$

Therefore, calculations show that an equilibrium temperature of  $-2.99^{\circ}C$  is recorded for the antenna, if it were to have an  $\beta$  angle of  $0^{\circ}$  with maximum solar flux. Calculations were conducted for  $\beta$  angles of  $0^{\circ}$  to  $90^{\circ}$  for both hot and cold cases, using minimum and maximum solar flux, as well iterations for power dissipated by a CubeSats system. The full list of calculations can be seen in Appendix F. Figure 4.16, depicts the thermal equilibrium temperatures of the various iterations, where the thermal equilibrium temperature is compared to the relevant  $\beta$  angle.

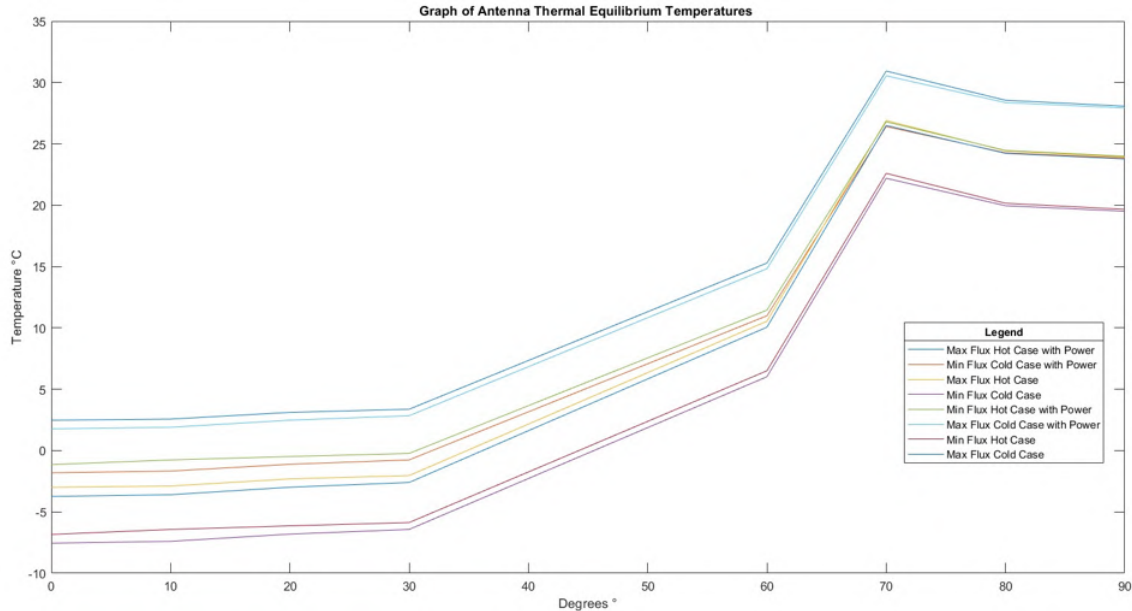


Figure 4.16: Antenna Thermal Equilibrium Temperatures

According to the data recorded on the graph. The lowest thermal equilibrium temperature experienced by the antenna is approximately  $-7.55^{\circ}C$ , at an  $\beta$  angle of  $0^{\circ}$ , experienced at minimum solar flux when the cold case is considered. The highest thermal equilibrium temperature experienced by the antenna is approximately  $30.94^{\circ}C$ , at an  $\beta$  angle of  $70^{\circ}$ , experienced at maximum solar flux when the hot case is considered, when 1W of power is dissipated within the satellite and is radiated to the antenna.

These initial calculations provide very promising results, considering the selected materials. ATSM A228 has a maximum service temperature of  $120^{\circ}C$ , while Acetal has a maximum service temperature of  $120^{\circ}C$  and a minimum of  $-40^{\circ}C$ . PETG, the material the testing model will be made of, has a maximum service temperature of  $70^{\circ}C$  and a minimum of  $-40^{\circ}C$ . Therefore, the equilibrium temperatures of the antenna fall within that of the material limits. However, while these results are



promising and provide a good meaningful basis for initial design, they are not as accurate as the space thermal simulations conducted in section 5.1.1.2. Therefore, the results need to be compared and scrutinised.

It is also important to note that thermal balance calculations, calculate the temperature at which heat radiated out by an object equals the heat absorbed, effectively as if it were a black body. Therefore, the temperatures calculated are not the actual temperatures of the satellite, however they still provide a good idea of what the average temperature of the satellite will be.

# Chapter 5

## Analysis

### 5.1 Finite Element Analysis

In this section of the report, finite element models are used to characterise the antenna. Simulations are conducted to validate theoretical calculations (where applicable) and determine, through simulations, the validity of the QHA design. Another purpose of the simulations is the determination of any unforeseen risks that may require reassessment. The theoretical approach and simulated models will be compared to determine the overall feasibility of the design, before physical testing begins. Simulations were conducted within the Siemens NX environment, using the Nastran solver.

#### 5.1.1 Simulation Setup

The QHA antenna design consists of complex structures. Modelling these structures can present challenges when finite element analysis is to be conducted. Having complex models can lead to computational simulations with extremely long run times. To avoid this, the finite element model of the antenna and deployment system must be simplified. Simplification of the finite element models, leads to less computationally taxing simulations with shorter run times, meaning more simulations can be conducted. However, models cannot be over-simplified, as over simplification can lead to inaccurate simulation results.

Initially, antenna structural simulations were conducted using 1D elements. 1D elements are simple elements consisting of 1 dimension. They are useful for displaying displacements and thermal simulations of complex models, however are very inaccurate in displaying the stresses present within and on a structure. Therefore, 3D elements were used for modelling the stresses present, when the spring antenna is compressed into the "tuna can".

For space systems thermal orbital simulations, 1D elements were used. Due to the complex geometry of the antenna, many shadows appear as it orbits the Earth. The orbital thermal simulations take all the shadows produced by the antenna model into account. This produces a simulation, which is extremely taxing, even for a model using 1D elements.

Therefore, structural simulations are performed using 3D elements (when looking at stresses), while orbital thermal analysis is conducted using 1D elements.

Siemens NX has many solver environments with various applications. Characterising the stresses present in the QHA, the thermal cycling expected, modal analysis and launch environment analysis are all accomplished using different solver environments. Table 5.1, shows the various solver environments used to characterise different aspects of the analysis.

Table 5.1: Solver Solutions Used for Analysis

<b>Analysis Type:</b>	<b>Solver Number:</b>	<b>Description:</b>
Spring Antenna Compression	SOL 402	Nonlinear Kinematics
Thermal Cycling	Simcenter 3D Space Systems Thermal	Space Systems Thermal
Modal	SOL 103	Response Dynamics
Quasi-Static	SOL 402	Nonlinear Kinematics
Sine Wave Sweep	SOL 111	Modal Frequency Response
Random Vibration	SOL 111	Modal Frequency Response
Shock Simulation	SOL 103	Response Dynamics

The following sections depict the simulations conducted on the QHA and antenna housing structure, including the simulation setup and results found.

#### 5.1.1.1 Antenna Spring Model Simulation

To determine the stresses present in and on the antenna model while stowed, the antenna needed to be simulated. Siemens NX with Nastran provides many solution environments where such a simulation can be conducted. Such simulation environments include SOL 101 and SOL 402. SOL 101 or solution 101, provides a linear simulation environment, while SOL 402 provides a nonlinear kinematic environment, which caters towards large displacements. SOL 402 is designed to constantly recalculate the stiffness matrix per an iteration, providing more accurate stresses for simulations of a nonlinear variety. Due to that the antenna is to be compacted from 88.7 mm to approximately 33 mm, the displacement experienced is relatively large. Thus, SOL402 was used to characterise the stresses present on the antenna structure as it's compacted into the "tuna can". The goal of the simulation is to prove that the QHA can be successfully compressed within the housing unit of the antenna deployment system.

To characterise the antenna, a suitable model and simulation setup is required. The antenna will be compressed into the "tuna can", however according to the

hand calculations completed in section 4.2.2, the outer diameter of the spring when compressed to solid height is 45,39 mm. Therefore, not all the "tuna can" area is required. Figure 5.1 depicts the model used for the simulation. The model consists of a rigid body cylinder of 46 mm diameter, which the antenna model is compressed within.

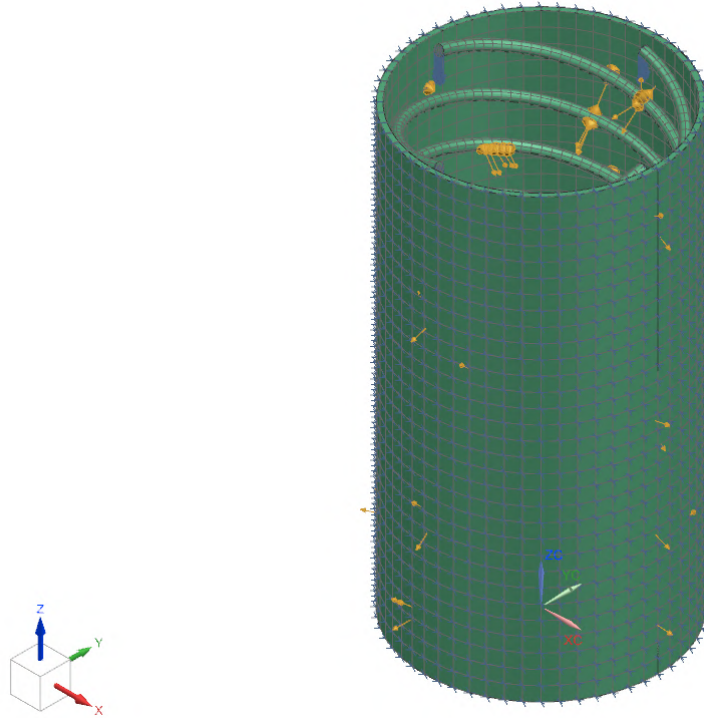


Figure 5.1: Simulation Setup

The simulation may look simple, but is complex in terms of element contact. The simulation is set up so that each filar of the QHA is able to make contact with the 46 mm diameter cylindrical wall, without penetrating the wall. Each filar is also setup to make contact with the filar that is  $+90^\circ$  and  $-90^\circ$  out of phase with that before and after it, without penetration. This ensures that the filars are able to stack up on one another. Figures 5.2 and 5.3, depict the contact regions of the simulation.

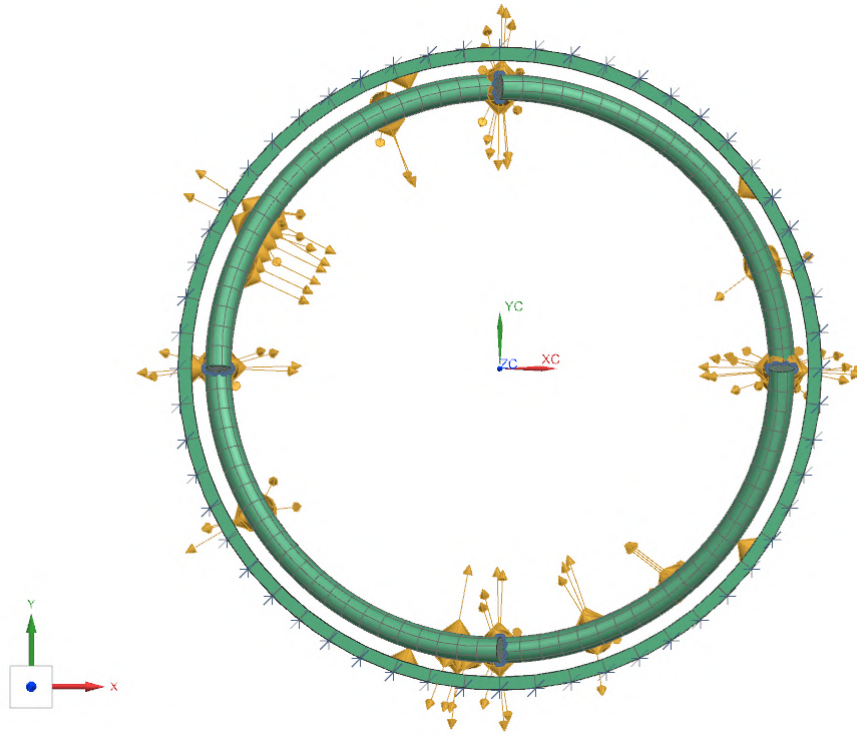


Figure 5.2: Simulation Setup Wall Contact

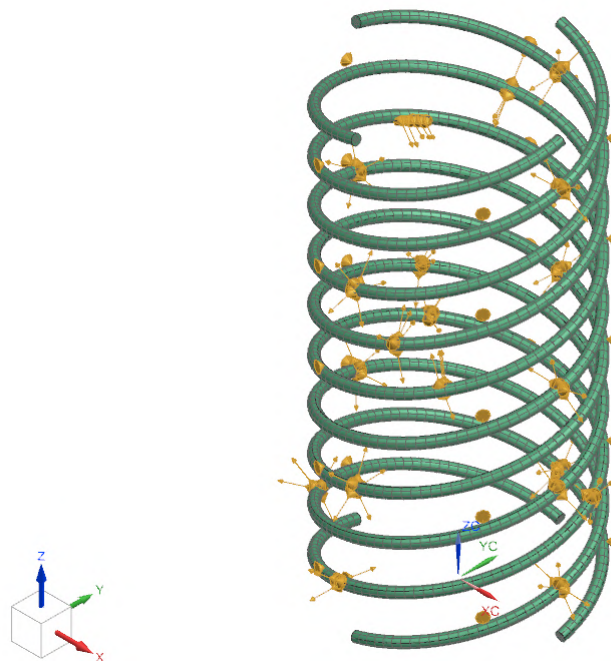


Figure 5.3: Simulation Setup Filar Contact

To ensure the filars do not push straight through the bottom of the cylinder,

the filars are kept in place by a fixed constraint, as shown in Figure 5.4. A fixed constraint locks all the degrees of freedom, therefore emulating how the filars will be fixed within the housing of the deployment system. The cylinder is also kept in place by a fixed constraint, this ensures that as the QHA is compressed, the cylinder will not try to move with it. Figure 5.5 depicts the fixed constraint of the cylinder.

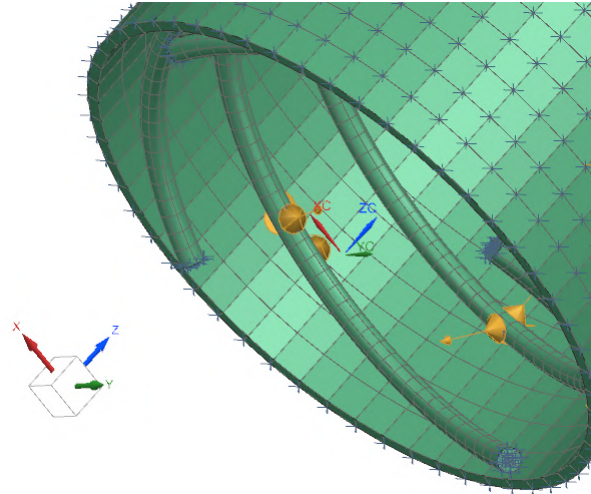


Figure 5.4: Fixed Filar Constraint

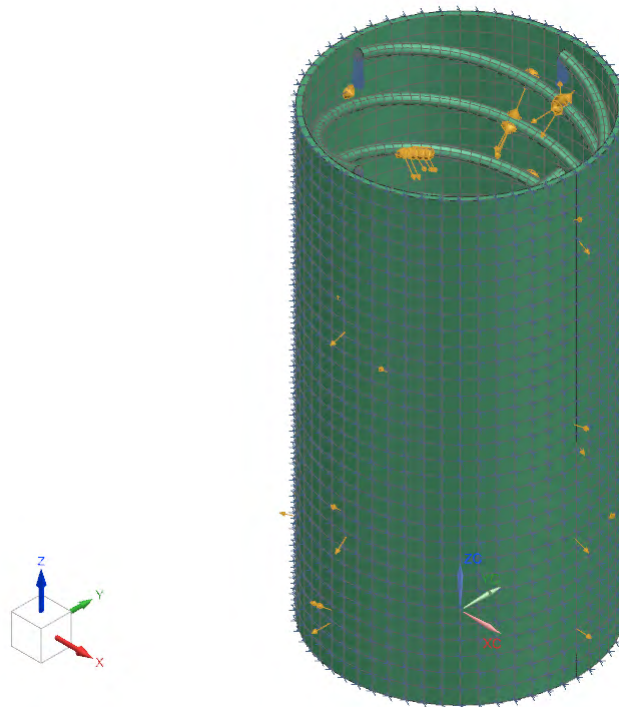


Figure 5.5: Fixed Cylinder Constraint

The overall purpose of the simulation is to create a realistic scenario where the stresses present in the QHA, while being compressed, can be characterised. To

properly accomplish this and to simulate accurate results, appropriate meshing of the elements are required. Figure 5.6, depicts the mesh used for each of the filars. The mesh consists of CHEXA (20) or hexagonal mesh, which is used to simulate parts where bending is to be experienced (such as the filars). The finer the mesh used, the more accurate the end results will be. However, finer mesh leads to more computationally taxing simulations. Therefore, an element size of 1.5 mm was selected for each filar. The mesh is fairly fine, while still being big enough to not be overly computationally taxing. The mesh was assigned to the steel mesh collector, where material properties of ASTM A228 (piano wire) were characterised. The cylinder was modelled using CHEXA (20) mesh too, however much coarser mesh was used, as the simulation is not interested in any results regarding the cylinder.

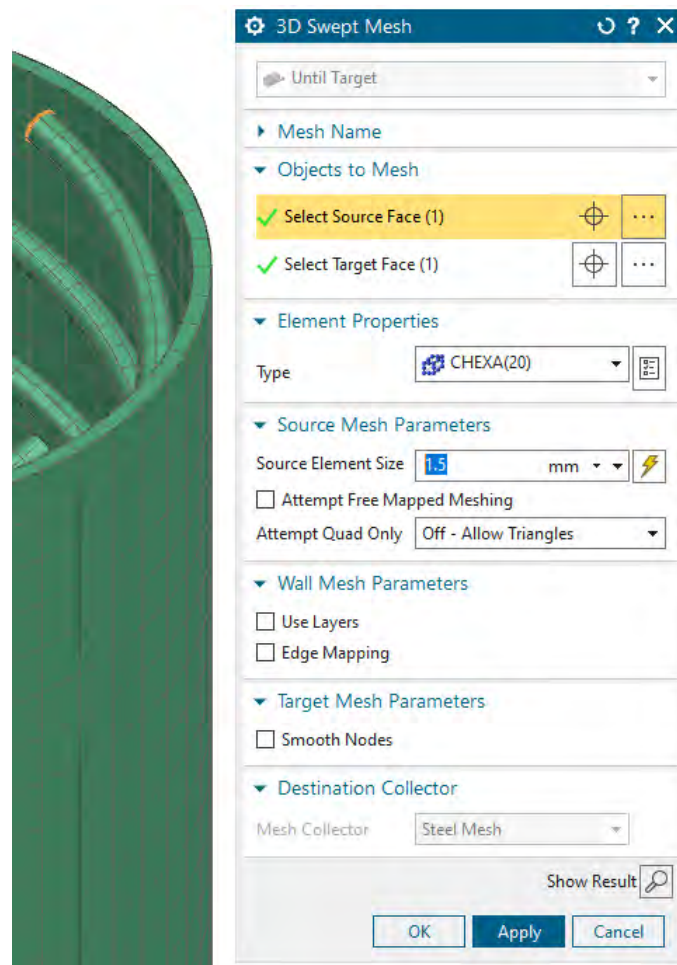


Figure 5.6: Filar Mesh

The last step of the simulation setup was compressing the filars within the cylinder. To accomplish this, an enforced displacement constraint was applied to each filar. The enforced displacement was set to allow the filar to be displaced along the Z-axis. The displacement was set to 55 mm, which would displace the filars to a height below that of the "tuna can" depth. Figure 5.7, depicts the enforced displacement constraint on the filars.

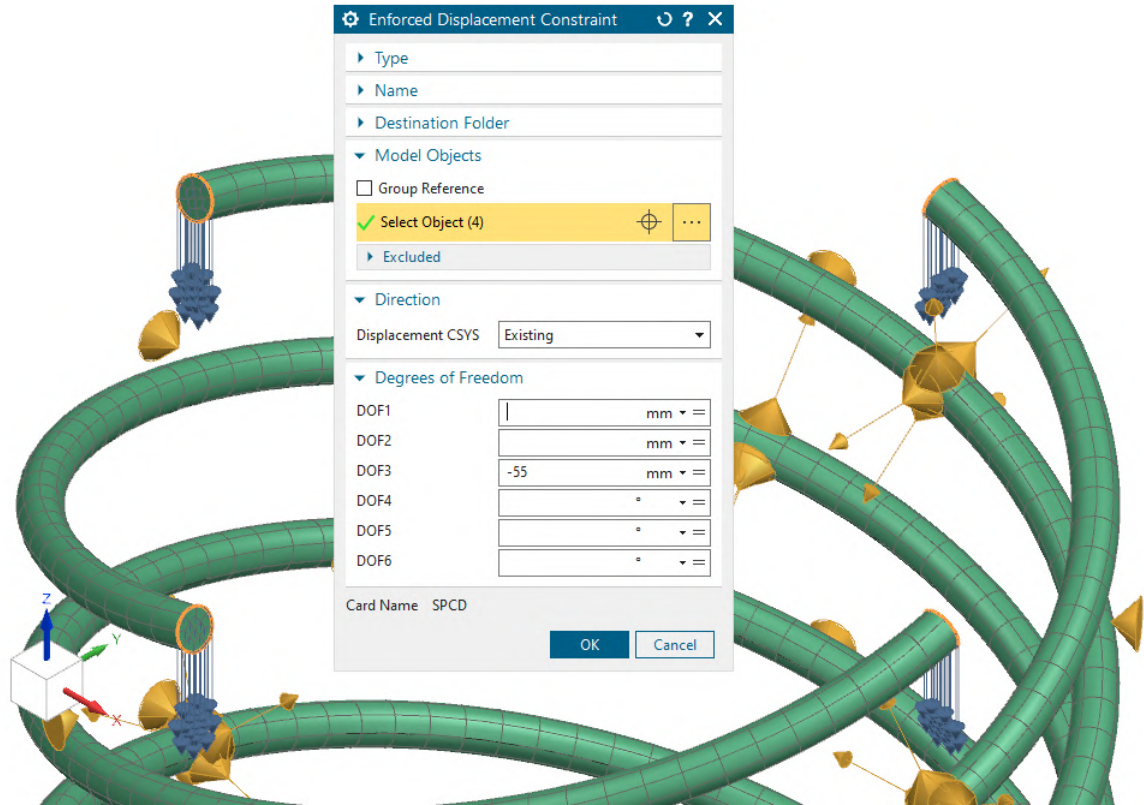


Figure 5.7: Enforced Displacement Constraint

With the simulation setup complete, the simulation was processed and results for the stress and displacement of the model were characterised. Figure 5.8 depicts the model post-processing.



4 Filar\_sim1 : 402 with Wire contact Result  
Subcase - Nonlinear Statics 1, Increment 10, 1.00s  
Displacement - Nodal, Magnitude  
Min : 0.00, Max : 55.19, Units = mm  
Deformation : Displacement - Nodal Magnitude

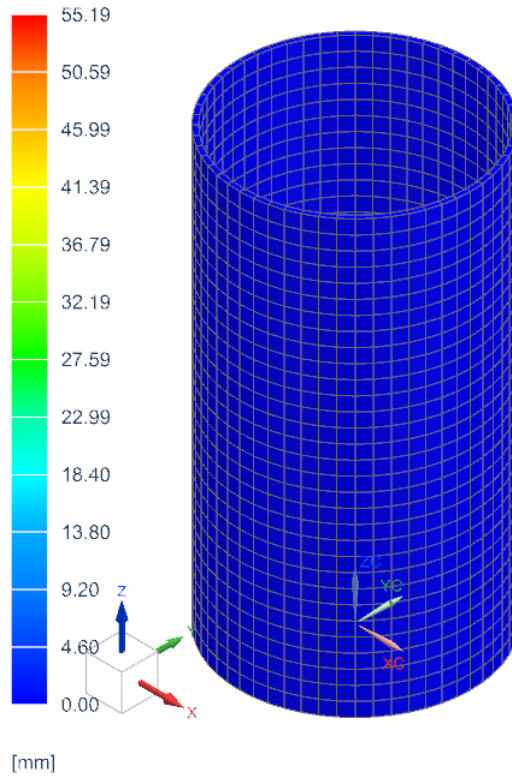


Figure 5.8: Simulation Results

Due to that the QHA model is encompassed by the cylinder, it is very hard to see the displacements and stresses present in the model. To work around this, a cross-section of the simulated model can be taken. Figure 5.9, depicts the cross-section of the displacement present.

4 Filar\_sim1 : 402 with Wire contact Result  
Subcase - Nonlinear Statics 1, Increment 10, 1.00s  
Displacement - Nodal, Magnitude  
Min : 0.00, Max : 55.19, Units = mm  
Coord sys : Native  
Deformation : Displacement - Nodal Magnitude

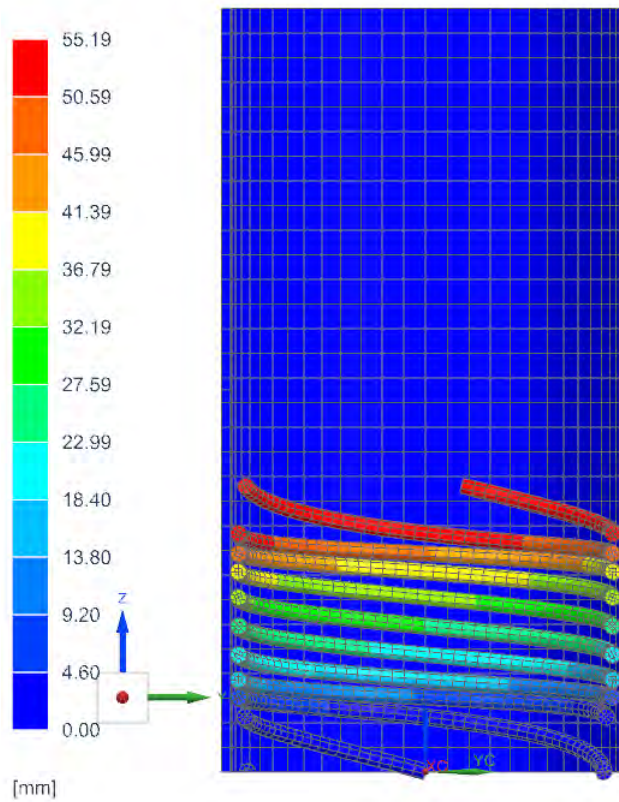


Figure 5.9: Simulated Displacement

The model shows that when the QHA is subjected to the enforced displacement constraint, it will be displaced to a height below that of the "tuna can" depth. Figure 5.9, also depicts the contact experienced by the model. The simulation shows that filars in contact with one another and the cylinder wall are not penetrating each other. There are two very important stresses which need to be analysed from the model, being the maximum shear stress and the Von-mises stress present in the model. Figure 5.10, depicts the Von-mises stress experienced by the QHA when compressed.

4 Filar\_sim1 : 402 with Wire contact Result  
 Subcase - Nonlinear Statics 1, Increment 10, 1.00s  
 Von-Mises Stress [PK2] - Element-Nodal, Unaveraged, Scalar  
 Min : 0.00, Max : 2577.61, Units = MPa  
 Coord sys : Native  
 Deformation : Displacement - Nodal Magnitude

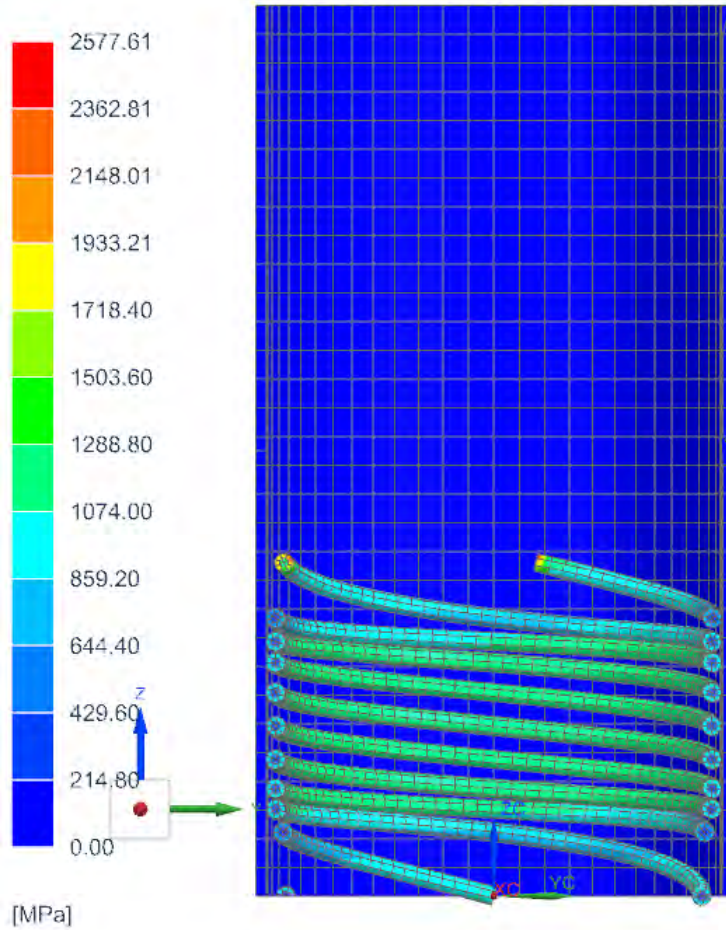


Figure 5.10: Model Cross-Section Von-Mises Stress

Looking at the simulation, the maximum Von-mises stress occurs at the top tips of the filars where the enforced displacement was applied. These stresses can be ignored, as they are contact stresses induced by the enforced displacement and don't affect the bending of the filars. Therefore, looking at the model, the maximum Von-mises stress within the filars occurs on the inner diameter (as is expected) and ranges from approximately 1074 MPa to 1718.40 MPa. Both these values fall below the yield stress of ASTM A228, which is recorded as 1970 MPa for 1.91 mm wire, as taken from Matweb materials database.

The single most important aspect of the simulation is analysing the maximum shear stress experienced by the QHA. Figure 5.11, depicts the simulated maximum shear stress experienced by the QHA model. As with the Von-mises stress, the maximum shear stress occurs at the point of the enforced displacement and can, therefore, be ignored for the same reason.

4 Filar\_sim1 : 402 with Wire contact Result  
 Subcase - Nonlinear Statics 1, Increment 10, 1.00s  
 Stress [PK2] - Element-Nodal, Unaveraged, Max Shear  
 Min : 0.00, Max : 1450.77, Units = MPa  
 Coord sys : Native  
 Deformation : Displacement - Nodal Magnitude

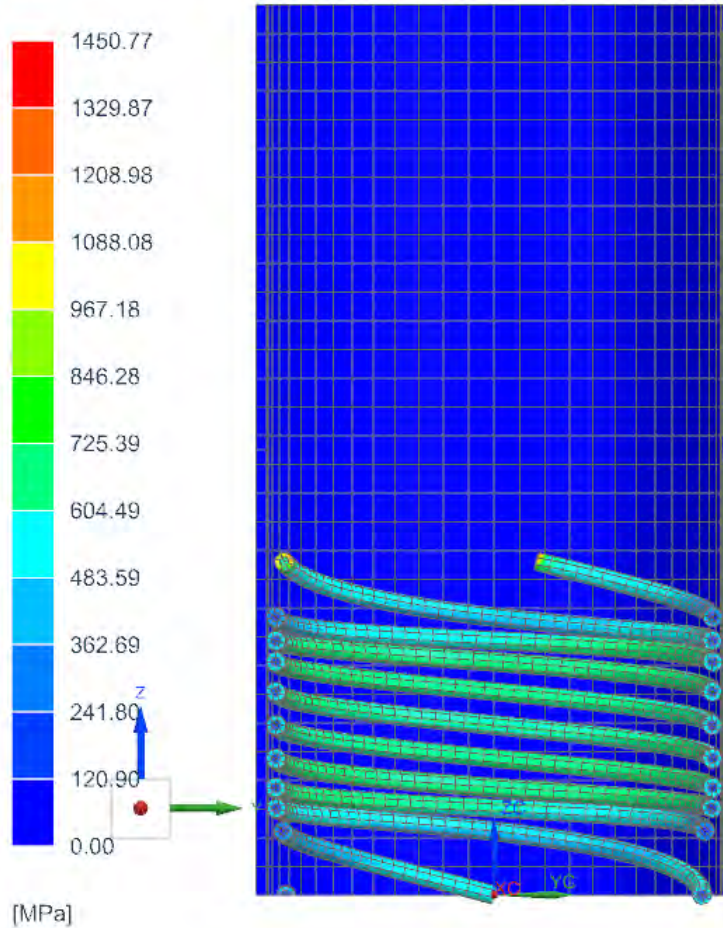


Figure 5.11: Model Cross-Section Shear Stress

Analysing the maximum shear stress shows that the maximum stress experienced by the model occurs on the inner diameter of the spring, as expected. Maximum shear stress in the model ranges from 604.49 MPa to 846,26 MPa. The maximum shear stress experienced by the model is extremely important for analysis, to obtain a better perspective of the stress present, the legend was manipulated to include all shear stresses up to 900 MPa, as shown in Figure 5.12.

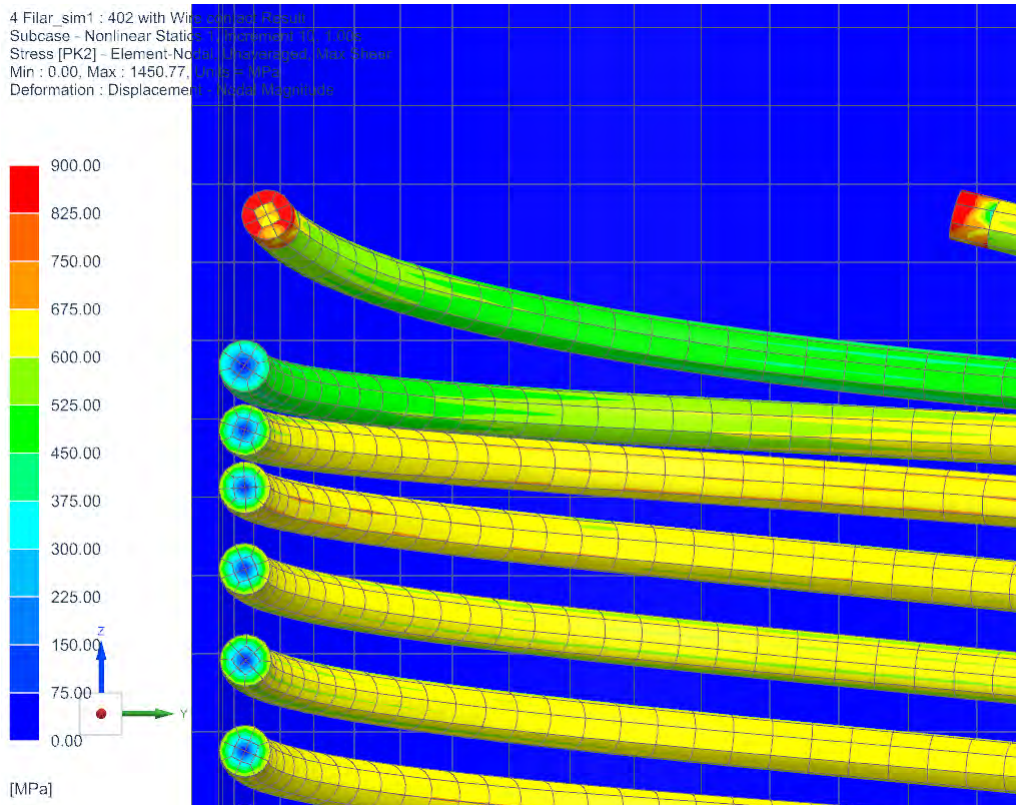


Figure 5.12: Shear Stress Manipulated Legend

The model shows that the shear stress experienced by the QHA may be less than the calculated values. On closer inspection, the simulation suggests that the QHA is subjected to shear stress predominantly in the range of 525 MPa to 750 MPa. With 750 MPa being the maximum shear stress experienced on the inner diameter of the springs. Therefore, the maximum shear stress experienced by the QHA is less than the calculated value and within the range of the maximum allowed shear stress for ASTM A228, which is 886.5 MPa.

Therefore, the simulation shows that the spring can be compressed to below the "tuna can" depth and not exceed the relevant stress parameters. Therefore, the spring can be tested.

### 5.1.1.2 Thermal Cycling Simulation

To determine the expected temperatures the antenna will experience while orbiting the Earth, a thermal cycling simulation is required. The simulation is conducted using Simcenter 3D Space Systems Thermal, the solution environment is tailored for simulating the thermal environment that a spacecraft or component is exposed to in a particular orbit. Orbit parameters are set so that they are similar to ZACube-1 and ZACube-2.

The geometry of the QHA casts many shadows as it orbits around the Earth, the

simulation environment needs to take all these shadows into account when determining the temperature cycles of the antenna. This can be extremely computationally taxing. Therefore, a simplified version of the QHA is required. Figure 5.13, depicts the mesh used to simulate the thermal conditions of the QHA. Each filar of the QHA consist of 200 1D beam elements, while this may not be as accurate as a 3D meshed simulation, it does provide a good basis for determining the thermal conditions the antenna and deployment system are to be exposed to. Figure 5.14, depicts the solid elements that are representative of the 1.91 mm diameter ASTM A228 wire. The following thermo-mechanical properties of ASTM A228 were used to set up the simulation, young's modulus,  $E = 210 \text{ GPa}$ , coefficient of thermal expansion,  $\alpha = 13.2 \mu\text{m}/\text{m}^\circ\text{C}$ , yield stress,  $\sigma_y = 1970 \text{ MPa}$ , shear modulus,  $G = 80 \text{ GPa}$  and density,  $\rho = 7860 \text{ kg}/\text{m}^3$ .

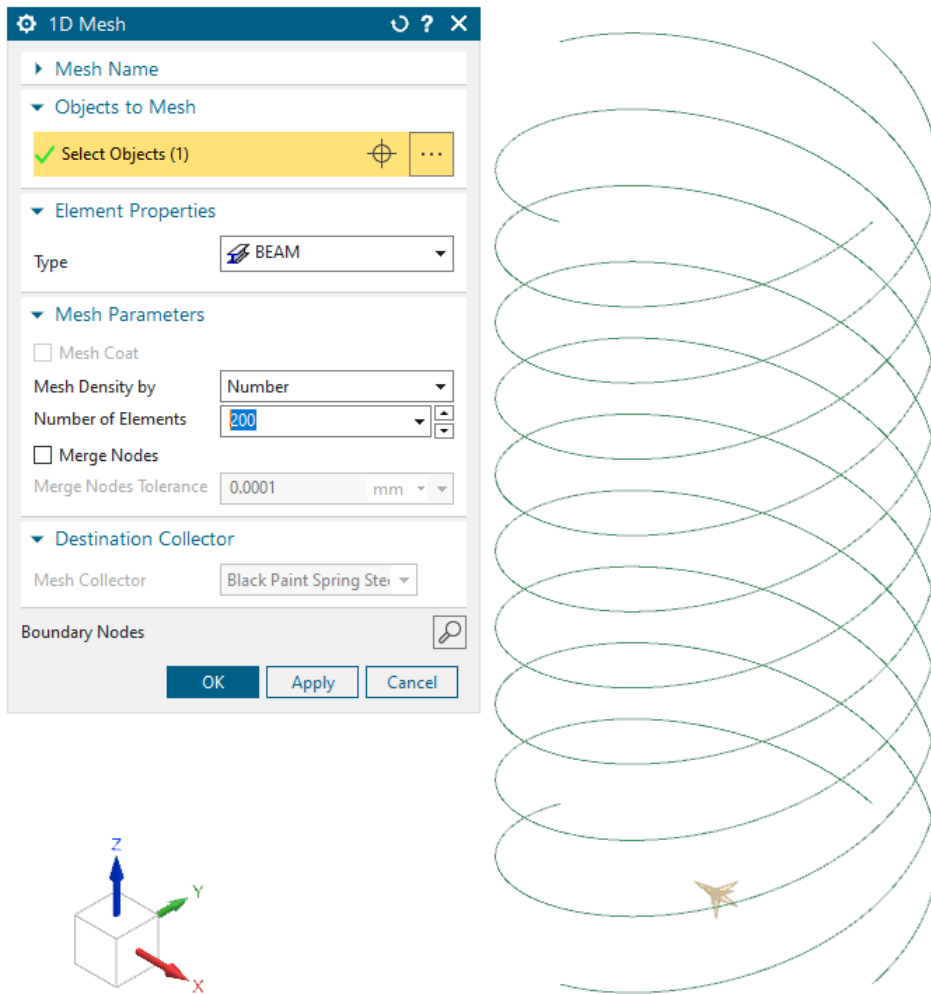


Figure 5.13: Thermal Cycling 1D Mesh

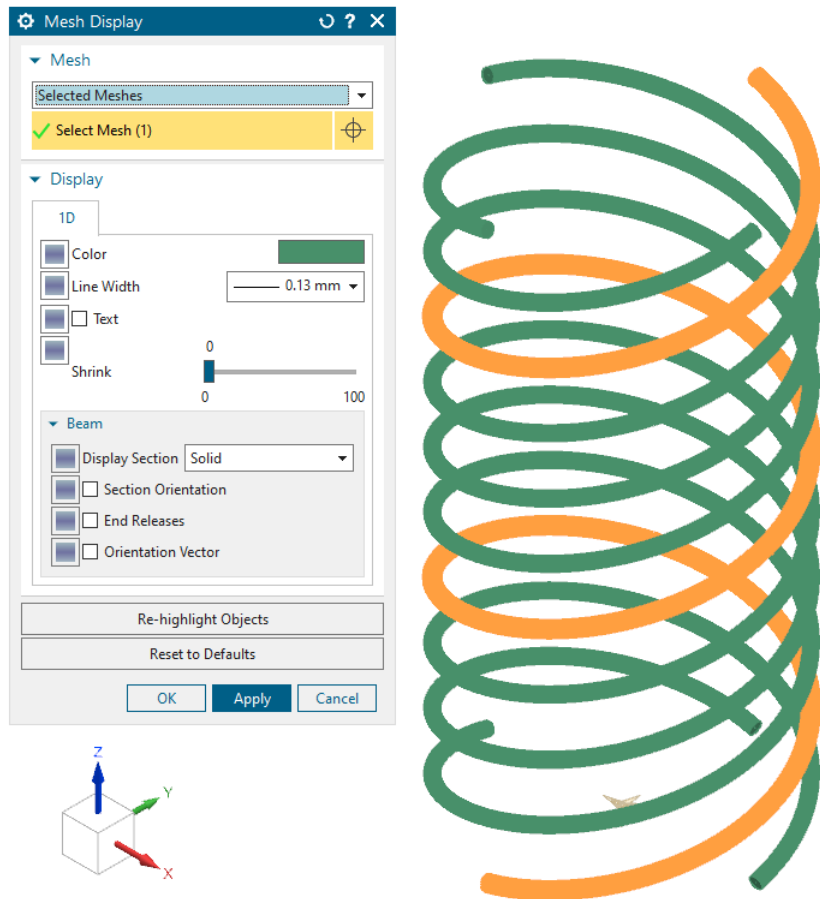


Figure 5.14: Thermal Cycling 1D Solid Mesh

Figure 5.15, depicts the material and thermo-optical properties used for the 1D mesh elements.

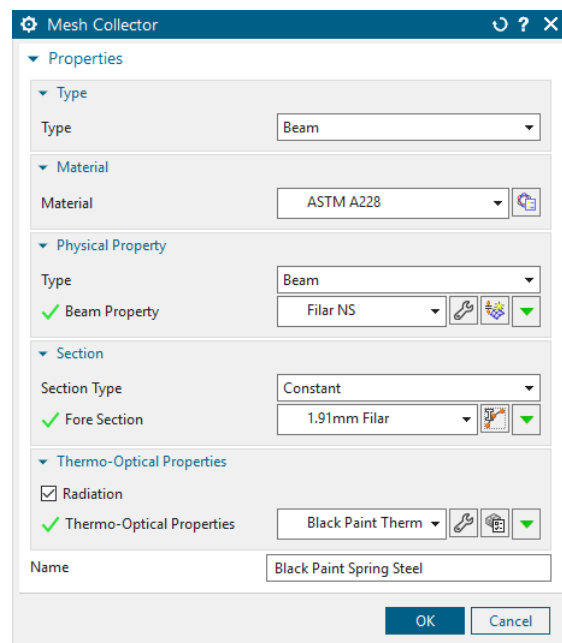


Figure 5.15: Thermal Mesh Collector

For the thermal simulation to work, the thermo-optical properties of the material need to be defined. In section 4.5, thermal equilibrium calculations were completed, thermal equilibrium occurs when the absorptance ( $\alpha$ ) divided by the emissivity ( $\varepsilon$ ) is approximately 1 (black body). However, finding material or surface finishes where,  $\frac{\alpha}{\varepsilon} = 1$  can be challenging. Therefore, materials which equate to approximately 1 were considered. Black paint was therefore selected and input into the thermo-optical properties. Black paint has an  $\varepsilon = 0.9$  and a  $\alpha = 0.95$  (Fortescue et al., 2011).

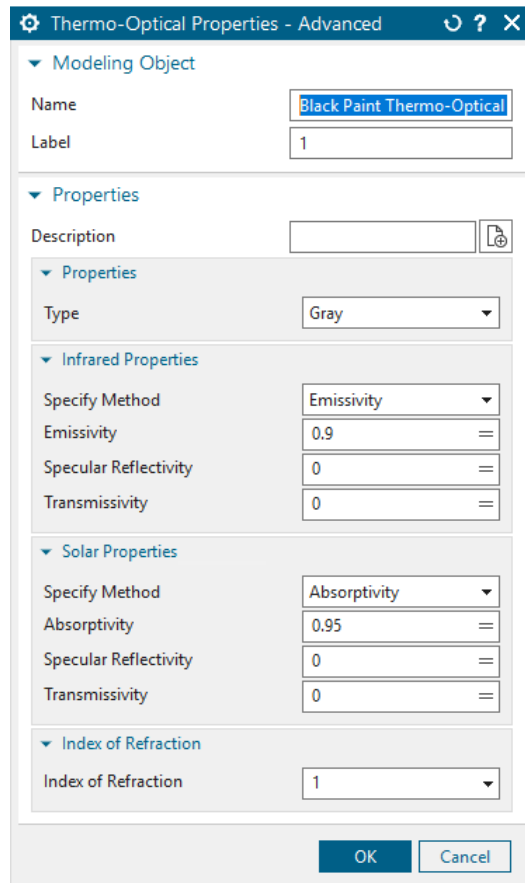


Figure 5.16: Thermo-optical Properties

The transient setup of the simulation is important for determining the sampling rate of the simulation and defining the time steps and number of orbits to be completed in the simulations. Figure 5.17, depicts the transient setup. The maximum number of orbits the simulation completes is 10, with a sampling rate in orbit set to every 3 minutes, which is similar to that of ZACube-1 and ZACube-2.



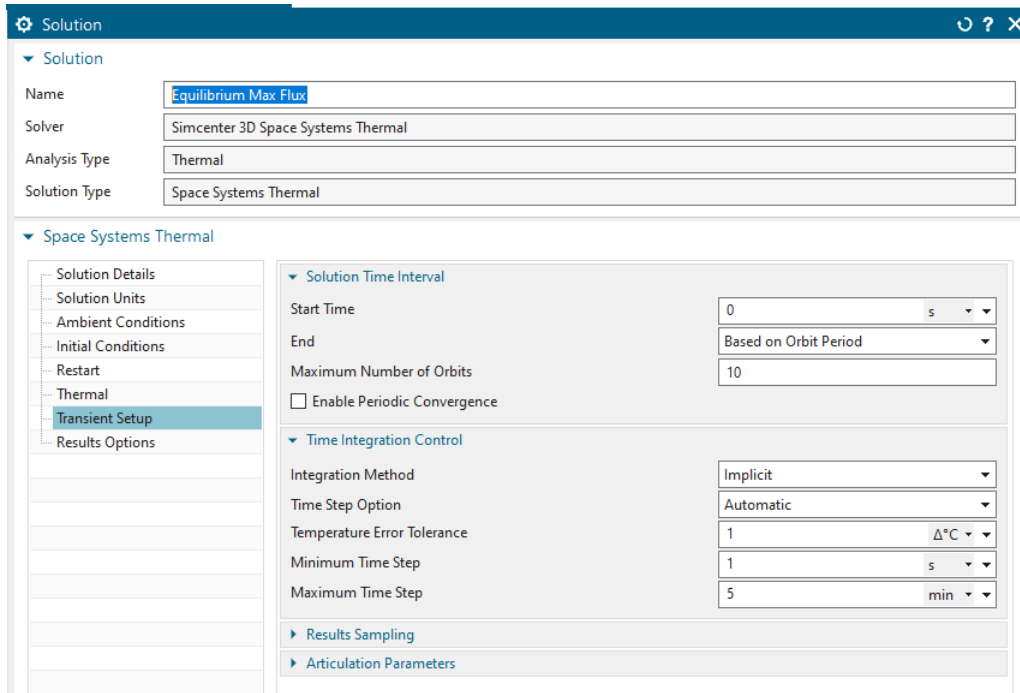


Figure 5.17: Thermal Cycling Transient Setup

Figure 5.18, depicts the ambient conditions of the simulation. The orbit altitude is set to 550 km, and the fluid temperature and radiative environment are set to 3 K, this is due to that the background temperature of space is 3 K. In other words if an object was left in space and didn't receive any radiative energy, it would radiate all its heat out, until it reached a temperature of 3 K (-270.15 °C).

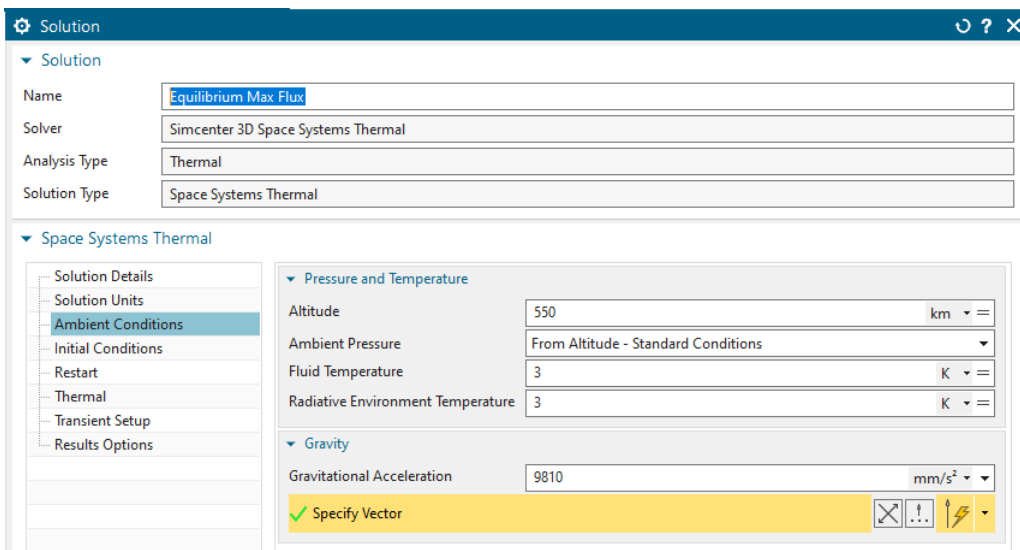


Figure 5.18: Thermal Cycling Ambient Conditions Setup

The orbital heating setup of the thermal cycling simulation is crucial for determining accurate thermal condition results. Figures 5.19 to 5.21, depict the process

for defining the orbital heating the QHA will experience, as it orbits around the Earth.

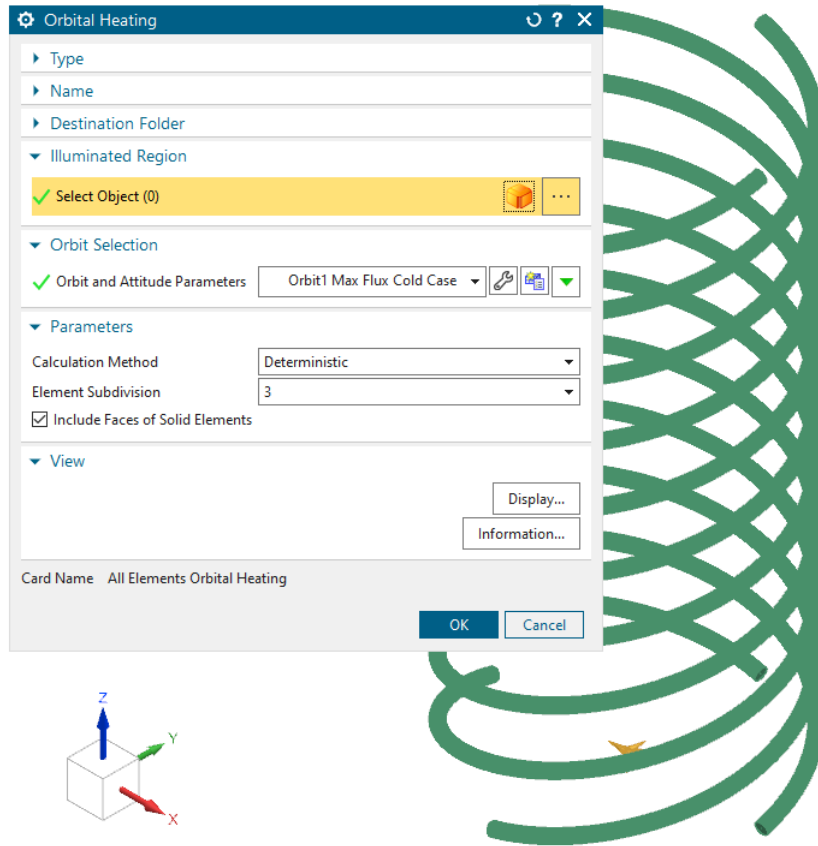


Figure 5.19: Thermal Cycling Orbital Heating Setup

Figure 5.20, depicts the orbital parameters used for defining the thermal environment. The orbit is set to a sun-synchronous orbit, with a minimum altitude of 550 km, with zero eccentricity, an orbit inclination of  $97.57^\circ$  and a local time at ascending node (LTAN) of 12:00.

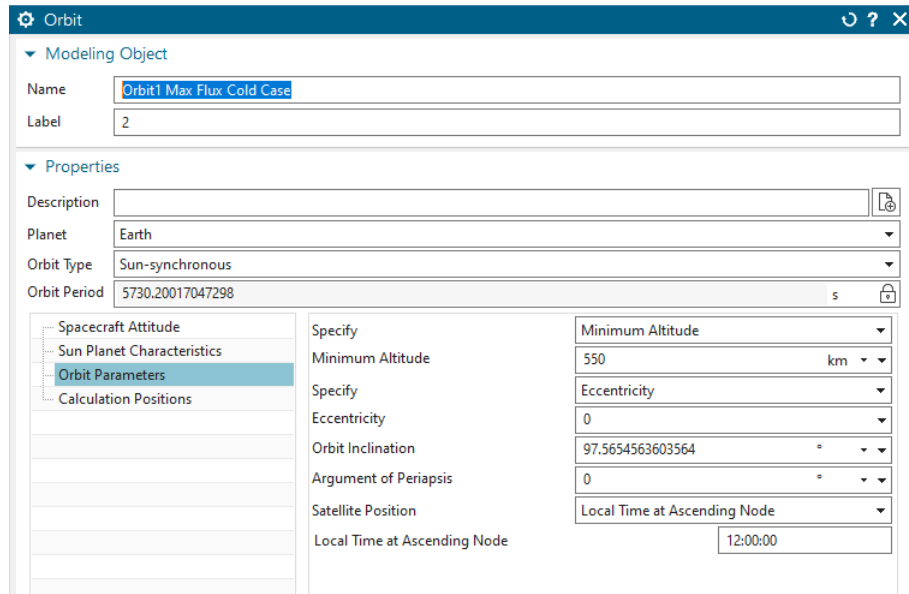


Figure 5.20: Thermal Cycling Orbital Parameters Setup

Figure 5.21, depicts the Sun and planet characteristics used for characterising the thermal environment of the QHA. Three important aspects which need to be defined are the solar flux density, albedo radiation and planetary radiation. Four thermal condition simulations were conducted. Two for maximum solar flux density, with a 'HOT' and 'COLD' case and two for minimum solar flux density, with a 'HOT' and 'COLD' case. This is conducted to determine the worst case thermal conditions the QHA could be exposed to. The albedo and planetary radiation change depending on whether the 'HOT' or 'COLD' case is experienced.

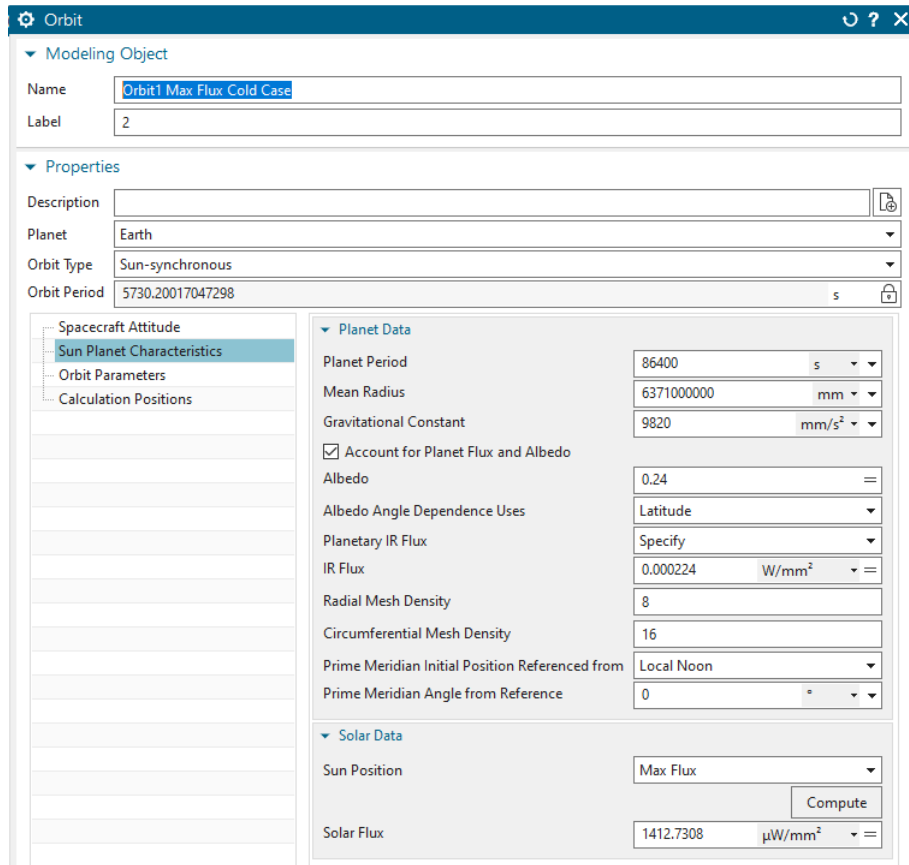


Figure 5.21: Thermal Cycling Sun-planet Characteristics

Figures 5.22 and 5.23, depicts the thermal cycling results of the QHA for the four different iterations. According to the simulations, the QHA can get as hot as  $37.96^{\circ}C$  and as cold as  $-53.446^{\circ}C$ , under worst case conditions, without internal power. However, in a more realistic scenario heat will be radiated through the QHA system, while the satellite is operational (internal components generate heat). Therefore, obtaining thermal results which includes heat that is radiated through a satellite, will depict better predictions of the thermal environment, the antenna could be exposed to.

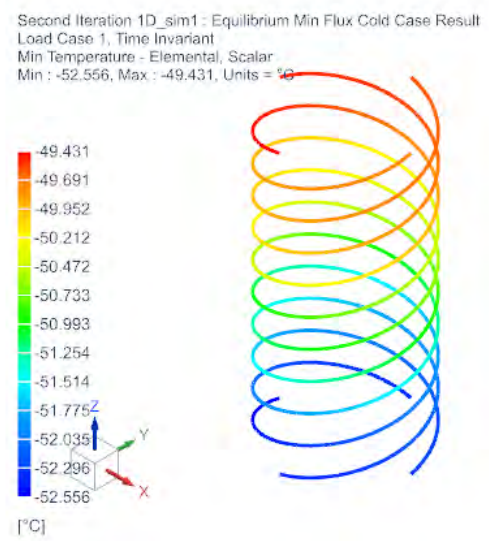
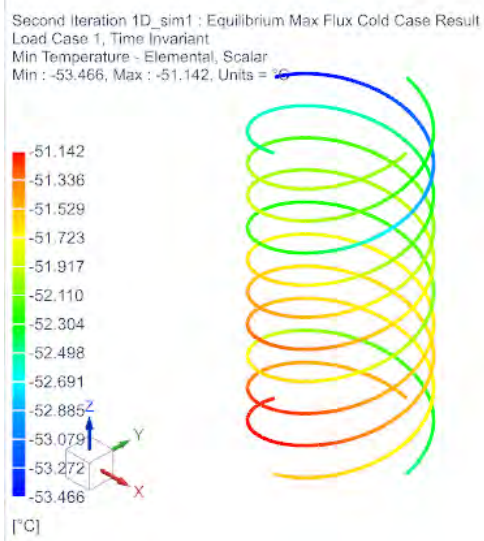
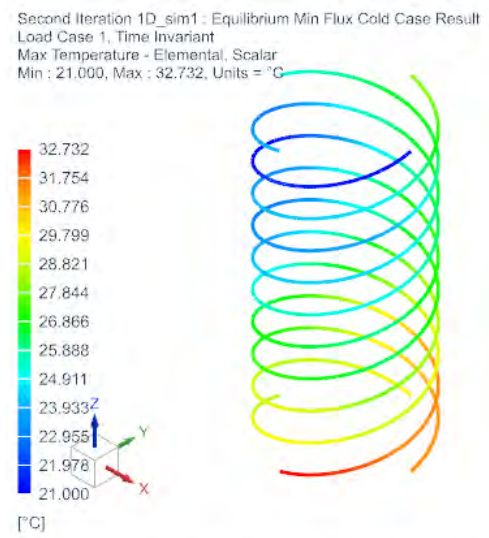
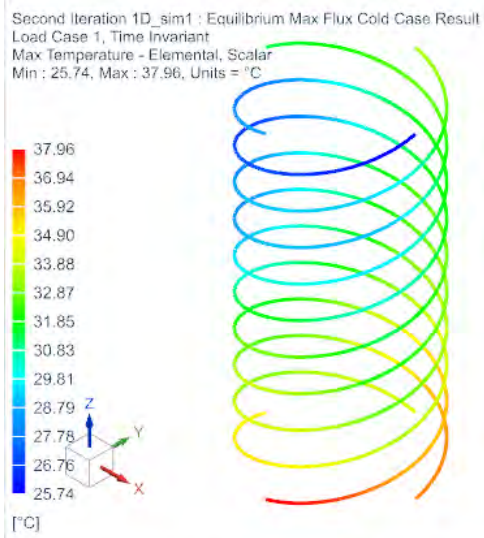


Figure 5.22: Maximum and Minimum Flux Cold Case Temperature Range

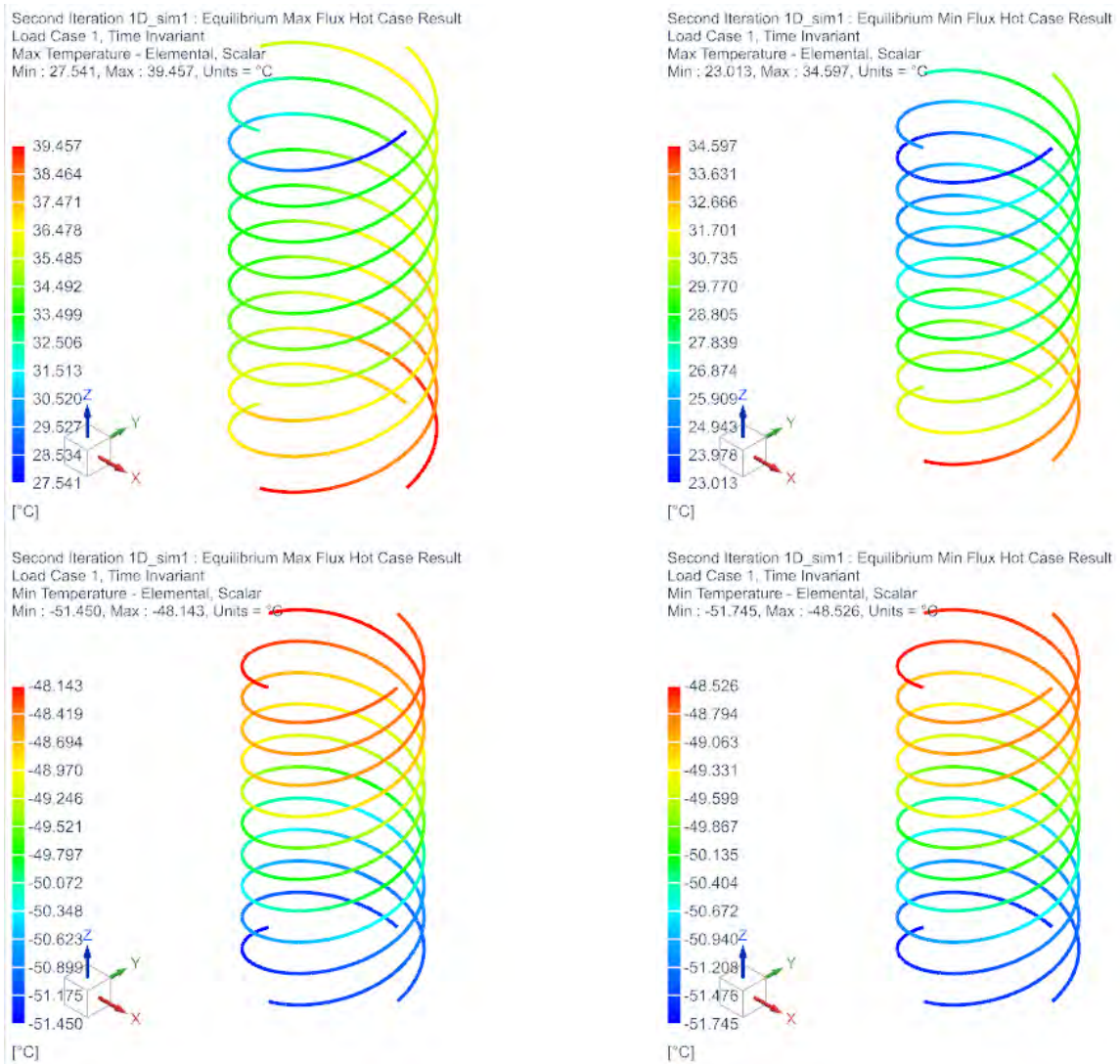


Figure 5.23: Maximum and Minimum Flux Hot Case Temperature Range

To simulate the temperature environment of the antenna when it is operational, internal power dissipated can be added to the simulation in the form of a thermal load, as shown in Figure 5.24. A thermal load of 1W was used in the simulation, as with the thermal balance calculations.

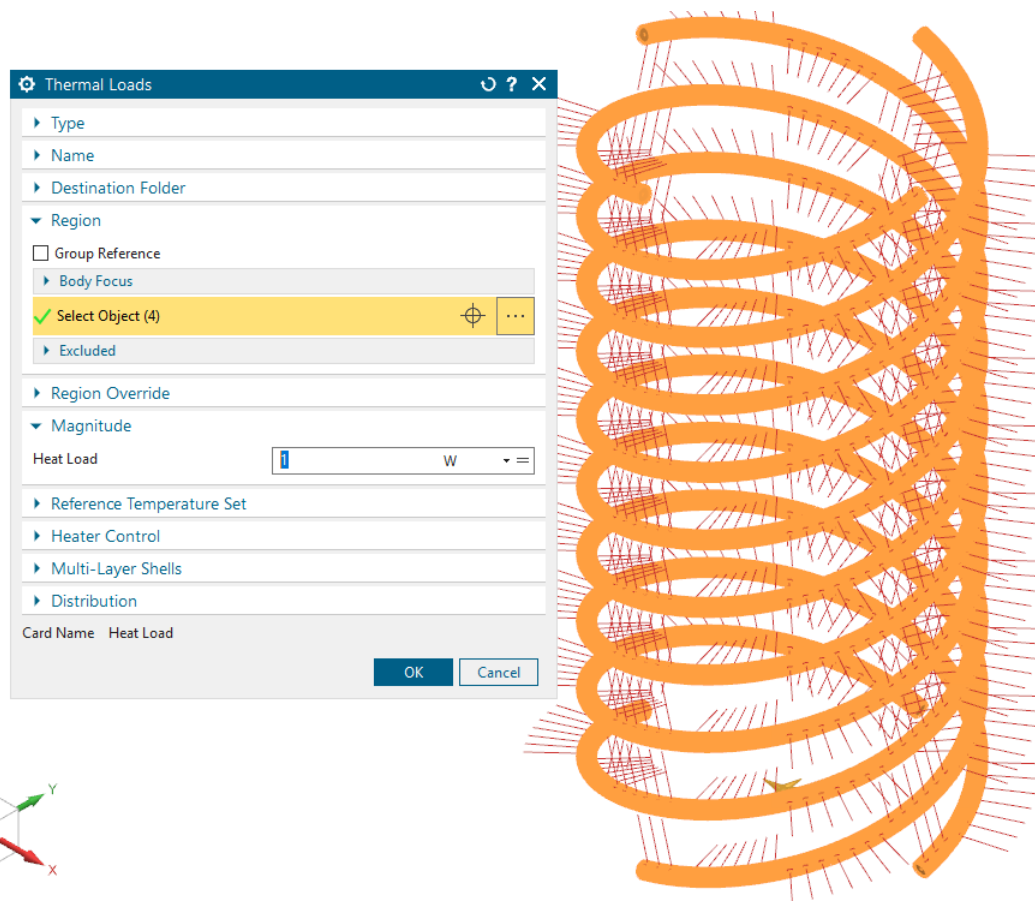
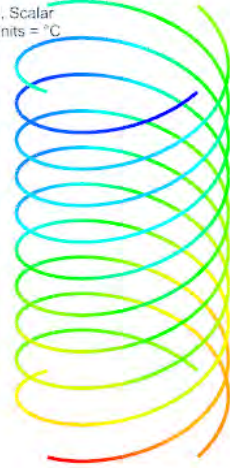
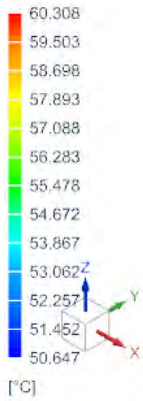


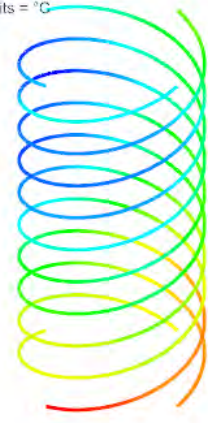
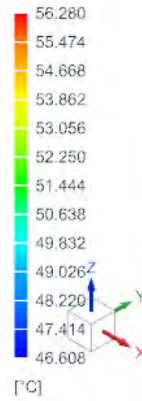
Figure 5.24: Thermal Load

Figures 5.25 and 5.26, depicts the thermal graphs and temperature cycling of the QHA for the four different iterations, when internal power is considered. According to the simulations, the QHA can get as hot as  $61.884\text{ }^{\circ}\text{C}$  and as cold as  $-14.727\text{ }^{\circ}\text{C}$ , under worst case conditions.

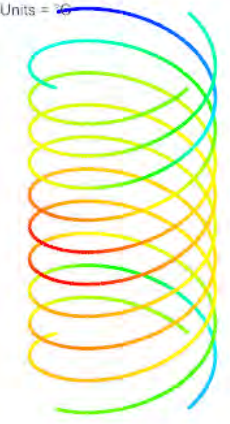
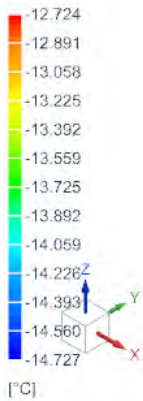
Second Iteration 1D\_sim1 : Equilibrium Max Flux Cold Case Power Result  
 Load Case 1, Time Invariant  
 Max Temperature - Elemental, Scalar  
 Min : 50.647, Max : 60.308, Units = °C



Second Iteration 1D\_sim1 : Equilibrium Min Flux Cold Case Power Result  
 Load Case 1, Time Invariant  
 Max Temperature - Elemental, Scalar  
 Min : 46.608, Max : 56.280, Units = °C



Second Iteration 1D\_sim1 : Equilibrium Max Flux Cold Case Power Result  
 Load Case 1, Time Invariant  
 Min Temperature - Elemental, Scalar  
 Min : -14.727, Max : -12.724, Units = °C



Second Iteration 1D\_sim1 : Equilibrium Min Flux Cold Case Power Result  
 Load Case 1, Time Invariant  
 Min Temperature - Elemental, Scalar  
 Min : -14.333, Max : -11.822, Units = °C

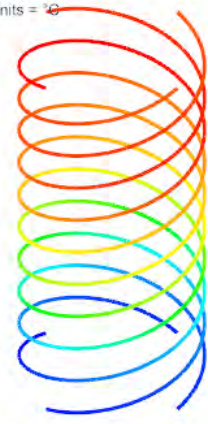
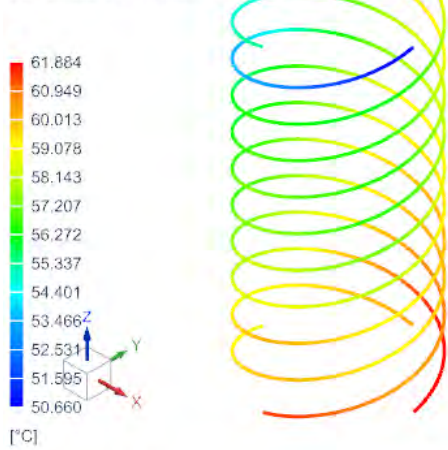


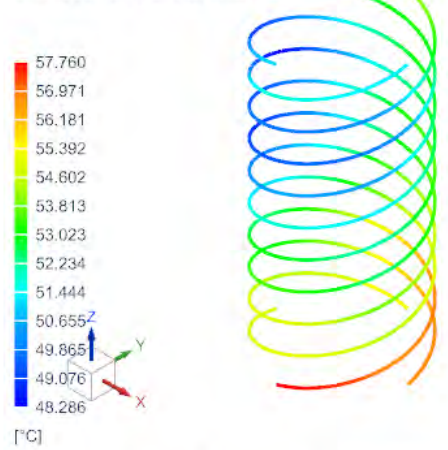
Figure 5.25: Maximum and Minimum Flux Cold Case Temperature Range with Power



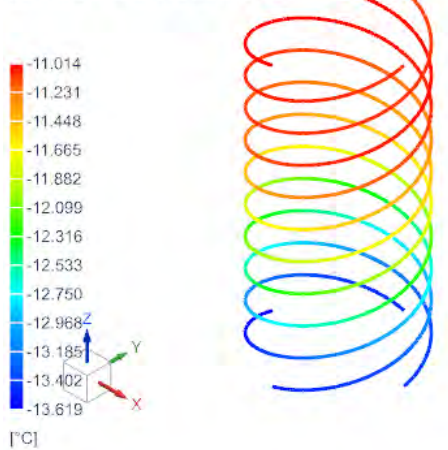
Second Iteration 1D\_sim1 : Equilibrium Max Flux Hot Case Power Result  
 Load Case 1, Time Invariant  
 Max Temperature - Elemental, Scalar  
 Min : 50.660, Max : 61.884, Units = °C



Second Iteration 1D\_sim1 : Equilibrium Min Flux Hot Case Power Result  
 Load Case 1, Time Invariant  
 Max Temperature - Elemental, Scalar  
 Min : 48.286, Max : 57.760, Units = °C



Second Iteration 1D\_sim1 : Equilibrium Max Flux Hot Case Power Result  
 Load Case 1, Time Invariant  
 Min Temperature - Elemental, Scalar  
 Min : -13.619, Max : -11.014, Units = °C



Second Iteration 1D\_sim1 : Equilibrium Min Flux Hot Case Power Result  
 Load Case 1, Time Invariant  
 Min Temperature - Elemental, Scalar  
 Min : -13.793, Max : -11.208, Units = °C

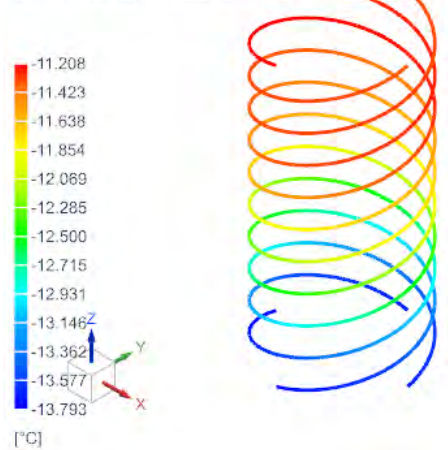


Figure 5.26: Maximum and Minimum Flux Hot Case Temperature Range with Power

It is of great interest to analyse the difference in thermal range recorded for the QHA with and without power. Figure 5.27, shows the full thermal range of simulated results for both sets of data.

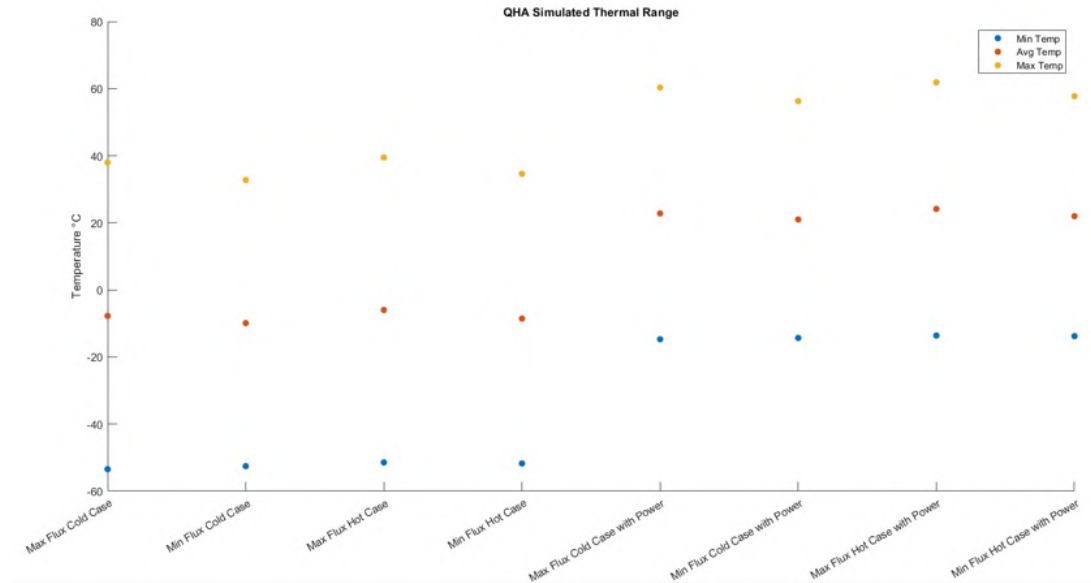


Figure 5.27: Simulated QHA Thermal Range

The scatter plot shows that there is a notable increase in the simulated temperatures of the QHA, when heat is radiated from within the satellite. By taking the averages of the simulated temperatures, it can be seen that similar temperatures are recorded for the thermal equilibrium equations conducted in section 4.5. This suggests that the QHA system is in thermal equilibrium.

Comparing the worst case conditions to the calculated values, shows a difference. However, this is to be expected. The hand calculations provide an idea of the thermal environment to be expected, while the simulations provide a more thorough and accurate approach to determining the worst case thermal conditions.

Simulations, conducted with heat radiated in the satellite, provides a more realistic view of the expected thermal range of the antenna system. This becomes more evident, especially when considering on board CubeSat components usually have a maximum thermal range between  $-20^{\circ}C$  and  $60^{\circ}C$ . Therefore, thermal expansion and contraction simulations will be conducted using the worst case hot and cold scenarios with power ( $-14.727^{\circ}C$  to  $61.884^{\circ}C$ ).

### 5.1.1.3 Thermal Expansion and Contraction Simulations

Having simulated the expected thermal environment of the antenna system, the thermal expansion and contraction of components can be determined based on worst case scenarios. To accomplish this, a thermal expansion simulation (SOL 153) must be conducted, as shown in Figure 5.28.

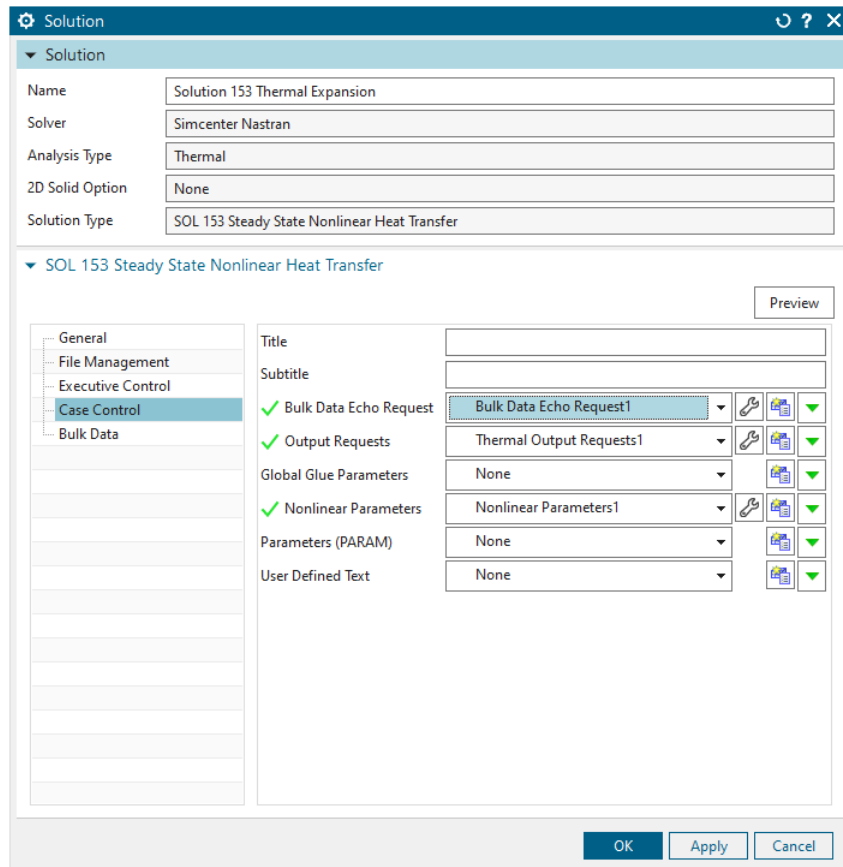


Figure 5.28: SOL 153 Thermal Expansion Simulation

To apply the worst case heating and cooling conditions, a thermal constraint is applied to the model. Two simulations must be conducted, one for worst case heating and one for worst case cooling. Both simulations follow the same setup. Figure 5.29, depicts the worst case heating constraint, where a temperature of 61.884 °C is applied to the model.

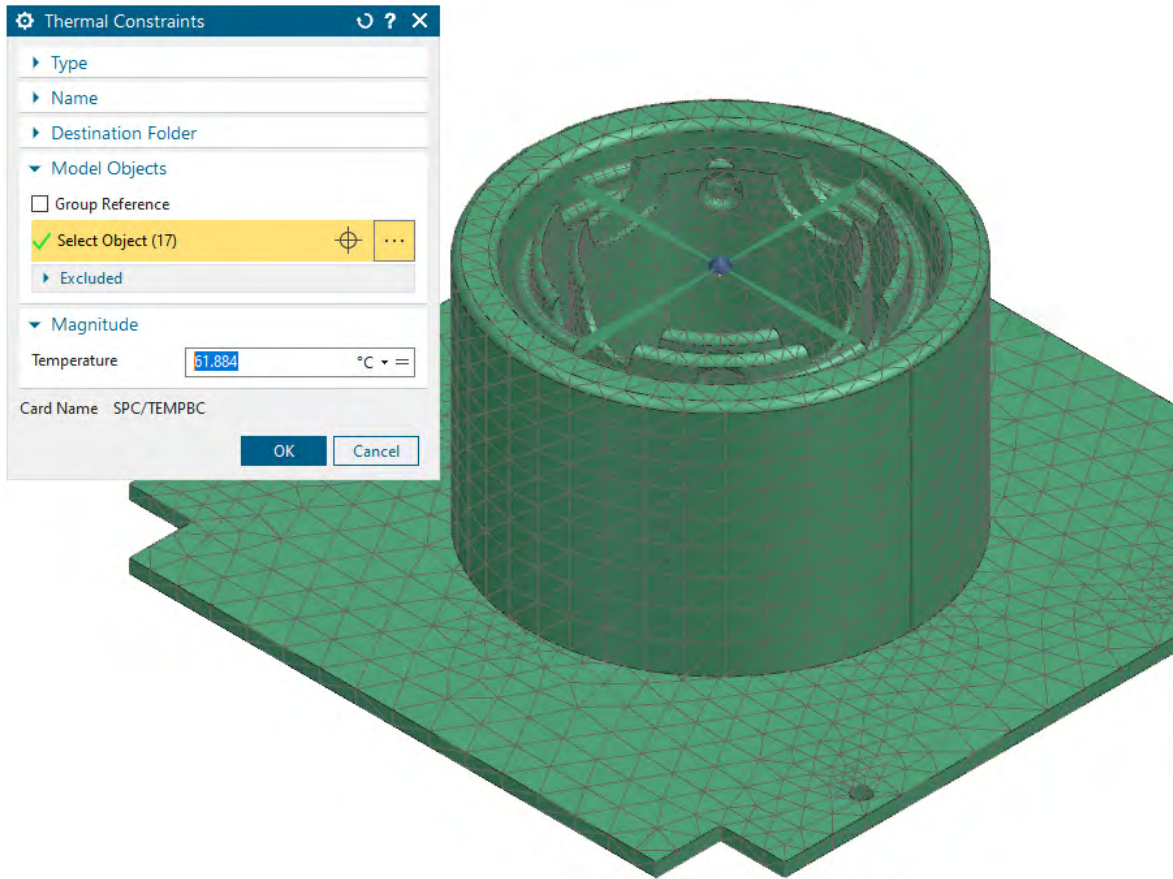


Figure 5.29: SOL 153 Thermal Heating Constraint

Once the thermal constraint has been applied, the simulation can be processed and produces results, as shown in Figure 5.30. The same is completed for the cold case ( $-14.727^{\circ}C$ ).

Final Assembly Rev2\_sim1 : Solution 153 Thermal Expansion Result  
Subcase - Loads, Constraints 1, Static Step 1, 1.00  
Temperature - Nodal, Scalar  
Min : 6.188E+01, Max : 6.188E+01, Units = °C

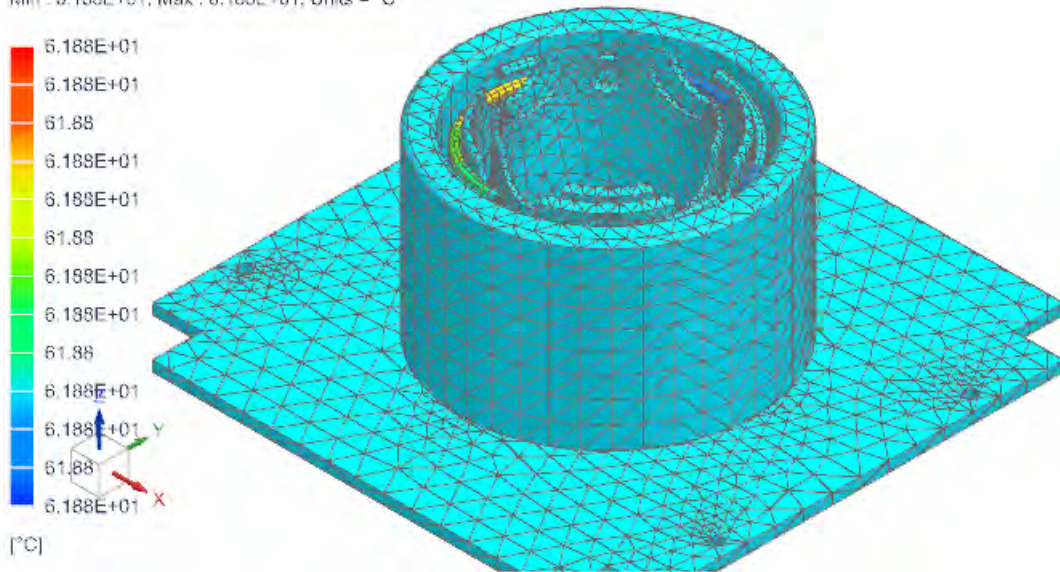


Figure 5.30: SOL 153 Thermal Environment (Hot Case)

The results show that the model is exposed to a temperature of 61.884 °C. To analyse the displacements and stresses caused by the heating or cooling of the model, the results of SOL 153 Thermal Expansion, must be imported to the SOL 101 linear solver. To do this, a SOL 101 simulation must be created, as shown in Figure 5.31.

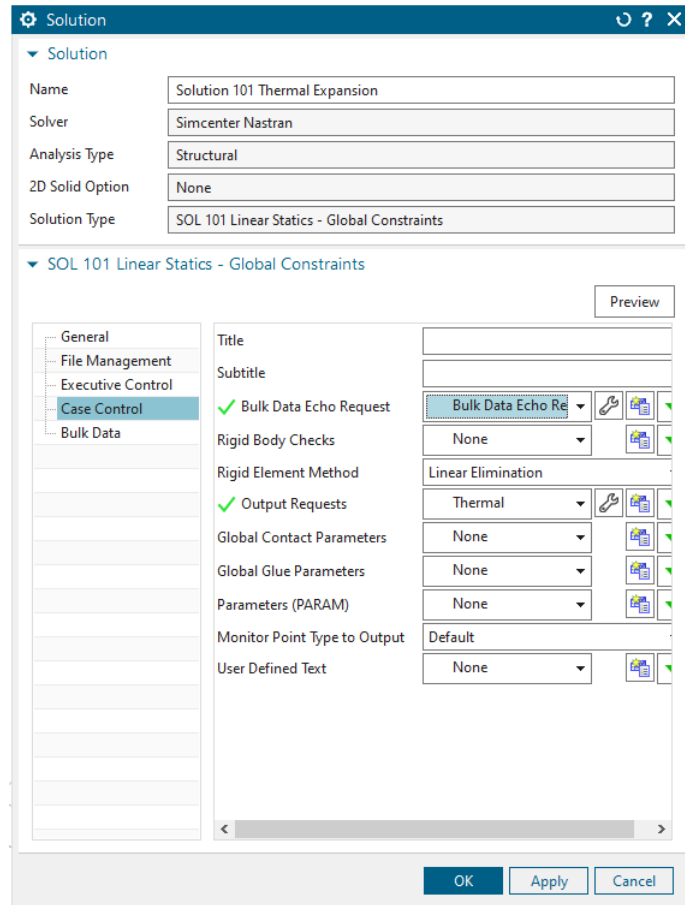


Figure 5.31: SOL 101 Thermal Expansion Simulation

For the simulation to calculate the displacements and stress present as a result of worst case temperature conditions, an initial temperature must be set as shown in Figure 5.32.

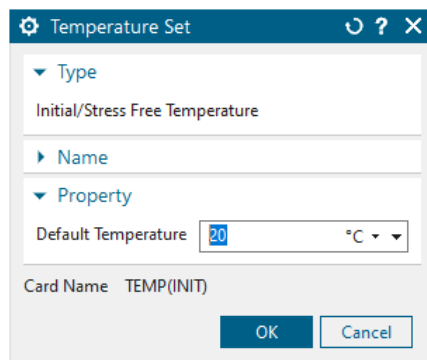


Figure 5.32: Initial Temperature Input

Within the subcase of SOL 101 Thermal Expansion, a temperature load is applied to the model, as shown in Figure 5.33. The temperature load is set up, so that it takes the results recorded in SOL 153 Thermal Expansion and applies it to the model of the antenna system in a SOL 101 environment, where displacements and

stresses can be analysed. The simulation is processed and repeated for the worst case cold conditions.

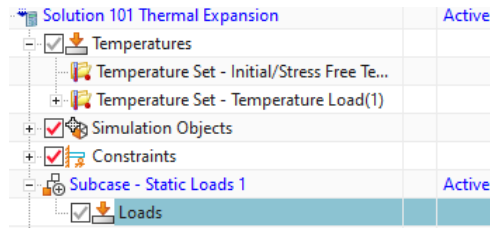


Figure 5.33: Solution 101 Thermal Expansion Subcase

After processing the simulations, the worst case hot and cold conditions results can be analysed. Figures 5.34 and 5.35, depict the thermal expansion simulation results, while Figures 5.36 and 5.37, depict the thermal contraction results.

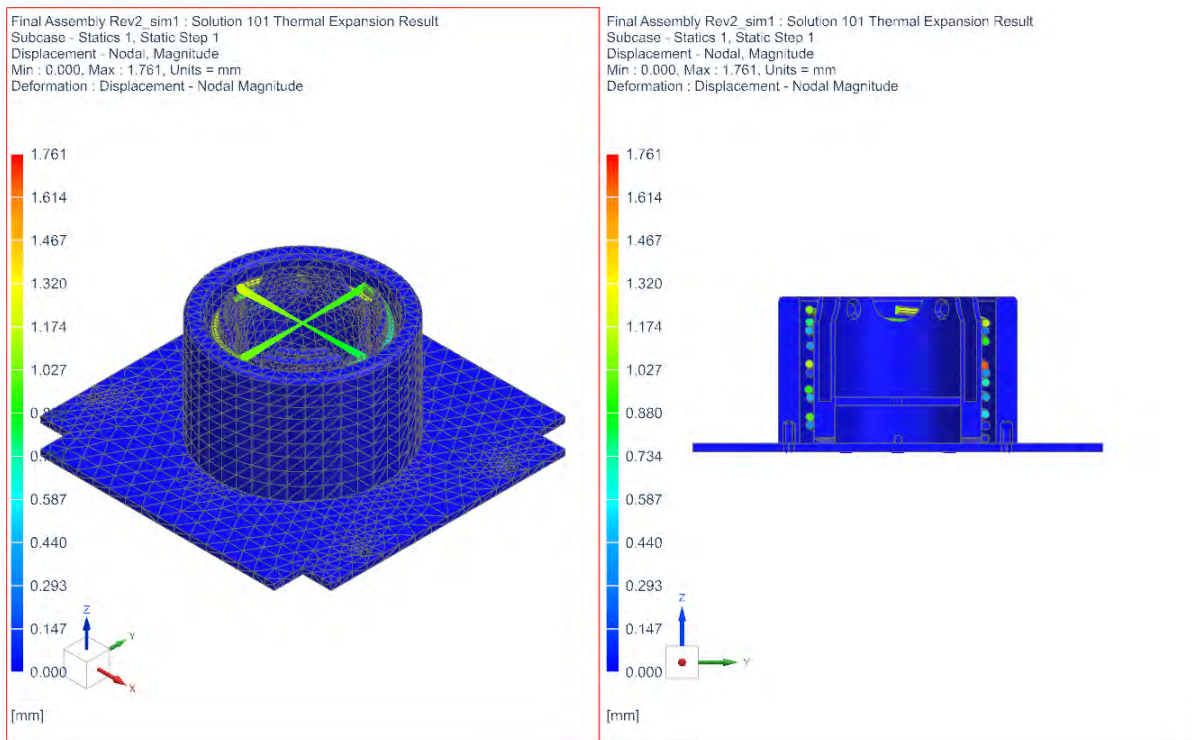


Figure 5.34: Thermal Expansion Displacement Results

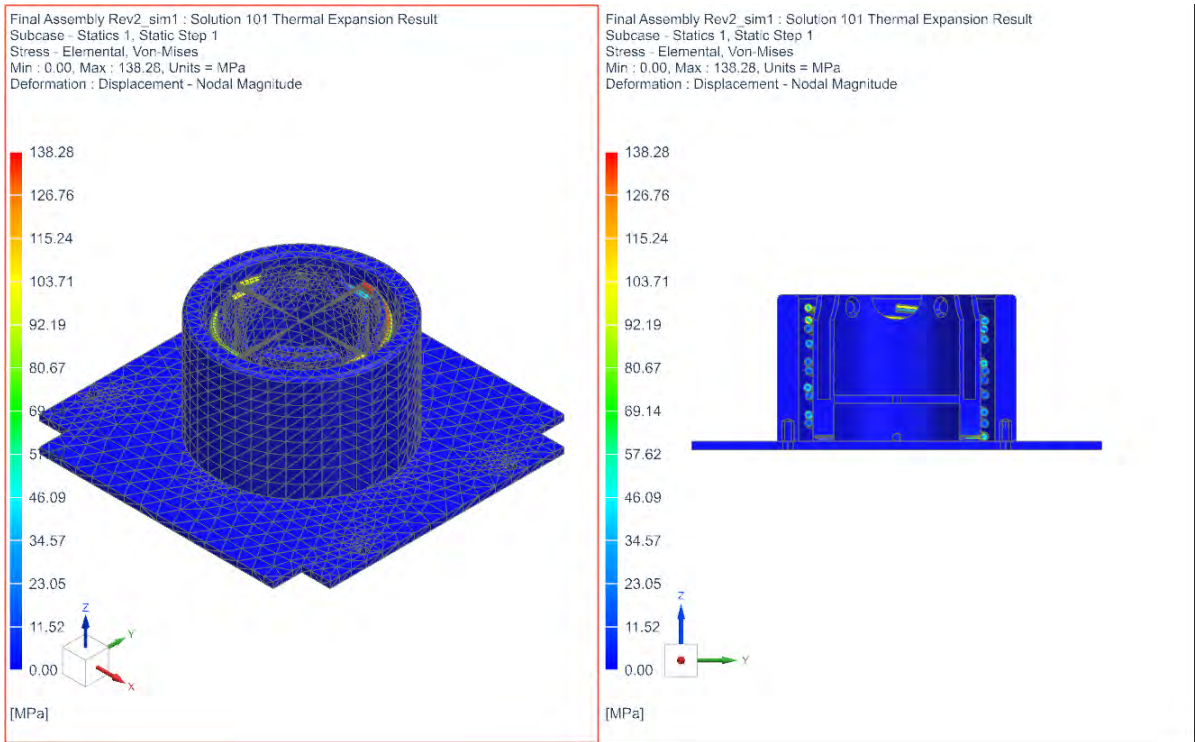


Figure 5.35: Thermal Expansion Stress Results

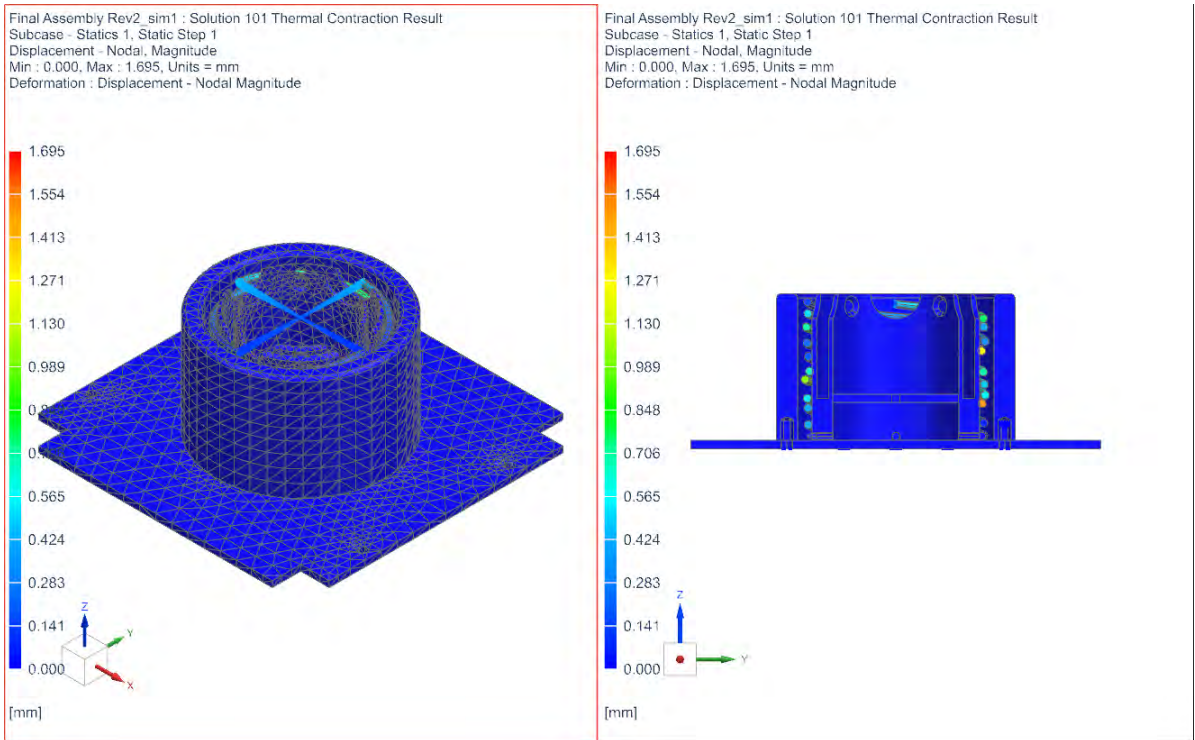


Figure 5.36: Thermal Contraction Displacement Results



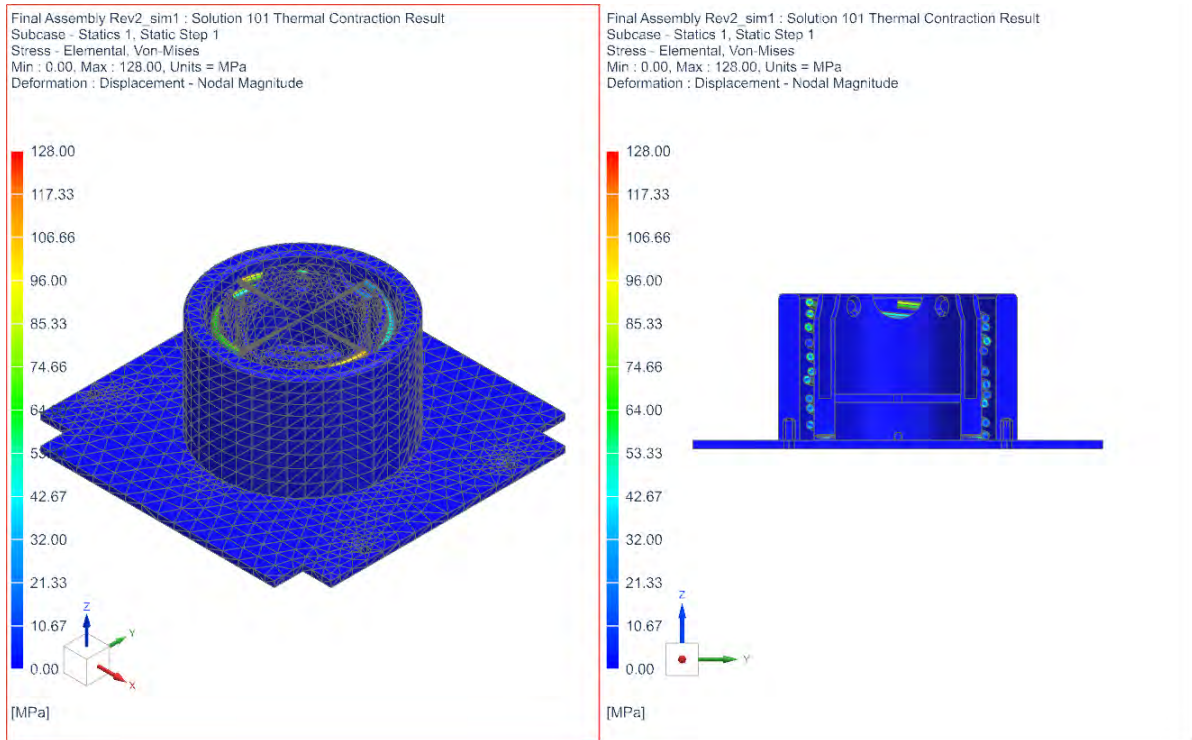


Figure 5.37: Thermal Contraction Stress Results

The simulations show that while the antenna is stowed and experiences heating under worst case conditions that a maximum displacement of 1.761 mm will occur. This maximum displacement is recorded for the filars of the antenna system. The other components of the antenna system experience minimal displacement as a result of thermal expansion. The highest stress recorded as a result of thermal expansion is recorded in the filars and has a magnitude of 138.28 MPa, which is well below the yield stress of ASTM A228 (1970 MPa). Looking at the rest of the antenna system shows, that very little stress is recorded as a result of thermal expansion.

The thermal contraction results depict a similar scenario. A maximum displacement of 1.695 mm is recorded in the filars. The maximum stress is recorded in the filars and has a magnitude of 128.00 MPa, which is well below the yield stress of ASTM A228. The rest of the system shows very little stress as a result of thermal contraction.

Overall, the simulations show that the antenna system can handle the worst case temperature scenarios. The antenna system was designed to allow for outwards movement of the filar (outer wall clearance), which helps with the thermal expansion that could be experienced by the antenna system. However, something which will need to be monitored in testing, is the contraction of the system. The design doesn't allow for large amounts of thermal contraction, especially where the filars touch the inner wall housing.

Taking the results recorded in section 4.5 and section 5.1.1.3, the acceptance and

qualification range of the antenna system can be set for testing in accordance with the methodology described in section 3.1.3. Therefore, the acceptance temperature range for testing will cover  $-19.73^{\circ}$  to  $66.19^{\circ}$  and the qualification temperature range will cover  $-24.73^{\circ}$  to  $71.19^{\circ}$ .

Taking the results into account, the acceptance and qualification test temperatures of the QHA can be set. However, it is also important to note that most components on a CubeSat have an operational temperature range of  $-20$  to  $60^{\circ}\text{C}$ . Therefore, should the PETG representative model show little or no deformation as a result of thermal cycling, while exposed to qualification temperatures, acceptance testing will not be conducted, as acetal has much a much wider operational temperature range.

## 5.1.2 Launch Simulations

Simulating the launch environment the antenna deployment system will be exposed to is extremely important. In order for the deployment system to be deemed feasible, it needs to be able to survive the launch environment it is exposed to. The launch environment refers to the vibration and separation events (fairing and stage separation) encountered during the launch of the CubeSat platform into space on a rocket provided by a launch provider. Vibration profiles differ from rocket to rocket, for the research the Soyuz rocket vibration profiles were selected for the launch environment, as explained in section 3.1.2.1.

According to the CDS, for CubeSats, four important tests or simulations for defining the launch environment need to be conducted to prove the survivability of a CubeSat or CubeSat component. These four tests include, quasi-static loading, sine wave sweep, random vibration and shock events. The following section covers the simulations conducted to characterise the possible launch environment of the QHA and deployment system to assess the feasibility and survivability of the structure.

### 5.1.2.1 Modal Simulation

When designing, it is always important to pay attention to the natural frequencies of a product, to determine at what frequency a product will resonate. Failure to design for resonance can lead to situations where a product fails unexpectedly, that could cause serious damage. To design for resonance and prior to quasi-static, sine sweep, random vibration, and shock simulations a modal simulation can be performed to mathematically determine the natural frequencies of the product. These modal frequencies can then be compared to the sine sweep, where recorded excitations should align with the natural frequencies of the product.

For the antenna deployment system, the modes of the system as a whole will be determined. As good practice, modes will be simulated until at least 80 % mass movement is recorded in one of the axes. Figures 5.38 and 5.39, depict the model

used, to determine the resonant frequencies of the antenna deployment structure. The model and constraints used for the modal analysis is also used for simulations proceeding the modal analysis.

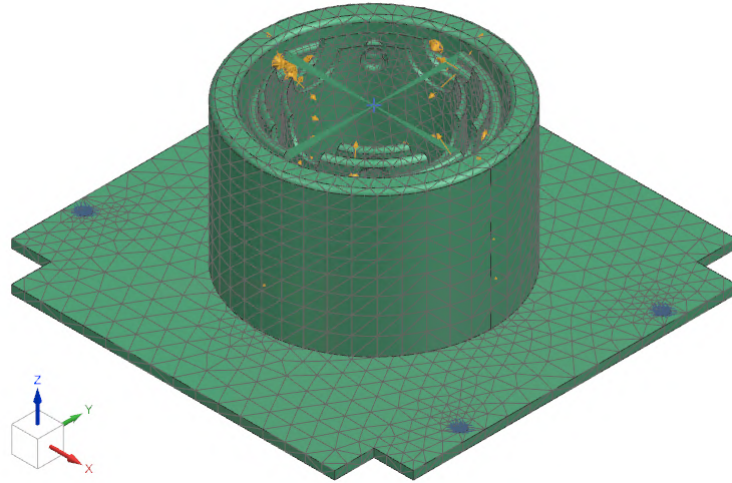


Figure 5.38: Modal Model

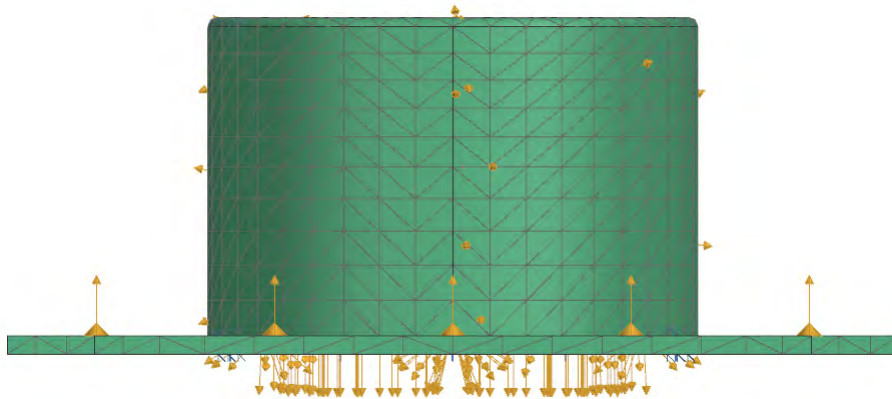


Figure 5.39: Modal Model Side View

Figure 5.40, depicts the simulation setup of the modal analysis. The simulation is created within the solution 103 response dynamics solver environment. The solver is used for mathematically calculating the natural frequencies of the antenna and deployment system.

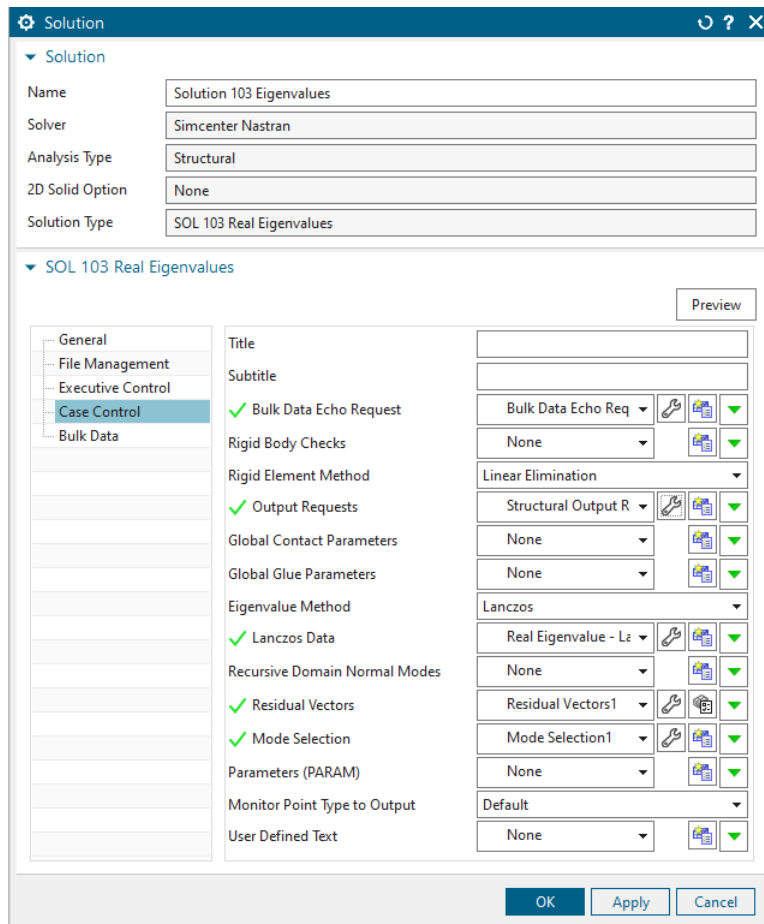


Figure 5.40: Solution 103 Real Eigenvalue Simulation Setup

The modal analysis was set up to calculate the residual vectors to reduce any response errors as shown in Figure 5.41. The simulation was also setup so that all modes are calculated, as shown in Figure 5.42.

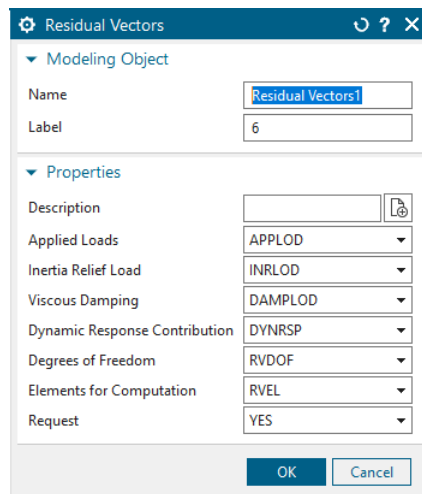


Figure 5.41: Residual Vectors Turned On

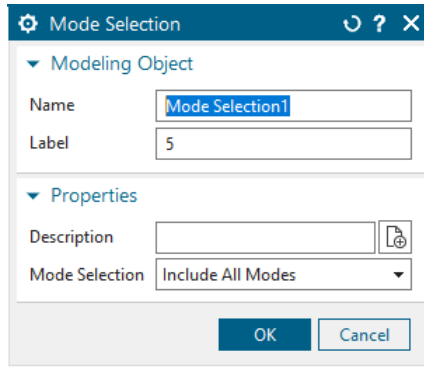


Figure 5.42: All Modes Turned On

To accurately simulate the natural frequencies the product will experience during its operational lifetime, it needs to be constrained properly. Properly constraining the deployment system requires simulation constraints to be applied in areas that would mimic how the system would be constrained in real life. Figure 5.43, depicts that the system is constrained by a fixed constraint on each mounting hole that would be bolted directly to the CubeSat frame.

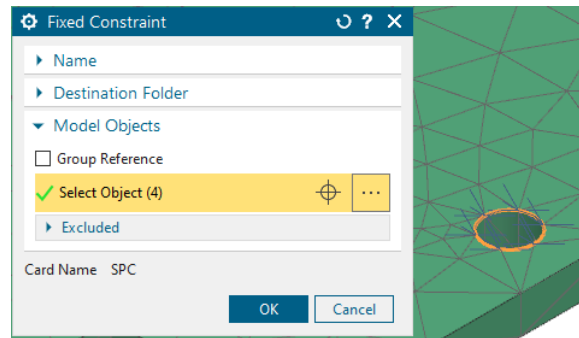


Figure 5.43: Model Fixed Constraint

To simulate how the deployment system acts in real life, various contact constraints exist to mimic how the antenna is predicted to act in service. The simulation consists of complex geometry that is constrained via contact conditions. Surface-to-surface contact exists between the antenna filars and the outer wall, as well as between each filar. These constraints prevent the filars from moving through the outer wall boundary and prevents the filars from moving through each other. Glue contact constraints are used to keep the antenna fixed to the inner holding wall. Surface-to-surface constraints are also used between the inner wall and filars to prevent movement through the components.

Fasteners also need to be simulated to show how the structure is held together. The simulation uses spider elements and RBE2 (rigid body elements) to simulate tapped holes and bolts, as shown in Figure 5.44, to fix the outer and inner bases to the plate at the bottom of the structure. This way 3D elements are not required, therefore reducing processing times and reducing simulation complexity.

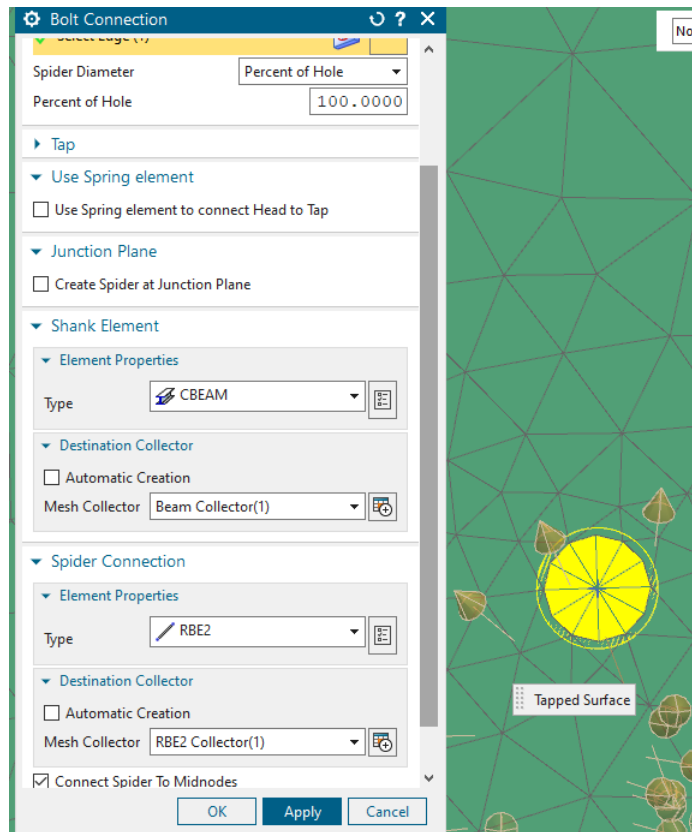


Figure 5.44: Tapped Bolt Connection

With the simulation setup, the solution can be executed so that the natural frequencies of the system can be calculated. Before analysis of the modes can be conducted, the effective mass movement of the system needs to be analysed. It is common practice when analysing modes of a product to record at least 80% mass movement in at least one of the axes. Modal analysis of the antenna system was conducted in the frequency range of  $0\text{ Hz}$  to  $2500\text{ Hz}$ , to achieve a mass movement percentage of at least 80 % as shown in Figure 5.45, which depicts the effective mass movement percentages recorded for the analysis.

# Mode	Frequency	%X_Mass	%Y_Mass	%Z_Mass	
* 1	7.333e+01	2.01391	8.42709	0.00000	
* 2	7.380e+01	8.47081	2.02438	0.01297	
* 3	7.642e+01	0.00931	0.00208	17.59284	
* 4	8.617e+01	0.01015	0.00058	0.37128	
* 5	1.490e+02	0.04210	2.20108	0.00642	
* 6	1.523e+02	2.60176	0.00003	0.00071	
* 7	1.582e+02	0.41121	1.21538	0.00878	
* 8	1.604e+02	0.86370	0.01634	0.00439	
* 9	1.665e+02	1.74902	0.15587	0.00001	
* 10	1.698e+02	0.47137	3.41367	0.00001	
* 11	1.807e+02	0.94416	0.17164	0.00174	
* 12	1.943e+02	0.10763	0.00956	0.01046	
* 13	2.009e+02	0.00628	0.00215	1.11685	
* 14	2.045e+02	0.00482	0.00033	0.04329	
* 15	2.117e+02	0.00000	0.00110	0.00000	

Total Effective Mass: X: 42.41372%; Y: 42.74062%; Z: 84.04860%; Rx: 84.90559%; Ry: 79.62943%; Rz: 43.0863

Figure 5.45: Effective Mass Movement

According to the simulation, a total effective mass of 84% is recorded in the Z-axis. Therefore, the modes of the antenna system can be analysed. Appendix E, contains the first 10 modes of the antenna system.

According to the simulation, the first natural resonant frequency occurs at 73.33 *Hz* and results in the antenna system being excited in a tilting motion towards the -Y-axis. This first frequency is linked to the QHA, in fact all the frequencies up to 2481 *Hz* are attributed to resonance of the antenna. The second mode occurs at 73.80 *Hz* and results in a similar excitation as the first mode, however is excited in the -X-axis direction. The third mode occurs at 76.42 *Hz* and results in a compressive mode. The fourth mode occurs at 86.17 *Hz* and results in a torsional mode, causing the antenna to be excited upwards in the Z-axis. The fifth mode occurs at 149.04 *Hz* and results in a combination of a compressive and tensional excitation. Compression occurs between the -Y-axis and X-axis, while tension is experienced between the Y-axis and -X-axis.

The sixth mode occurs at 152.30 *Hz* and results in a similar excitation as the fifth mode, however compression is experienced by the spring between the X and Y axes, while tension occurs between the -X and -Y axes. The seventh mode occurs at 158.22 *Hz* and is excited in the same way as the sixth mode. The eighth mode occurs at 160.36 *Hz* and caused the antenna to experience a torsional excitation along the Z-axis. The ninth mode occurs at 166.48 *Hz* and results in similar excitation to the eight mode, just not as strong. The tenth mode occurs at 169.81 *Hz* and results in similar excitation to mode the fifth mode. However, the system as a whole does adhere to Soyuz launch provider guidelines, stating that the first natural frequency of a system must be above 40*Hz*. Therefore, further simulation analysis can be conducted.

### 5.1.2.2 Quasi Static Simulation

During the launch phase, the QHA and deployment system will be subjected to acceleration as a result of the launch process. In order to account for the effects these accelerational forces have on the antenna components, a static or quasi-static acceleration simulation needs to be performed. The purpose of acceleration tests is to demonstrate that the structure of the QHA and deployment system under application of static or quasi-static loads are capable of surviving the launcher, and dynamic accelerations present during launch without suffering permanent damage.

By definition, a quasi-static simulation is a transient simulation where the load is applied gradually over time, so that the effect of dynamic loading is negligible. Therefore, two simulations were conducted to characterise the quasi-static loads that the antenna and deployment system would be exposed to. One simulation was conducted in Siemens NX Solution 101 for linear statics. This is a full static simulation environment. The other simulation was conducted in Siemens NX Solution 402 for nonlinear kinematic analysis, which can simulate transient conditions. By comparing a static simulation to a transient simulation, a better understanding and characterisation of the launch environment can be achieved.

The setup for Solution 101 and 402 are identical, both output the acceleration, reaction forces, stresses, and displacement present. The only difference between simulation setup is that solution 402 requires a time step and duration. The time step for solution 402 is set to 1 second and duration per iteration set to 0.1 seconds, as shown in Figure 5.46. The model is constrained as mentioned in section 5.1.2.1.

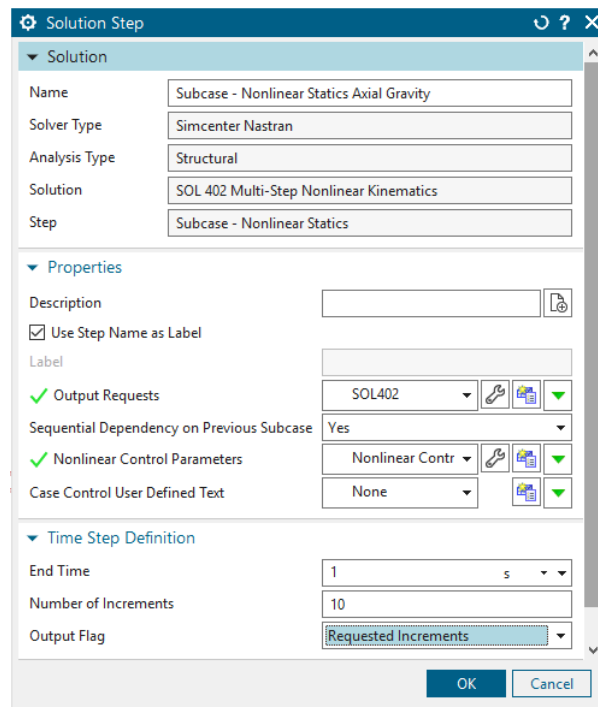


Figure 5.46: Solution 402 Time Step



According to the Soyuz rocket specification, the QHA deployment system must be subjected to approximately 10 G's in the axial direction and 9 G's in the lateral direction. To accomplish this for both solution 101 and 402, a gravitational force of,  $98100 \text{ mm/s}^2$  is applied to the model, along the axial direction, as indicated in Figure 5.47 and a lateral gravitational force of  $88\ 290 \text{ mm/s}^2$ , as indicated in Figure 5.48.

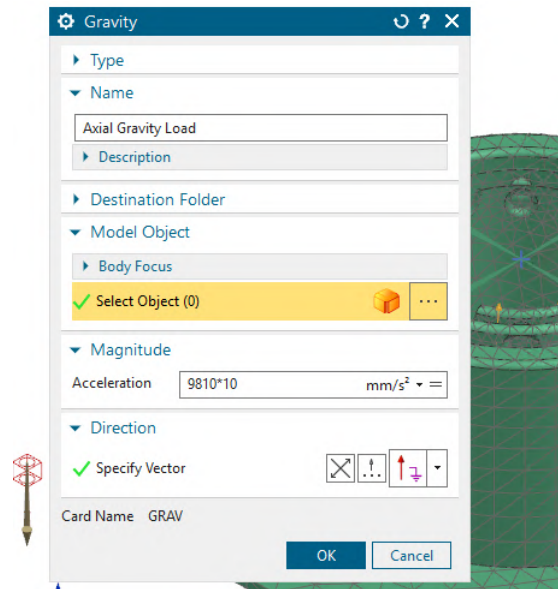


Figure 5.47: Axial Gravitational Load

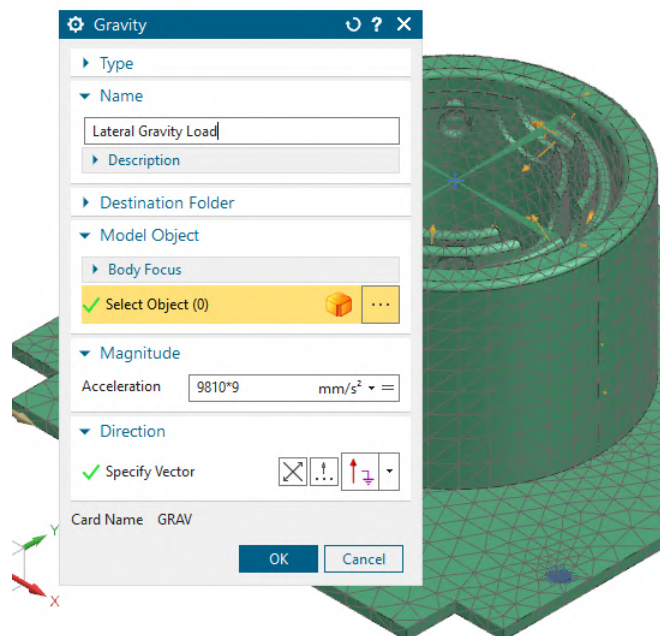


Figure 5.48: Lateral Gravitational Load

With the simulation setup, the results of the simulations can be compared. The results of the static simulation are shown in Figures 5.49 and 5.51, while quasi-static

results are shown in Figures 5.53 and 5.56.

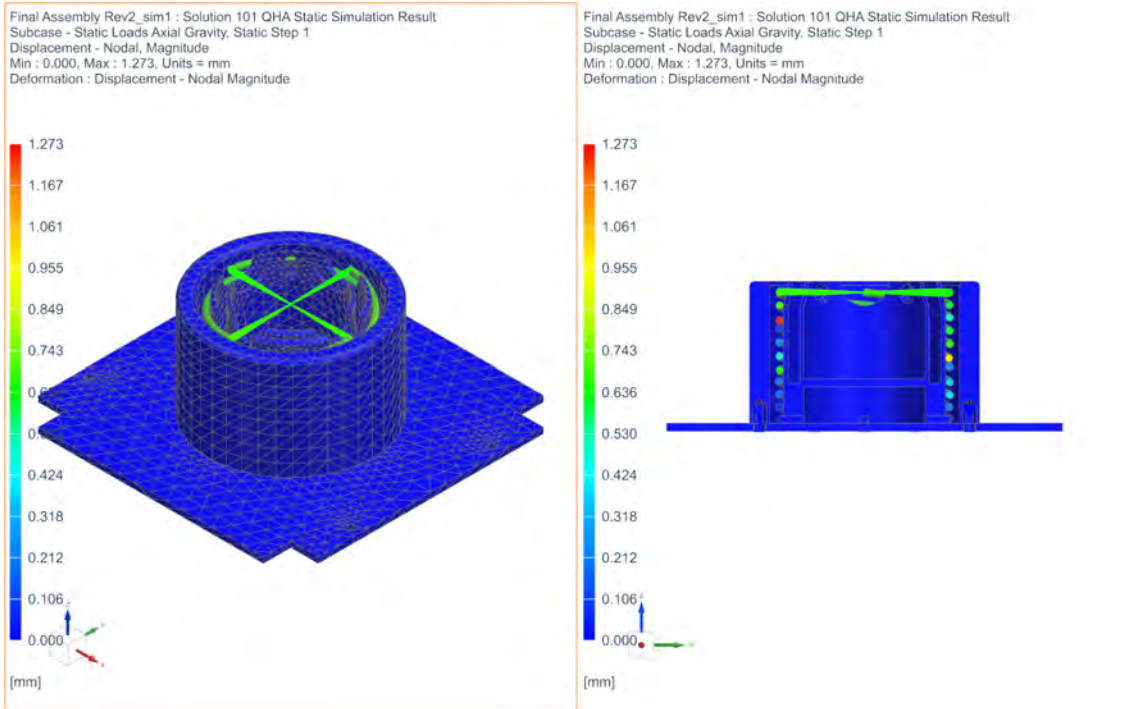


Figure 5.49: SOL101 Static Axial Displacement Results

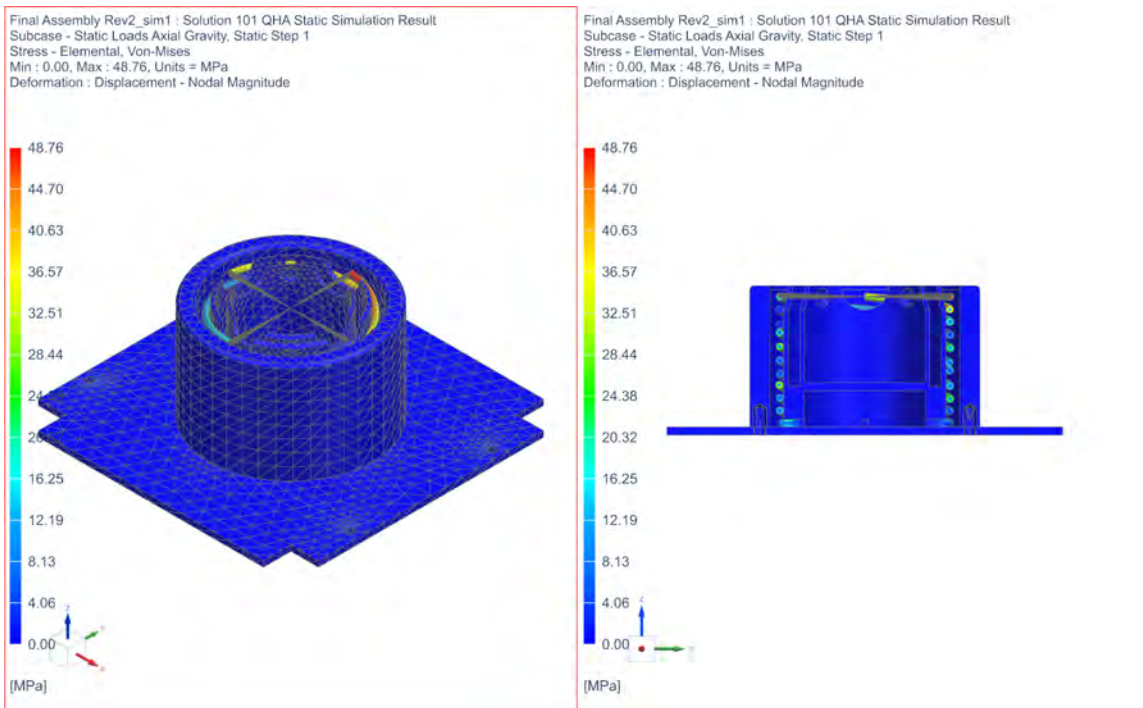


Figure 5.50: SOL101 Static Axial Stress Results

The results of the axial static simulation, conducted on the QHA system shows that a maximum displacement of 1.27 mm occurs and is attributed to the movement

of the filars, during launch. This small displacement causes a maximum Von-Mises stress in the antenna system of 46.78 MPa. This stress is attributed to the filars. The filars are manufactured out of ASTM A228, which has a yield stress of 1970 MPa. Therefore, the stress experienced, as a result of axial acceleration experienced by the antenna system during launch, is also well below yielding stress values.

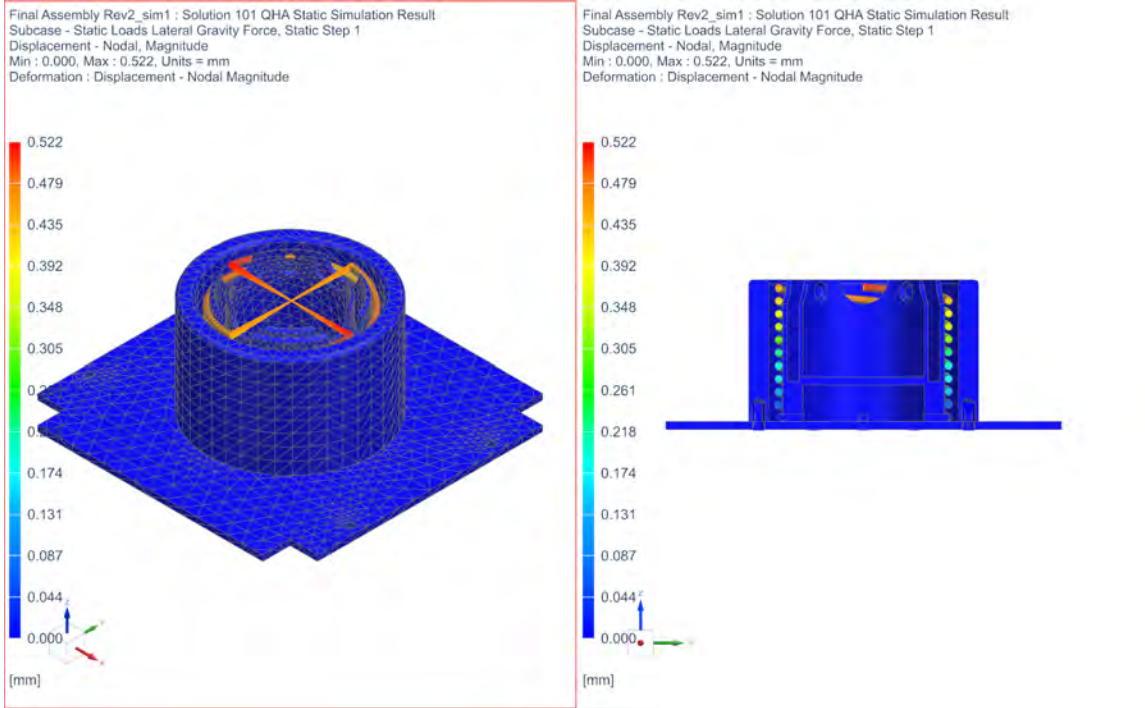


Figure 5.51: SOL101 Static Lateral Displacement Results

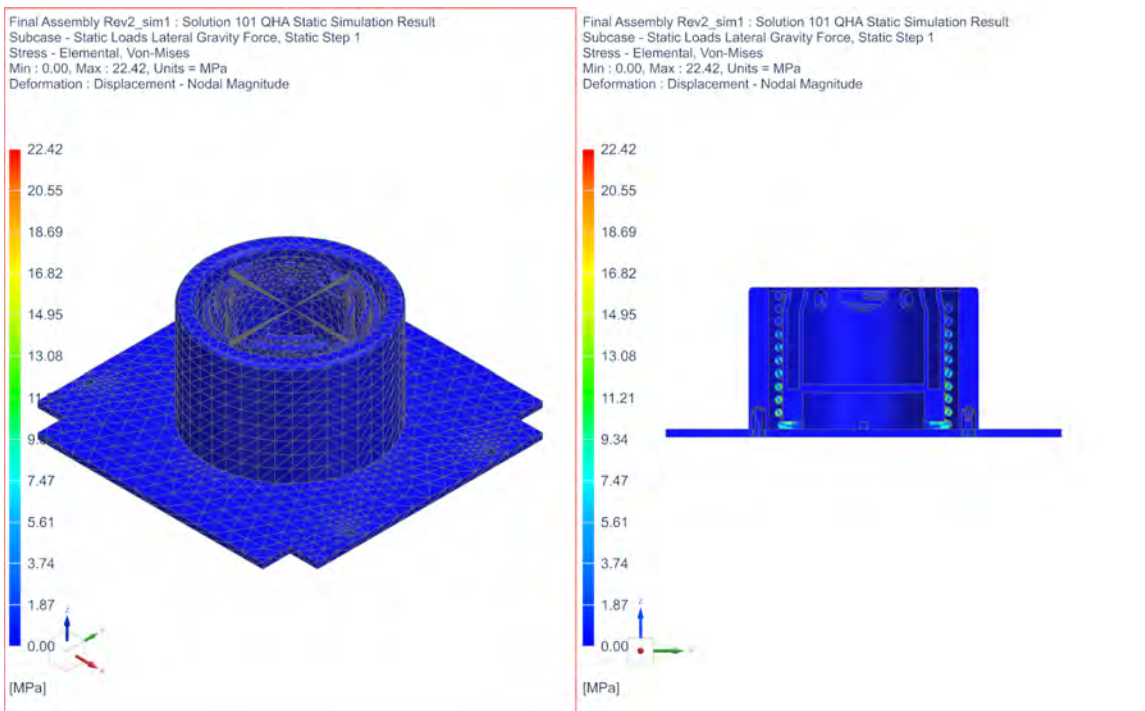


Figure 5.52: SOL101 Static Lateral Stress Results

The results of the lateral static simulation, conducted on the QHA system shows that a maximum displacement of 0.52 mm occurs and is also attributed to the movement of the filars, during launch. This small displacement causes a maximum Von-Mises stress in the antenna system of 22.42 MPa. Therefore, the stress experienced, as a result of lateral acceleration, is well below yielding stress values.

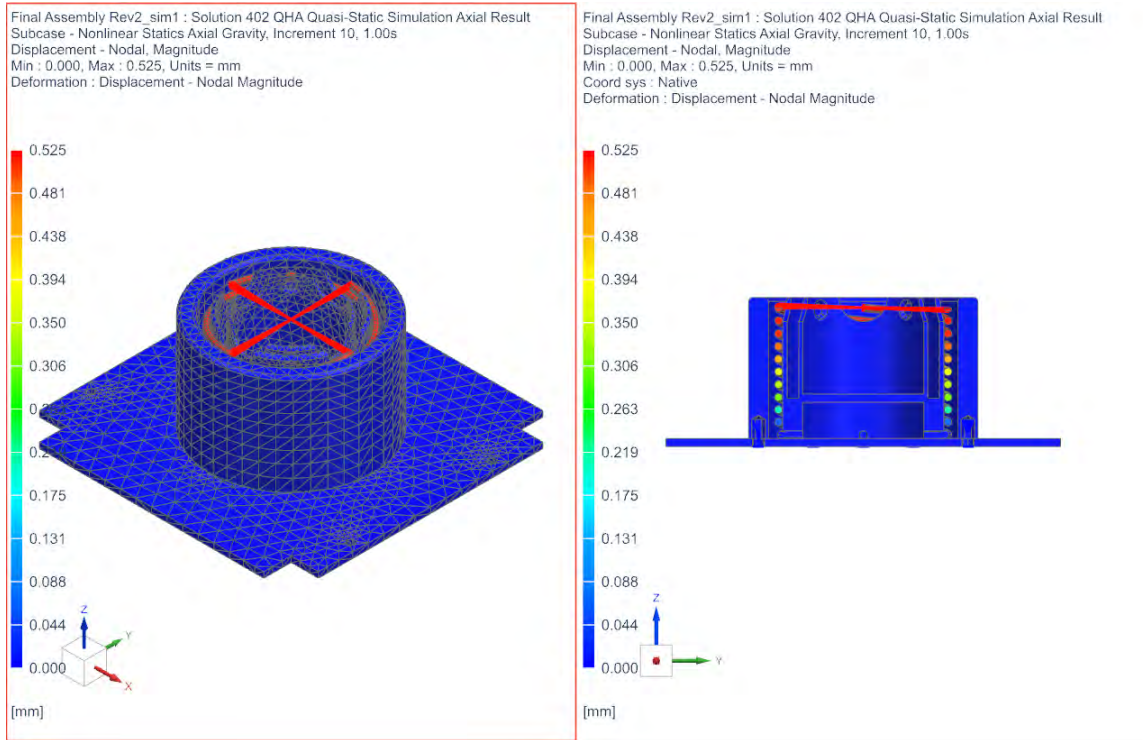


Figure 5.53: SOL402 Quasi-Static Axial Displacement Results

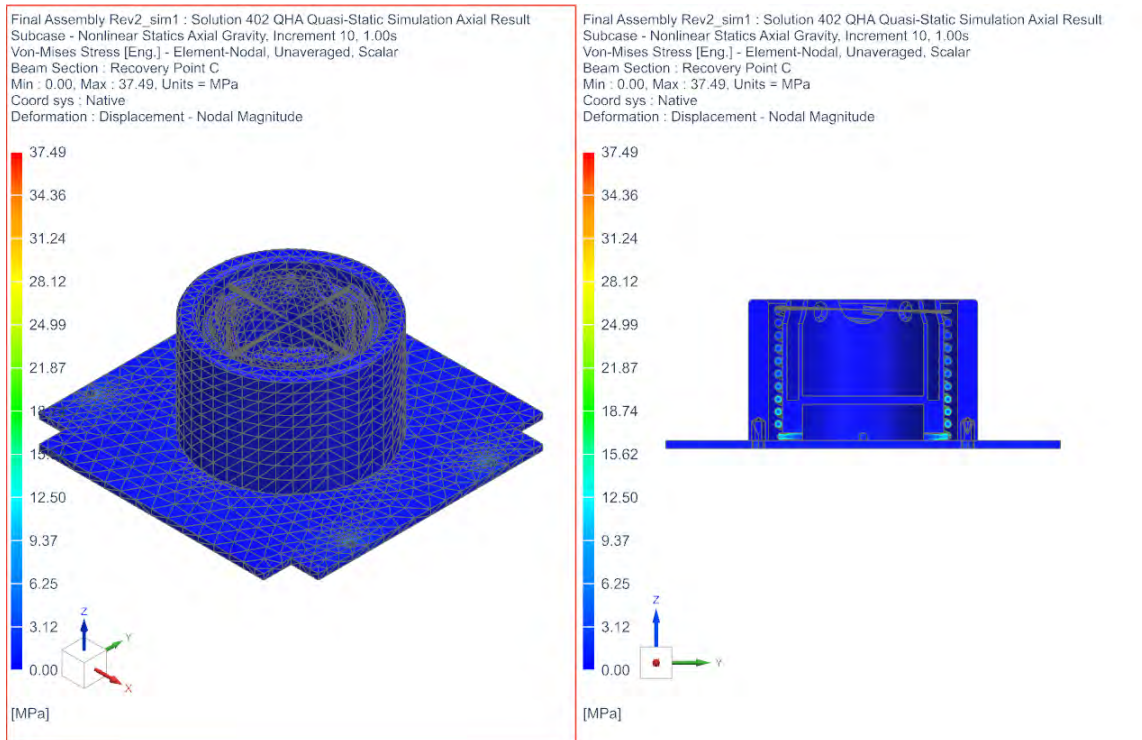


Figure 5.54: SOL402 Quasi-Static Axial Stress Results

The results of the axial quasi-static simulation, conducted on the QHA system shows that a maximum displacement of 0.525 mm occurs and is attributed to the movement of the filars, during launch. This small displacement causes a maximum Von-Mises stress in the antenna system of 37.49 MPa. This stress is attributed to the filars. Therefore, the stress experienced, as a result of axial acceleration, is also well below yielding stress values.

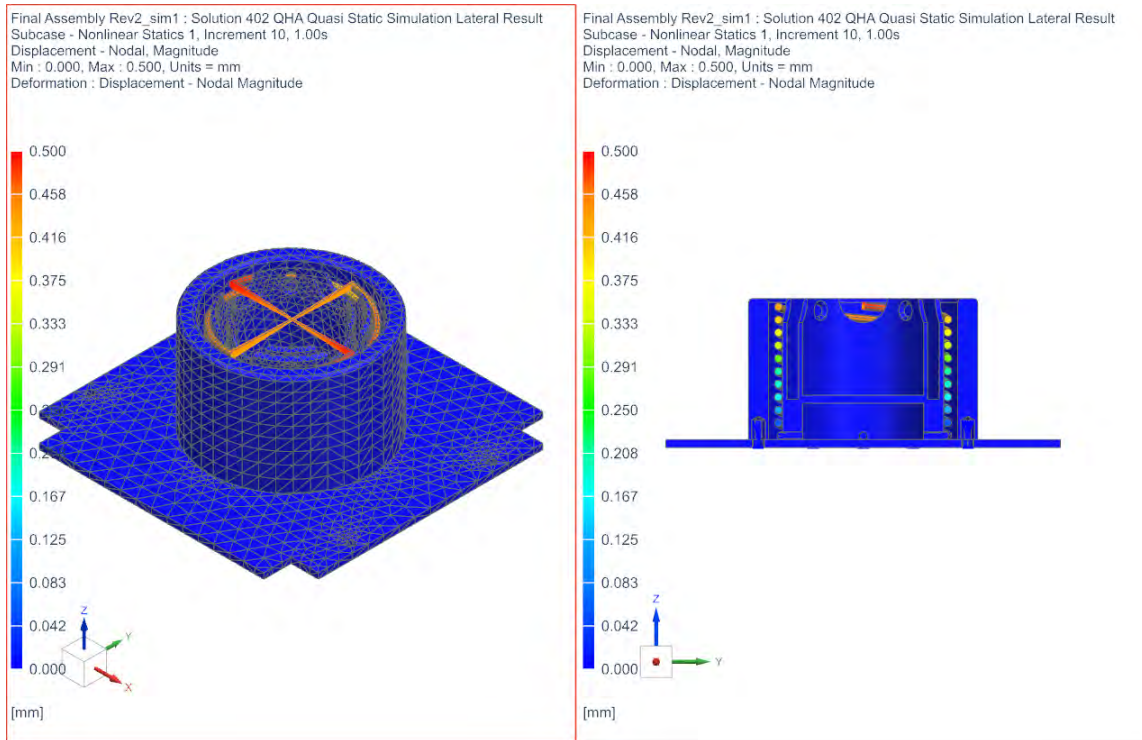


Figure 5.55: SOL402 Quasi-Static Lateral Displacement Results

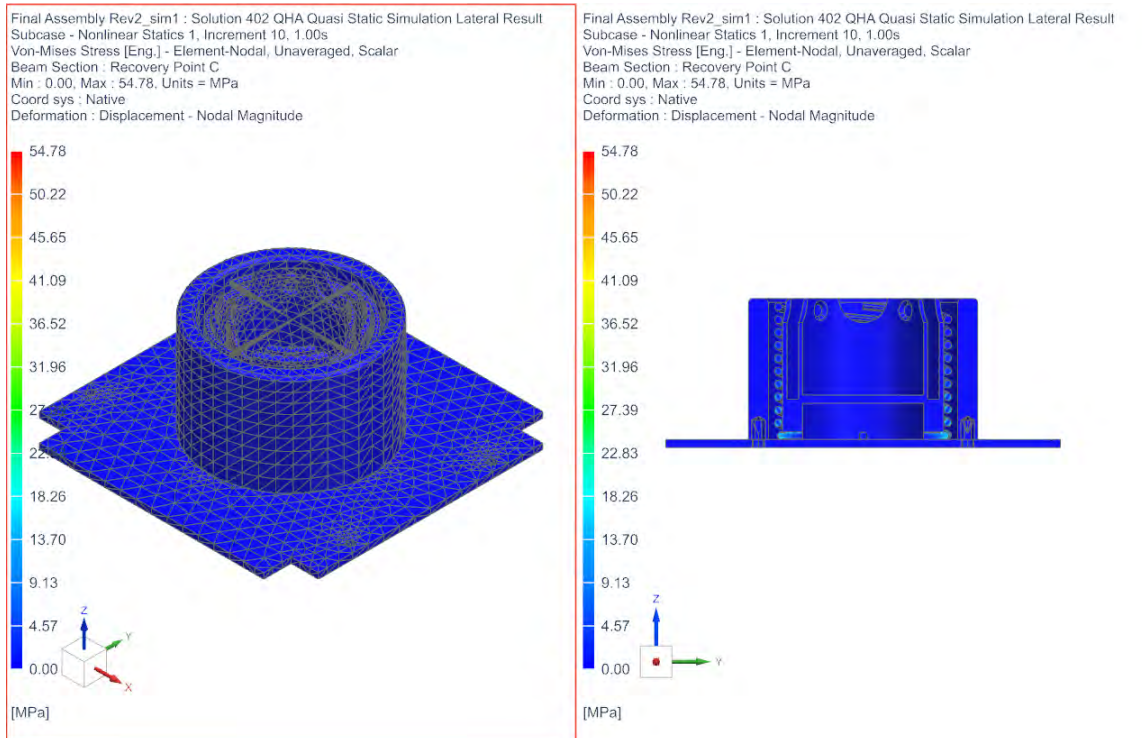


Figure 5.56: SOL402 Quasi-Static Lateral Stress Results

The results of the lateral quasi-static simulation, conducted on the QHA system shows that a maximum displacement of 0.5 mm occurs and is also attributed to

the movement of the filars, during launch. This small displacement causes a maximum Von-Mises stress in the antenna system of 54.75 MPa. Therefore, the stress experienced, as a result of lateral acceleration, is well below yielding stress values.

Comparing the quasi-static and static simulations shows a mark-able difference in displacements and stress experienced by the QHA structure. The static axial simulation shows a maximum displacement and stress of 1.27 mm and 46.78 MPa, respectively. The quasi-static axial simulation shows a maximum displacement and stress of 0.525 mm and 37.49 MPa, respectively. Analysing the results shows that the displacement experienced in the quasi-static simulation is less than half of that experienced by the static simulation. However, the stress experienced has not reduced proportionally. This may be attributed to that quasi-static simulations are transient and, therefore, are conducted over time. Loads are applied gradually over time, as opposed to all at once, which is experienced in static simulations. Therefore, quasi-static simulation present a more realistic scenario of real life, when compared to static simulation.

In the lateral simulations. The displacement recorded for both the static and quasi-static simulation were 0.52 mm and 0.5 mm, respectively. These values were almost identical, however the stress recorded are different. A maximum stress of 22.42 MPa was recorded in the static simulation, while 54.78 MPa was recorded in the quasi-static simulation.

By comparing the results of the quasi-static and static simulation, it can be seen that the QHA system is not subject to stresses above yield stress and therefore will survive the space environment under the given launcher specifications.

### **5.1.2.3 Sine Wave Sweep Simulation**

Sine Vibration has the shape of a sine wave. Sine vibration is generally expressed as an amplitude, which is usually either a displacement or acceleration that is applied over a frequency range, consisting of a sweep rate and number of sweeps. The vibration wave forms of a sine wave sweep are swept through frequencies, which are discrete of amplitude, frequency and phase at any given time.

In real life, sine vibration is not generally experienced, unless a product is attached to a motor at a fixed frequency. However, it is good for finding the natural frequencies of a product, under simple motion and produces a constant acceleration versus frequency graph. In the case of the Soyuz rocket specifications, the sine vibration specification, helps describe the launch environment, and therefore helps find any resonant frequencies experienced as a result of the sine sweep frequency range, as specified by the Soyuz rocket launch environment specification. Overall, the purpose of sine vibration simulation is to demonstrate that the space vehicle withstands the vibration environment encountered during launch.

The sine vibration simulation is set up using the same finite element model as the modal analysis in section 5.1.2.1. However, a different simulation environment

is used. For the sine vibration simulation, solution 111 will be used. Solution 111, is a modal frequency response environment. The setup required for the simulation and the results of the simulation are described in this section.

Three sine sweep simulations are required, one for each axis of the product. The simulation operates by exciting a product in a certain direction, at a specific amplitude over a frequency range. Figure 5.57, depicts the sine wave solutions for the x, y and z-axes.



Figure 5.57: Sine Wave Sweep Solutions

The Soyuz launch specifications state that the frequency range of the sine sweep is from 10Hz to 100Hz, however according to the Nastran user manual, it is good practice to inspect three times the range of the frequency range being examined for a sine wave sweep simulation. Therefore, the simulation covers frequencies from 10Hz to 300Hz. Figure 5.58, shows the case control or setup of the simulation.



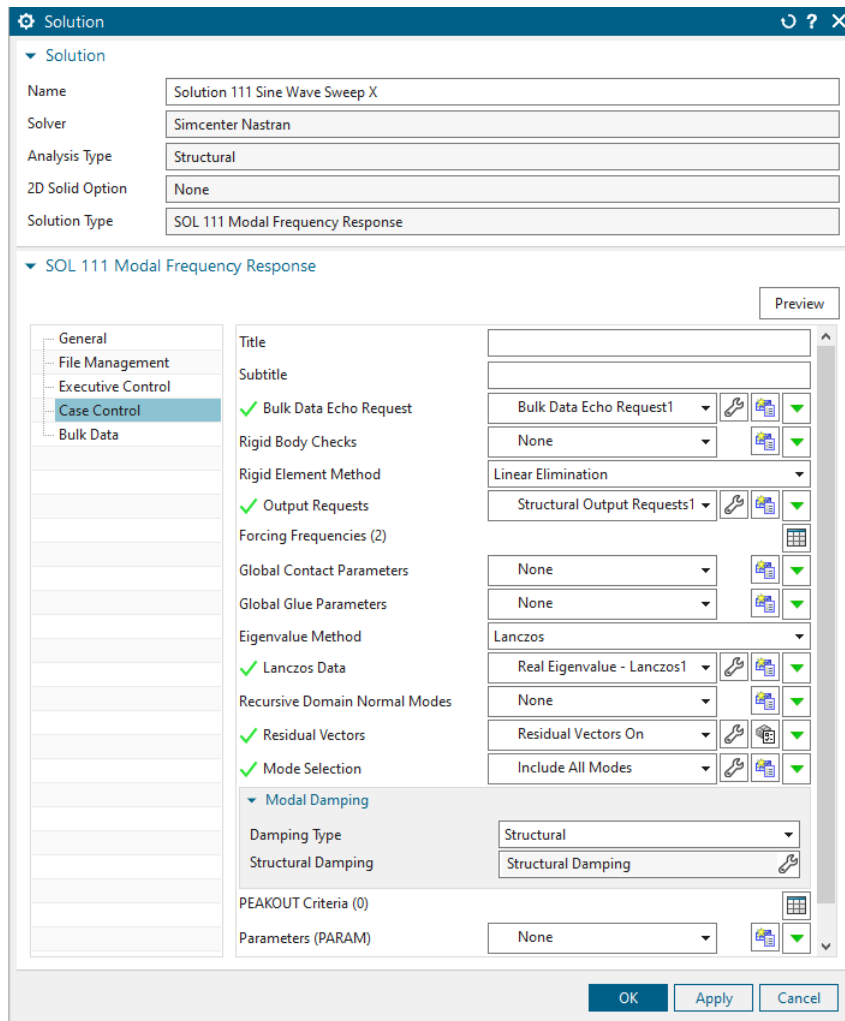


Figure 5.58: Sine Sweep Setup Case Control

The simulation is set up to output acceleration, displacement and stress present in the model. The simulation is set up so that all modes are included within the examined frequency spectrum, and residual vectors are turned on, for more accurate results. Structural damping is added to the simulation over the frequency range and is defined as shown in Figure 5.59. Structural damping of 0.02 was chosen, as the majority of the mode frequencies recorded are as a result of the QHA, which is made of ASTM A228 steel. Steel components generally have a structural damping of 0.02.

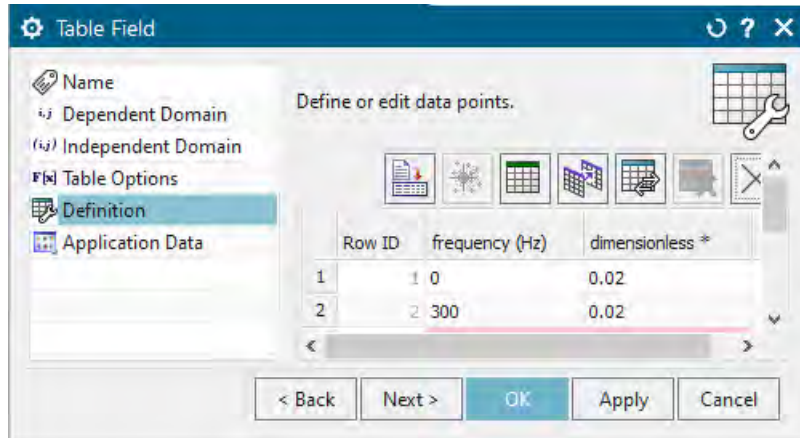


Figure 5.59: Structural Damping Input

Defining the sine sweep is the next step. Frequency ranges within the SOL 111 environment are controlled by forcing frequencies. To subject the model to a sine sweep, **FREQ2** or a logarithmic sweep entry needs to be assigned, as shown in Figure 5.60. A **FREQ4**, frequency input is also required, which controls the spread of frequency intervals around the simulated natural frequencies, as shown in Figure 5.61.

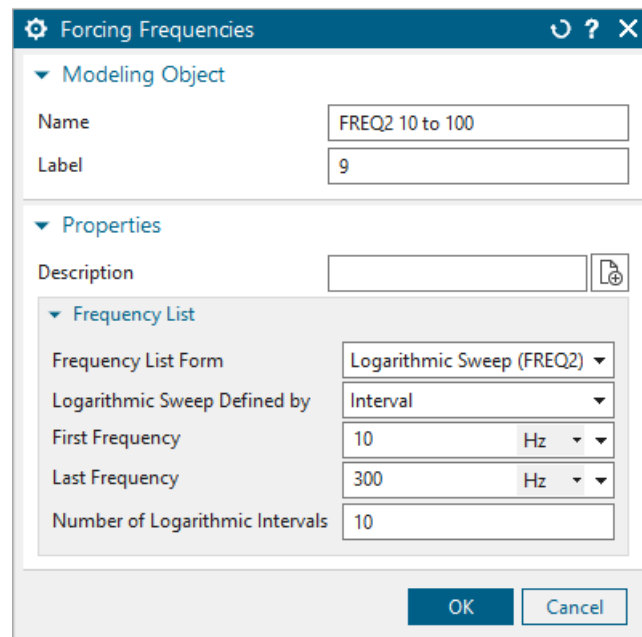


Figure 5.60: Logarithmic Sweep Input (FREQ2)

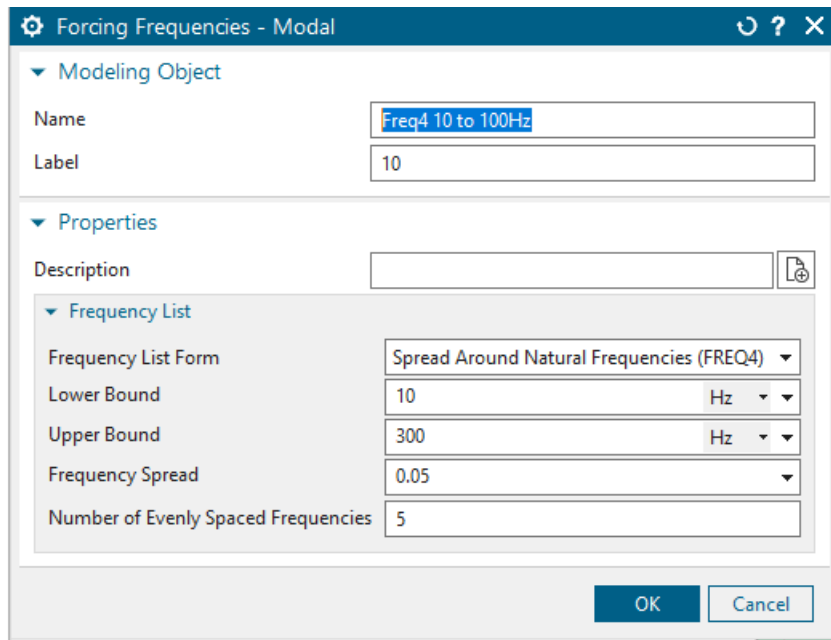


Figure 5.61: Spread Around Natural Frequencies Input (FREQ4)

The next step in the simulation setup is to define the frequency excitation set and the direction of excitation. These areas are defined in the modal frequency subcase of the main simulation, as shown in Figure 5.62.

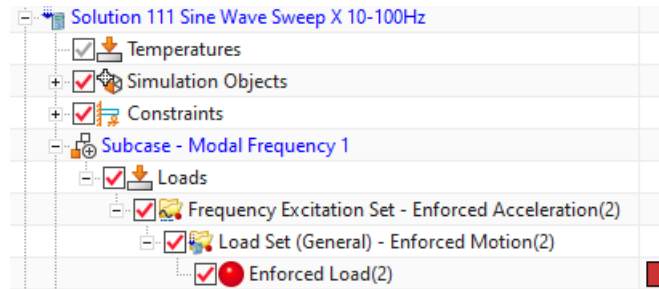


Figure 5.62: Sine Sweep Subcase

The Soyuz rocket excitation profile is input into the frequency excitation set, as shown in Figure 5.63 and 5.64. Figure 5.63, shows that an applied acceleration is applied to the model, while Figure 5.64, shows the Soyuz sine sweep acceleration values, as per specification in  $mm/s^2$ .

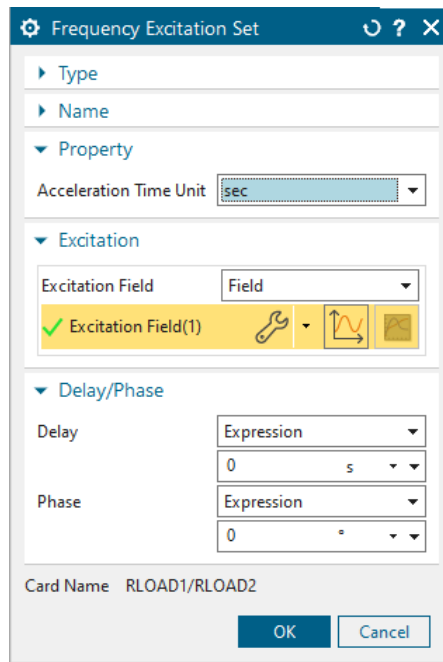


Figure 5.63: Excitation Input

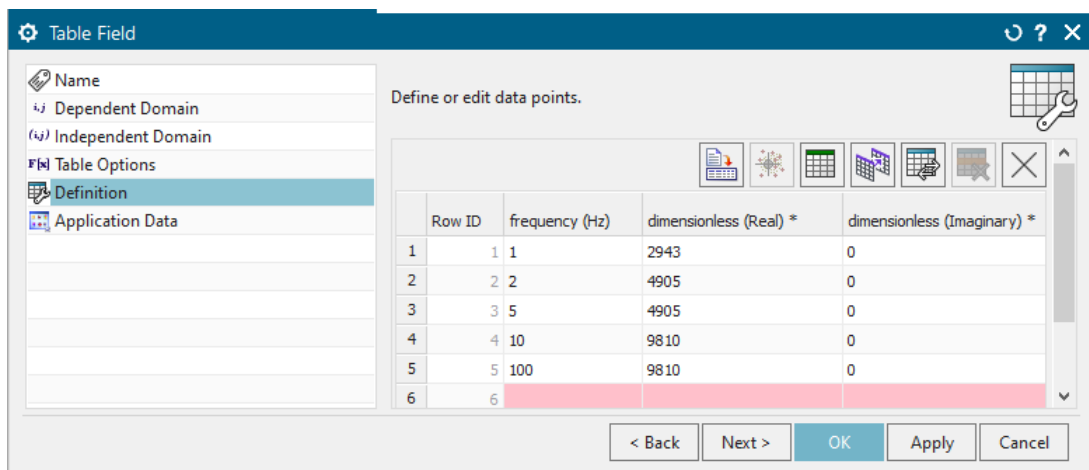


Figure 5.64: Soyuz Excitation Profile

After defining the Soyuz specification for the sine vibration simulation, an enforced motion load is applied to the direction which needs to be examined as shown in Figure 5.65. For the x-axis motion, degree of freedom 1 (DOF1) is set to 1 mm (per unit). This is the last step of the simulation setup. Simulations for the y and z axes are set up in the same way, just that the DOF defined in the enforced motion load is set to the corresponding axis to be examined.

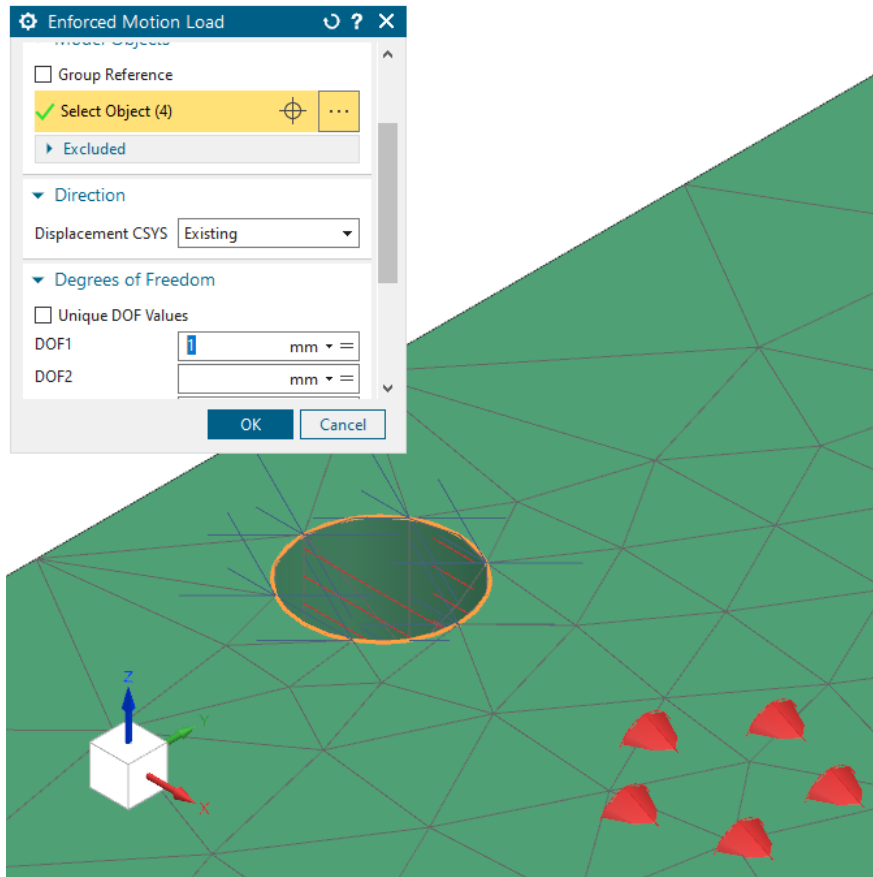


Figure 5.65: Enforced Motion Load

With the simulation setup, the results of the sine wave sweep in each axis were simulated and recorded as graphs in Figures 5.66 to 5.68.

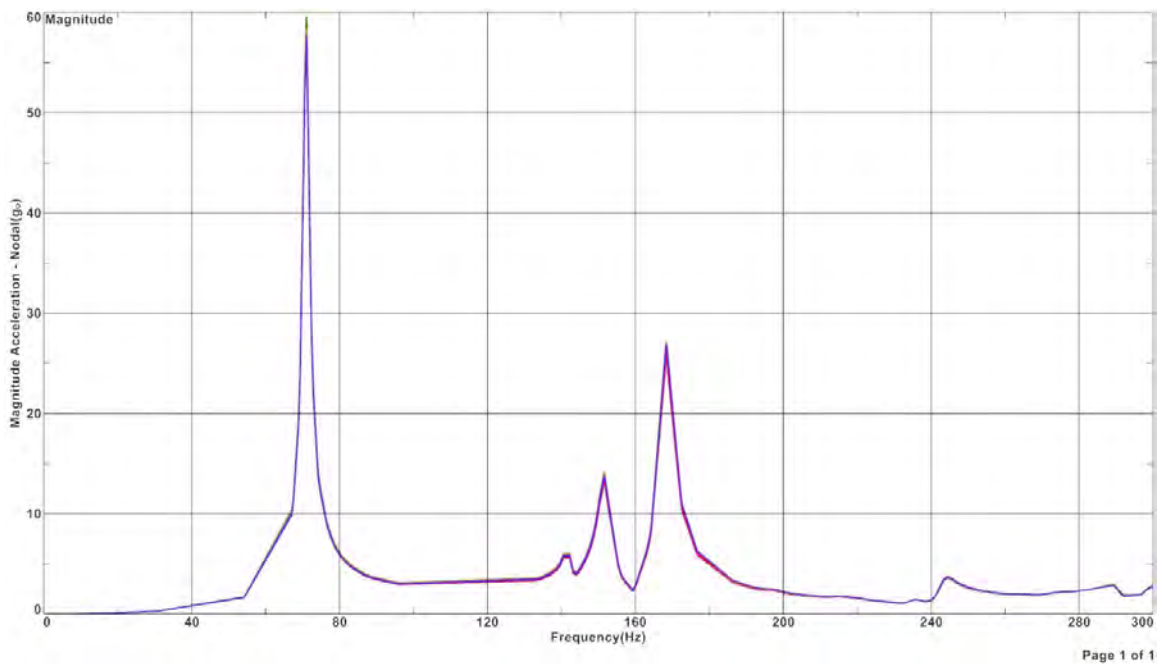


Figure 5.66: X-Axis Acceleration Versus Frequency Graph

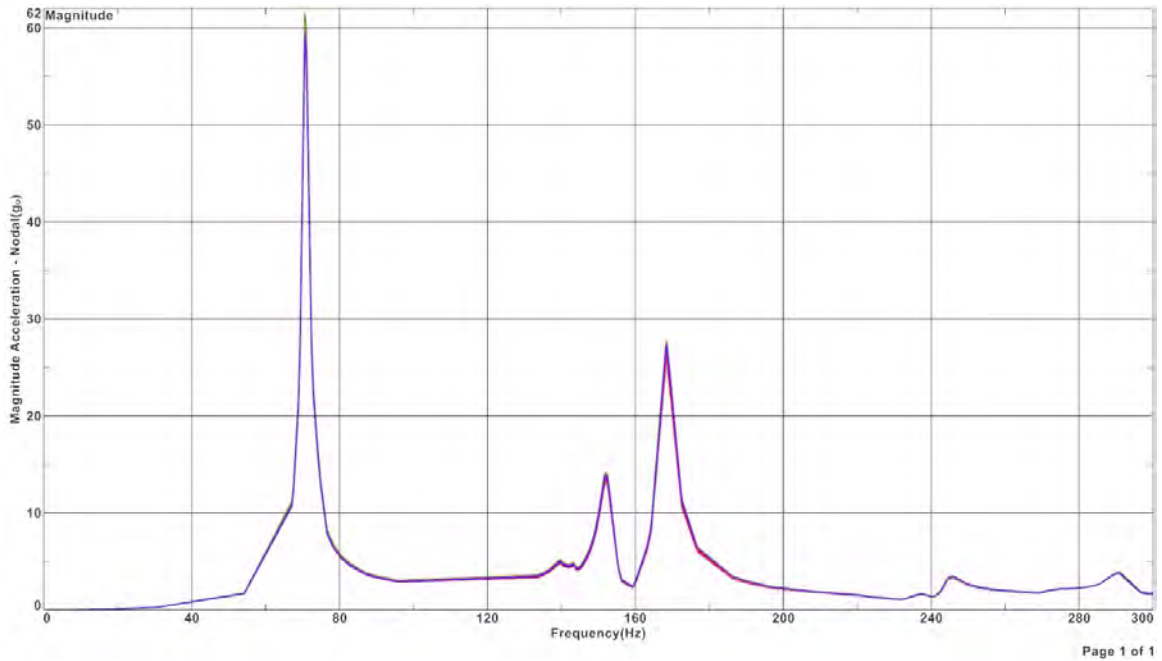


Figure 5.67: Y-Axis Acceleration Versus Frequency Graph

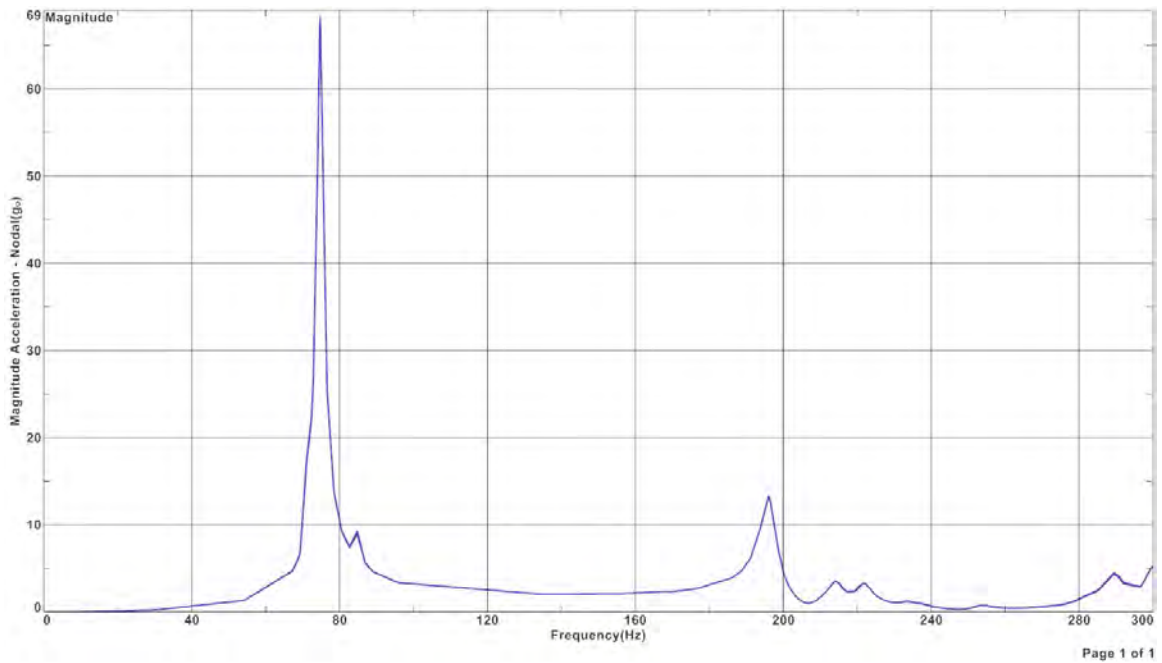


Figure 5.68: Z-Axis Acceleration Versus Frequency Graph

The acceleration versus frequency graphs shows that the first resonance point occurs between 60 Hz and 80 Hz. This coincides with the modal survey, which showed that the first resonant frequency was at approximately 73 Hz. Therefore, the sine wave sweep simulation further proves that the antenna system design adheres to launcher requirements, where the first resonant frequency must be above 40 Hz.

Another aspect of interest is the acceleration experienced in each axis by the

antenna system. According to the graphs, the antenna experiences a maximum acceleration of approximately 69G's in the Z-axis, while approximately 60G's and 62G's are experienced in the X and Y axes, respectively. The magnitude of acceleration is quite high, however, the stress caused by the vibrational acceleration is the ultimate determining factor of whether the design will work or not. Figures 5.69 to 5.74, depict the stress and acceleration profiles of the antenna system in each axis. The profiles depict a more accurate view of the acceleration and stress experienced by the antenna system, compared to the graphs.

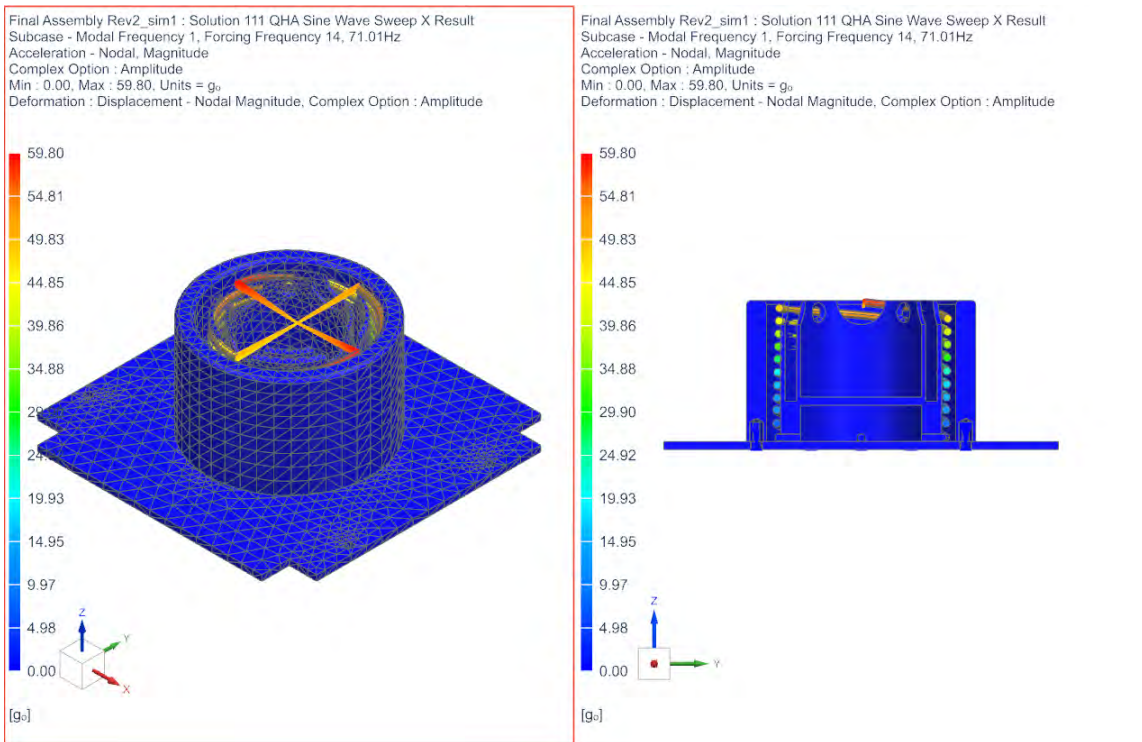


Figure 5.69: Sine Wave Sweep X-Axis Acceleration Results

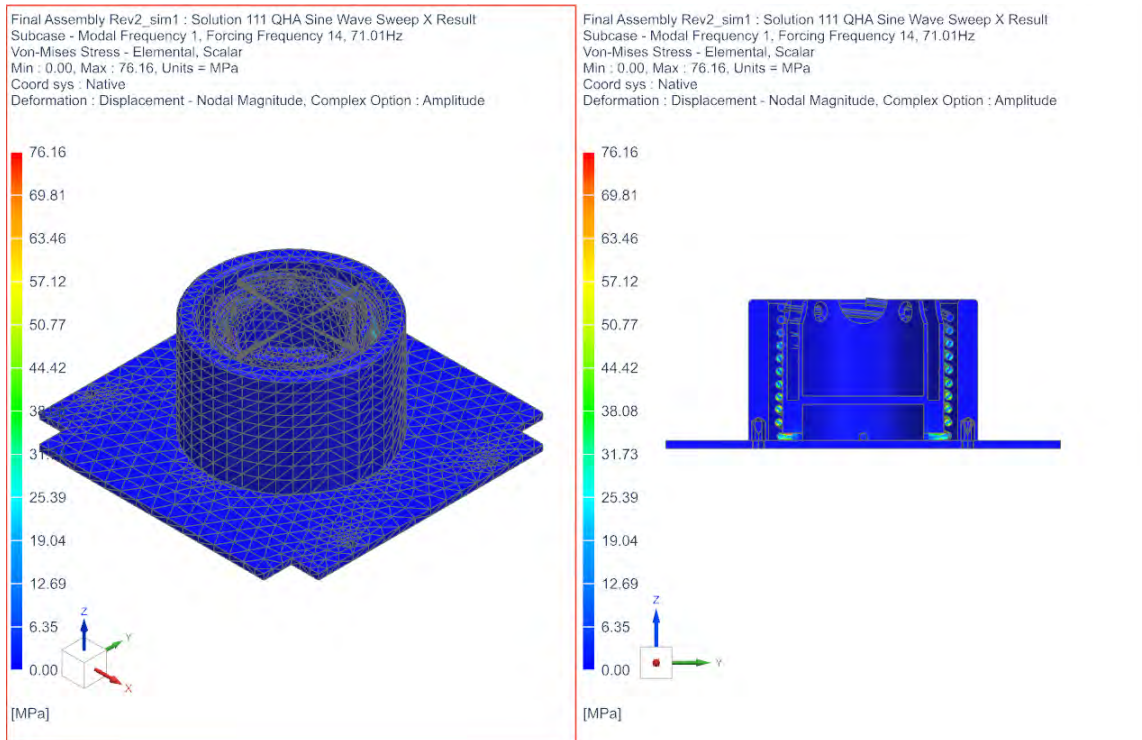


Figure 5.70: Sine Wave Sweep X-Axis Stress Results

Studying the X-axis acceleration and stress, shows that the antenna system experiences a maximum acceleration of 59.80 G's, when excited in the X-axis. This acceleration, results in the antenna system experiencing a maximum stress of 76.16 MPa. This stress occurs on the feet of the filars, specifically where the filars are constrained by the inner housing wall. The filars have a yield stress of 1970 MPa, therefore, the filars are not subjected to yielding and will not permanently deform, as a result of forces experienced during launch.



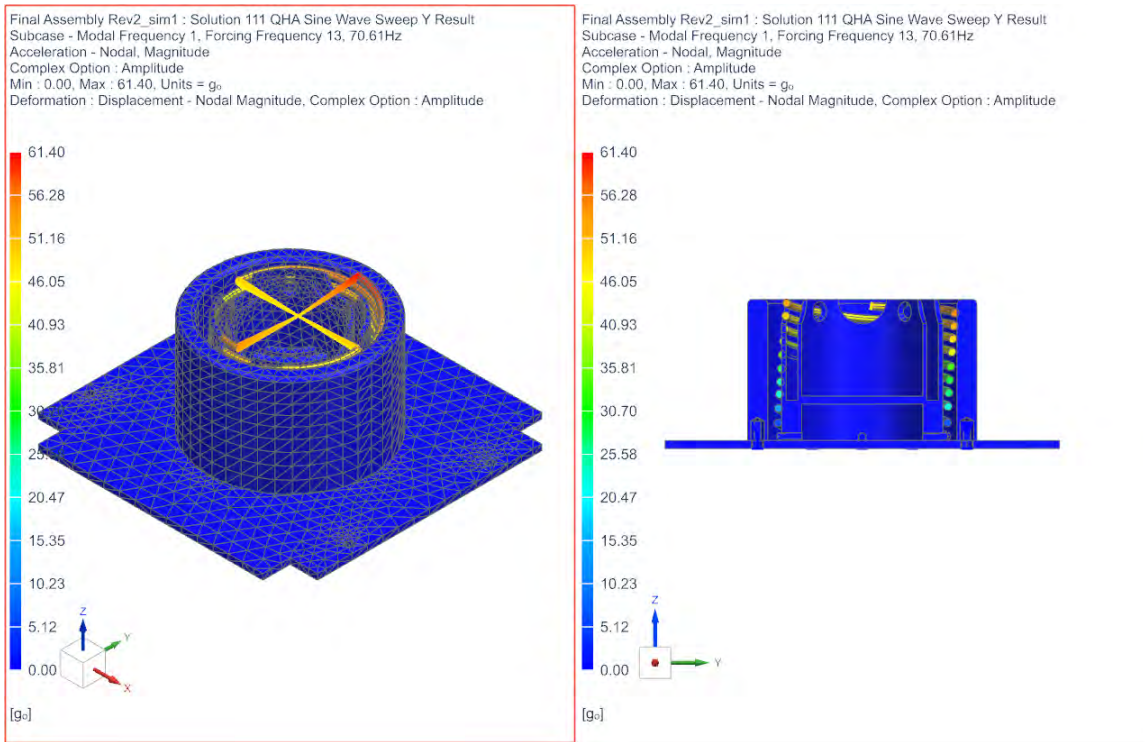


Figure 5.71: Sine Wave Sweep Y-Axis Acceleration Results

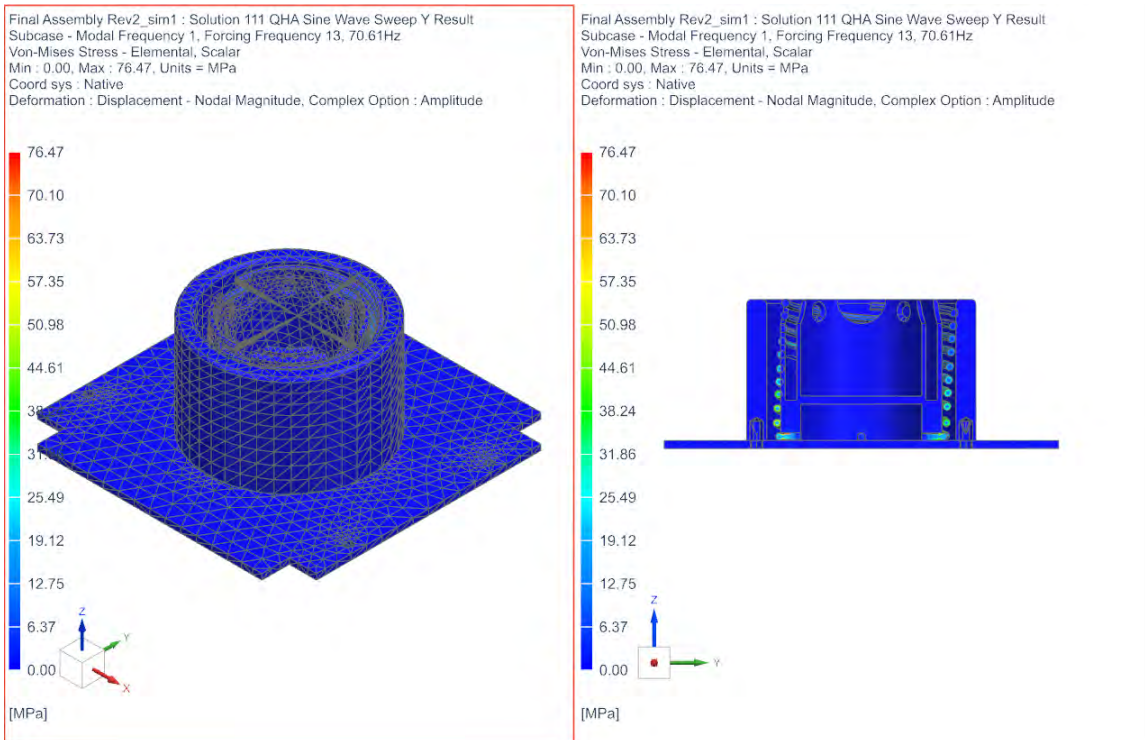


Figure 5.72: Sine Wave Sweep Y-Axis Stress Results

Studying the Y-axis acceleration and stress, shows that the antenna system experiences a maximum acceleration of 61.40 G's, when excited in the Y-axis. This acceleration, results in the antenna system experiencing a maximum stress of 76.47

MPa. This stress occurs on the feet of the filars, specifically where the filars are constrained by the inner housing wall. The filars have a yield stress of 1970 MPa, therefore, the filars are not subjected to yielding and will not permanently deform, as a result of forces experienced during launch.

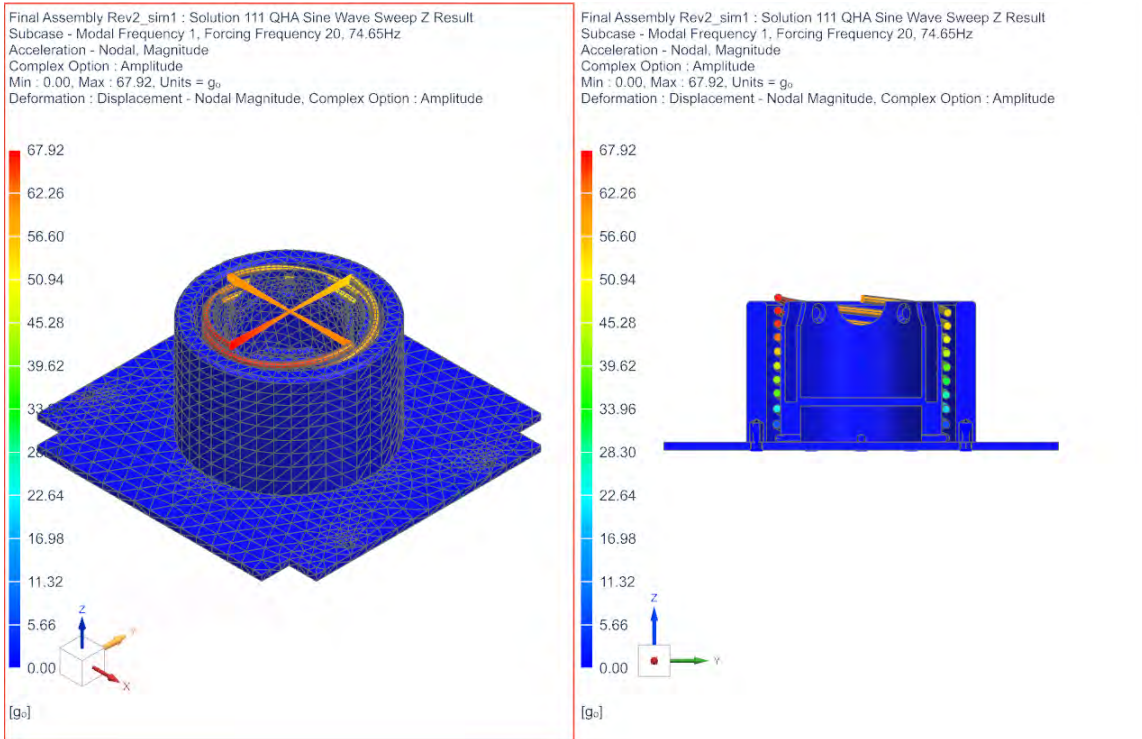


Figure 5.73: Sine Wave Sweep Z-Axis Acceleration Results

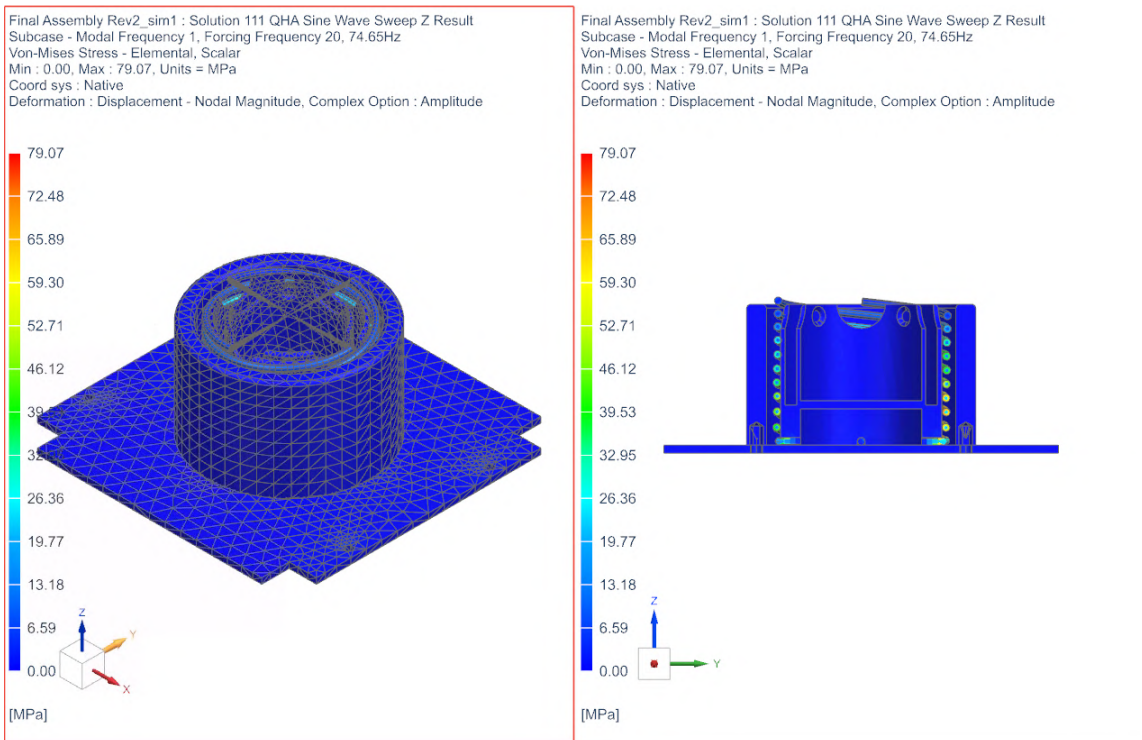


Figure 5.74: Sine Wave Sweep Z-Axis Stress Results

Studying the Z-axis acceleration and stress, shows that the antenna system experiences a maximum acceleration of 67.92 G's, when excited in the Z-axis. This acceleration, results in the antenna system experiencing a maximum stress of 79.07 MPa. This stress occurs on the filars of the system. The filars have a yield stress of 1970 MPa, therefore, the filars are not subjected to yielding and will not permanently deform, as a result of forced experienced during launch.

Comparing the results recorded in each axis of the antenna system shows, that a maximum acceleration of 67.11 G's is recorded in the Z-axis, while the maximum stress of 79.07 MPa is also recorded in the Z-direction. The stresses recorded within the simulation are all below the yield points of the materials used. Overall, the simulations show that the antenna system will survive the launch environment, when exposed to launch vibrations as outlined by launch specifications, under a sine wave loading profile.

#### **5.1.2.4 Random Vibration Simulation**

Vibration in the real world generally are of the random type. Random vibration is a varying waveform, where the intensity is defined by a power spectral density (PSD) . While a sine wave vibration occurs at distinct frequencies, random vibration subjects a product/model to all frequencies within a specified range simultaneously. With random vibration tests and simulations, the resonant frequencies of a product are all excited simultaneously, which could be worse than the excitation experienced in sine wave vibration, where resonant frequencies are excited individually. For the project, random vibration simulations are conducted to demonstrate, how the QHA deployment system can withstand the vibration environment encountered during launch and provides a more realistic scenario of the vibration the product will experience during launch, compared to sine wave analysis.

In this section, the setup and results of the random vibration simulation will be explored. The random vibration simulation is set up in the same way as the sine vibration simulation, however a random subcase is added and the frequency range of interest is changed from 10 Hz to 300 Hz, to 10 Hz to 2000 Hz. The Soyuz PSD specifications are input within the random subcase of the simulation environment, as shown in Figures 5.75 and 5.76.

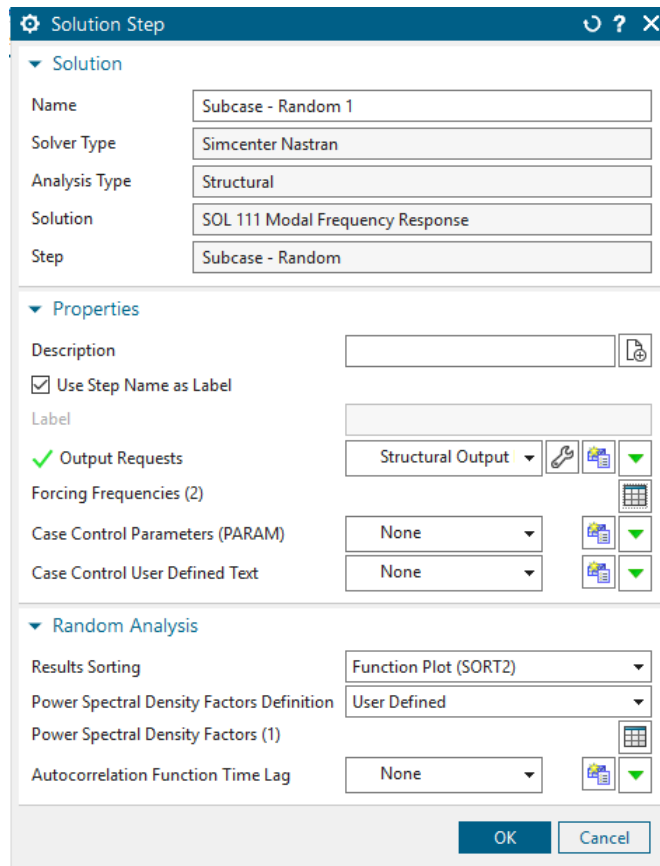


Figure 5.75: Random Vibration Setup

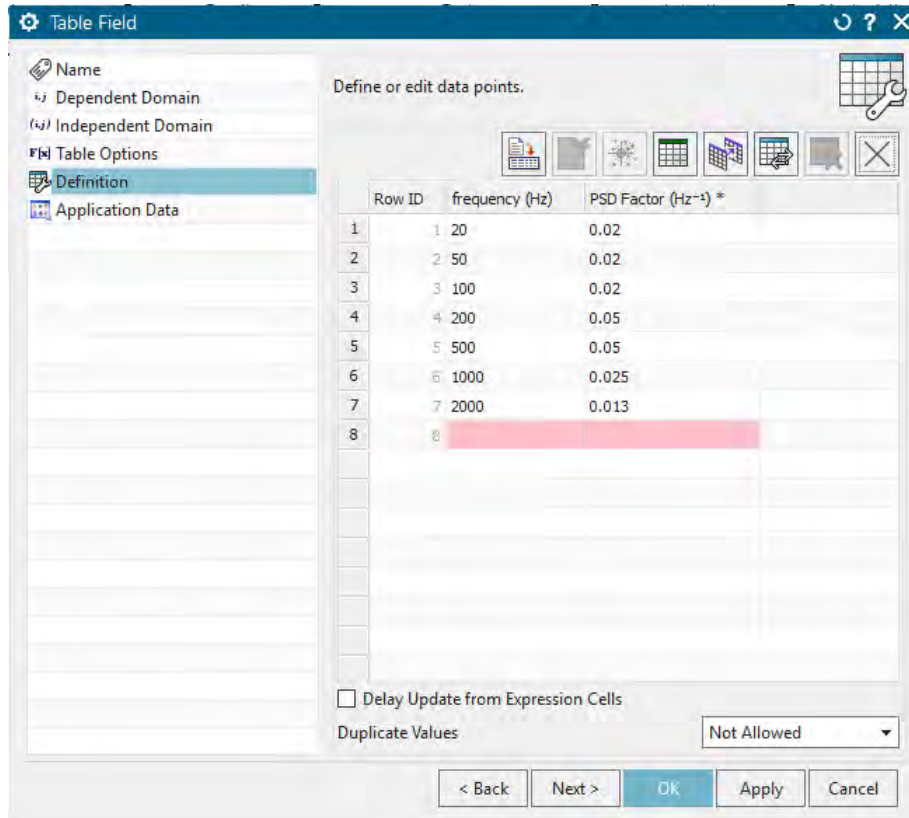


Figure 5.76: Soyuz Power Spectral Density Specification Input

It is important to note that by default, the frequency response output for frequency simulations in the random subcase environment are not output. To enable this for the random vibration simulation, parameters in the system control needs to be changed. By setting the RANFRF(524) parameter to 1 (RANFRF = 1), as shown in Figure 5.77, both the random and frequency response subcase results will be output.

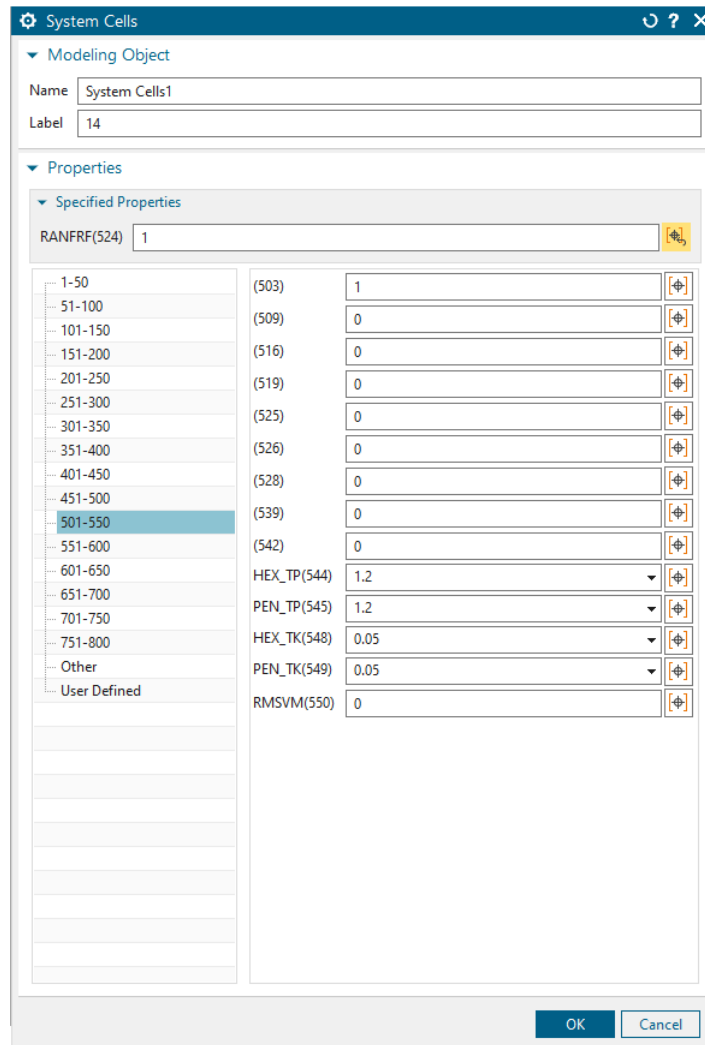


Figure 5.77: RANFRF(524) Parameter Input

The rest of the random vibration simulation setup is exactly the same as the sine vibration. With the simulation setup, the results of the random vibration recorded in the x, y and z axes can be analysed.

The results the analyses are most interested in are the RMS stresses generated by the random simulation. The RMS stresses need to be analysed in a statistical format using the Gaussian bell distribution curve, as shown in Figure 5.78.

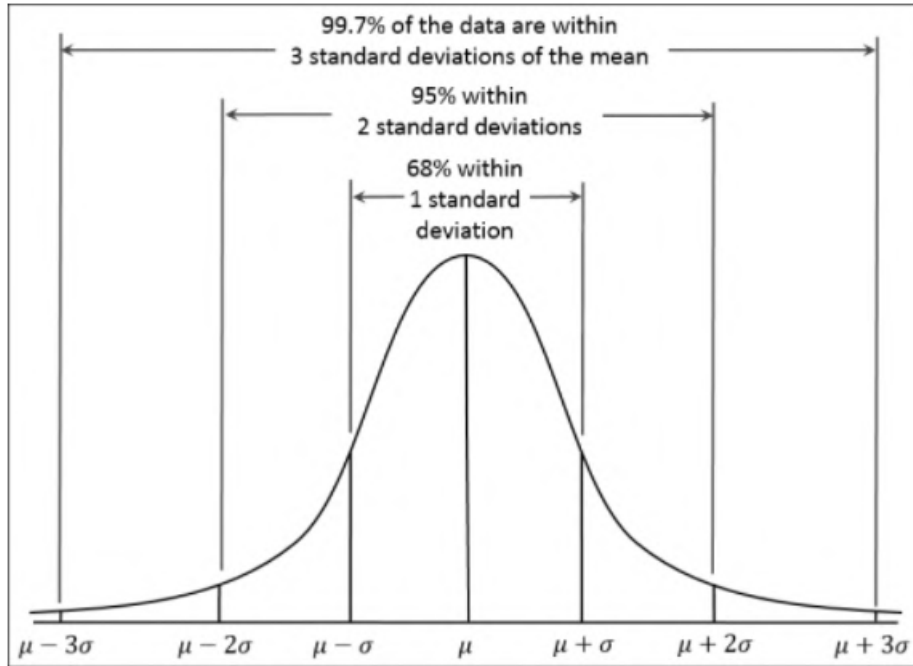


Figure 5.78: Gaussian Bell-Shaped Distribution

The RMS stress values recorded in the random vibration analysis correspond to  $1\sigma$ . Therefore, the  $1\sigma$  stress recorded will be experienced 68.3% of the time by the antenna structure. The stress of two standard deviations will be experienced 27.1% of the time, while three standard deviations will be experienced 4.3% of the time, and four standard deviations 0.3%. Structural components are usually designed to withstand  $3\sigma$  stress levels at all times, and the antenna system is no different.

Figures 5.79 to 5.84, show the RMS accelerations and stresses recorded in each axis of the antenna system for the random vibration analysis.

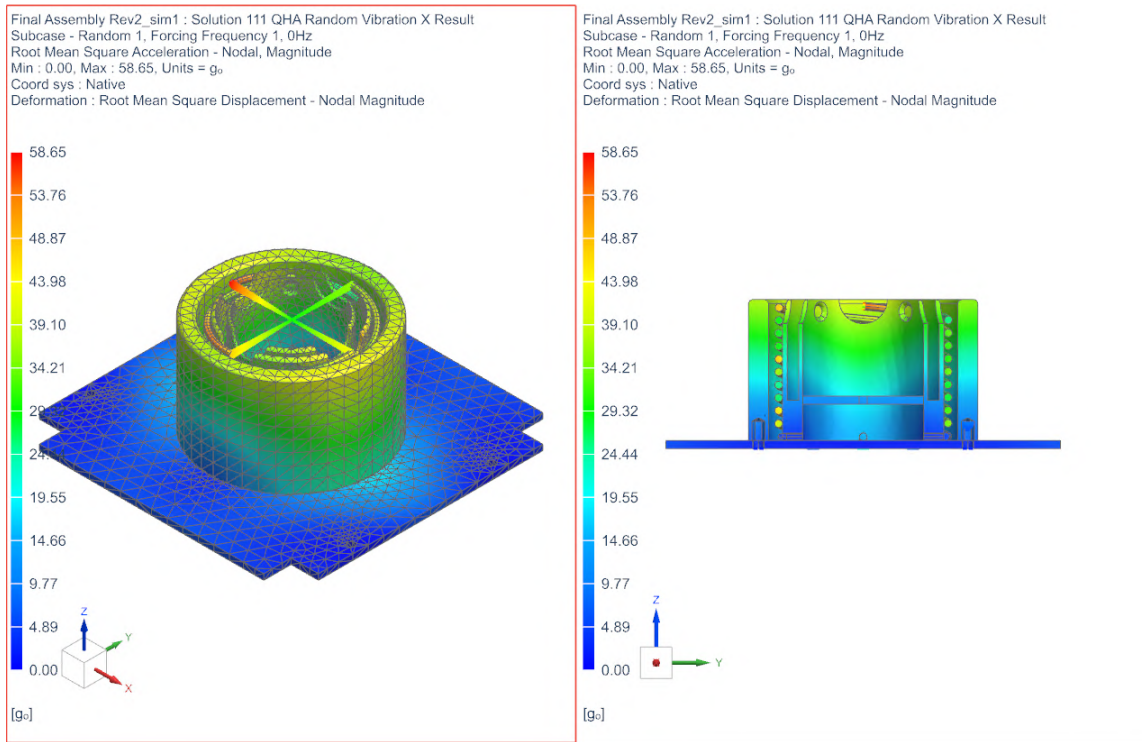


Figure 5.79: X-axis RMS Acceleration Results

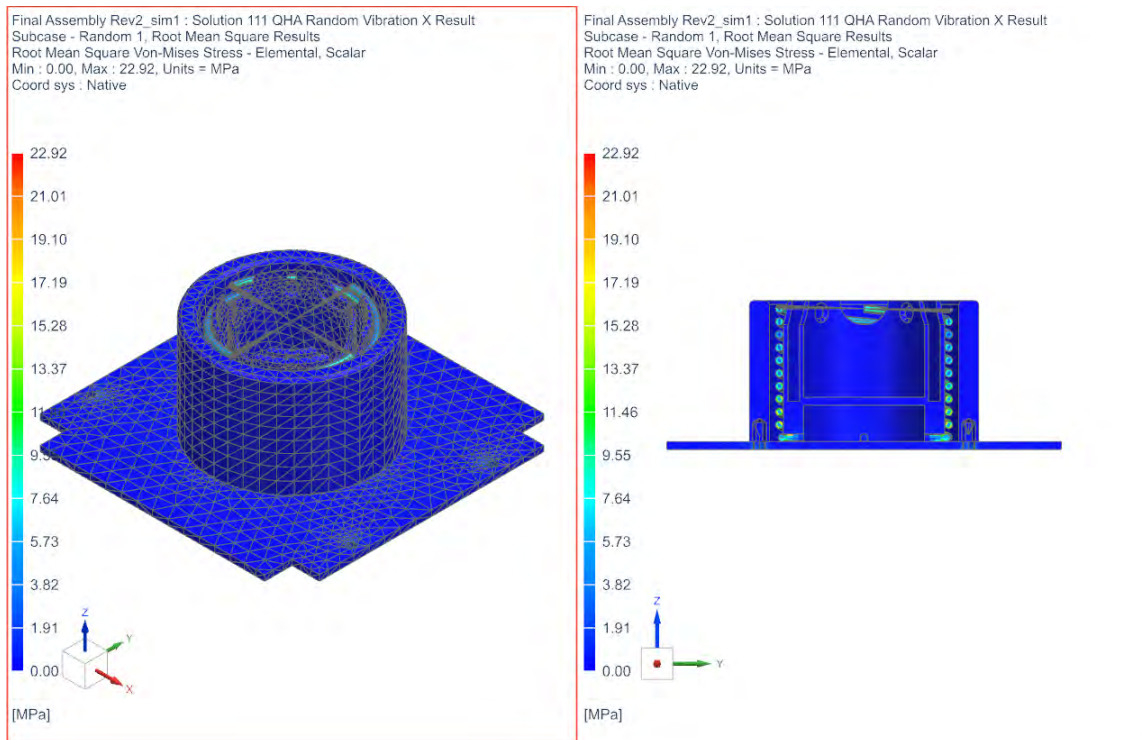


Figure 5.80: X-axis RMS Stress Results



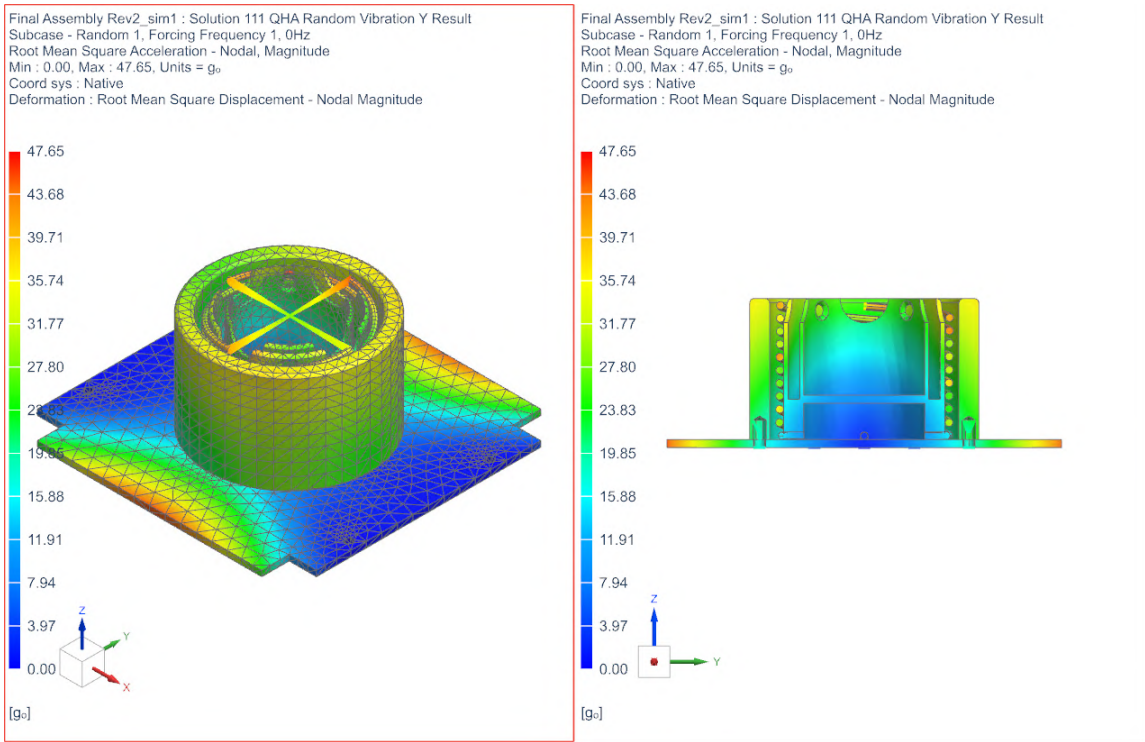


Figure 5.81: Y-axis RMS Acceleration Results

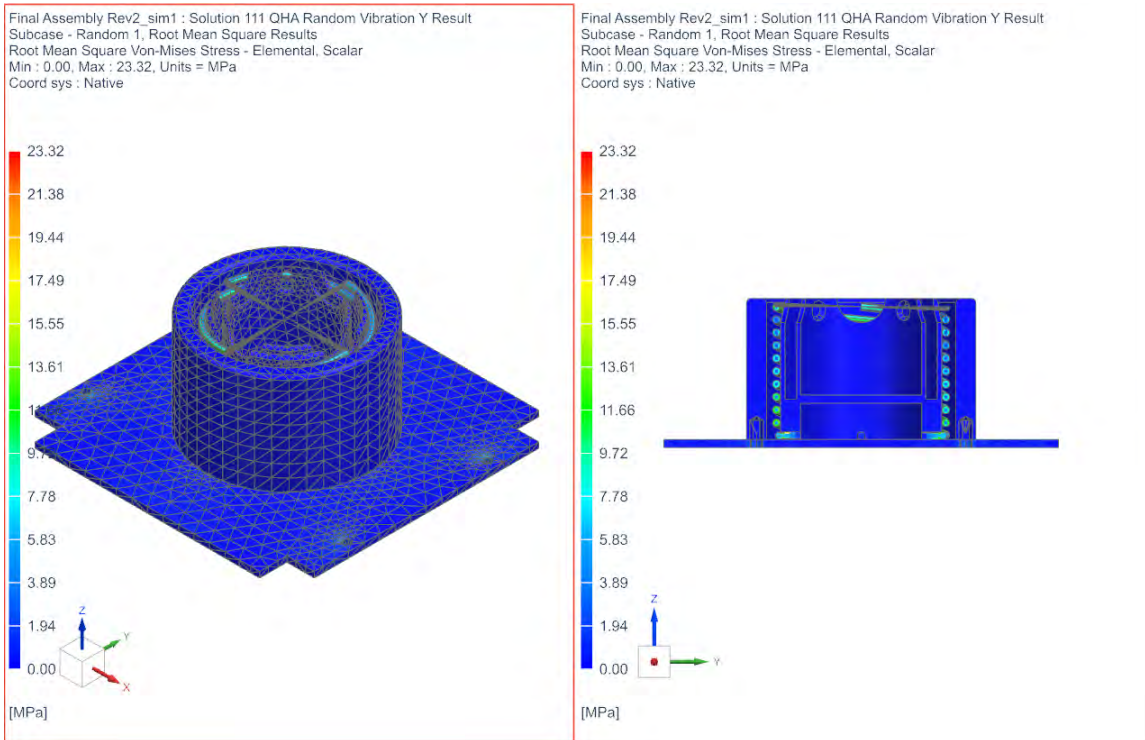


Figure 5.82: Y-axis RMS Stress Results

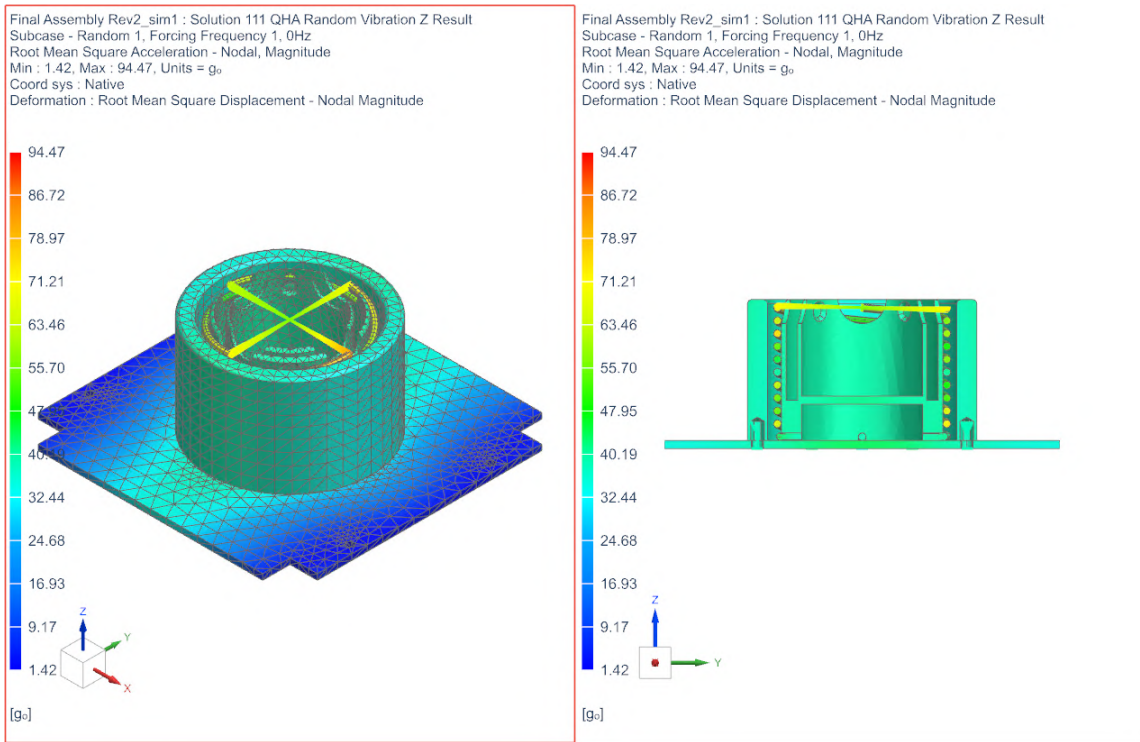


Figure 5.83: Z-axis RMS Acceleration Results

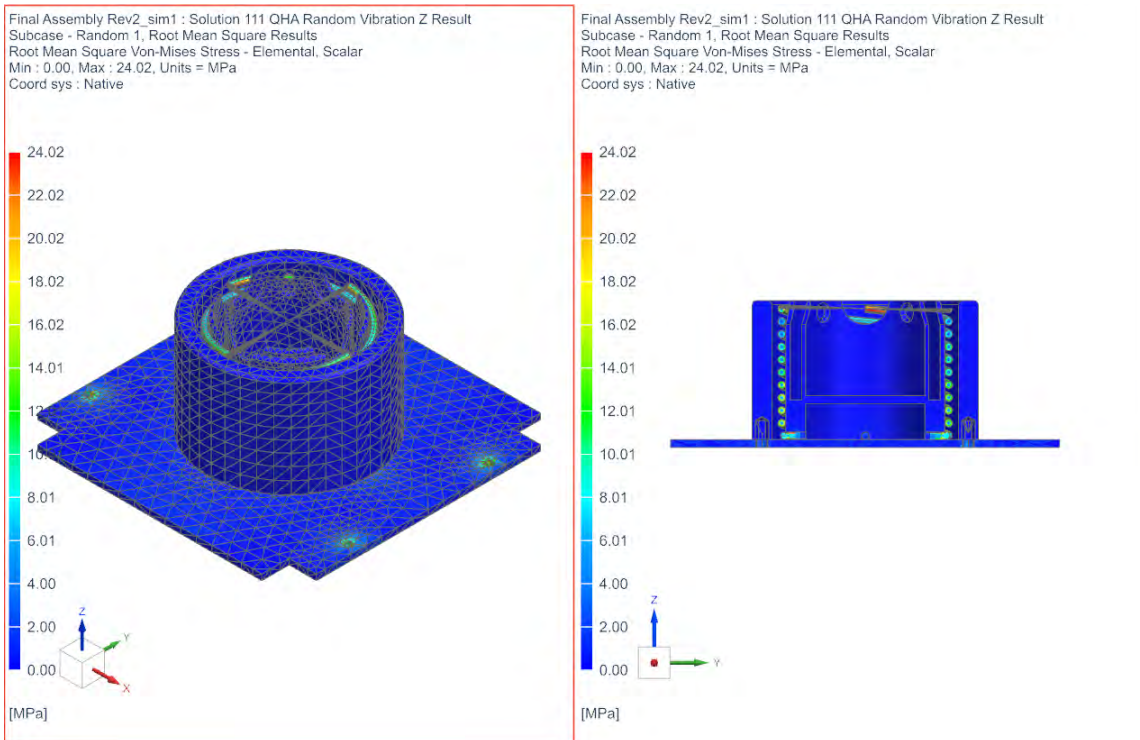


Figure 5.84: Z-axis RMS Stress Results

Analysing the RMS acceleration of the antenna system shows a difference when compared to the sine wave sweep acceleration. The sine wave sweep recorded acceleration results of 59.80 G's, 61.40 G's and 67.92 G's, for the X, Y and Z-axis,

respectively. The random vibration simulation recorded results of 58.65, 47.65, and 94.47, for the X, Y and Z-axis, respectively. The X-axis acceleration results showed similar values, while the Y-axis differs slightly between the two simulations. The Z-axis acceleration results show a vast difference between the two simulations. These differences in recorded results are due to how the random and sine wave vibrations are conducted. Sine wave vibration is conducted at distinct frequencies (one at a time), while random vibration analysis is conducted all at once (all frequencies are excited at the same time), which is more characteristic of real-life scenarios. Therefore, the random acceleration values are more accurate than the sine wave values.

The results of the RMS stress profiles show that the  $1\sigma$  stresses of the antenna system are 22.92 MPa for the X-axis, 23.32 MPa for the Y-axis and 24.02 MPa for the Z-axis. By taking these  $1\sigma$  stresses and multiplying them by a magnitude higher, up to four times the original stress, the full Gaussian bell-shaped stress distribution of each axis can be found. Figure 5.85 to 5.87, depicts the full Gaussian distribution.

X-Axis RMS $\sigma$ -Stresses				
Standard Deviation	$1\sigma$	$2\sigma$	$3\sigma$	$4\sigma$
Stress Present (MPa)	22,92	45,84	68,76	91,68

Figure 5.85: X-RMS Standard Deviation Stress

Y-Axis RMS $\sigma$ -Stresses				
Standard Deviation	$1\sigma$	$2\sigma$	$3\sigma$	$4\sigma$
Stress Present (MPa)	23,32	46,64	69,96	93,28

Figure 5.86: Y-RMS Standard Deviation Stress

Z-Axis RMS $\sigma$ -Stresses				
Standard Deviation	$1\sigma$	$2\sigma$	$3\sigma$	$4\sigma$
Stress Present (MPa)	24,02	48,04	72,06	96,08

Figure 5.87: Z-RMS Standard Deviation Stress

The tables show that the antenna never reaches the yield stress of ASTM A228 over the full four standard deviations of the distribution, showing that the antenna will be able to survive the launch environment.

### 5.1.2.5 Shock Simulation

Shock tests demonstrate that the satellite can withstand shock levels and frequency spectrum as predicted for flight. Shocks encountered during the mission originate from shroud jettison, separation of the launcher and the space vehicle, pyrotechnic devices, actuated release of covers or appendages, and latching of such appendages.

Shock simulations cover a wide frequency range that requires vast amounts of processing power. Whether using a simplified model or a fully representative model of the antenna, conducting such a simulation is extremely taxing on computer resources and requires vast amounts of storage space. Due to the large amounts of storage space processing required, shock simulations fall far outside the capabilities of the simulation computer at the PLMCC and were not conducted.

## 5.2 Debris Assessment

For the antenna system to be deployed in space, it must also adhere to IADC guidelines and CDS standards, which looks to decrease space debris. For this assessment, DAS (supplied by NASA), was used to assess whether the antenna would disintegrate upon re-entry into Earth's atmosphere, should it be flown on a mission.

When considering payload re-entries, the most concerning components are those that consist of metallic materials. Plastics easily burn up in the extreme heat associated with atmospheric re-entry, however metals, due to their high melting points, are able to survive the hostile environment. Therefore, only the filars of the antenna system were assessed using DAS.

DAS works by entering specific entries such as mission duration, orbital parameters, mass of the component/system and the area to mass ratio of the part/component. Figure 5.88 to 5.90, depicts the parameter input used for the QHA filars. Two entries were made, one entry for the filars to be assessed as a payload and another entry for the filars acting as if they were mission related debris (debris created as part of a mission).

The screenshot shows the DAS software interface. At the top, the 'Mission Definitions' section includes a text box for 'Mission Name' containing 'QHA Filars' and a 'Launch Year' field set to '2022'. Below this is a tree view for 'Mission Components' with 'Payloads' expanded to show 'QHA Filars'. To the right are buttons for 'Apply Changes', 'Reject Changes', and 'Help'. At the bottom, the 'Define Payload Properties' section contains a table with the following data:

Row	Payload Name	Mission Duration (yrs)	Operational Perigee Alt (km)	Operational Apogee Alt (km)	Operational Inclination (deg)
1	QHA Filars	5	550	550	99.7
*					

Figure 5.88: DAS Payload Input 1

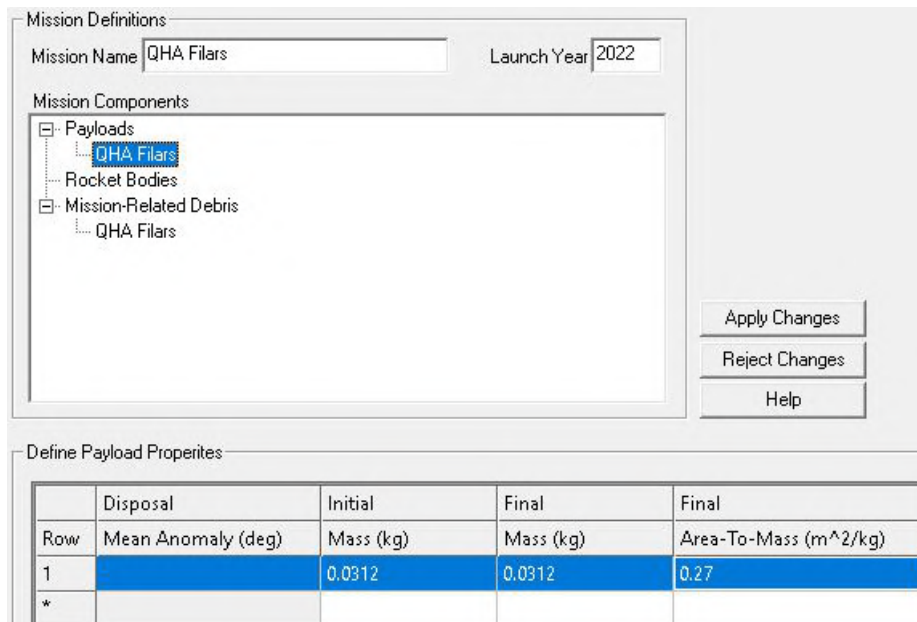


Figure 5.89: DAS Payload Input 2

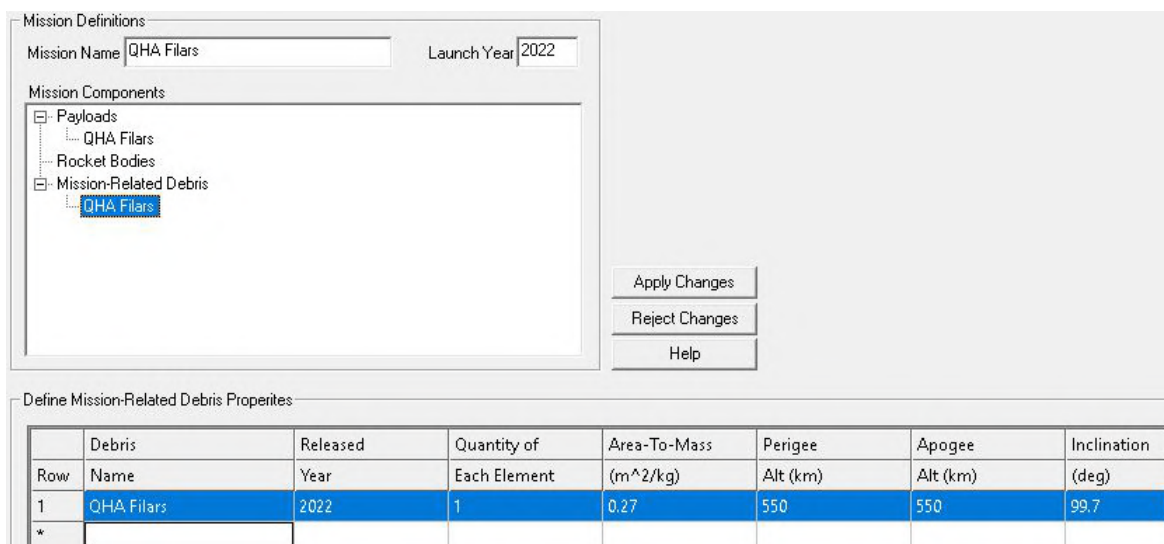


Figure 5.90: DAS Mission-Related Debris

Orbital parameters, similar to ZACube-1 and ZACube-2, were used for the altitudes and inclination inputs. The mass of the filars, was calculated to be approximately 0.0312 kg and the area as 0.00842727 m<sup>2</sup>. These two parameters led to an area to mass ratio of 0.27. Figure 5.91, depicts the assessment requirements, which the antenna system must be compliant for. Requirement 4.8-1 for collisions hazards of space tethers was not assessed, as the antenna system does not consist of any space tethers.

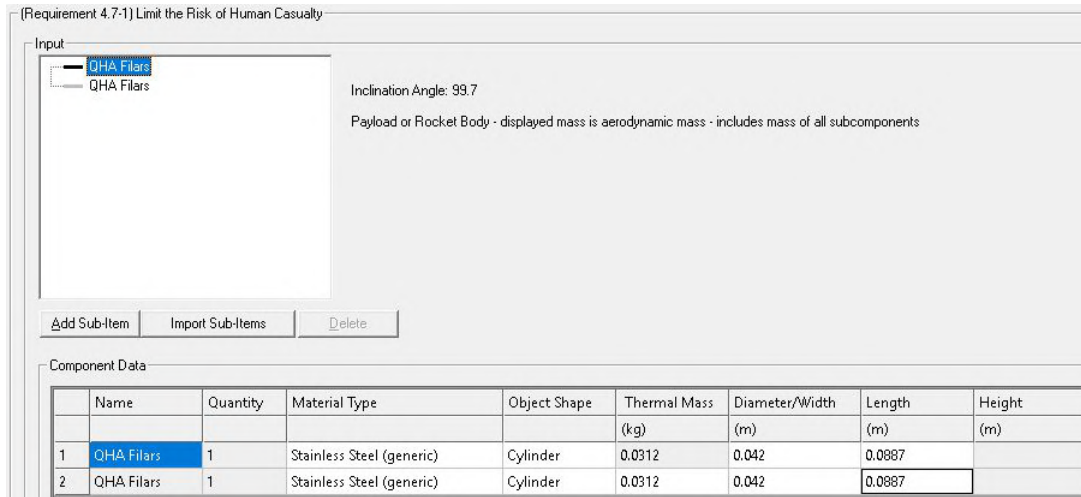


Figure 5.91: DAS Requirement Assessments

The main objective of the debris assessment is to determine, what risks space debris, that re-enters the atmosphere, poses to human lives. To accomplish this, some more inputs are required. Figure 5.92, depicts the additional input fields required, to assess the threat space debris has on humans, should the filars not properly disintegrate upon re-entry.

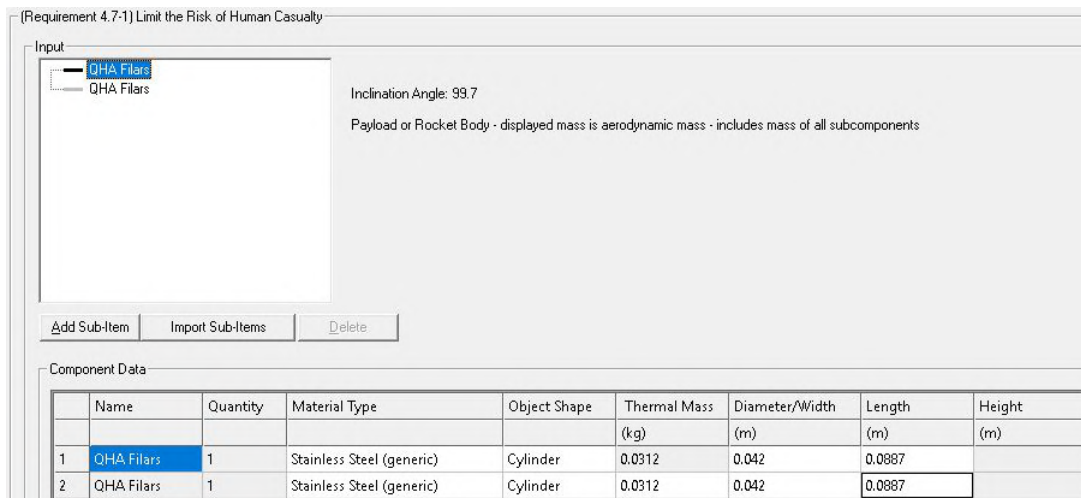


Figure 5.92: Human Casualty Requirements Input

The assessment requires material type, object shape, mass, and dimensional entries based on object shape. For the filars, the closest material entry available on the system to ASTM A228 was generic stainless steel. A cylinder shape was selected for the filars as the other options (box, flat plate and sphere), would not have accurately represented the filars. Therefore, the filars are assessed as being a cylinder consisting of a mass of 0.0312 kg, with a diameter of 0.042 mm and a length of 88.7 mm, which are the main characteristics of the electrically designed antenna.

Following the assessment setup, the DAS assessment was executed. According to the results, the filars and therefore antenna system pass all criteria, as shown in Figure 5.93. This is indicated by the green ticks on the left side of Figure 5.93. The only requirement, which was not met, was the collision hazards of space tethers assessment. This assessment was not conducted, due to that the antenna system does not consist of any space tethers.

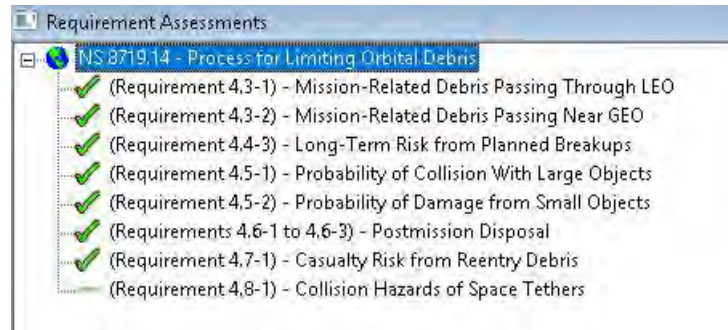


Figure 5.93: Antenna System Side View

Therefore, the antenna system complies with IADC and CDS requirements, for the mitigation of space debris and can move on to the testing phase.

# Chapter 6

## Testing

In this section of the report, the antenna system is subjected to rigorous testing to determine how reliable the system is and to determine how physical tests compare to theoretical and simulated results. During testing, various optimisations were made.

### 6.1 Deployment Test

The deployment testing is a crucial part of the research project. The testing phase ultimately determines whether the antenna design will work or not. The antenna system was rigorously tested to determine possible deployment issues and possible optimisations which could be carried out. The methodology described in section 3.2.1 was used to test deployment of the antenna system.

#### 6.1.1 Pre-Deployment Test Checks

Figures 6.1 and 6.2 depict the antenna system used for the pre-deployment test. An inspection of the components was conducted. The inspection showed that the filars were not all completely identical. This can be seen from the form factors of the 4 filars in Figure 6.1 and the helix diameters of the four filars not completely aligning in Figure 6.2. Therefore, due to the high spring index of the filars, tolerances were difficult to keep. However, even with the present tolerance issues, the antenna could still be mechanically tested.



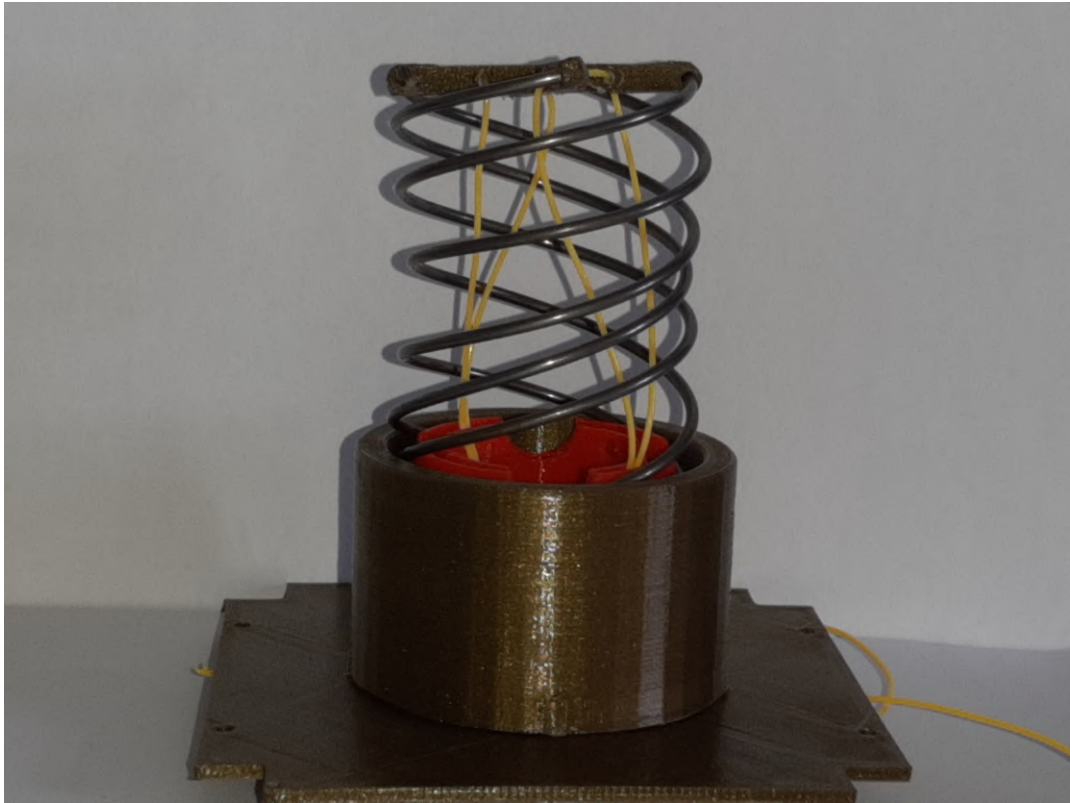


Figure 6.1: Antenna System Side View

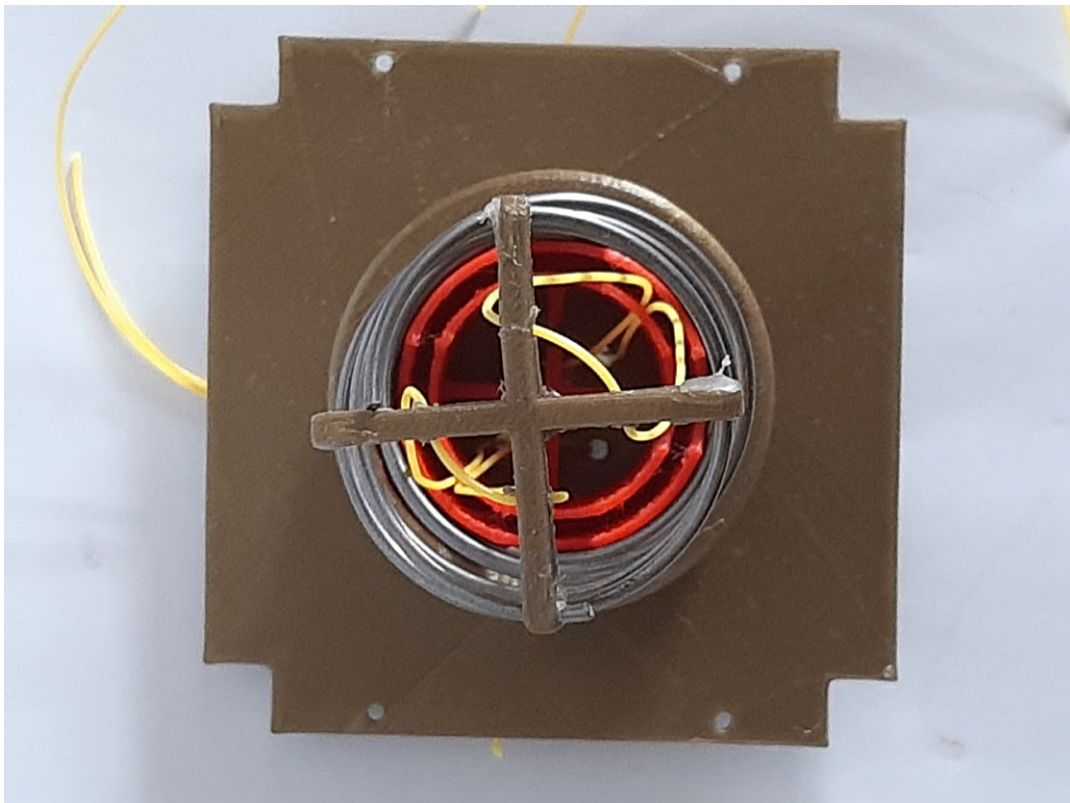


Figure 6.2: Antenna System Top View

Following the visual inspection, a bifilar setup of the antenna was constructed, as shown in Figure 6.3. This setup was used to check for any overhangs or stowing issues that might occur due to the tolerance issues of the manufactured filars. As seen in Figure 6.3, the filars deform in the lateral plane in such a way, that they would encounter the top of the outer stowing wall, making stowing the antenna extremely difficult. Another key observation was the inadequate performance of the top brace, used to stow the antenna. To counter the overhang, the outer stowing wall diameter was increased.

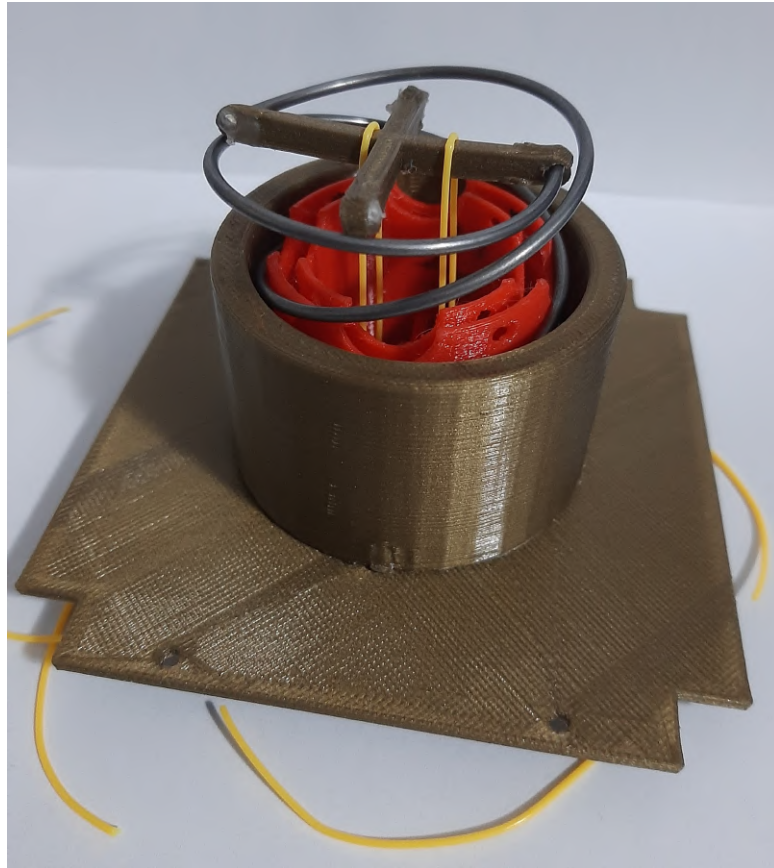


Figure 6.3: Bifilar Antenna Test Setup

The top brace is a key aspect to how the antenna is stowed. An inadequate top brace would lead to improper stowing of the filars and possible damage to the filars. Therefore, the top brace was optimised. Appendix G, depicts the various antenna top brace iterations. The final top brace, which was selected, can be seen in Figure 6.4.



Figure 6.4: Optimised Antenna Top Brace

The newly optimised top brace was more robust than its predecessor, as shown in Figure 6.5. The optimised brace allows for the antennas to be stowed, while also limiting the upwards vertical travel of the antenna as it is being stowed, with the use of flanges along its perimeter.

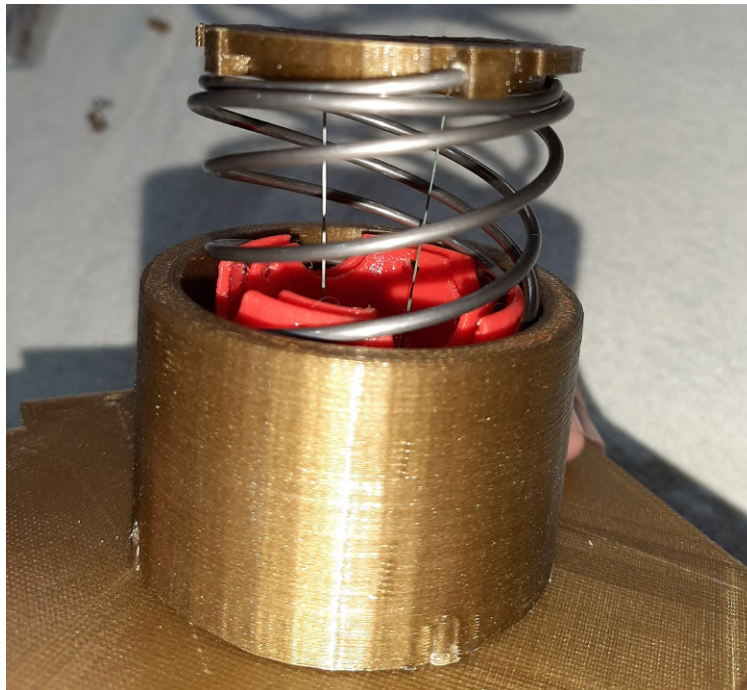


Figure 6.5: Compressed Antenna With Optimised Top Brace

Finally, the last optimisation made for the system was the shortening of the inner stowing wall, so that the full antenna length including the top brace could sit

perfectly within the confines of the "tuna can" space. Figure 6.6, depicts the final setup, which was used for testing.

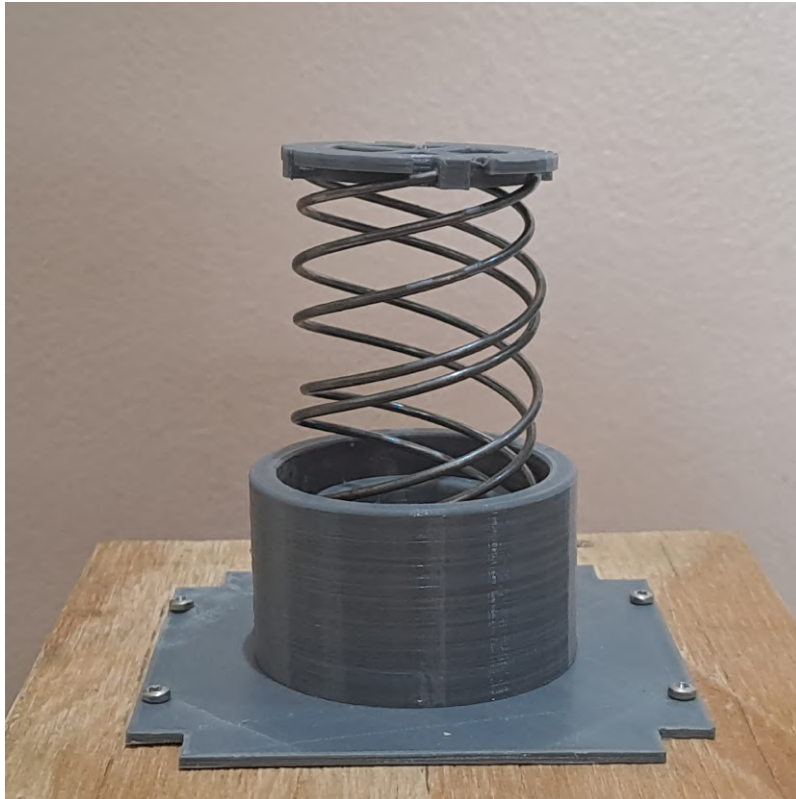


Figure 6.6: QHA Test Model

An aspect of the pre-deployment test, which was noted, was the stiffness of the springs. The springs are incredibly stiff, making stowing of the filars troublesome. However, the antenna filars could still be stowed. With the test model defined, deployment tests and reliability assessment could be conducted on the antenna deployment system.

### 6.1.2 Deployment Test

The deployment test is conducted in accordance with the test methodology described in section 3.2.1. The antenna is mounted to the stowing jig, where it is stowed and then released for deployment. Figure 6.7, depicts the mounted antenna in the jig.

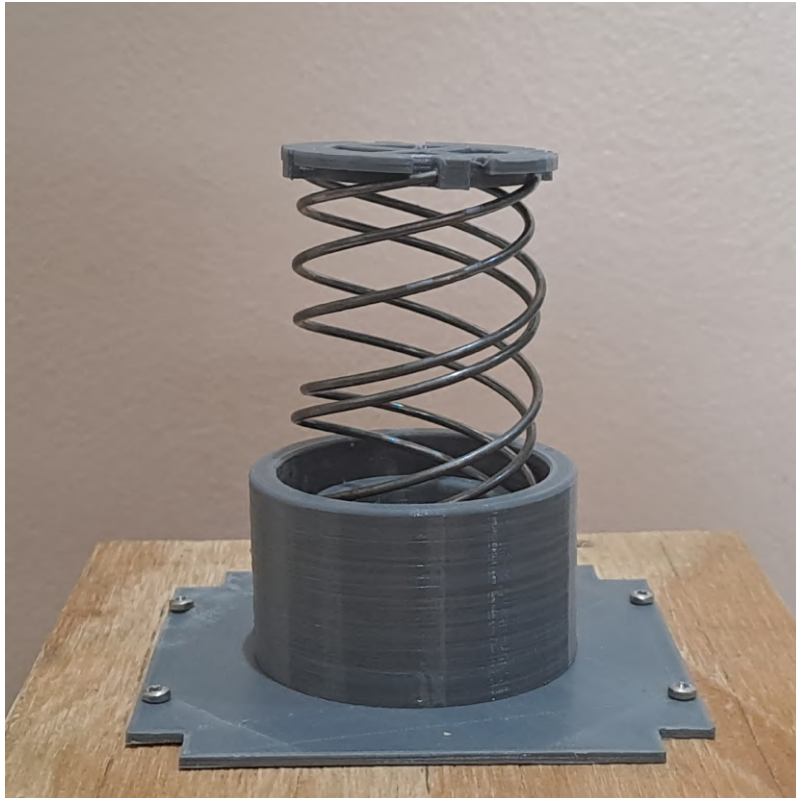


Figure 6.7: Antenna Mounted to Deployment Jig

The antenna is stowed using burn wire and released by burning the burn wire, emulating a burn wire mechanism. As per the described methodology, the deployment test is conducted 5 times. The deployment height, form factor and ease of deployment and stowing are assessed. The results of the antenna tests were captured through video recordings. Appendix H, contains pictures from the recordings at different increments of the antenna deployment.

The results of the deployment test are as follows. Of the five tests conducted, each test resulted in the top brace being launched off of the antenna system due to the excessive energy stored within the springs. Figure 6.8, shows the deployed state of the antenna for test one.



Figure 6.8: Antenna Deployment Test 1 Result

As seen in the figure above, the brace is not on the spring, leaving behind an antenna with no noticeable form factor. This is worrying, because if the antenna cannot be reliably and safely deployed, without losing the top brace, which keeps the antenna together, then it can't be used in a real mission. Table 6.1, depicts the reliability scores of the antenna tests.

Table 6.1: 1.91 mm Deployment Reliability Assessment

1,91mm Deployment Tests				
Criteria:	Deployed Height	Deployed Form Factor	Controlled Deployment	Ease of Stowing
Test 1	3	0	1	3,5
Test 2	3	4	1	3,5
Test 3	3	0	1	3,5
Test 4	4	0	1	3,5
Test 5	4	0	1	3,5
Average:	3,4	0,8	1	3,5
Total Score:			8,7	of 20

The table shows that the deployment strategy for the antenna system is inadequate and is therefore not reliable. This is due to the excessive stored energy in the

springs, as a result of the stowed antenna. As per the design and testing methodology, a new strategy for mitigating the spring deployment forces would need to be considered.

To accomplish this new strategy, two approaches were considered. One approach looked at reducing the antenna wire diameter to reduce the deployment forces. While the second approach looked at the deploying the antenna in stages.

### **6.1.3 Deployment Test with Decreased Antenna Wire Diameter**

An effective and easy way to mitigate the deployment force of the antenna is to decrease the spring wire diameter. By decreasing the wire diameter, the overall stiffness of the spring decreases, which in turn would make it easier to stow and therefore deploy the spring. A smaller spring stiffness would mean that less force is required to stow the spring antenna, at the expense of antenna robustness. An added advantage of using smaller diameter wire, is that there is more space available within the confines of the "tuna-can", meaning the spring antenna will not have to be fully compressed to its solid height, thus also resulting in lower compressive and reactive/deployment forces.

While decreasing the antenna wire diameter provides the design with more manageable stowing and deployment scenarios, there are disadvantages present. The major disadvantage is that by decreasing the wire diameter, the spring index of the antenna increases. If the spring index is too large or too small, it can become extremely difficult to keep design tolerances. The change in wire diameter would also affect the impedance of the antenna, shift the centre frequency and shorten the bandwidth of the antenna, especially if the wire diameter is much smaller than 1.91 mm. Therefore, by taking into account locally available ASTM A228 wire diameters, the 1.1 mm and 1.6 mm wire diameters were explored. Calculations for the 1.1 mm and 1.6 mm QHA springs can be found in Appendix F.

The 1.1 mm and 1.6 mm wire diameter antennas were manufactured. From receiving the new antennas, it was immediately observed that tolerances were difficult to keep with these configurations. The spring index for both the 1.1 mm and 1.6 mm wires are in excess of 25, where 25 is considered the highest limit at which tolerances can be kept. Figures 6.9 and 6.10 depict the respective configurations.

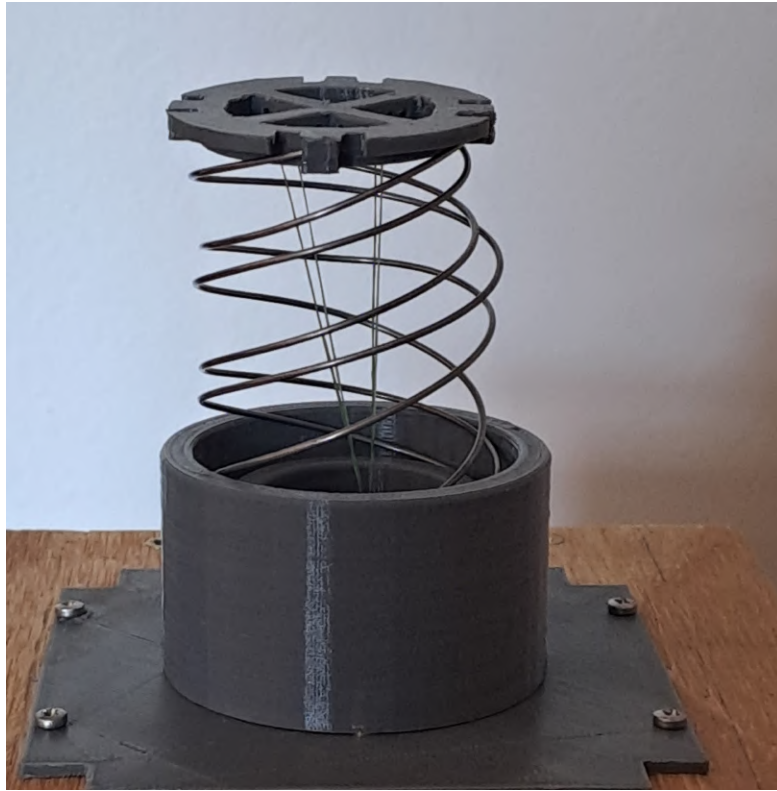


Figure 6.9: 1.1 mm Wire Diameter Antenna Configuration



Figure 6.10: 1.6 mm Wire Diameter Antenna Configuration

The figures show that the form factors of the antennas are not desirable. For the QHA to work, each filar must be  $90^\circ$  out of phase with one another and must



be uniform in that regard from the bottom of the filar to the top. For both the 1.1 mm and 1.6 mm wires, the respective form factors are not close to being uniform. This alone can eliminate the smaller diameter wire optimisation/approach, due to that the antenna would most likely not be able to receive and send signals expected of an QHA, due to the irregularities of the filars. However, even so, the antennas were mechanically tested to gauge how well the approach mitigated the deployment force. Appendix H, depicts the deployment testing of the 1.1 mm and 1.6 mm wire. Table 6.2, depicts the reliability study of the 1.6 mm configuration.

Table 6.2: 1.6 mm Deployment Reliability Assessment

1,6mm Deployment Tests				
Criteria:	Deployed Height	Deployed Form Factor	Controlled Deployment	Ease of Stowing
Test 1	4	2,5	3	2
Test 2	1	0	3	1,5
Test 3	3,5	2,5	3	3
Test 4	4	0	3	1
Test 5	3	2,5	3	0,5
Average:	3,1	1,5	3	1,6
Total Score:			9,2	of 20

The 1.6 mm wire configuration shows much more promise in the stowing and deployment of the antenna. According to the calculations, the 1.6 mm only requires 100 N of force to be compressed. This resulted in a noticeable difference in stowing the antenna. The antenna also exhibited a less explosive deployment force compared to the 1.9 mm wire. However, while the results are promising, the forces are still excessive. 100 N is still equivalent to approximately 10 kg of force and while it may be easier to stow and deploy, the form factor irregularities hardly make this configuration workable. The form factor irregularities, due to tolerances not being kept, also made stowing of the antenna much harder. As the filars were compressed, they deformed laterally much more than what was experienced for the 1.91 mm configuration. As a result, they often got caught on the outer guide wall and required extra attention, when being stowed. Table 6.3, depicts the reliability study of the 1.1 mm configuration.

Table 6.3: 1.1 mm Deployment Reliability Assessment

Staged 1,1mm Deployment Tests				
Criteria:	Deployed Height	Deployed Form Factor	Controlled Deployment	Ease of Stowing
Test 1	4	1	4	4
Test 2	4	1	4	4
Test 3	4	1	4	4
Test 4	4	1	4	4
Test 5	4	1	4	4
Average:	4	1	4	4
Total Score:			13	of 20

The 1.1 mm wire configuration depicts the most promising scenario regarding the stowing and deployment of the antenna. According to the calculations, the 1.1 mm

wire only requires 25 N of force to be compressed. This resulted in the antenna being stowed with relative ease, much easier and less resistive to compression compared to the other configurations. The antenna also exhibited the least explosive deployment force compared to the other antenna configurations. However, similarly to the 1.6 mm wire, the form factor irregularities hardly make this configuration workable.

Therefore, taking into account that both the smaller diameter wire springs, have a spring index of above the recommended tolerance limit of 25 and both suffer from form factor irregularities. It can be concluded that none of these optimisations will work. In order to find the "middle ground" between the smaller diameter wire antennas and the original design, a QHA that consists of springs with a spring index equal to or lower than 25 is required. As previously mentioned, the helix diameter (42 mm) is locked in part fulfilment of the S-band frequency requirements. Therefore, in order to achieve a spring index of 25, the wire diameter would need to be changed.

According to calculations in Appendix F, the "optimal" solution would be a spring that has a wire diameter of 1.68 mm. This 1.68 mm wire produces a spring index of 25, which would make the important spring tolerance more achievable. However, issues are also encountered with this approach. 1.68 mm wire is not a standard wire size and therefore would need to be custom-made at great expense. Furthermore, the QHA constructed with this wire, would require 133.67 N of force to compress. While less than the 1.91 mm, it is still quite excessive. Therefore, it's concluded that optimisation of the antenna design by reducing the wire diameter, will not yield favourable electrical results due to irregularities in the antenna form factor. However, if in future studies and if adopted by industry, research is conducted to achieve required tolerance at higher spring indexes, this approach can be and should be reconsidered.

### **6.1.3.1 Deployment Test with Staged Deployment**

Following previous tests, the force exerted by the deployment of the antenna was quite excessive. A method using staged deployment of the antenna was explored to help mitigate the overall deployment force of the antenna.

Using this method, the antenna was released in stages using burn wire of varying length to limit the deployment capabilities of the antenna when deployment commences. Figure 6.11 to 6.13, depicts the stages of the antenna as it is deployed.

Staged deployment results were recorded using video recordings. Results of the various deployment stages can be found in Appendix H. Testing of the staged approach showed promising results. The force exerted by the deployment of the antenna was notably different to the approach without stages, with the antenna also reaching the required height of approximately 88.7 mm. Table 6.4, depicts the reliability assessment of the staged deployment approach.



Figure 6.11: 1.91 mm Staged Deployment Stage 1 (Stowed)



Figure 6.12: 1.91 mm Staged Deployment Stage 2



Figure 6.13: 1.91 mm Staged Deployment Stage 2 (Deployed)

Table 6.4: 1.91 mm Staged Deployment Reliability Assessment

Staged 1,91mm Deployment Tests				
Criteria:	Deployed Height	Deployed Form Factor	Controlled Deployment	Ease of Stowing
Test 1	4	4	4	3
Test 2	4	3,5	4	3
Test 3	4	3,5	4	3
Test 4	4	3,5	4	3
Test 5	4	3,5	4	3
Average:	4	3,6	4	3
Total Score:			14,6	of 20

The reliability assessment shows that the staged approach successfully addressed the issue of excessive deployment forces. The staged approach works due to that each stage is limited by the strong burn wire, each being able to hold a force of 13 kN. Therefore, each burn wire works in keeping the antenna stowed, once ready for deployment, the first stage is triggered causing the antenna to be caught by the second stage.

Therefore, the antenna is released in smaller bursts, until it is eventually fully deployed. Multiple tests were conducted, and it was found, that using 3-4 stages produces greatly improved results compared to approaches without stages. Any more stages result in the tangling of the burn wires. The reason this approach works is that the closer the spring antenna reaches full deployment, the less force it exerts on the burn wire, due to it having less stored energy within the coils of the spring.

Therefore, the antenna system reliably deploys and can move onto thermal and

electrical testing.

## 6.2 Thermal Cycling Test

In this section, the antenna system is tested using a thermal chamber. The test is conducted, to determine whether the antenna system can withstand the expected temperature cycling it would be exposed to in space, with temperatures based on calculations and simulations. The Binder MKT115 thermal chamber was used for the thermal test, as seen in Figure 6.14.



Figure 6.14: Binder MKT115 Thermal Chamber

### 6.2.1 Chamber Setup and Thermal Cycling Test

In order to conduct a test using the thermal chamber, the chamber must first be setup and programmed to the required specifications. According to the thermal simulation in section 5.1.1.2, the antenna system needs to be exposed to a temperature range of  $-24^{\circ}\text{C}$  and  $73^{\circ}\text{C}$ . To accomplish this, the thermal chamber is set up and programmed to cycle between a maximum temperature of  $73^{\circ}\text{C}$  and a minimum of  $-24^{\circ}\text{C}$  as shown in Figure 6.15. Once at the required temperature, the chamber is programmed to linger at the given temperature, based on expected orbital exposure times. The thermal chamber is also setup, so temperature change

occurs at  $1^{\circ}\text{C}$  per minute. This helps ensure that the thermal chamber gradually heats up and cools down, so that lingering temperatures are appropriately reached.

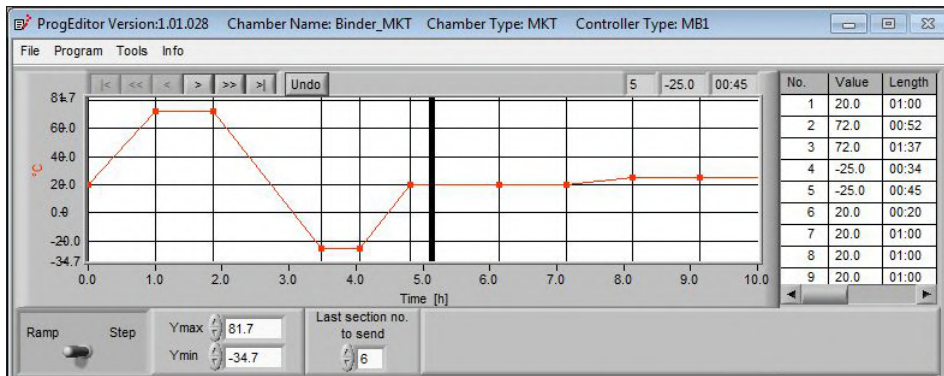


Figure 6.15: QHA Thermal Test Input

Once programmed, the measurements set for the test are sent to the thermal chamber, where testing can begin. The antenna system was placed in the Binder Thermal chamber as shown in Figures 6.16 to 6.17.



Figure 6.16: QHA Placed in Thermal Chamber



Figure 6.17: QHA Placed in Thermal Chamber Close Up

Following placement of the antenna system in the thermal chamber, the door of the chamber is closed and the thermal test program is started. With the chamber setup, the antenna system was tested within the chamber and results were recorded.

## 6.2.2 Thermal Cycling Results

Figure 6.18, depicts the antenna system during the thermal test. During testing, the antenna system showed no signs of deformation and remained robust throughout the test. This is promising as it shows that the antenna system is able to withstand the maximum qualification temperature set between  $-25\text{ }^{\circ}\text{C}$  and  $72\text{ }^{\circ}\text{C}$ ,



Figure 6.18: Antenna System In Test Check Up

Once the test was completed, the antenna system was visually assessed for any deformations, that may have occurred during the test. Figure 6.19, depicts the antenna system post thermal testing.



Figure 6.19: Antenna System Post Thermal Test

The antenna system printed out of PETG filament, showed slight signs of warping, when exposed to qualification temperatures, as shown in Figure 6.20. This is most likely due to PETG having a maximum service temperature of  $\pm 80^{\circ}\text{C}$ . The thermal test pushes the PETG to its upper usable limit, however, even though it's close to the maximum temperature, it should not have warped. The warping experienced could be due to the fact the prototype is 3D printed. It's possible that due to the layering and how layers are deposited for 3D prints, the maximum service temperature is affected, possibly due to pockets of air caught within the 3D printed parts.



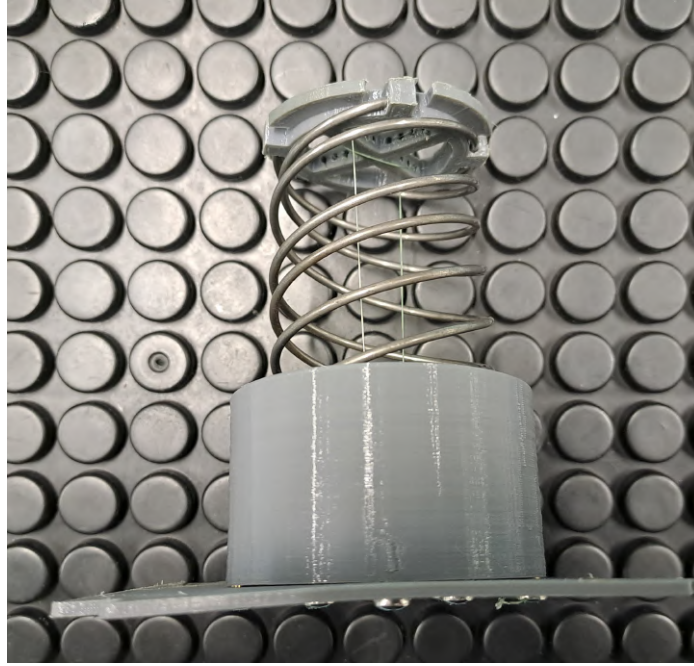


Figure 6.20: Thermal Test Antenna Deformation

Acetal which was selected during material selection has a far greater operational range from  $-40\text{ }^{\circ}\text{C}$  to  $110\text{ }^{\circ}\text{C}$ . Therefore, considering the results of the PETG test, it is more than likely that the antenna system manufactured from Acetal would be able to survive and handle the space thermal environment it is exposed to.

The temperatures used for the qualification test are also fairly excessive when considering the maximum operating temperatures of the on-board CubeSat components, which generally have an operating temperature of  $-20\text{ }^{\circ}\text{C}$  to  $60\text{ }^{\circ}\text{C}$ . Therefore, acceptance testing was not conducted due to that antenna system survived qualification with minimal deformations.

The antenna system manufactured from 3D printed PETG filament, therefore will survive the thermal environment. The actual antenna system will be manufactured from Acetal, which is a more robust material than PETG and therefore, should have no problems surviving the space environment as well.

### 6.3 Electrical Test

Electrical testing was conducted by the electronics department of CPUT. It was determined, that an S11 reflection coefficient test would be conducted to examine whether the antenna will operate at the specified frequency range, which is centred at 2.15 GHz, according to the simulated electrical models of the second antenna iteration as seen in Appendix A.

An S11 reflection coefficient test measures how much power supplied to the an-

tenna is actually radiated by the antenna and not reflected back to the transmitter. The smaller the dB (negative) value, the better the antenna will be able to radiate a signal. For the antenna system, a reflection coefficient of -10 dB is satisfactory.

Before the antenna can be tested, a feed network needs to be constructed to power the antenna. A Wilkinson splitter feed network was suggested for testing the antenna system. The Wilkinson splitter feed network consists of 4 feed points for the antenna system as seen in Figure 6.21, which are 90° out of phase with one another.

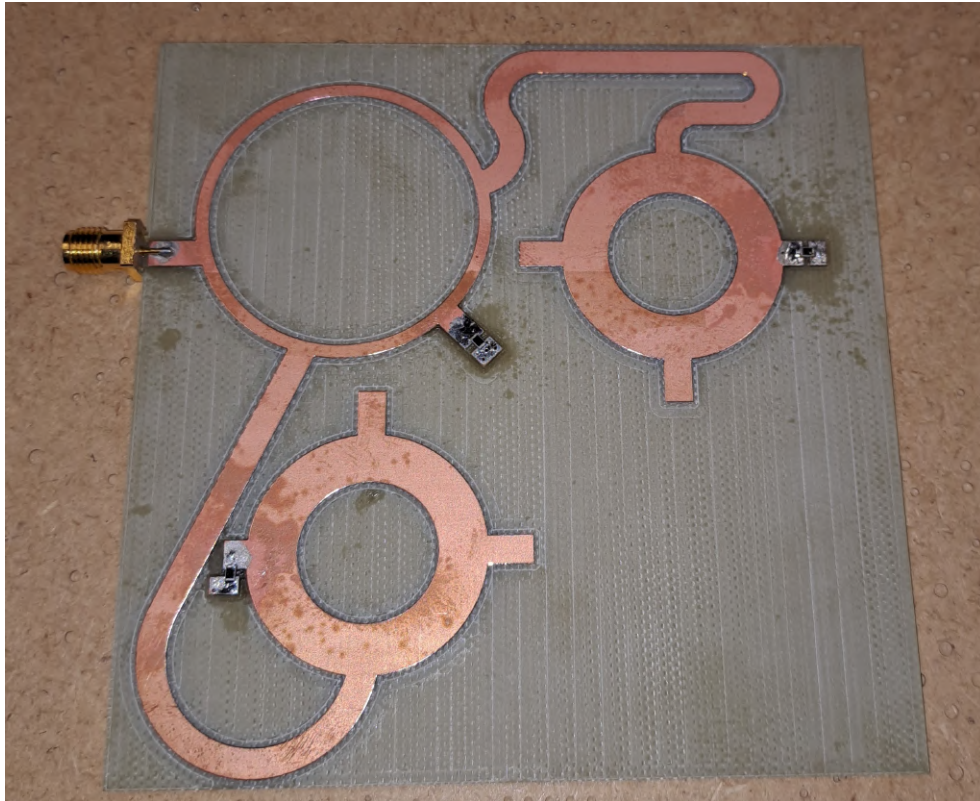


Figure 6.21: Antenna PCB

The feed network was manufactured in house at CPUT and consists of FR4 PCB material, which has been through hole plated, three 50 ohm resistors and an edge mounted SMA jack, which are soldered onto the board. Once the board was manufactured, the antenna system was mounted onto the board. To avoid any adverse effects, the antenna was mounted on the board using a basic setup. Instead of using screws, the antenna was mounted to the board using epoxy, as shown in Figure 6.22.

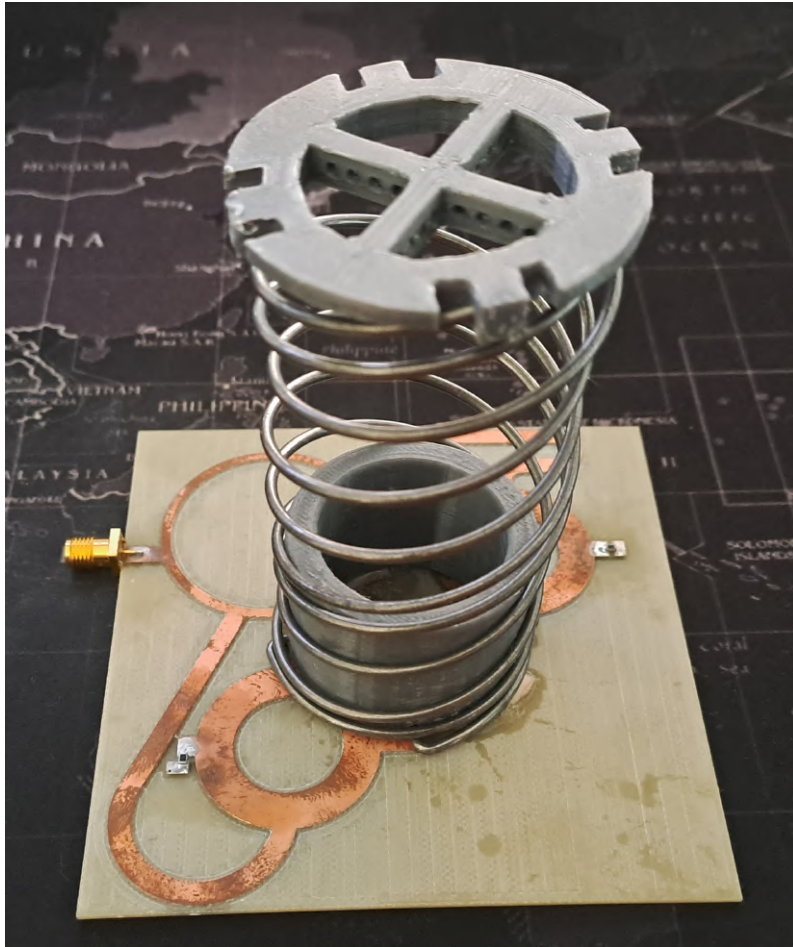


Figure 6.22: Antenna Mounted PCB

Once the epoxy cured, the antenna system was tested using the vector network analyser (VNA) at CPUT's laboratory. The antenna and PCB was connected to the VNA, where it was then calibrated to account for any interferences caused by the network cable. Once calibrated, the S11 reflection test was conducted.

Once the test was completed, results were exported and plotted against the simulated values in MatLab. Figure 6.23, shows simulated versus actual S11 Reflection coefficient results.

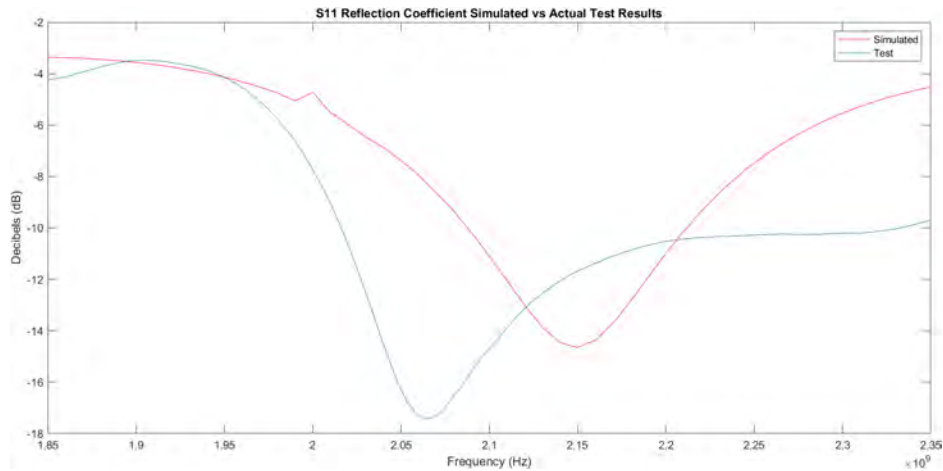


Figure 6.23: VNA S11 Reflection Coefficient Actual Versus Simulation Results

Comparing the physical, electromagnetic test to the simulated results does show a discrepancy in terms of centre frequency and reflection coefficient (which relates to electrical matching of the antenna to the driving circuit). The simulated results show that the antenna should have a reflection coefficient of approximately -14.5 dB around the designed centre frequency of 2.15 GHz. The test yields a reflection coefficient of approximately -12 dB at centre frequency of around 2.055 GHz. These differences can be ascribed to a few factors, such as the non-uniform form factor of the antenna and possible multiple contact points between the feed network and the antenna housing. The simulated model was simulated without the antenna housing, which will further contribute to the difference in results. However, overall the antenna, as it is, performs satisfactory and therefore passes the electrical testing phase.

## 6.4 Sine Wave Sweep and Random Vibration Test

Sine wave sweep and random vibration tests are conducted on a shaker table. While various companies within the local vicinity are capable of performing such tests, few are able to conduct the required test to the Soyuz launcher specifications as previously outlined.

Local companies that are able to conduct the tests to the required launcher specification, include Hensholdt and CubeSpace Satellite Systems. Unfortunately, due to time and budget constraints, neither of the above-mentioned companies was able to assist with the required vibration tests. Therefore, the tests were not conducted and the sine sweep and random vibration simulation results will be used to assess the overall integrity of the antenna deployment system when stressed to Soyuz launch provider specifications.

The simulation results suggest that the antenna system would be able to survive the launch environment, however, it is strongly recommended that the antenna

design be physically tested on a shaker table, before any use.

# Chapter 7

## Conclusion and Recommendations

### 7.1 Conclusion

The research project looked into the development of a CubeSat QHA system, which uses SMAs or traditional springs for the development of an antenna system, that could be deployed from the "tuna can" space of a CubeSat, while adhering to CubeSat standards. CDS and ECSS design philosophies were considered and adhered to during the design, development, and testing process.

The advantages of QHA's, especially compared to patch antennas were established. It was determined that QHA's offer wider beam patterns, with higher gain compared to patch antennas, as well as isoflux radiation patterns (if long enough), allowing for the transmission of a signal on all planes. This provides, a significant advantage over patch antennas, which have to be pointed directly at the ground station for communication purposes.

Various materials were considered and assessed for the construction of the QHA and the antenna housing. For the SMA approach, widely used Nitinol wire was procured and tested. SMA test results showed promise but unfortunately fell short, due to the change in form factor recorded as a result of cooling, which could be detrimental to communications payload. Multiple spring steels were considered for the traditional spring approach. A design matrix assessment showed that of these steels, piano wire or ASTM A228 provided the best qualities in terms of strength and availability for the research. Furthermore, a design matrix assessed various plastics, such as PLA, PETG, Acetal, etc. for use as a part of the QHA structure. The research showed through the design matrix, that Acetal was the most robust plastic of the available options.

Methodologies for the design and testing of the prototype were established. Methodologies were implemented with ECSS design philosophy (where applicable) and were implemented for mechanical design, simulation, and physical testing. Simulations were conducted to characterise the compression of the spring into the "tuna

can” space, as well as how well the QHA system survived the thermal and launch environments. Spring compression simulations showed promising results and confirmed hand calculations, stating that the QHA spring could be compressed within the ”tuna can” space and not exceed the torsional stress limits of the piano wire. Launch simulations exposed the QHA system to modal analysis, static and quasi-static loading, sine wave sweep, and random vibrations. The launch simulations showed promising results. The modal analysis, sine wave sweep, and random vibration simulations confirmed that the first mode of the antenna system occurs at approximately 71 Hz, which is above the required minimum of 40 Hz for the Soyuz launcher and therefore complies with ECSS standards. Furthermore, sine wave sweep and random vibration results showed that the antenna system survived the launch environment when exposed to Soyuz launch provider excitations.

The SMA approach was tested through the use of a kiln for shape setting, whereby Nitinol wires were constrained to bolts and shape trained at different temperatures over varying amounts of time. The SMAs were then exposed to additional testing, where activation temperatures were recorded by observation, with the use of a conventional house oven. Tests showed that as the wire cooled, it started to lose its shape, making it undesirable for the QHA design.

The traditional spring approach was tested through a deployment jig, where various iterations of thick and thinner wire, as well as staged and non-staged approaches, were tested. Deployment tests were criticised with a reliability assessment, which took into account deployed form factor, how controlled the deployment was, ease of stowing, and deployed height. Excessive forces were experienced in the deployment of the thicker 1.91 mm wire when the non-staged deployment was tested. This resulted in an unsafe design and alternatives were explored, using thinner wire diameters of 1.6 mm and 1.1 mm. Test results showed promising results for the thinner wire iterations in terms of deployment forces, however, the form factor of the thinner wires, due to tolerance issues, resulted in an infeasible design. The 1.91 mm wire was then tested with staged deployment, which resulted in a design, which effectively mitigated the stored energy of the spring. Therefore, the antenna was reliably deployed to its height of 88.7 mm, with a helix diameter of 42 mm and a form factor that could be attributed to that of a QHA.

Following deployment tests, the antenna system was subjected to electrical and thermal tests. Electrical tests were conducted by CPUT’s engineering team and consisted of an S11 reflection coefficient test, to determine how well the antenna radiates a signal at a particular frequency. Test results showed, that at the desired QHA centre frequency a reflection coefficient of -12dB was recorded, which is satisfactory for the research project. Therefore, the QHA system will work at the required frequency of 2.15 GHz. Thermal cycling tests were conducted with a representative model, which used PETG in place of acetal. Qualification tests showed that the antenna system showed slight signs of warping when exposed to temperatures between  $-25^{\circ}\text{C}$  and  $72^{\circ}\text{C}$ . This is promising as acetal has a higher service temperature of  $110^{\circ}\text{C}$ , compared to PETG’s  $80^{\circ}\text{C}$ . Therefore, the design was deemed feasible and able to survive thermal environmental tests. Sine wave sweep and random vibration tests were not conducted due to time and budget constraints.

The research looked into CubeSat design philosophy, as described by the CDS. The CDS was followed for general, mechanical, and electrical requirements, that needed to be adhered to for CubeSat design. CubeSat "tuna can" dimensions and CubeSat form factors were followed, based on the CDS dimensions. ESA's ECSS and NASA's GEVS, were explored for the design of the QHA payload. The research showed, that the ECSS and GEVS design philosophies were very similar. However, due to the fact that FSATI follows ECSS guidelines, ECSS payload design philosophies were adhered to for the design of the QHA. ECSS design philosophies follow an iterative design process, with multiple design reviews, to fully scrutinise designs for the most effective outcome. Following the ECSS guidelines, a QHA spring-like antenna design was established, prototyped, and tested.

The reliable deployment of the QHA system was established. For the QHA to have been reliably deployed it would need to keep its form factor, have the correct deployed height (approximately 88.7 mm), have a controlled deployment, and be relatively easy to stow. These parameters were assessed through a reliability assessment, that took into account the form factor, deployment height, ease of deployment, and ease of stowing. Antenna iterations were tested and results were recorded. Tests showed that the staged 1.91mm antenna iteration posed the best workable solution for deploying the antenna system.

Various design limits of the QHA system were established. Design limits implemented were based on locally available materials, space materials database outgassing data, ECSS and CDS CubeSat and payload design philosophy, design stresses, resonance limitations, manufacturing limitations, the thermal environment and deployment forces were considered. Only locally sourced materials were considered for the construction of the QHA system. From locally available materials, acetal was selected for the QHA housing, while ASTM A228 was selected for the antenna filars. CVCM and TML limits were considered during material selection to comply with outgassing requirements.

CDS guidelines were considered for defining the available space and form factor of the QHA extra volume, known as the "tuna can", which limited the overall allowable compressed height of the QHA system, as well as its diameter. ECSS design limits were explored, requiring designed payloads, to have a FOS of 1.5. In circumstances where this is not achievable the design would need to be proven to reliably and safely work, as is the case with the QHA. Maximum torsional and tensile stresses of materials had to be considered to design a safe and reliable QHA system that complies with ECSS guidelines.

Launch provider limitations were also considered due to the possibility of resonance as a result of the rocket, which would transport the payload to space, should it be flown. Launch provider specifications were established based on Soyuz rocket specifications, which required the first mode of the payload to be above 40 Hz, which the QHA design complied with. Spring manufacturing limitations were considered due to the high spring indexes associated with the antenna designs. The higher the spring index, the harder it is to keep tolerances during spring manufacturing. Filars with a spring index greater than 25, showed very poor form factors, however, re-



sulted in lower spring deployment forces. The thermal environment was established through Space Systems Thermal simulations and thermal equilibrium calculations. Simulations and calculations were scrutinised were applicable, by physical testing of the representative prototype, which culminated in satisfactory results. Deployment forces were considered, which ultimately led to a design, which mitigated deployment forces through staged deployment.

Therefore, the research showed that a QHA system could be reliably deployed and mechanically tested by following CDS and ECSS CubeSat standards, which limited the overall design. Following these guidelines, it was shown that the QHA could be reliably designed, deployed, and tested as a spring-like system. By testing different wire diameters and deployment system iterations, a process to reliably deploy the S-band QHA was established. This process implemented staged burn wires to stage the deployment of the antenna system, thus limiting the reaction force of the antenna being deployed, making its safer and more reliable to deploy with the required form factor.

Overall, the research aimed to create a robust QHA system, which conforms to CubeSat standards and can be mechanically implemented and tested for use on a CubeSat. The research shows that through simulations and tests (except for vibration tests), a QHA system can survive the launch and space environment while being stowed and deployed from the confines of the "tuna can" space. A reliability assessment was implemented and showed that the QHA could be reliably deployed from the "tuna can" space. A validation and test process was implemented, where calculations were validated through simulations and simulations were validated by tests, where applicable. Overall, an iterative design methodology was implemented to mitigate risks and push for a reliable design, that safely deploys the antenna.

In conclusion, all research questions were answered, and all research objectives were satisfied, except for vibration testing (due to budget and time constraints). Therefore, a mechanically implemented robust QHA system can be reliably stowed and deployed from the "tuna can" space, while surviving the launch and space environment, so that the CubeSat space can be more efficiently optimised.

## 7.2 Recommendations

Various recommendations can be made to improve the overall design of the antenna deployment system. Firstly, the spring filars used were not completely identical. It can be very hard to achieve tolerances on spring-like elements, especially when the spring index is fairly high. Therefore, for future work, it is recommended that a methodology and process be created for producing near identical spring-like filars. This will help in the stowing and deployment of the antenna, but will also improve the electrical characteristics of the antenna so that it aligns more with simulated results.

Another avenue that can be explored for future work is the characterisation of

Nitinol. Finding material data sheets for Nitinol is extremely challenging, especially if looking for material data of specific compositions. Furthermore, finding meaningful data of the shape setting temperature and training durations of specific Nitinol compositions and wire thickness seems to be non-existent. The literature suggested that training duration and temperature be determined per specimen, which can be difficult to accomplish with a limited supply.

Another avenue to be explored thoroughly is designing the antenna with the use of larger Nitinol wire sizes. The project looked into how available material could be used to construct the antenna. Results showed that the available wire was too thin to hold its shape once cooled. For future work, different wire thicknesses can be trained and examined for space-bound antenna solutions. A Nitinol antenna essentially eliminates the need for a deployment mechanism, as only heat is required to deploy the antenna.

Furthermore, additional Nitinol compositions could be tested. Changing the composition of the Nitinol used affects the activation temperatures. Experimenting with different Nitinol compositions may result in a Nitinol antenna, which does not require excessive power from the CubeSat battery to deploy the antenna.

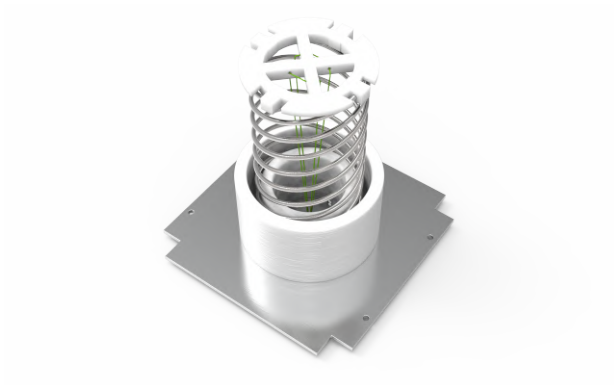
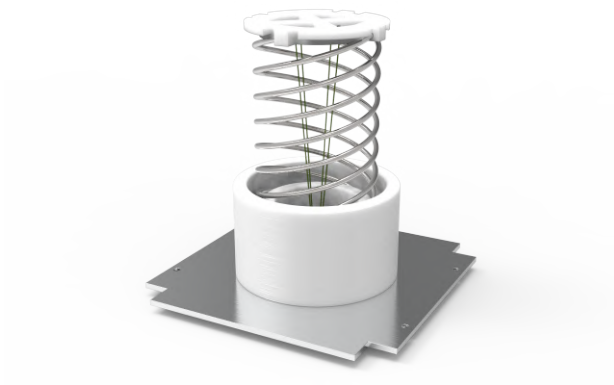
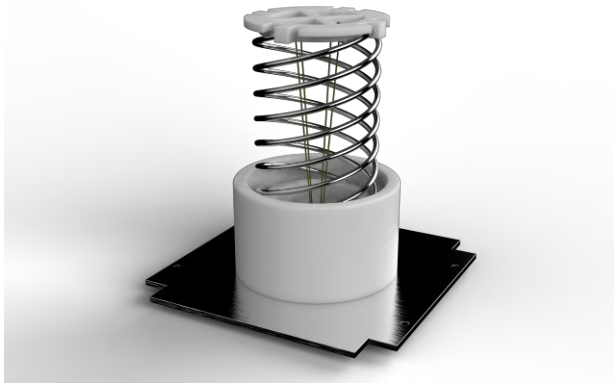
It is strongly recommended that sine wave sweep and random vibrations tests on a shaker be performed on the actual prototype, before any use. The tests will depict a more accurate scenario of how the antenna system copes with the stresses induced during launch, as opposed to the simulations. Tests and simulations can then also be compared, to determine and discuss discrepancies between results.

Accuracy between simulation models and test models could be improved. Simulation models consisted of simplified geometry, parts, and elements, especially when compared to the actual parts used for testing. This caused slight differences in results and caused unseen errors, such as those experienced in the top brace and spring guiding wall designs, which resulted in design changes.

A study into the effects 3D printing has on materials regarding temperature analysis could be studied. During testing, PETG filament, 3D printed parts experienced warping below its maximum service temperature. This could be due to how layers are deposited on 3D prints, or possibly due to unseen particles interfering with the 3D printed layers. A study into this could produce more accurate maximum temperature values, or rather prove that the temperature variation depends on the 3D printer used.

Finally, alternative deployment solutions could be explored. During testing, releasing the antenna without cutting or burning the burn wire, while on the deployment jig led, to slower and more controlled deployments. This is most likely due to that the jig is able to convert some linear stored energy into rotational energy. As a result, the antenna unwinds itself as it deploys, as opposed to a sudden release.





# Chapter 8

## Bibliography

- Arianespace (2011), Ariane 5 User's Manual, Technical Report 5.
- Bhavikatti, S. (2005), *Finite element analysis.*, New Age International P Ltd., Publishers., New Delhi.
- Buehler, W., Gilfrich, J. and Wiley, R. (1963), 'Effects of low-temperature phase changes in the mechanical properties of alloys near composition TiNi', *Journal of Applied Physics* **34**, 1475.
- Case, L. (2004), 'Shape Memory Alloy Shape Training Tutorial', *Transformation* pp. 8–13.
- Chen, Z. (2018), 'Universal CubeSat Platform Design Technique', *2018 2nd International Conference on Mechanical, Material and Aerospace Engineering (2MAE 2018)* **179**, 1–6.
- Costantine, J., Tawk, Y., Sakovsky, M., Olsen, G., Pellegrino, S. and Christodoulou, C. G. (2016), 'UHF Deployable Helical Antennas for CubeSats', *IEEE Transactions on Antennas and Propagation* **64**(9), 3752–3759.
- Drotzky, J., ed. (1984), *Strength of Materials for Technicians*, Butterworth-Heinemann.
- ECSS (2013), *ECSS-E-HB-32-26A, Space engineering Spacecraft mechanical loads analysis handbook*, 1 edn, ESA Requirements and Standards Division, Noordwijk, The Netherlands.  
**URL:** <https://ecss.nl/hbstms/ecss-e-hb-32-26a-spacecraft-mechanical-loads-analysis-handbook/>
- ESA (2018), 'Isoflux antenna coverage'. [Accessed 9/09/2020].  
**URL:** <https://www.esa.int/ESAMultimedia/Images/2018/11/Isofluxantennacoverage>
- Fortescue, P., Stark, J. and Swinerd, G. (2011), *Spacecraft Systems Engineering*, fourth edition edn, Wiley, Chichester.
- Fraseer, H. (2010), Parametrisation and Design of Quadrifilar Helices for use in S-band Satellite Communications, Master's thesis, University of the Witwatersrand.
- Gilmore, D. G. and Donabedian, M. (2002), *Spacecraft thermal control handbook*, Vol. 1, AIAA.
- Goodship, V. (2004), *ARBURG Practical Guide to Injection Moulding*, Smithers Rapra. [Accessed 10/11/2021].  
**URL:** <https://library-books24x7-com.libproxy.cput.ac.za/toc.aspx?bookid=28299>
- Hartl, D. J. and Lagoudas, D. C. (2007), 'Aerospace applications of shape memory alloys', *Proceedings of the Institution of Mechanical Engineers, Part G: Journal of Aerospace Engineering* **221**(4), 535–552.

- HCT (2020), ‘HCT 400 or 437MHz Heritage UHF QHA’. [Accessed 30/10/2020].  
**URL:** <https://www.helicomtech.com/helios-deployable-antenna>
- Herring, D. H. (2010), ‘Heat Treatment of Nitinol Alloys (Part 1)’. [Accessed 29/10/2020].  
**URL:** <https://www.industrialheating.com/blogs/14-industrial-heating-experts-speak-blog/post/88984-heat-treatment-of-nitinol-alloys-part-1>
- Imbriale, W. A., Gao, S. and Boccia, L. (2008), *Space Antenna Handbook*, first edition edn, John Wiley & Sons. <https://doi.org/10.1002/9781119945147>.
- Ippolito, L. (2008), *Satellite Communications Systems Engineering: Atmospheric Effects, Satellite Link Design and System Performance*, John Wiley & Sons. © 2008.
- Johnson-Matthey (2015), ‘Nitinol Technical Properties’, *Johnson Matthey Medical Components* pp. 1–2. [Accessed 30/10/2020].  
**URL:** <https://matthey.com/en/products-and-services/medical-components/resource-library/nitinol-technical-properties>
- Johnson Matthey (2021), ‘Nitinol shape setting’. [Accessed 23/08/2021].  
**URL:** <https://matthey.com/en/products-and-services/medical-components/resource-library/nitinol-shape-setting>
- Kriedte, W. and El Gammal, Y. (1995), ‘A New Approach to European Space Standards’, *ESA Bulletin* (2).
- Kumar, K., Ranjan, K. and Paulo Davim, J. (2020), *Five Axis CNC Machines*, Springer International Publishing, Cham.  
**URL:** <https://doi.org/10.1007/978-3-030-41279-1-7>
- Lagoudas, D. C., A, A. and B, B. (2008), *Shape Memory Alloys Modeling and Engineering Applications*, Springer, New York, New York.
- Lips, T. and Fritsche, B. (2005), A comparison of commonly used re-entry analysis tools, in ‘Acta Astronautica’, Vol. 57.
- Longela, M. S. (2013), The development of an artificial hand using nickel-titanium as actuators., Master’s thesis, Cape Peninsula University of Technology.
- Ma, J., Huang, H. and Huang, J. (2013), ‘Characteristics analysis and testing of SMA spring actuator’, *Advances in Materials Science and Engineering* **1**, 1–4.
- Mejía-Kaiser, M. (2020), IADC Space Debris Mitigation Guidelines, in ‘The Geostationary Ring’.
- Munakata, R., Lee, S., Hutputanasin, A., Toorian, A., Lan, W., Carnahan, J., Pignatelli, D. and Mehrparvar, A. (2009), ‘Cubesat design specification rev. 13’, *The CubeSat Program, California Polytechnic State ...* **8651**.
- Najah Saud Al-Humairi, S. (2019), ‘Cu-Based Shape Memory Alloys: Modified Structures and Their Related Properties’, *Recent Advancements in the Metallurgical Engineering and Electrodeposition. IntechOpen* p. 5.
- Olsen, G., Pellegrino, S., Banik, J. and Costantine, J. (2018), ‘Deployable Helical Antennas for CubeSats’, *American Institute of Aeronautics and Astronautics* pp. 1–14. <https://authors.library.caltech.edu/42601/1/DeployableHelicalAntennaforCubeSatsFinal.pdf>.
- Otsuka, K. and Wayman, C. (1999), *Shape Memory Materials*, Cambridge University Press, Cambridge.
- Raiesh, G., Swetha, C., Privanka, R. and Vaishnavi, R. (2017), ‘Congestion Control in 6Lo WPAN Networks using Fuzzy Logic (FLCC)’, *2017 Ninth International Conference on Advanced Computing (ICoAC)* pp. 369–374.

Sanusi, K. O., Ayodele, O. L. and Khan, M. T. E. (2014), 'A concise review of the applications of NiTi shape-memory alloys in composite materials', *South African Journal of Science* **110(7-8)**, 22-26.

Shigley, J. and Mischke, C. R. (1996), *Standard Handbook of Machine Design Second Edition*, 2 edn, McGraw-Hill, New York.

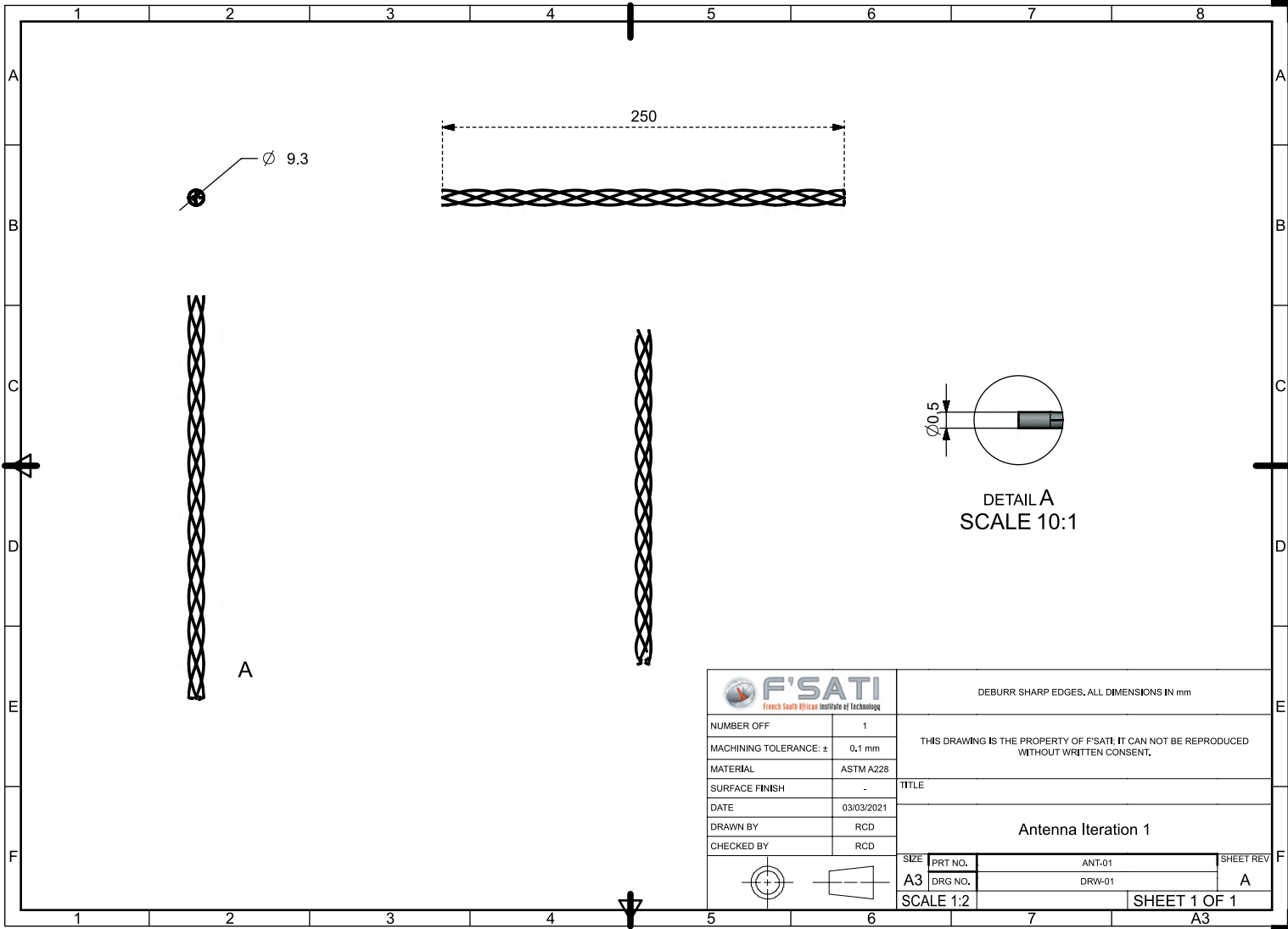
Weik, M. (2000), 'Circular Polarization', *Computer Science and Communications Dictionary* **34**, 210.


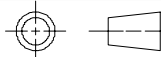
# A P P E N D I X



# Appendix A

## Antenna Dimensions and Simulations



 <b>F'SATI</b> <small>French South African Institute of Technology</small>		DEBURR SHARP EDGES, ALL DIMENSIONS IN mm			
NUMBER OFF	1	THIS DRAWING IS THE PROPERTY OF F'SATI. IT CAN NOT BE REPRODUCED WITHOUT WRITTEN CONSENT.			
MACHINING TOLERANCE: ±	0,1 mm				
MATERIAL	ASTM A228	TITLE			
SURFACE FINISH	-	<b>Antenna Iteration 1</b>			
DATE	03/03/2021				
DRAWN BY	RCD				
CHECKED BY	RCD				
		SIZE	PRT NO.	ANT-01	SHEET REV
		A3	DRG NO.	DRW-01	A
SCALE 1:2		SHEET 1 OF 1			
		A3			

# QHA\_Isoflux\_S\_Band\_rev2

---

*C:/Users/Gideon\_Wiid/Documents/CPUT\_Work/2021\_CPUT\_Postgraduate  
2021-03-08 14:43*

# QHA\_Isoflux\_S\_Band1

---

Total Gain [dBi]

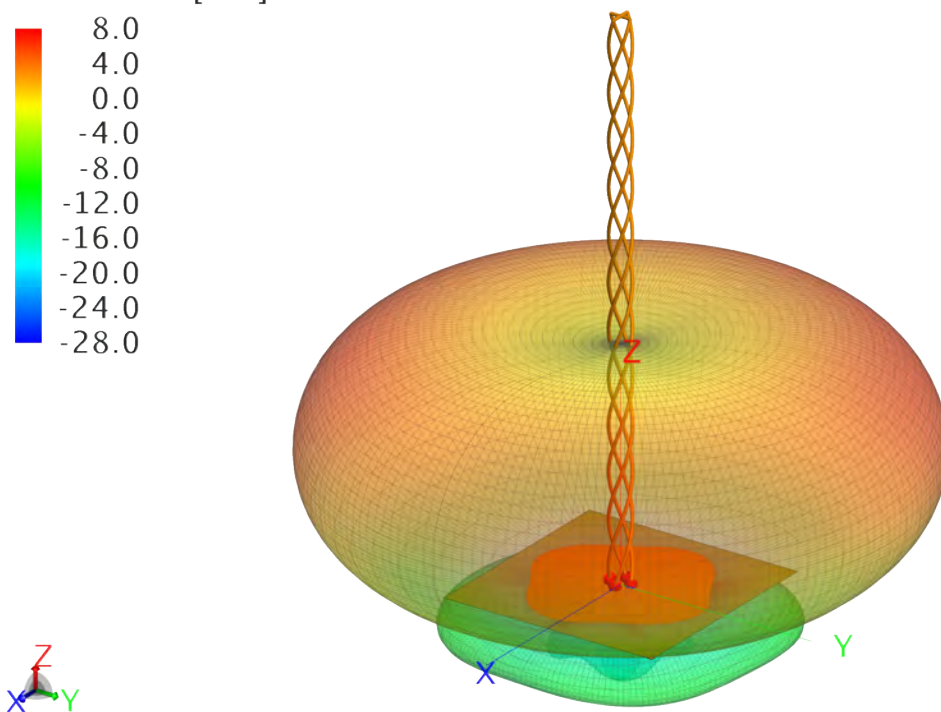
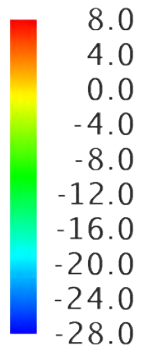


Figure 1: 3D View

# QHA\_Isoflux\_S\_Band\_rev21

---

Total Gain [dBi]

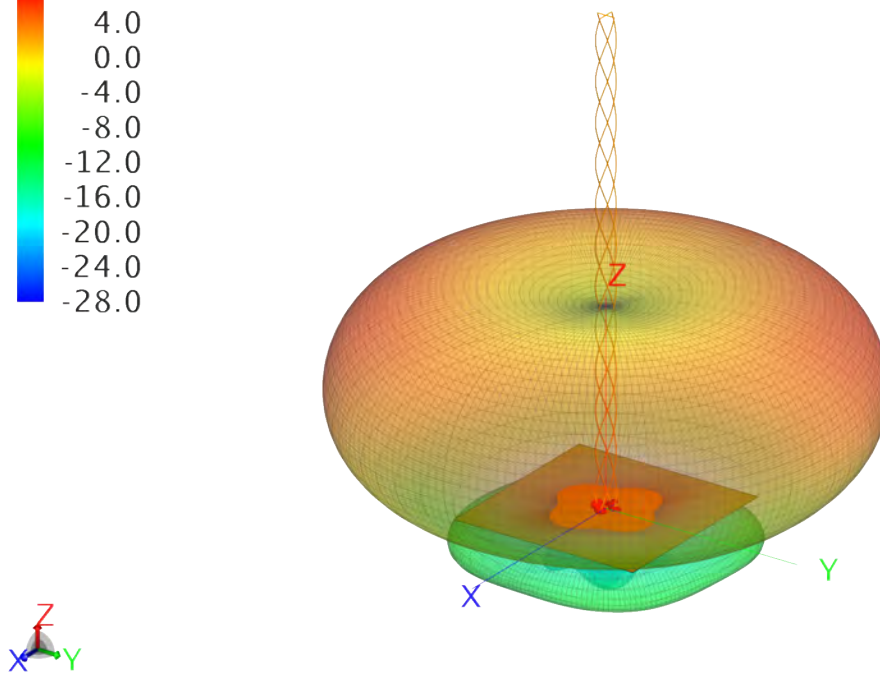
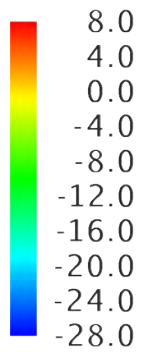


Figure 2: 3D View

## Port 1 of 4 - Reflection Coefficient

---

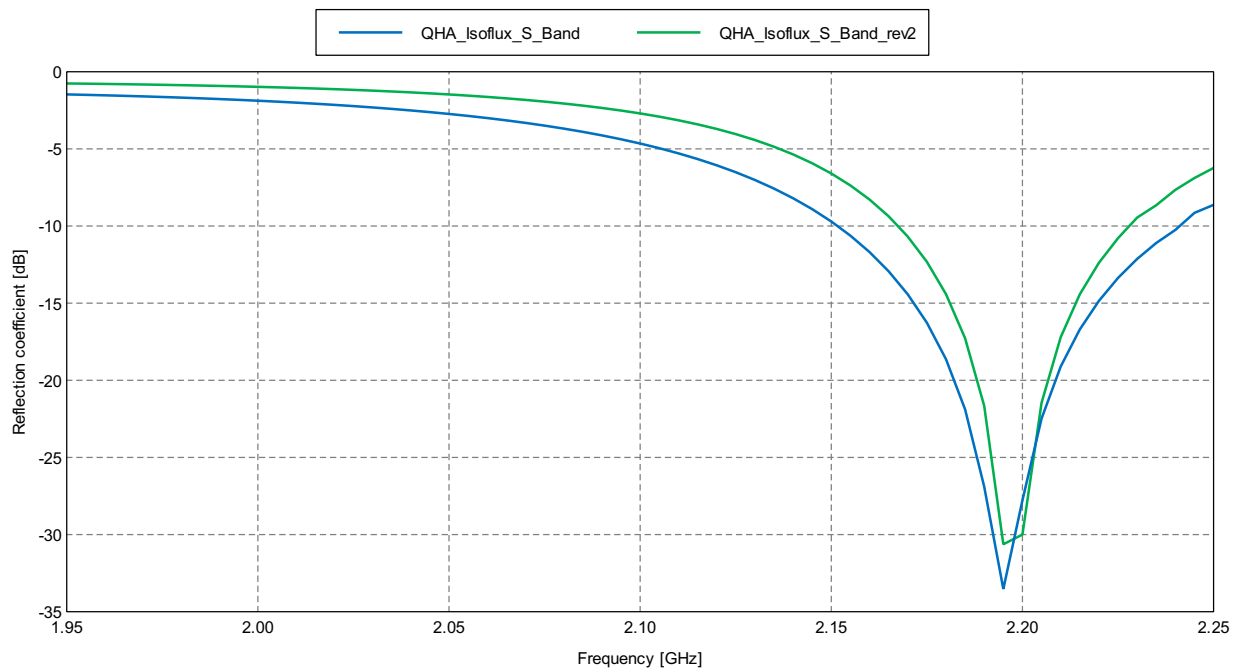


Figure 3: Reflection coefficient Magnitude

## Port 1 of 4 - Impedance

---

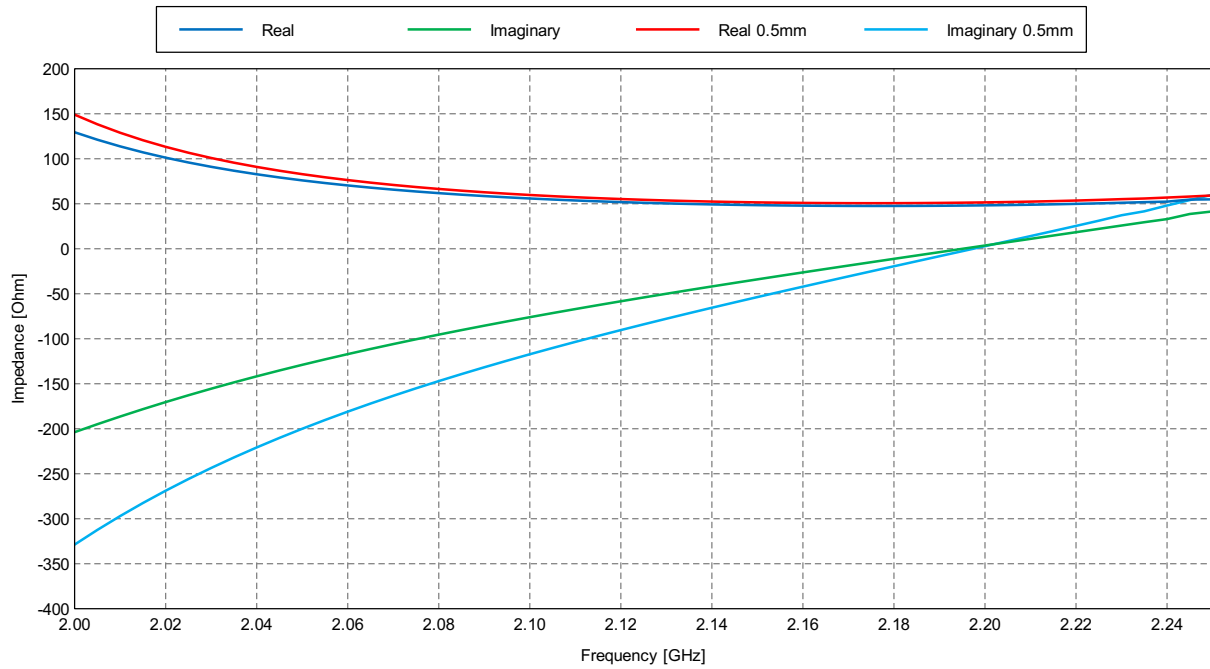


Figure 4: Impedance

## Far Field Total Gain Polar Plot

---

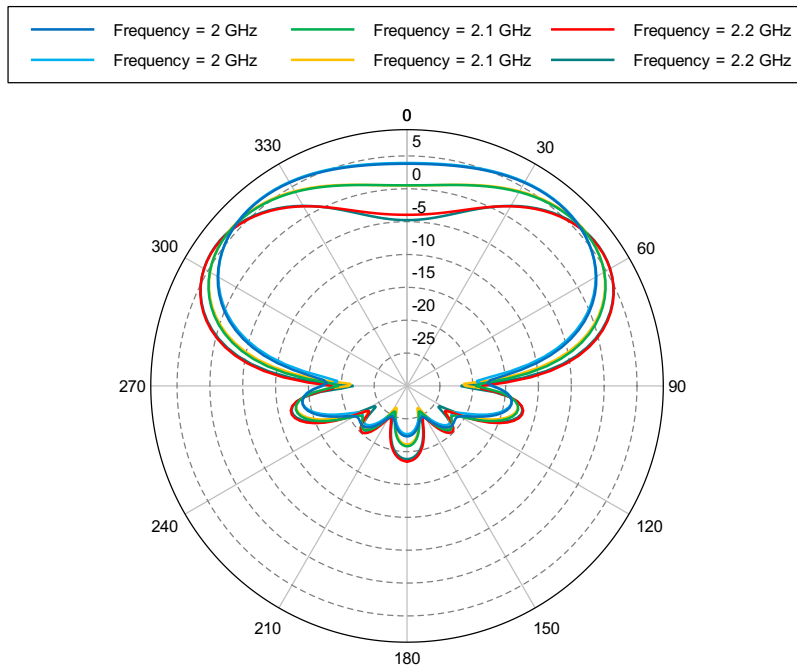


Figure 5: Total Gain (Phi = 0 deg)



## Far Field Total Gain

---

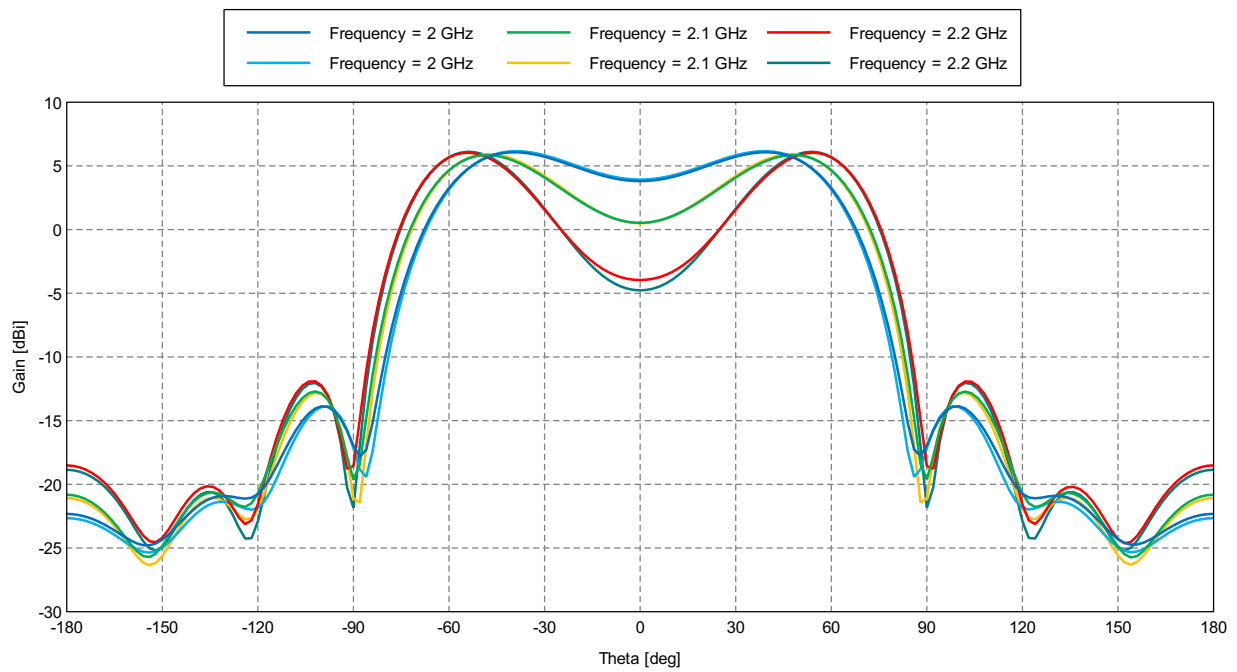


Figure 6: Total Gain (Phi = 0 deg)

## Far Field Total Gain - Zoomed In

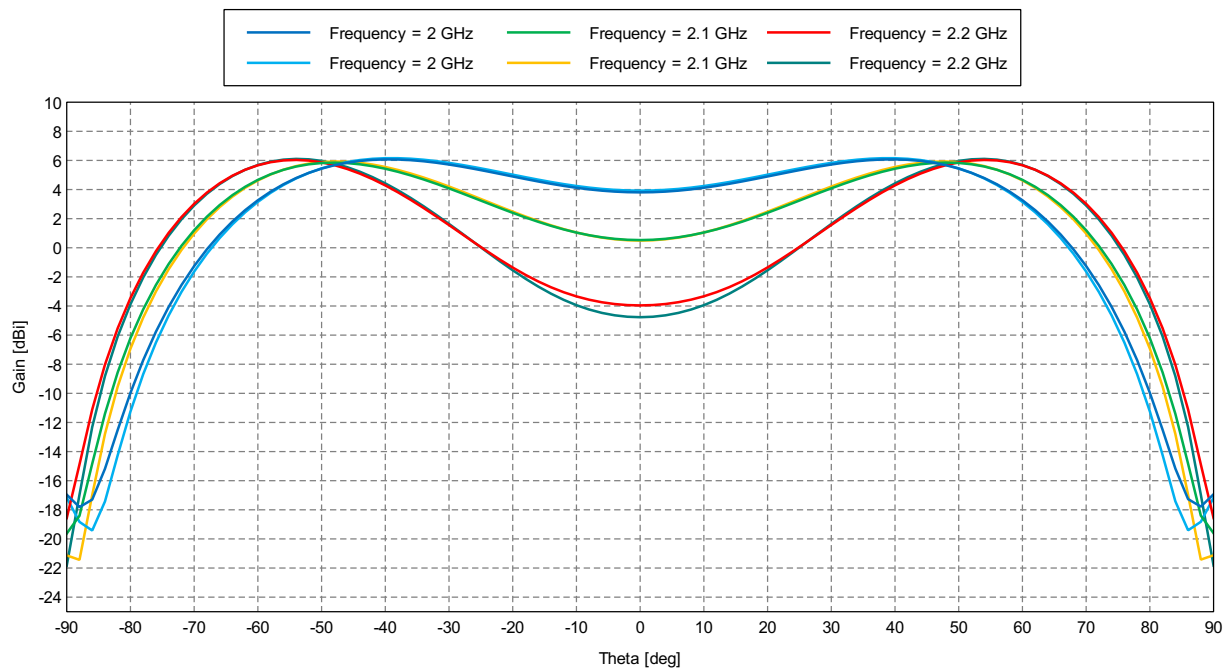


Figure 7: Total Gain (Phi = 0 deg)

# Axial Ratio

---

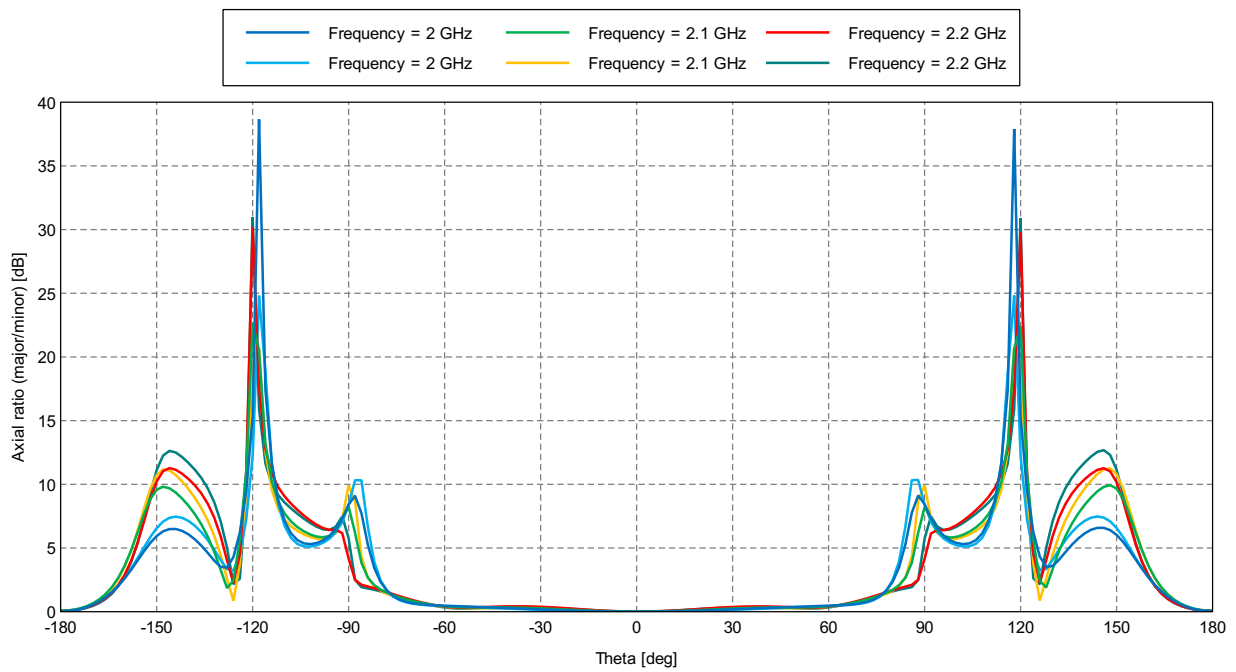


Figure 8: Axial ratio (major/minor) (Phi = 0 deg)

## Axial Ratio - Zoomed In

---

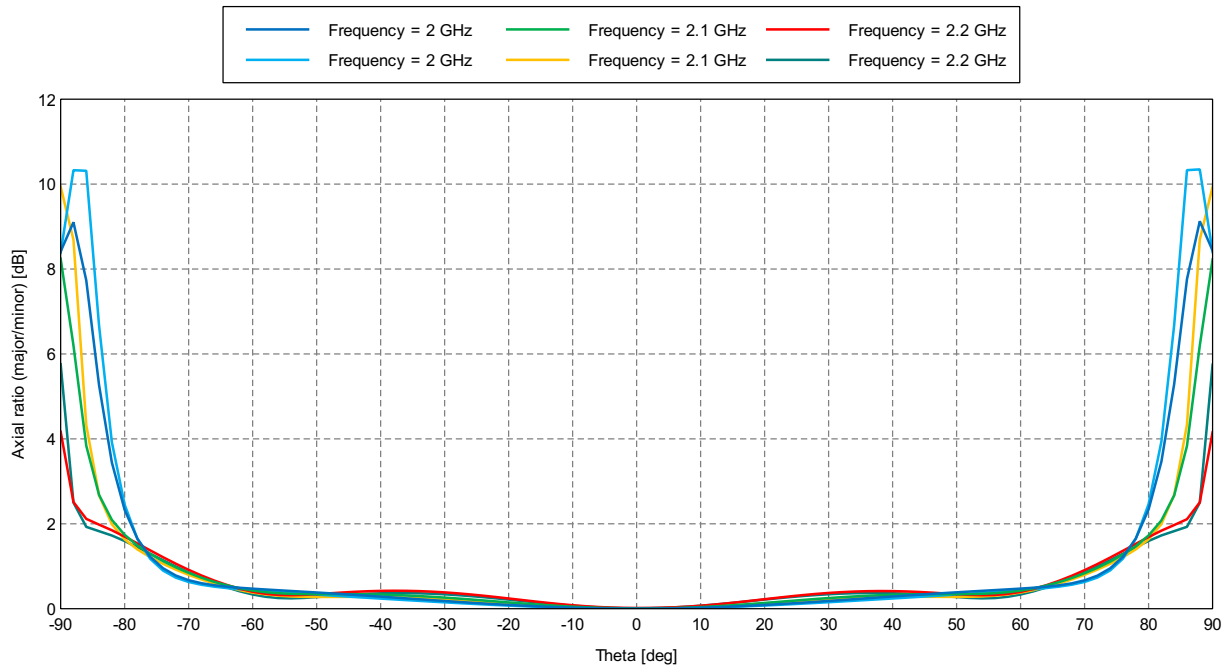
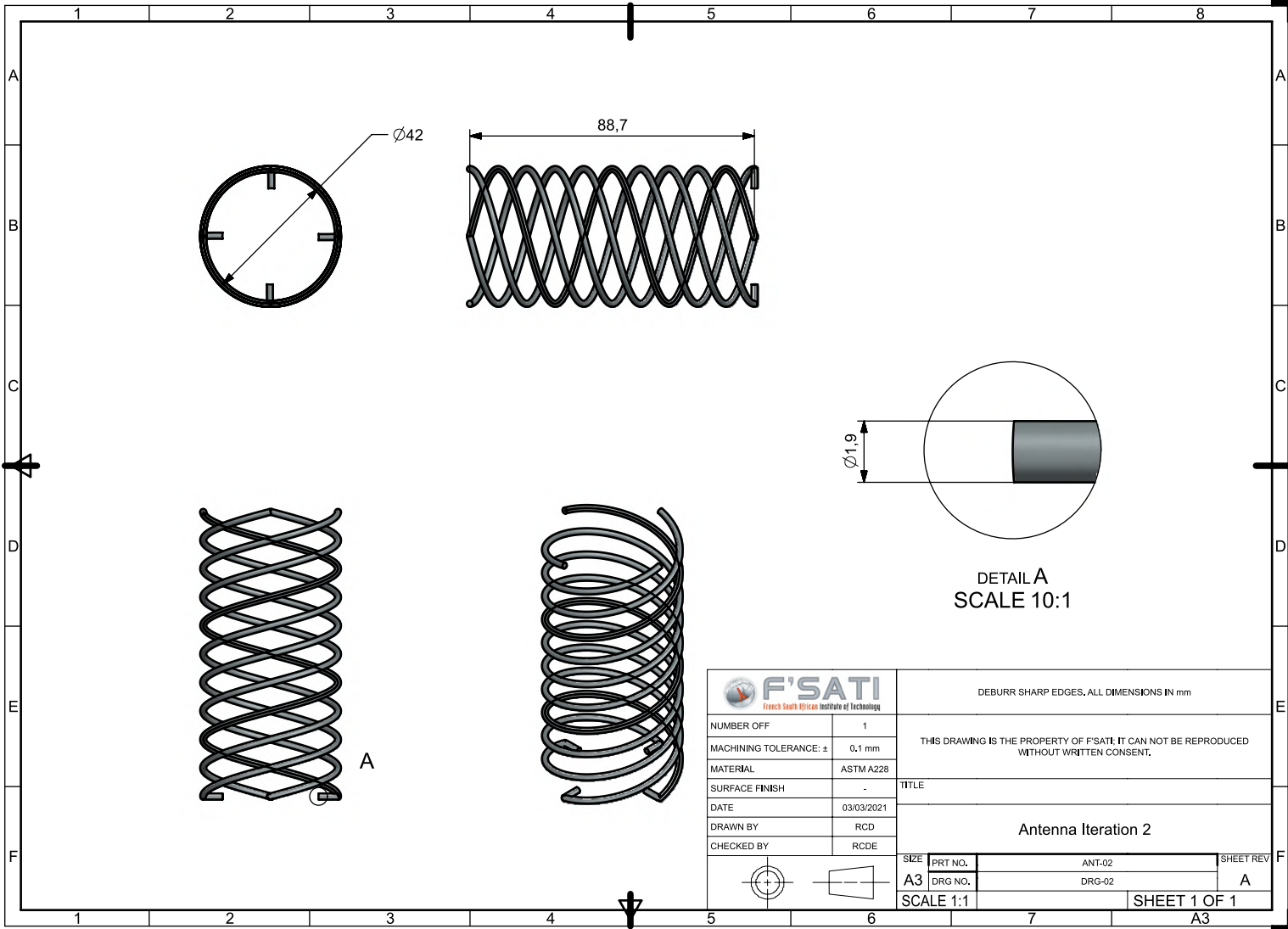

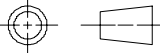


Figure 9: Axial ratio (major/minor) (Phi = 0 deg)



DETAIL A  
SCALE 10:1

 <b>F'SATI</b> <small>French South African Institute of Technology</small>		DEBURR SHARP EDGES, ALL DIMENSIONS IN mm			
NUMBER OFF	1	THIS DRAWING IS THE PROPERTY OF F'SATI. IT CAN NOT BE REPRODUCED WITHOUT WRITTEN CONSENT.			
MACHINING TOLERANCE: ±	0,1 mm				
MATERIAL	ASTM A228	TITLE			
SURFACE FINISH	-	<p style="text-align: center;"><b>Antenna Iteration 2</b></p>			
DATE	03/03/2021				
DRAWN BY	RCD				
CHECKED BY	RCDE				
		SIZE	PRT NO.	ANT-02	SHEET REV
		A3	DRG NO.	DRG-02	A
		SCALE 1:1			SHEET 1 OF 1
					A3

# QHA\_S\_Band\_Revised - 2.5 Turns 1.9 mm wire

---

*C:/Users/Gideon\_Wiid/Documents/CPUT\_Work/2021\_CPUT\_Postgraduate/  
2021\_CPUT\_Advisory\_Robert\_Daniels\_Deployable\_Helix\_Antenna\_CubeSat  
2021-06-15 12:25*

## QHA 3D Gain Pattern 2.2 GHz

---

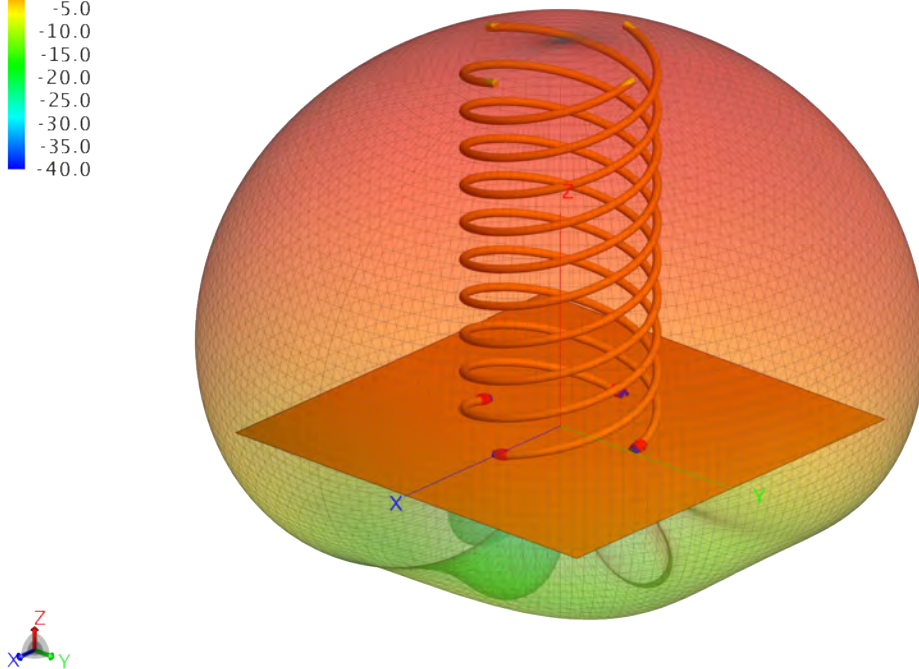
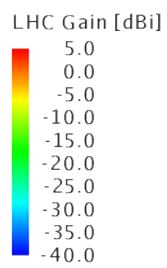


Figure 1: 3D Gain Pattern 2.2 GHz

## Reflection coefficient

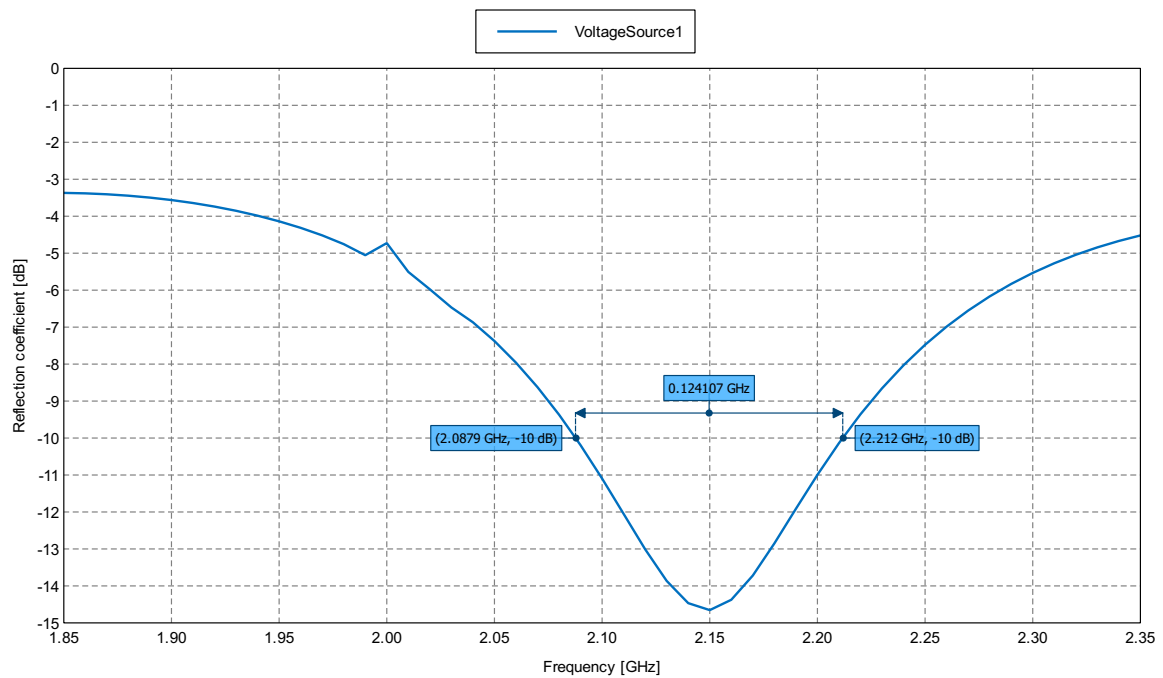


Figure 2: Reflection coefficient Magnitude [dB] - QHA\_S\_Band\_rev2



# Far Field Gain

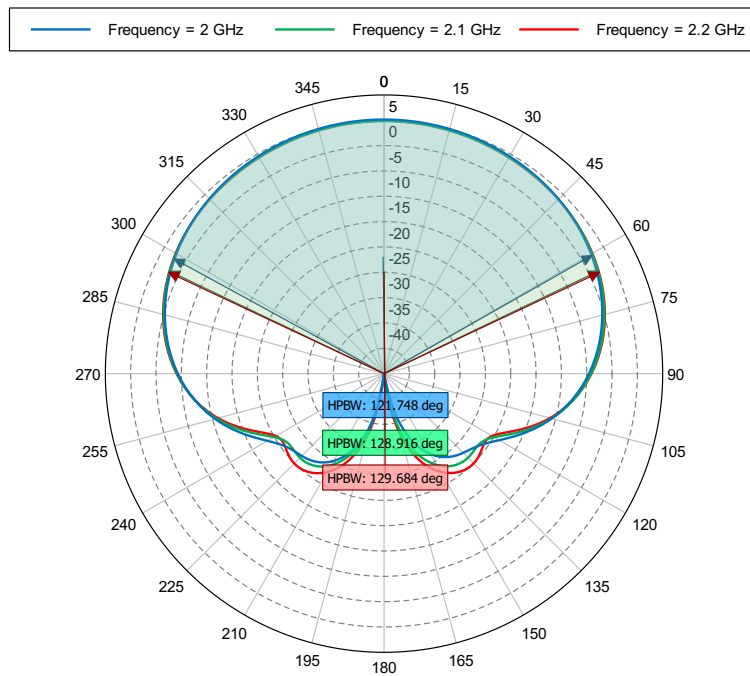


Figure 3: LHC Gain (Phi = 0 deg) - QHA\_S\_Band\_rev2

# Far Field Gain

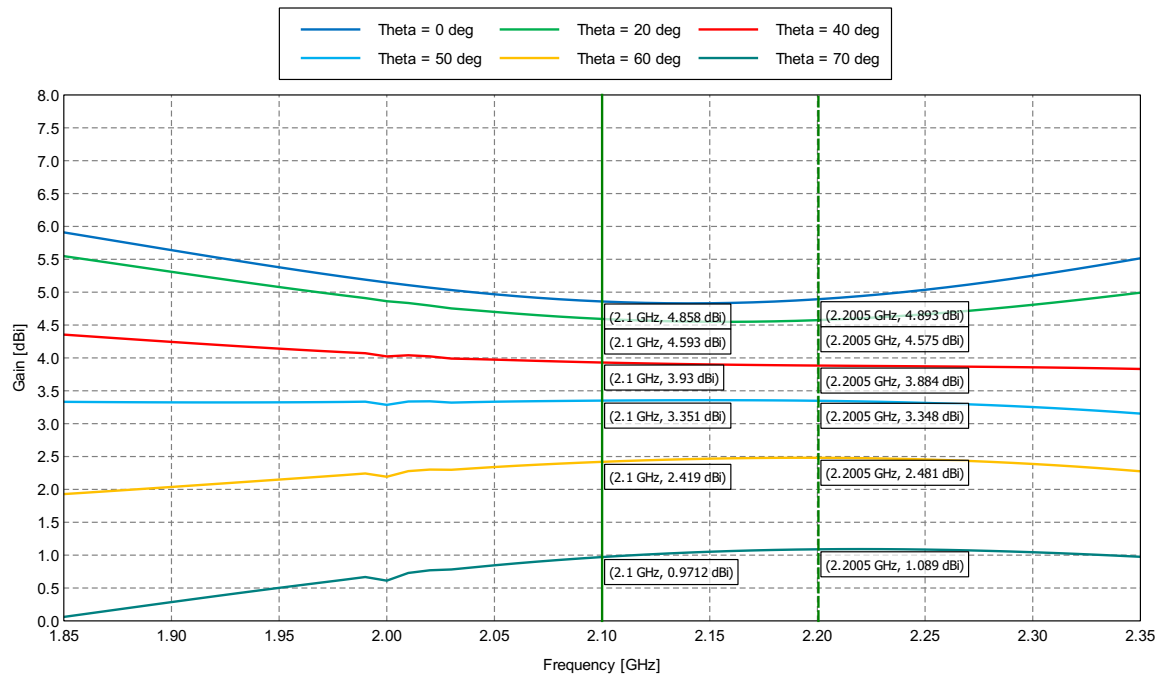


Figure 4: LHC Gain (Phi = 0 deg) - QHA\_S\_Band\_rev2

# Axial Ratio

---

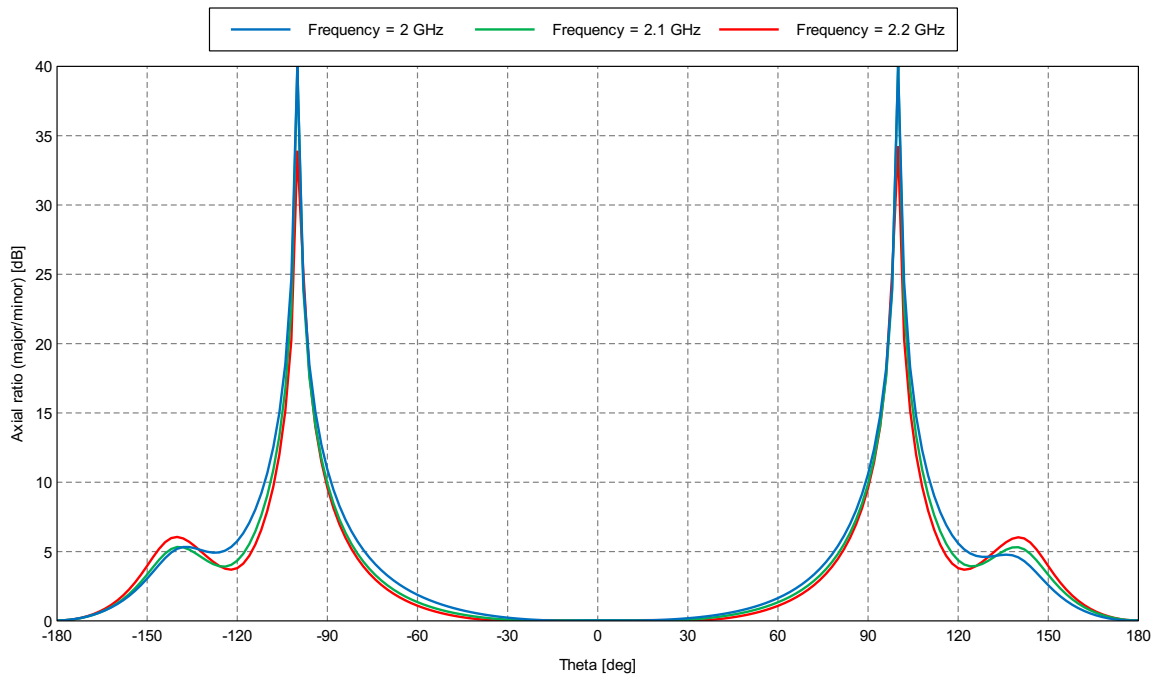


Figure 5: Axial ratio (major/minor) (Phi = 0 deg) - QHA\_S\_Band\_rev2

## Axial Ratio Zoomed

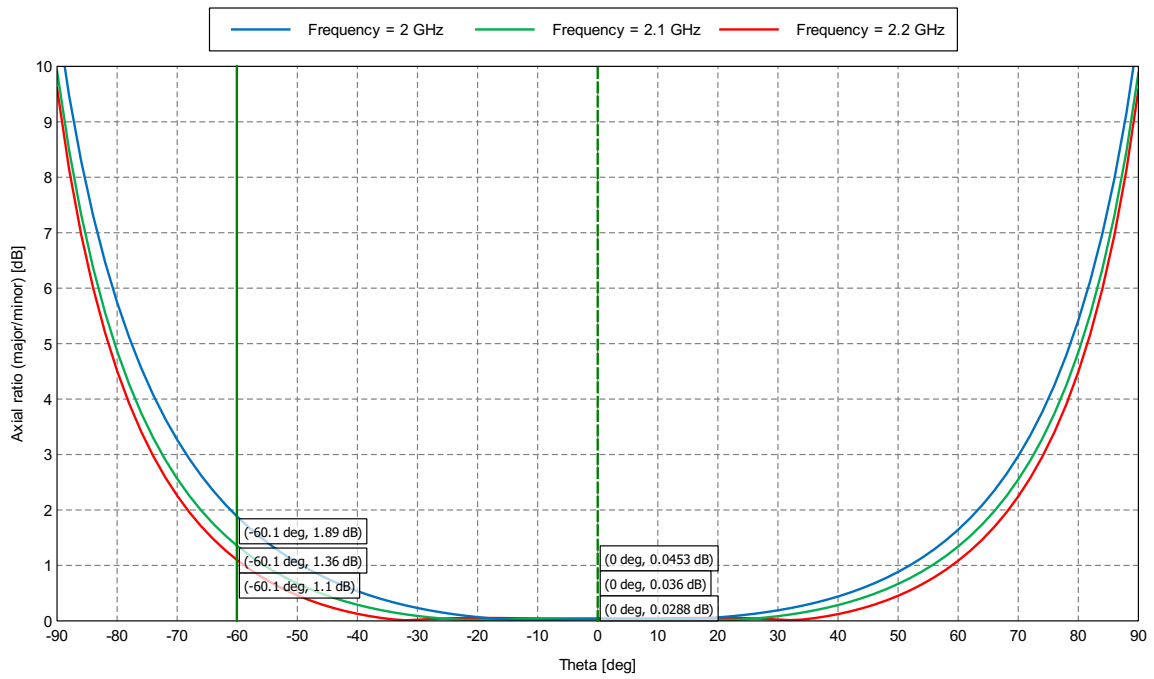


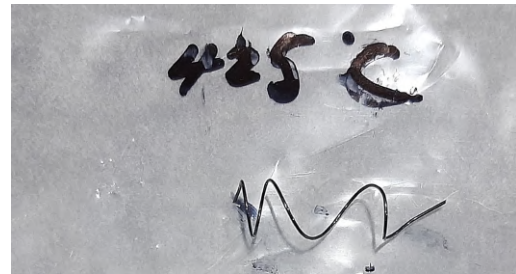
Figure 6: Axial ratio (major/minor) (Phi = 0 deg) - QHA\_S\_Band\_rev2

# Appendix B

## Nitinol Specimen Testing



Trained 1



Trained 2

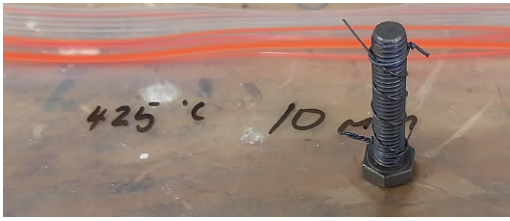


Elongated

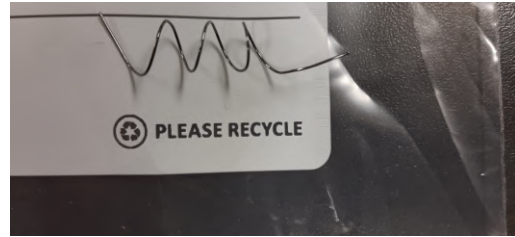


Measured Dimensions After Cooling

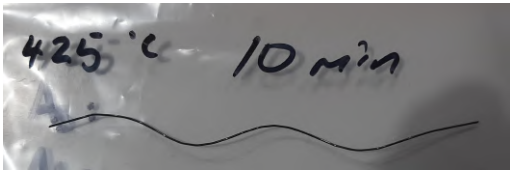
425 °C 10 Minute Left in Training



Trained 1



Trained 2

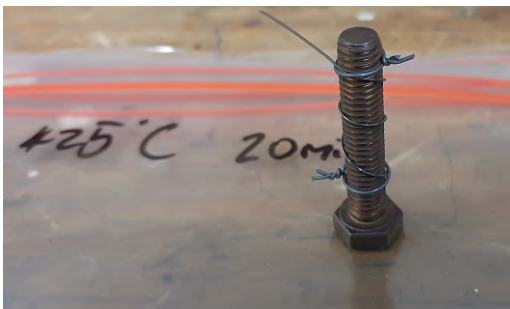


Elongated

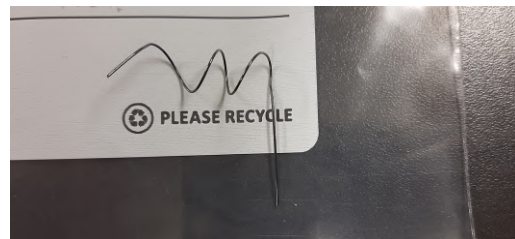


Measured Dimension After Cooling

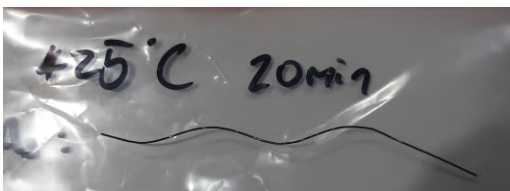
425 °C 10 Minute Training



Trained 1



Trained 2

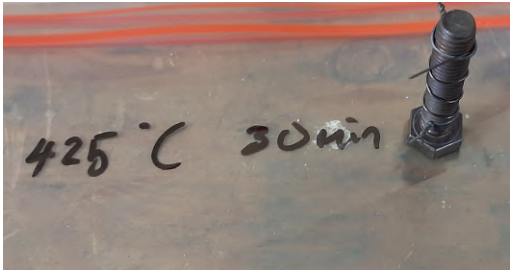


Elongated

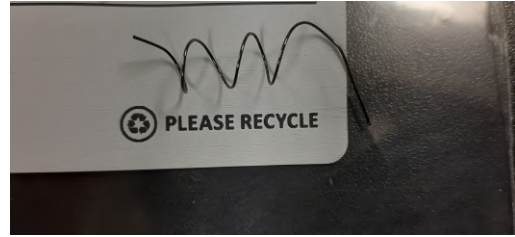


Measured Dimension After Cooling

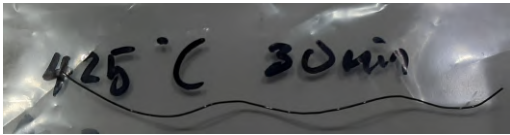
425 °C 20 Minute Training



Trained 1



Trained 2

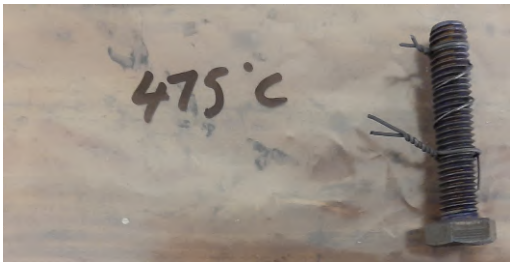


Elongated

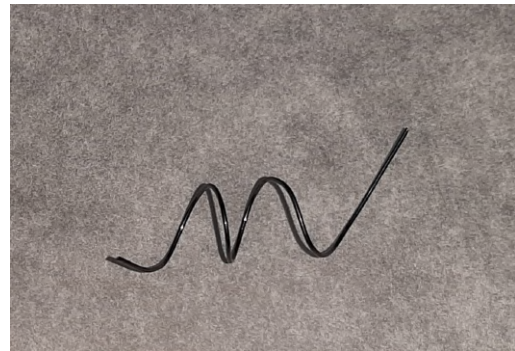


Measured Dimension After Cooling

425 °C 30 Minute Training



Trained 1



Trained 2

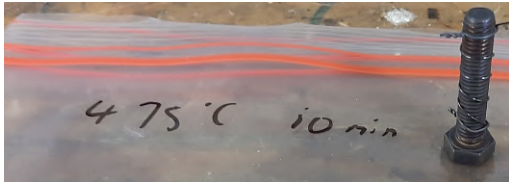


Elongated

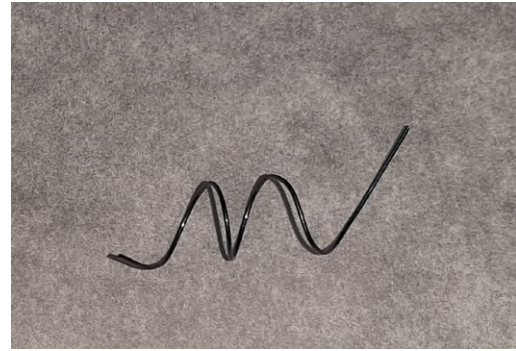


Measured Dimension After Cooling

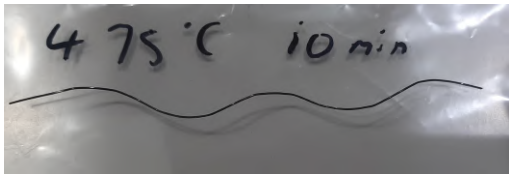
475 °C 10 Minute Left in Training



Trained 1



Trained 2



Elongated

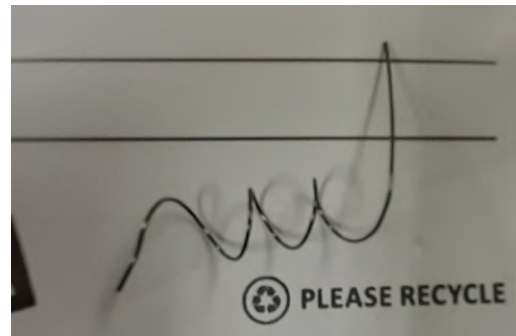


Measured Dimension After Cooling

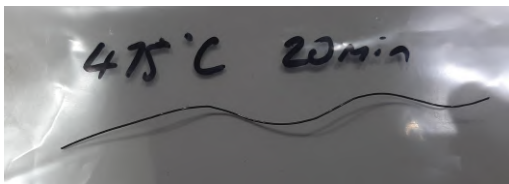
475 °C 10 Minute Training



Trained 1



Trained 2



Elongated



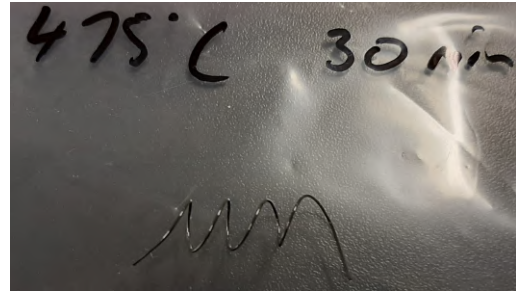
Measured Dimension After Cooling

475 °C 20 Minute Training

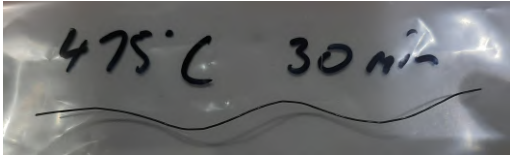




Trained 1



Trained 2

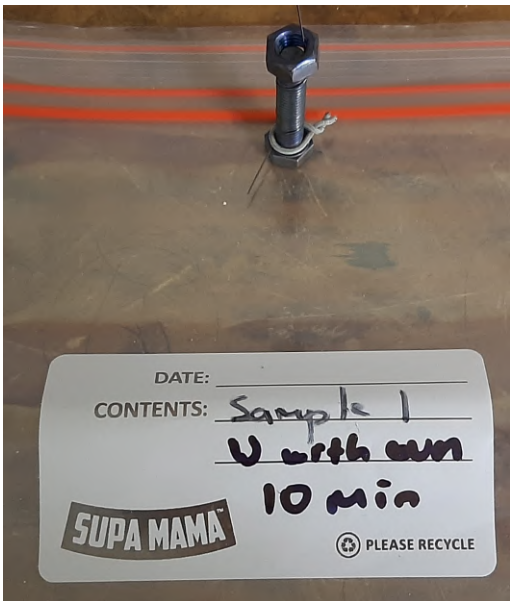


Elongated

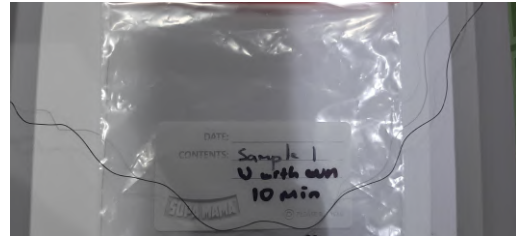


Measured Dimension After Cooling

475 °C 30 Minute Training



Trained 1

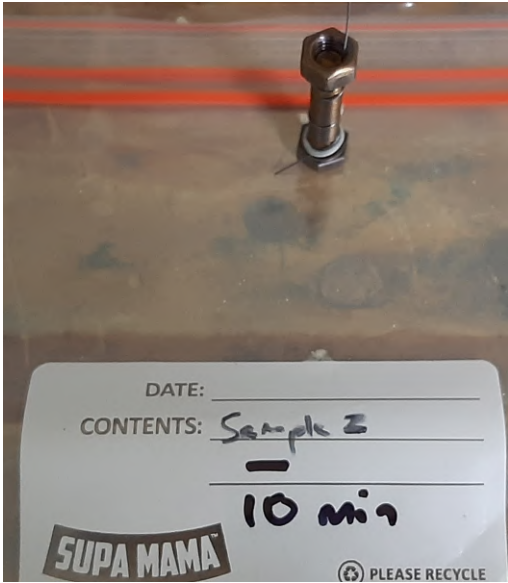


Elongated

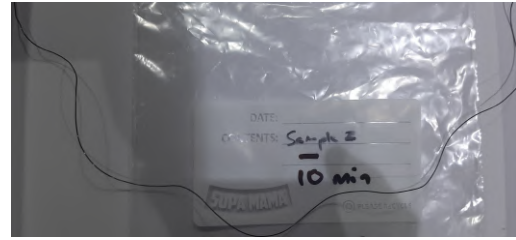


Measured Dimension After Cooling

525 °C 10 Minute Left in Training



Trained 1

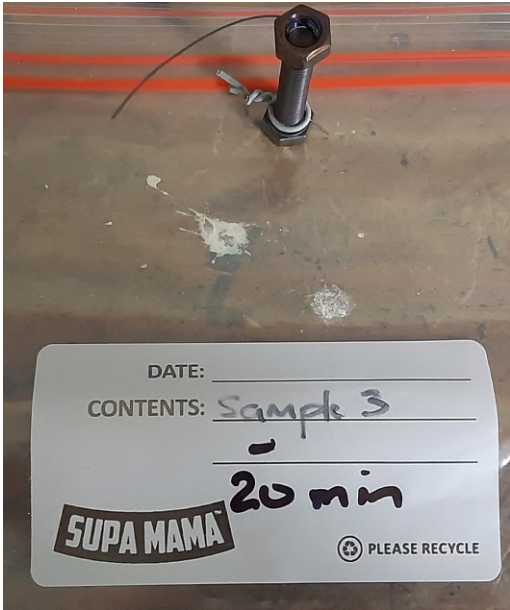


Elongation

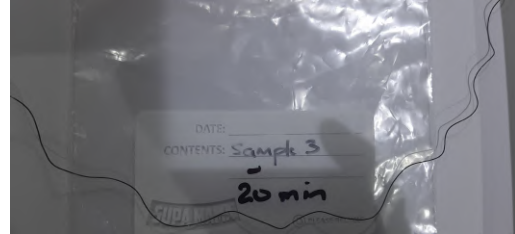


Measured Dimension After Cooling

525 °C 10 Minute Training



Trained 1

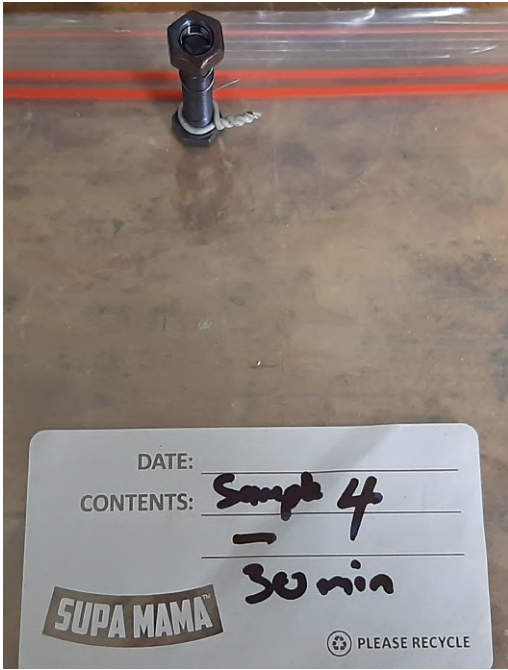


Elongation

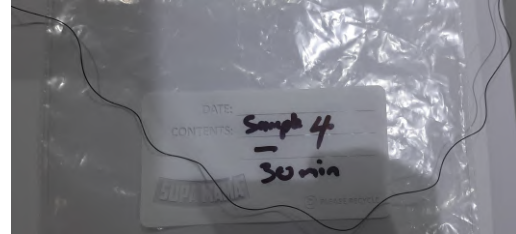


Measured Dimension After Cooling

525 °C 20 Minute Training



Trained



Elongated



Measured Dimension After Cooling

525 °C 30 Minute Training

# Appendix C

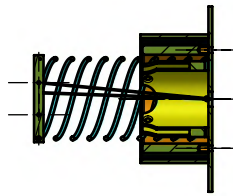
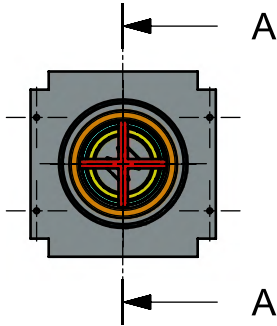
## Material Data

		Spring Material			
Criterion	Unit	ASTM A228	ASTM A227	ASTM A313 (302)	ASTM A313 (631)
Coefficient of Thermal Expansion	$\mu\text{m}/\text{m}\cdot^{\circ}\text{C}$	13,2	12	17,6	11
Corrosion Status (Stress)	-	Table 1	Table 1	Table 1	Table 1
Relative Cost	-	1,4	1	4,7	8,7
Density	$\text{kg}/\text{m}^3$	7860	7860	7920	7810
Service Temperature	$^{\circ}\text{C}$	120	150	260	315
Tensile Strength	MPa	1590 - 3340	1180 - 2510	895 - 2450	1400 - 2035

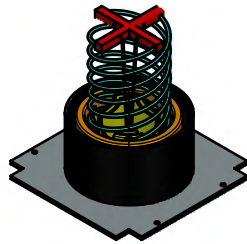
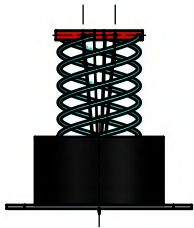
		Material Score (1-5)										
Criterion	Unit	Acetal	Nylon 6	Cast Nylon	PETP	HDPE	PE500	UHMWPE	PVC	PTFE	PETG	PLA
Cost per kg (approximate)	R	41,74	33,69	33,69	14,65	14,35	29,29	52,14	11,86	351,52	439,41	307,58
Density/Weight	$\text{kg}/\text{m}^3$	1410	1140	1150	1400	950	950	940	1380	2180	1270	1290
Dielectric Constant	-	3,4 - 5	3,1 - 12	3,1 - 12	3,3	2 - 2,6	2,3	2,3	3 - 3,3	2 - 2,1	2,4 - 3,46	2,2
Tensile Strength (average)	Mpa	66	80	85	75	31	32	40	30	25	40,6	64,5
Total Mass Loss	%	0,37 - 0,64	0,65 - 1,5	0,65 - 1,5	0,31	0,13	0,14	0,02	1,14	0,24 - 0,76	0,35	x
CVCM	%	0,01 - 0,04	0,01 - 0,17	0,01 - 0,17	0	0,03	0,02	0	0,16	0,01	0,02	x
Service Temperature (max)	$^{\circ}\text{C}$	110	85	100	115	80	80	80	50	260	70	60
Service Temperature (min)	$^{\circ}\text{C}$	-40	-40	-30	-20	-50	-100	-200	-10	-260	-40	-40


# Appendix D

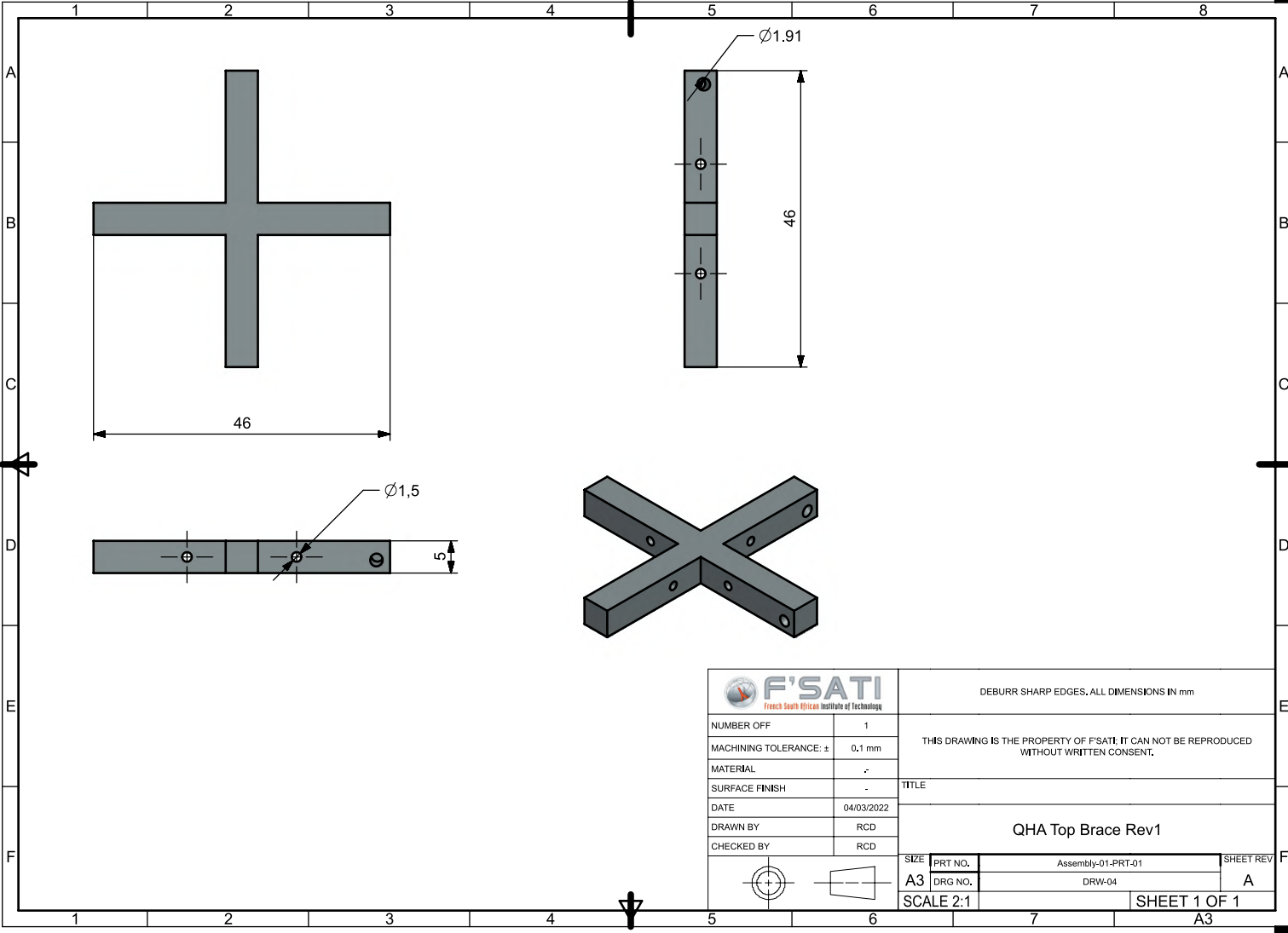
## Engineering Drawings


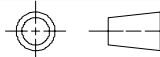


SECTION A-A

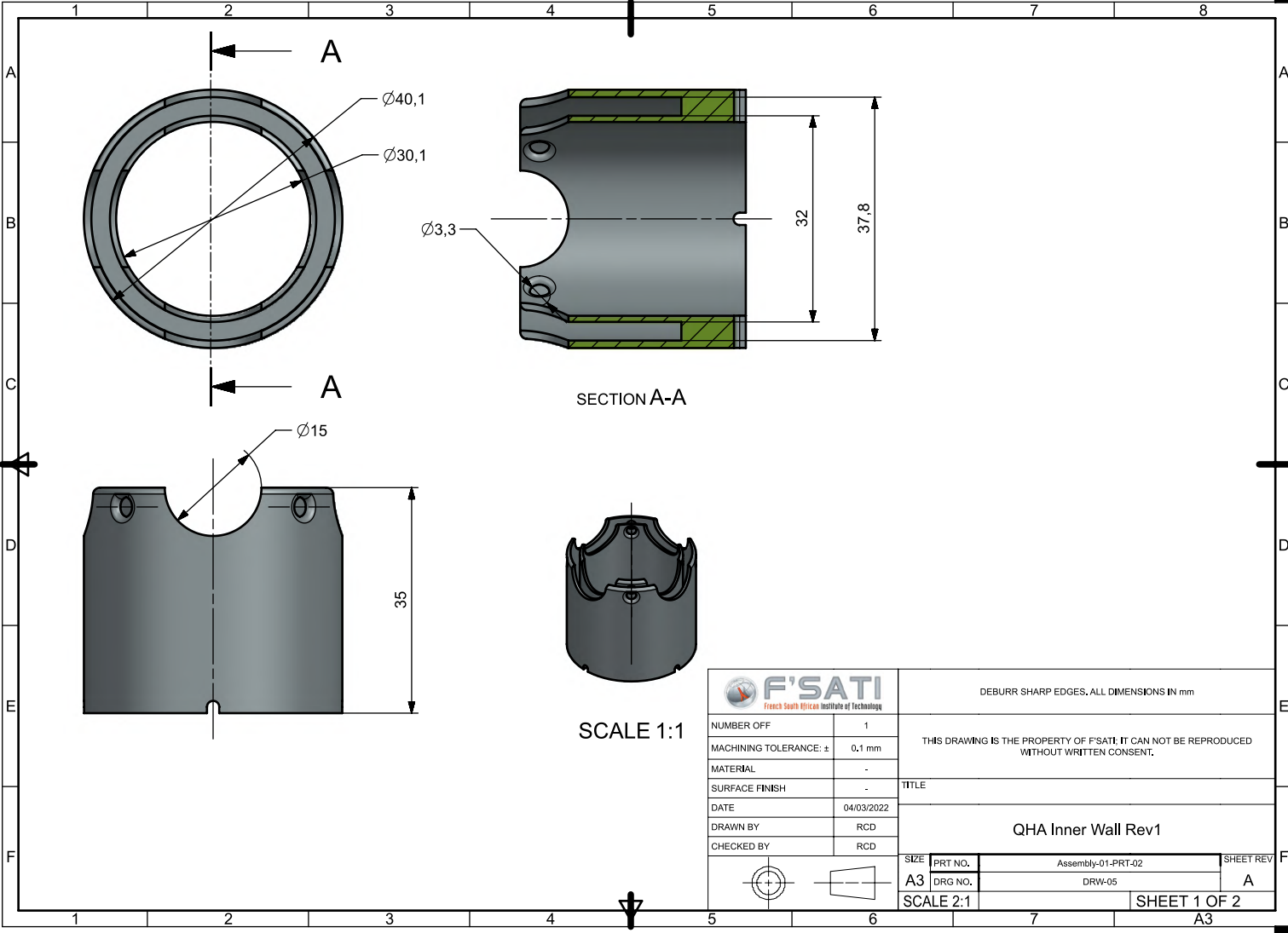


 <b>F'SATI</b> <small>French South African Institute of Technology</small>		DEBURR SHARP EDGES, ALL DIMENSIONS IN mm	
NUMBER OFF	-	THIS DRAWING IS THE PROPERTY OF F'SATI. IT CAN NOT BE REPRODUCED WITHOUT WRITTEN CONSENT.	
MACHINING TOLERANCE: ±	0,1 mm		
MATERIAL	-		
SURFACE FINISH	-		
DATE	04/01/2022		
DRAWN BY RCD		TITLE	
CHECKED BY RCD		<b>Concept 1 Deatiled Design</b>	
SIZE	PRT NO.	Assembly-01	SHEET REV
A3	DRG NO.	DRW-03	A
SCALE 1:1		SHEET 1 OF 1	
		A3	




 <b>F'SATI</b> <small>French South African Institute of Technology</small>		DEBURR SHARP EDGES, ALL DIMENSIONS IN mm			
NUMBER OFF	1	THIS DRAWING IS THE PROPERTY OF F'SATI. IT CAN NOT BE REPRODUCED WITHOUT WRITTEN CONSENT.			
MACHINING TOLERANCE: ±	0,1 mm				
MATERIAL	-				
SURFACE FINISH	-				
DATE	04/03/2022				
TITLE		<b>QHA Top Brace Rev1</b>			
DRAWN BY	RCD				
CHECKED BY	RCD	SIZE	PRT NO.	Assembly-01-PRT-01	SHEET REV
		A3	DRG NO.	DRW-04	A
		SCALE 2:1		SHEET 1 OF 1	
				A3	

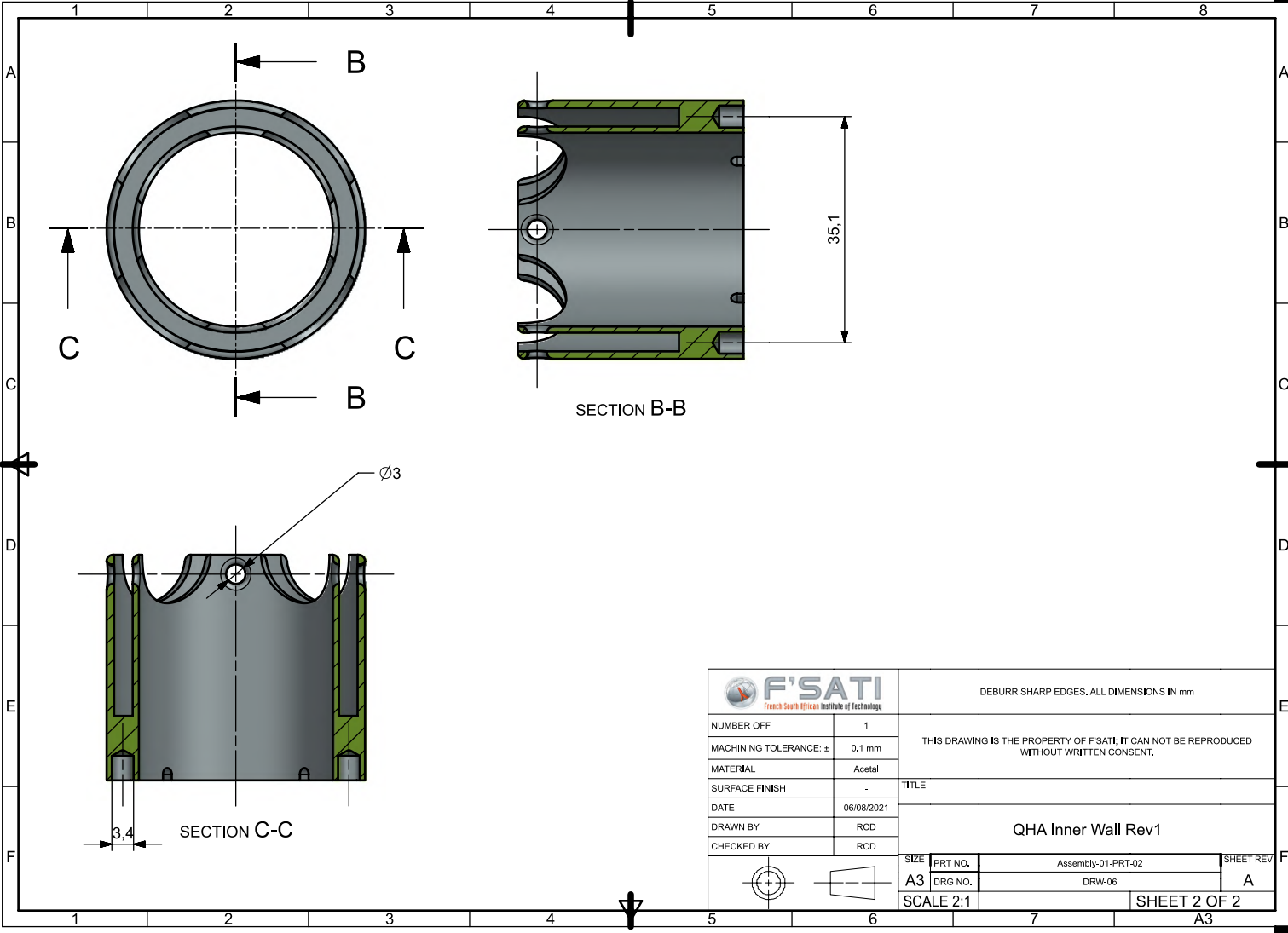





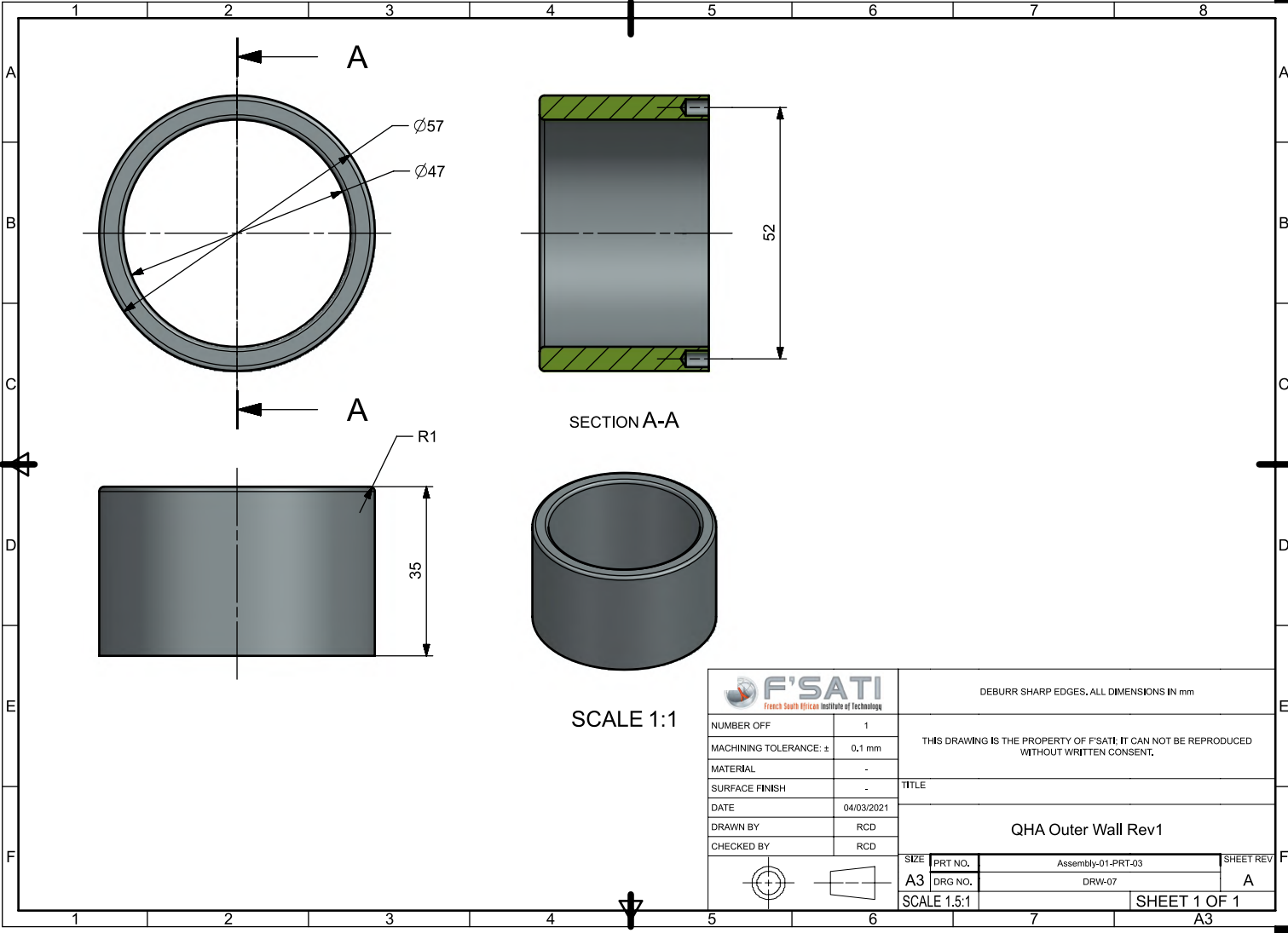
SECTION A-A

SCALE 1:1


 <b>F'SATI</b> French South African Institute of Technology		DEBURR SHARP EDGES. ALL DIMENSIONS IN mm	
NUMBER OFF	1	THIS DRAWING IS THE PROPERTY OF F'SATI. IT CAN NOT BE REPRODUCED WITHOUT WRITTEN CONSENT.	
MACHINING TOLERANCE: ±	0.1 mm		
MATERIAL	-		
SURFACE FINISH	-		
DATE	04/03/2022		
DRAWN BY	RCD	TITLE	
CHECKED BY	RCD	QHA Inner Wall Rev1	
SIZE	PRT NO.	Assembly-01-PRT-02	SHEET REV
A3	DRG NO.	DRW-05	A
SCALE 2:1		SHEET 1 OF 2	
		A3	

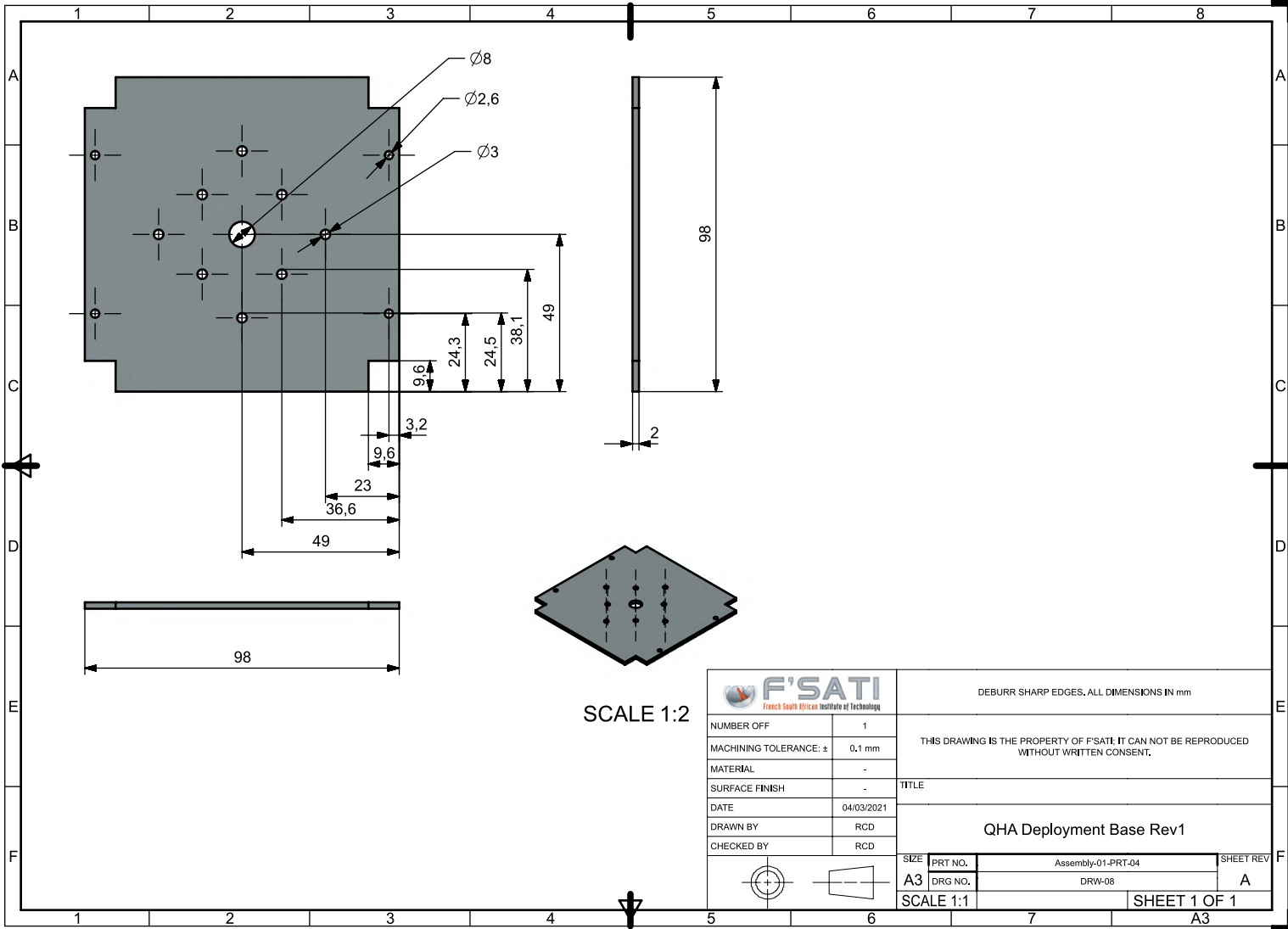


 <b>F'SATI</b> French South African Institute of Technology		DEBURR SHARP EDGES, ALL DIMENSIONS IN mm	
NUMBER OFF	1	THIS DRAWING IS THE PROPERTY OF F'SATI. IT CAN NOT BE REPRODUCED WITHOUT WRITTEN CONSENT.	
MACHINING TOLERANCE: ±	0,1 mm		
MATERIAL	Acetal	TITLE	
SURFACE FINISH	-	<b>QHA Inner Wall Rev1</b>	
DATE	06/08/2021		
DRAWN BY	RCD		
CHECKED BY	RCD		
SIZE	PRT NO.	Assembly-01-PRT-02	SHEET REV
A3	DRG NO.	DRW-06	A
SCALE 2:1		SHEET 2 OF 2	
		A3	




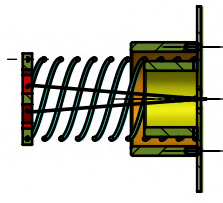
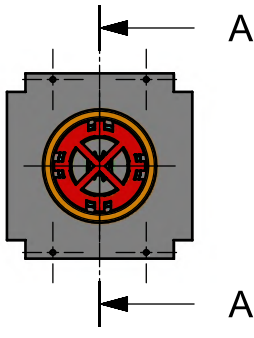
SCALE 1:1

 <b>F'SATI</b> French South African Institute of Technology		DEBURR SHARP EDGES, ALL DIMENSIONS IN mm	
NUMBER OFF	1	THIS DRAWING IS THE PROPERTY OF F'SATI. IT CAN NOT BE REPRODUCED WITHOUT WRITTEN CONSENT.	
MACHINING TOLERANCE: ±	0,1 mm		
MATERIAL	-		
SURFACE FINISH	-		
DATE	04/03/2021		
DRAWN BY	RCD	TITLE	
CHECKED BY	RCD	QHA Outer Wall Rev1	
SIZE	PRT NO.	Assembly-01-PRT-03	SHEET REV
A3	DRG NO.	DRW-07	A
SCALE 1.5:1			SHEET 1 OF 1
			A3

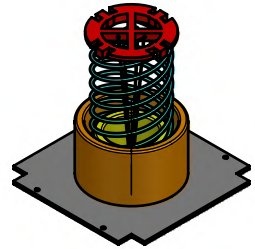
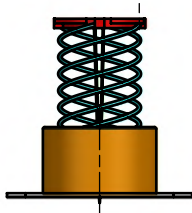



SCALE 1:2

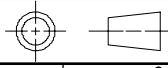
 <b>F'SATI</b> French South African Institute of Technology		DEBURR SHARP EDGES, ALL DIMENSIONS IN mm	
NUMBER OFF	1	THIS DRAWING IS THE PROPERTY OF F'SATI. IT CAN NOT BE REPRODUCED WITHOUT WRITTEN CONSENT.	
MACHINING TOLERANCE: ±	0,1 mm		
MATERIAL	-		
SURFACE FINISH	-		
DATE	04/03/2021		
DRAWN BY	RCD	<b>QHA Deployment Base Rev1</b>	
CHECKED BY	RCD		
SIZE	PRT NO.	Assembly-01-PRT-04	SHEET REV
A3	DRG NO.	DRW-08	A
SCALE 1:1		SHEET 1 OF 1	
		A3	

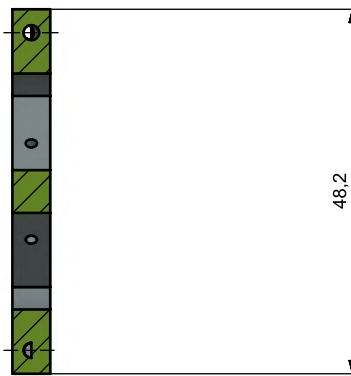
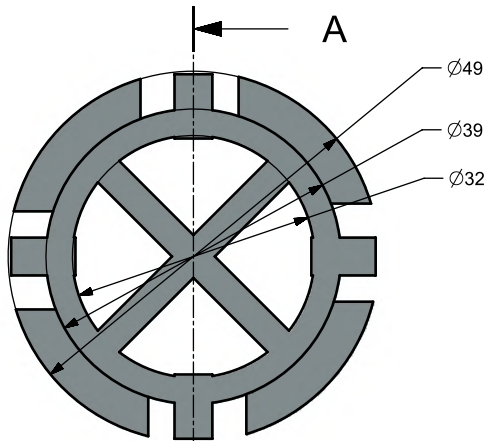


SECTION A-A

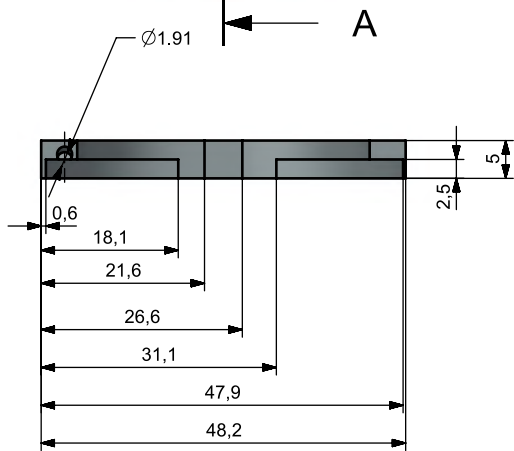


 <b>F'SATI</b> French South African Institute of Technology		DEBURR SHARP EDGES, ALL DIMENSIONS IN mm	
NUMBER OFF	1	THIS DRAWING IS THE PROPERTY OF F'SATI. IT CAN NOT BE REPRODUCED WITHOUT WRITTEN CONSENT.	
MACHINING TOLERANCE: ±	0,1 mm		
MATERIAL	-	TITLE	
SURFACE FINISH	-	<b>QHA Final Detailed Design</b>	
DATE	06/08/2021		
DRAWN BY	RCD		
CHECKED BY	RCD		
SIZE	PRT NO.	Assembly-02	SHEET REV
A3	DRG NO.	DRW-09	A
SCALE 1:1		SHEET 1 OF 1	
		A3	




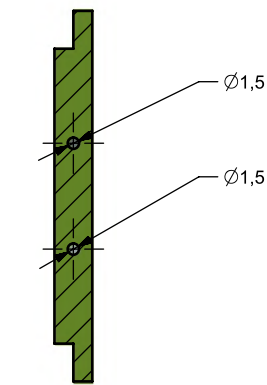
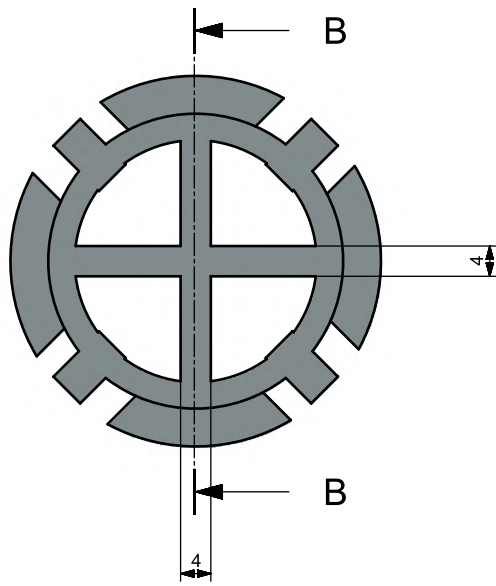


SECTION A-A




SCALE 1:1

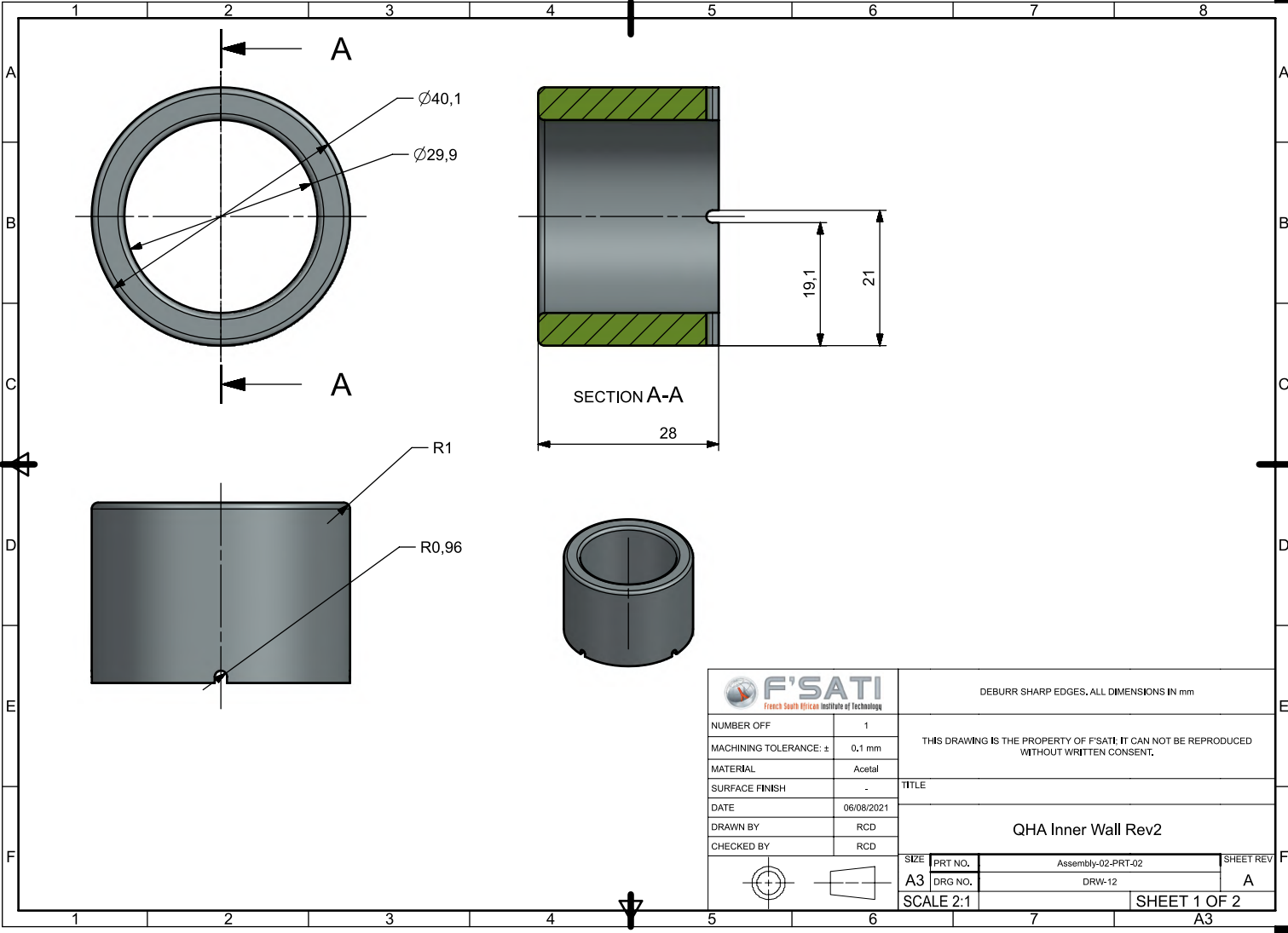
 <b>F'SATI</b> French South African Institute of Technology		DEBURR SHARP EDGES, ALL DIMENSIONS IN mm	
NUMBER OFF	1	THIS DRAWING IS THE PROPERTY OF F'SATI. IT CAN NOT BE REPRODUCED WITHOUT WRITTEN CONSENT.	
MACHINING TOLERANCE: ±	0,1 mm		
MATERIAL	Acetal	TITLE	
SURFACE FINISH	-	<b>QHA Top Brace Rev2</b>	
DATE	06/08/2021		
DRAWN BY	RCD		
CHECKED BY	RCD		
SIZE	PRT NO.	Assembly-02-PRT-01	SHEET REV
A3	DRG NO.	DRW-10	A
SCALE 2:1		SHEET 1 OF 2	
		A3	



SECTION B-B



 <b>F'SATI</b> French South African Institute of Technology		DEBURR SHARP EDGES, ALL DIMENSIONS IN mm	
NUMBER OFF	1	THIS DRAWING IS THE PROPERTY OF F'SATI. IT CAN NOT BE REPRODUCED WITHOUT WRITTEN CONSENT.	
MACHINING TOLERANCE: ±	0,1 mm		
MATERIAL	Acetal	TITLE	
SURFACE FINISH	-	<b>QHA Top Brace Rev2</b>	
DATE	06/08/2021		
DRAWN BY	RCD		
CHECKED BY	RCD		
SIZE	PRT NO.	Assembly-02-PRT-01	SHEET REV
A3	DRG NO.	DRW-11	A
SCALE 2:1		SHEET 2 OF 2	
		A3	



DEBURR SHARP EDGES, ALL DIMENSIONS IN mm

NUMBER OFF	1
MACHINING TOLERANCE: ±	0,1 mm
MATERIAL	Acetal
SURFACE FINISH	-
DATE	06/08/2021
DRAWN BY	RCD
CHECKED BY	RCD

THIS DRAWING IS THE PROPERTY OF F'SATI. IT CAN NOT BE REPRODUCED WITHOUT WRITTEN CONSENT.

TITLE

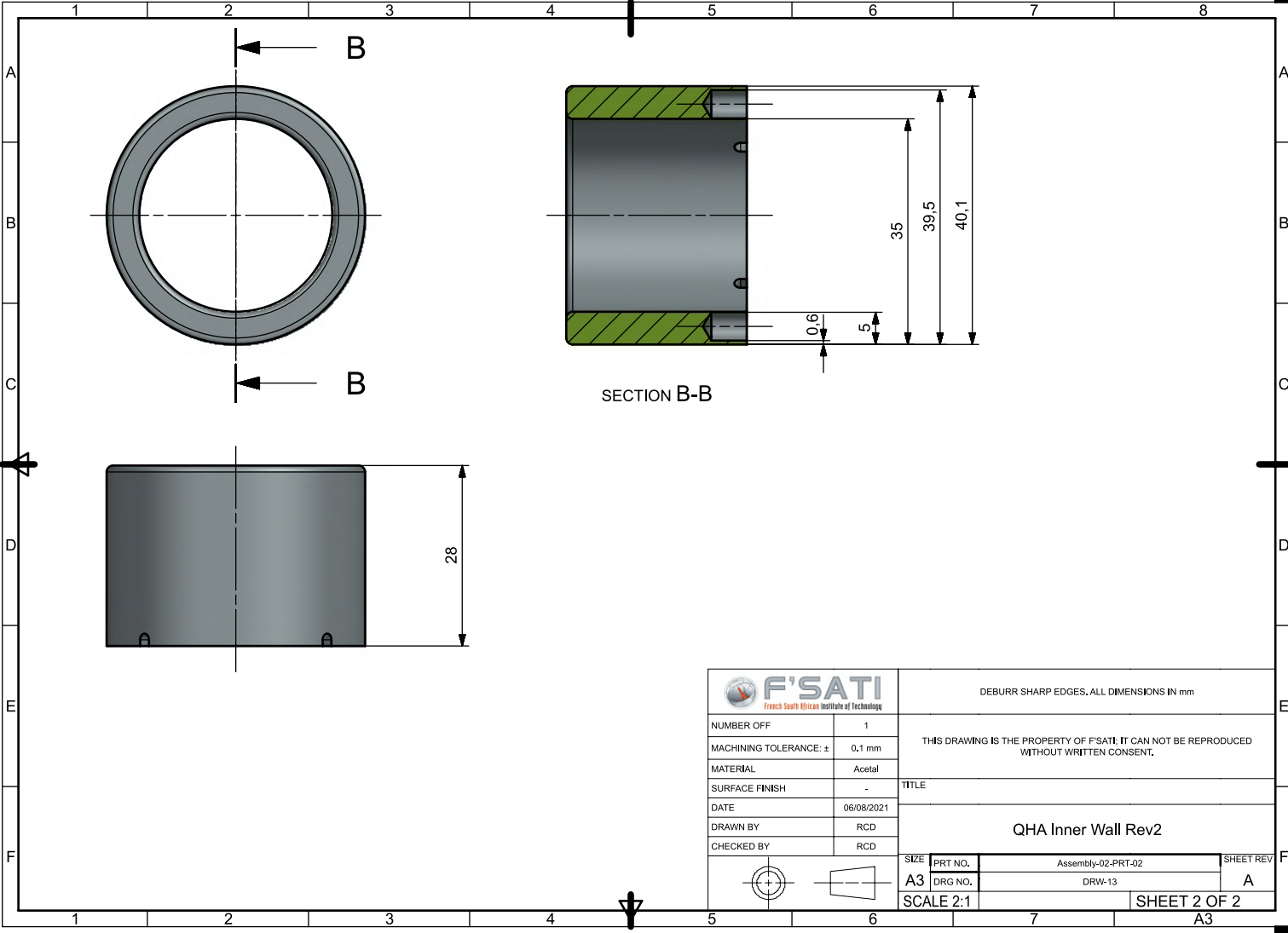
QHA Inner Wall Rev2




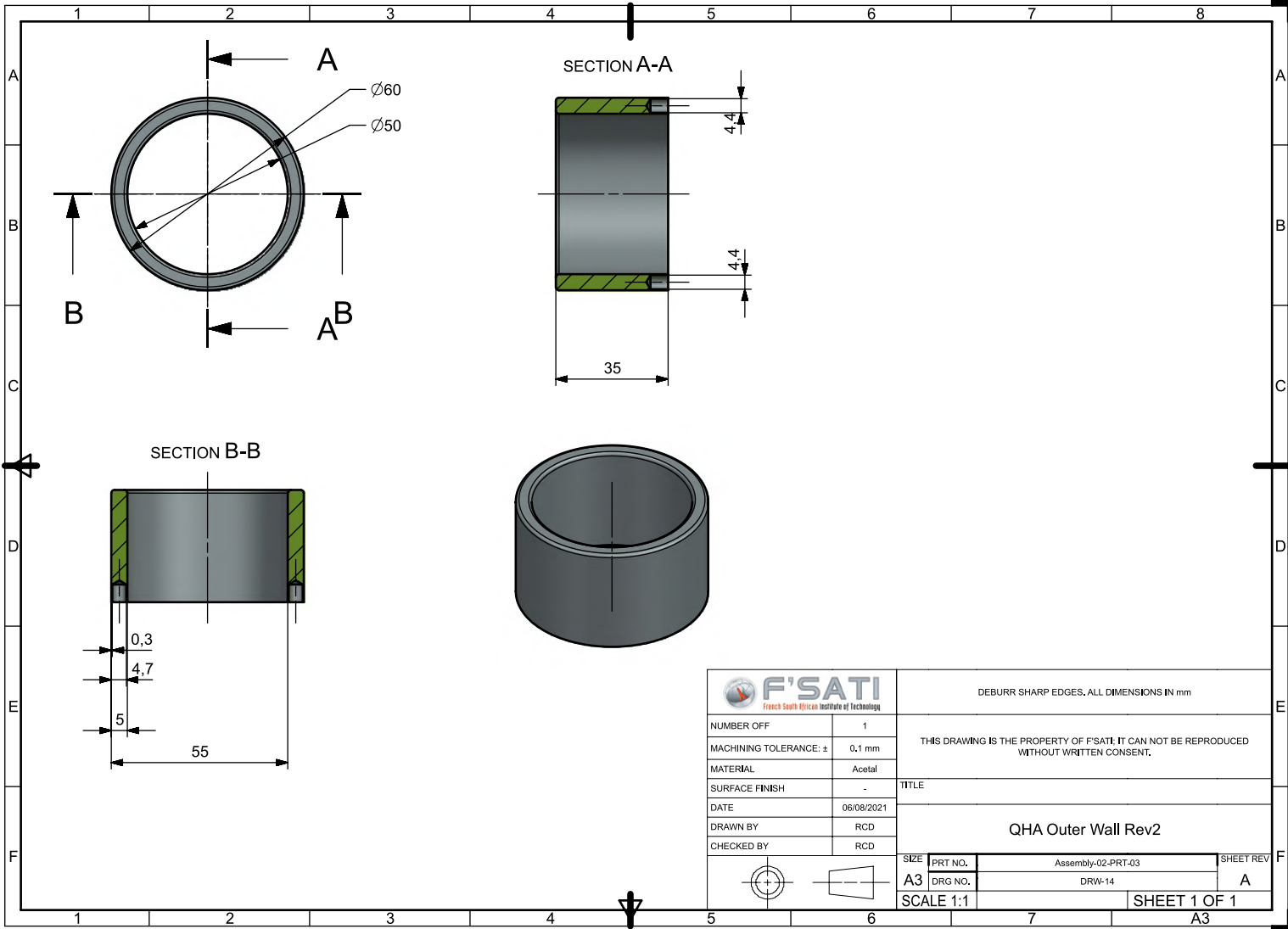
SIZE	PRT NO.	Assembly-02-PRT-02	SHEET REV
A3	DRG NO.	DRW-12	A
SCALE 2:1			SHEET 1 OF 2

A3





 <b>F'SATI</b> French South African Institute of Technology		DEBURR SHARP EDGES, ALL DIMENSIONS IN mm	
NUMBER OFF	1	THIS DRAWING IS THE PROPERTY OF F'SATI. IT CAN NOT BE REPRODUCED WITHOUT WRITTEN CONSENT.	
MACHINING TOLERANCE: ±	0,1 mm		
MATERIAL	Acetal		
SURFACE FINISH	-		
DATE	06/08/2021		
TITLE		QHA Inner Wall Rev2	
DRAWN BY	RCD	SIZE	PRT NO.
CHECKED BY	RCD	A3	Assembly-02-PRT-02
		DRG NO.	DRW-13
		SCALE	2:1
		SHEET REV	
		A	
		SHEET 2 OF 2	
		A3	



DEBURR SHARP EDGES, ALL DIMENSIONS IN mm

NUMBER OFF	1
MACHINING TOLERANCE: ±	0.1 mm
MATERIAL	Acetal
SURFACE FINISH	-
DATE	06/08/2021
DRAWN BY	RCD
CHECKED BY	RCD

THIS DRAWING IS THE PROPERTY OF F'SATI. IT CAN NOT BE REPRODUCED WITHOUT WRITTEN CONSENT.

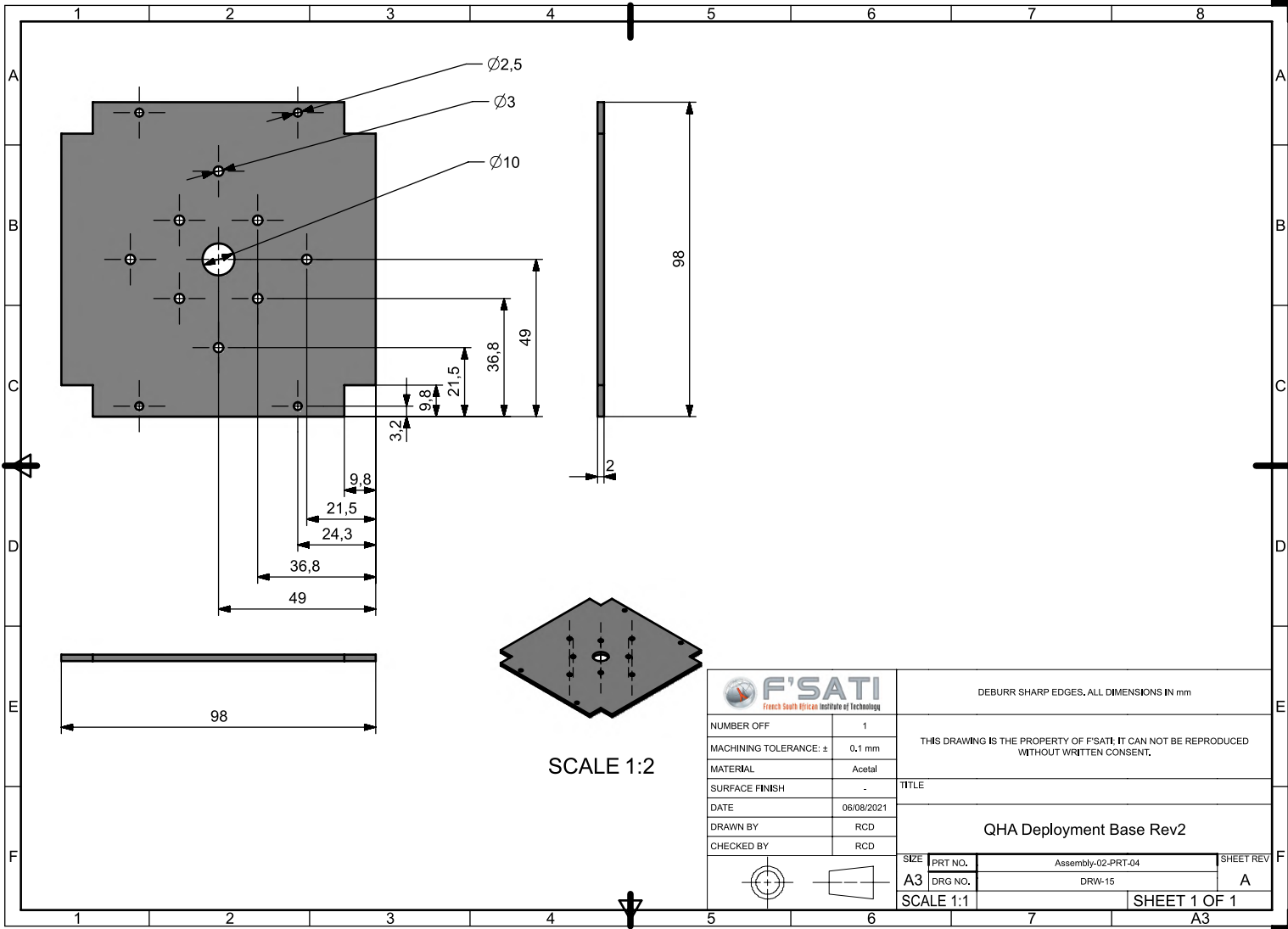
TITLE

QHA Outer Wall Rev2



SIZE	PRT NO.	Assembly-02-PRT-03	SHEET REV
A3	DRG NO.	DRW-14	A
SCALE 1:1			SHEET 1 OF 1

A3



DEBURR SHARP EDGES, ALL DIMENSIONS IN mm

NUMBER OFF	1
MACHINING TOLERANCE: ±	0,1 mm
MATERIAL	Acetal
SURFACE FINISH	-
DATE	06/08/2021
DRAWN BY	RCD
CHECKED BY	RCD

THIS DRAWING IS THE PROPERTY OF F'SATI. IT CAN NOT BE REPRODUCED WITHOUT WRITTEN CONSENT.

TITLE  
QHA Deployment Base Rev2



SIZE	PRT NO.	Assembly-02-PRT-04	SHEET REV
A3	DRG NO.	DRW-15	A
SCALE 1:1			SHEET 1 OF 1

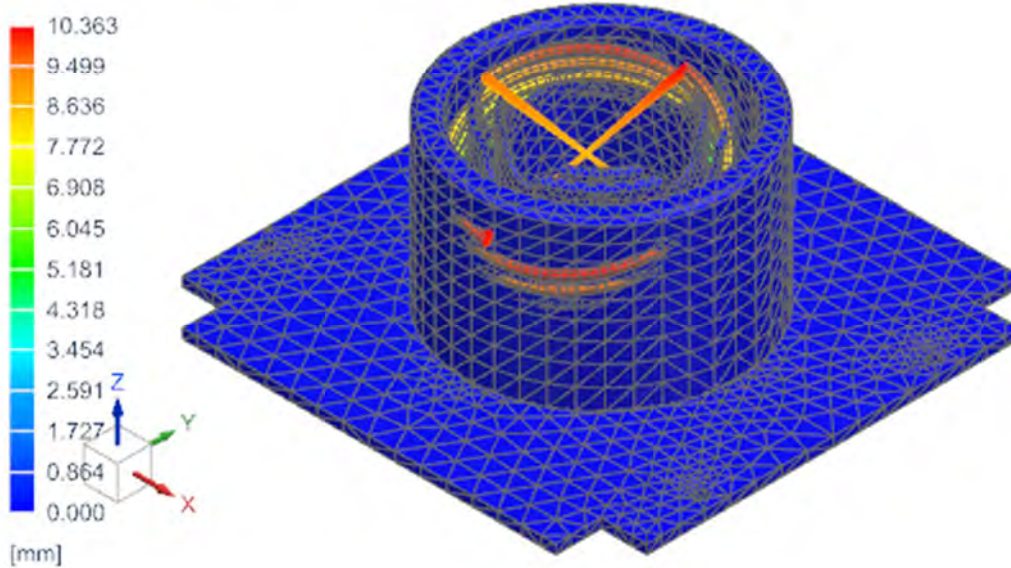
A3

# Appendix E

## Modal Frequencies

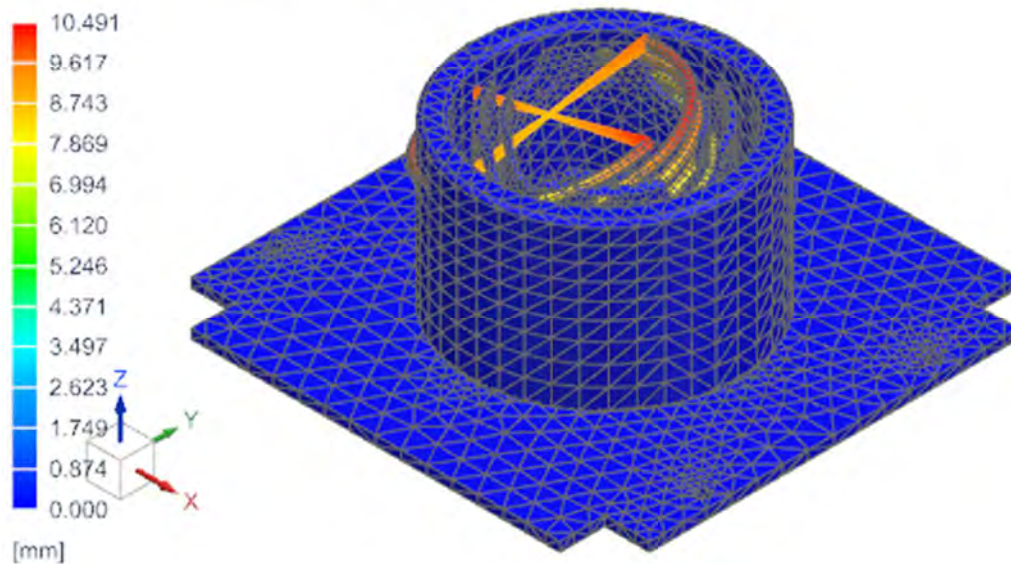
### Mode 1: 73.3 Hz

Final Assembly Rev2\_sim1 : Solution 103 Response Dynamics Modal Survey Result  
SUBCASE - DYNAMICS SUBCASE 3, Mode 1, 73.33Hz  
Displacement - Nodal, Magnitude  
Min : 0.000, Max : 10.363, Units = mm  
Deformation : Displacement - Nodal Magnitude



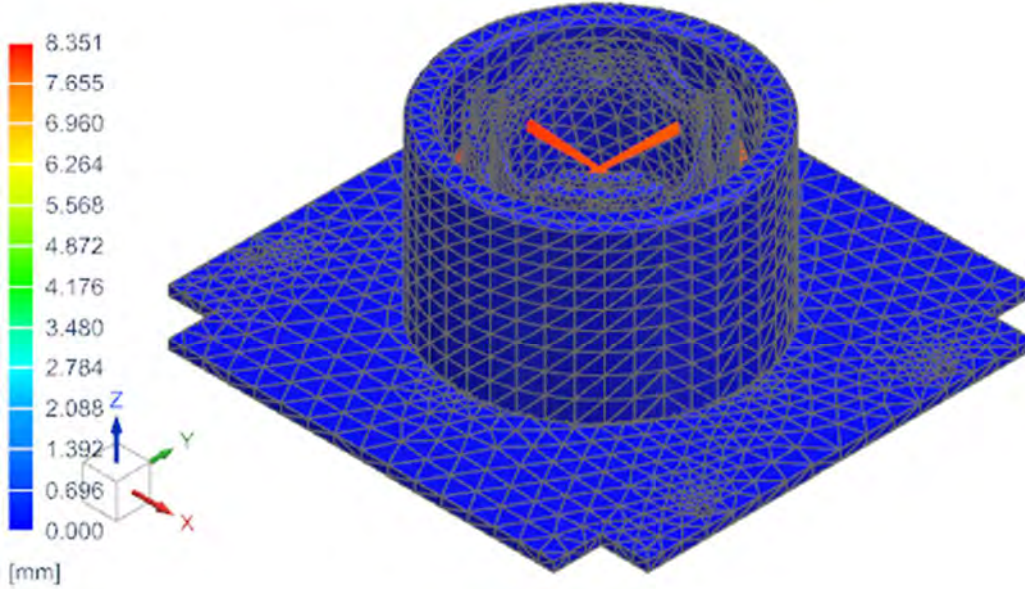
### Mode 2: 73.80 Hz

Final Assembly Rev2\_sim1 : Solution 103 Response Dynamics Modal Survey Result  
SUBCASE - DYNAMICS SUBCASE 3, Mode 2, 73.80Hz  
Displacement - Nodal, Magnitude  
Min : 0.000, Max : 10.491, Units = mm  
Deformation : Displacement - Nodal Magnitude



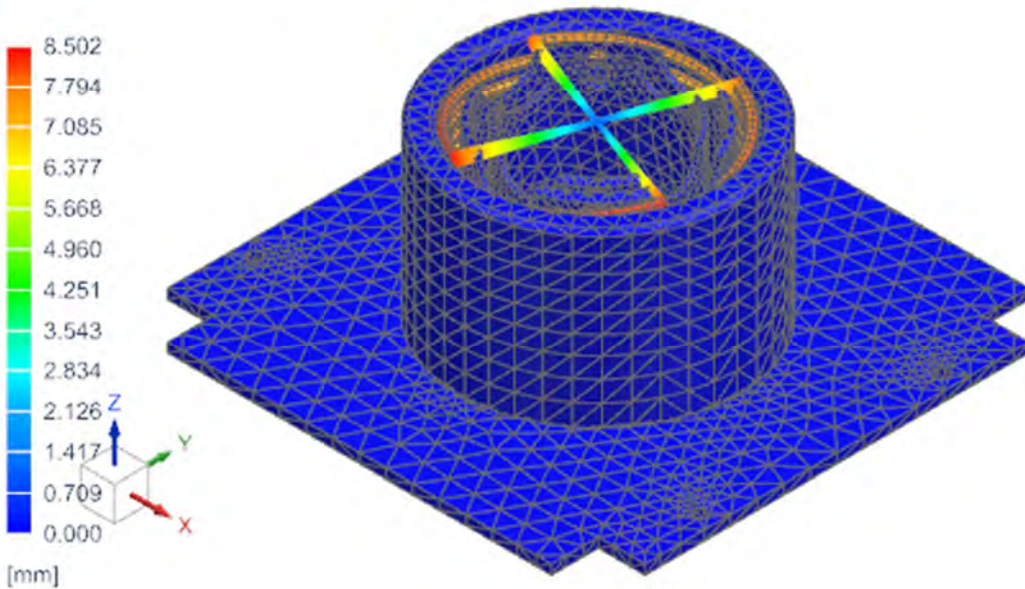
### Mode 3: 76.42 Hz

Final Assembly Rev2\_sim1 : Solution 103 Response Dynamics Modal Survey Result  
SUBCASE - DYNAMICS SUBCASE 3, Mode 3, 76.42Hz  
Displacement - Nodal, Magnitude  
Min : 0.000, Max : 8.351, Units = mm  
Deformation : Displacement - Nodal Magnitude



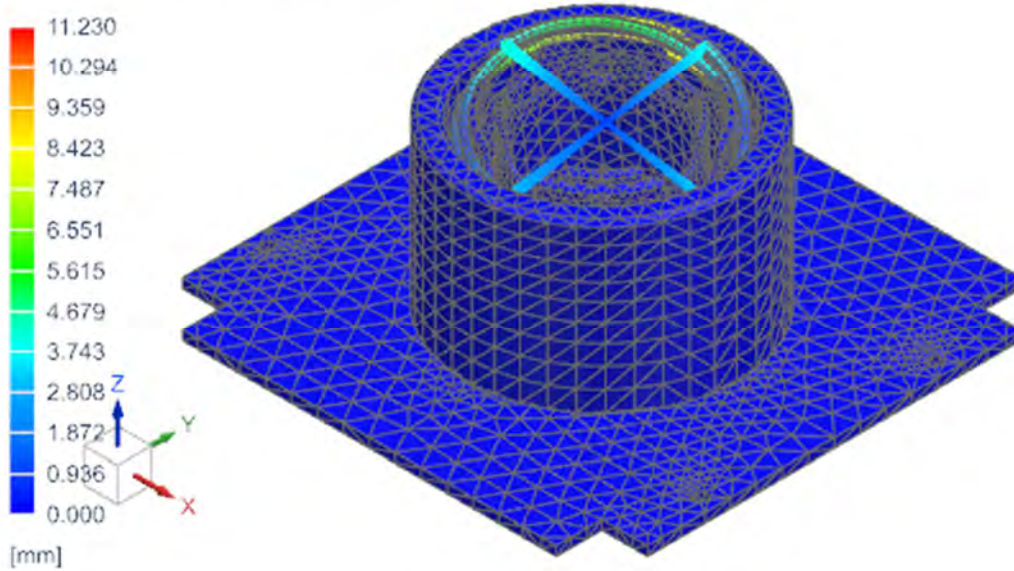
### Mode 4: 86.17 Hz

Final Assembly Rev2\_sim1 : Solution 103 Response Dynamics Modal Survey Result  
SUBCASE - DYNAMICS SUBCASE 3, Mode 4, 86.17Hz  
Displacement - Nodal, Magnitude  
Min : 0.000, Max : 8.502, Units = mm  
Deformation : Displacement - Nodal Magnitude



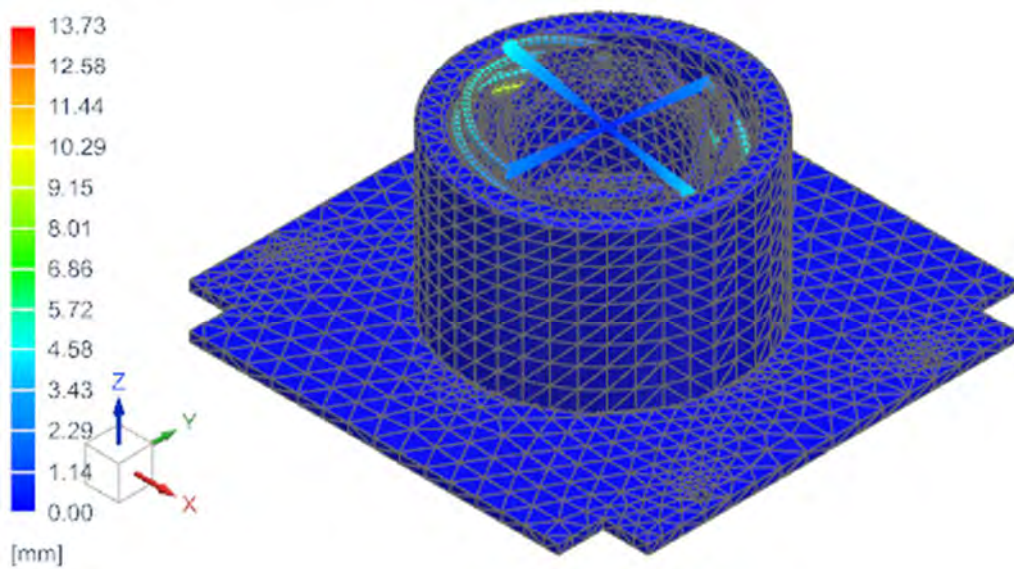
### Mode 5: 149.04 Hz

Final Assembly Rev2\_sim1 : Solution 103 Response Dynamics Modal Survey Result  
SUBCASE - DYNAMICS SUBCASE 3, Mode 5, 149.04Hz  
Displacement - Nodal, Magnitude  
Min : 0.000, Max : 11.230, Units = mm  
Deformation : Displacement - Nodal Magnitude



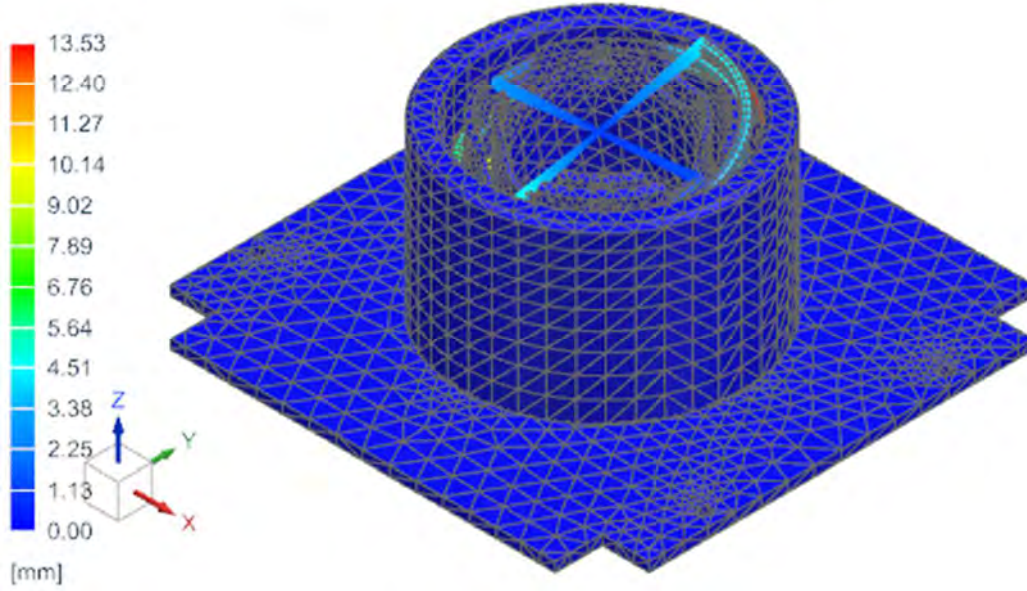
### Mode 6: 152.30 Hz

Final Assembly Rev2\_sim1 : Solution 103 Response Dynamics Modal Survey Result  
SUBCASE - DYNAMICS SUBCASE 3, Mode 6, 152.30Hz  
Displacement - Nodal, Magnitude  
Min : 0.00, Max : 13.73, Units = mm  
Deformation : Displacement - Nodal Magnitude



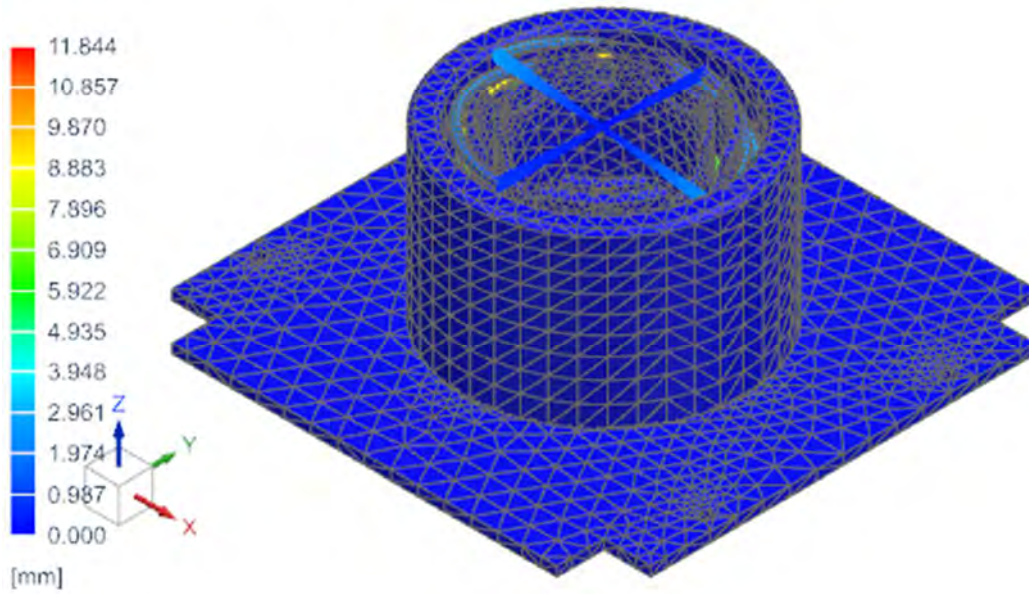
Mode 7: 158.22 Hz

Final Assembly Rev2\_sim1 : Solution 103 Response Dynamics Modal Survey Result  
SUBCASE - DYNAMICS SUBCASE 3, Mode 7, 158.22Hz  
Displacement - Nodal, Magnitude  
Min : 0.00, Max : 13.53, Units = mm  
Deformation : Displacement - Nodal Magnitude



Mode 8: 160.36 Hz

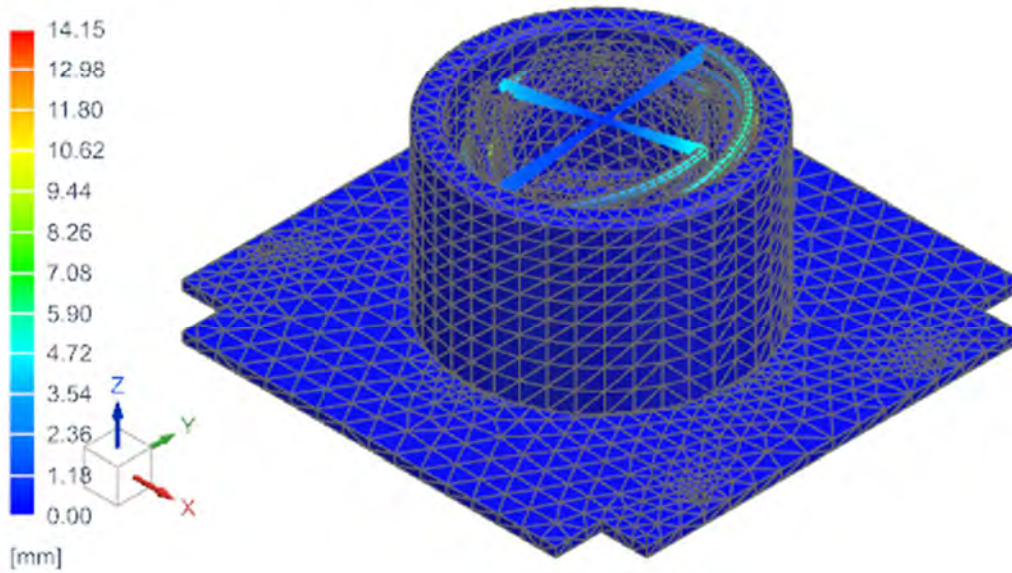
Final Assembly Rev2\_sim1 : Solution 103 Response Dynamics Modal Survey Result  
SUBCASE - DYNAMICS SUBCASE 3, Mode 8, 160.36Hz  
Displacement - Nodal, Magnitude  
Min : 0.000, Max : 11.844, Units = mm  
Deformation : Displacement - Nodal Magnitude





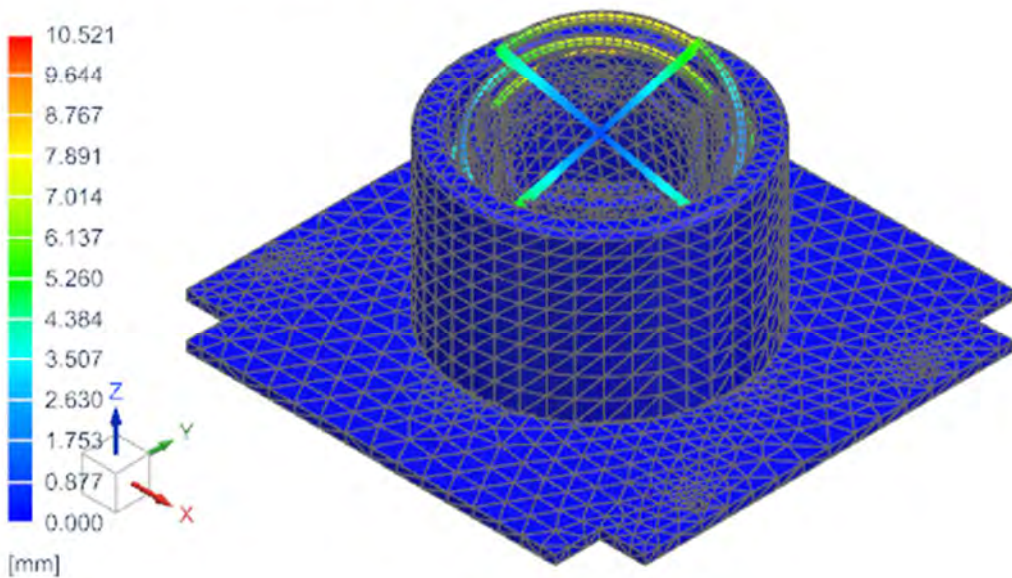
### Mode 9: 166.48 Hz

Final Assembly Rev2\_sim1 : Solution 103 Response Dynamics Modal Survey Result  
SUBCASE - DYNAMICS SUBCASE 3, Mode 9, 166.48Hz  
Displacement - Nodal, Magnitude  
Min : 0.00, Max : 14.15, Units = mm  
Deformation : Displacement - Nodal Magnitude



### Mode 10: 169.81 Hz

Final Assembly Rev2\_sim1 : Solution 103 Response Dynamics Modal Survey Result  
SUBCASE - DYNAMICS SUBCASE 3, Mode 10, 169.81Hz  
Displacement - Nodal, Magnitude  
Min : 0.000, Max : 10.521, Units = mm  
Deformation : Displacement - Nodal Magnitude

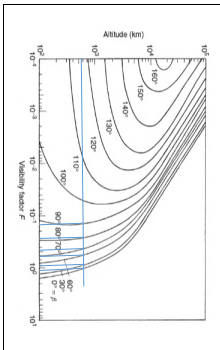


# Appendix F

## Calculations

### F.1 Thermal Balance Calculations

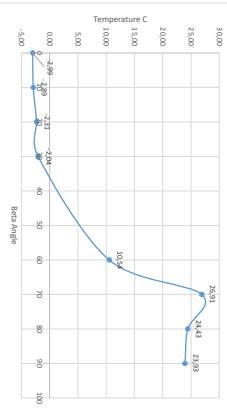
Parameters	Value	Unit	Description
$J_s$	1414	W/m <sup>2</sup>	Solar radiation intensity (constant)
$f$	1.25		Wobler factor
$a$	0.8		Absorbance (black paint)
$e$	0.8		Emissance (black paint)
$a/e$	1.12		
$Q$	0 W		Internal power
$f_{in}$	0.628	W/m <sup>2</sup>	Fraction of sunlit orbit
$L_E$	550 km		Orbit alt.
$J_p$	232	W/m <sup>2</sup>	Planetary radiation intensity
$A_{s,surface}$	0.048839	m <sup>2</sup>	A <sub>s,surface</sub>
$A_{s,absorb}$	0.031891	m <sup>2</sup>	A <sub>s,absorb</sub>
$A_{s,planetary}$	0.003	m <sup>2</sup>	A <sub>s,planetary</sub>
$A_{s,albedo}$	0.27		albedo
$J_a$	572.67	W/m <sup>2</sup>	
$B$	0	Wm <sup>-2</sup> K <sup>-4</sup>	
$B_0$	5.67E-08	Wm <sup>-2</sup> K <sup>-4</sup>	
$T$	2701581	K	
$T(TC)$	-2.99193	C	



2705236  
6928  
0.890479

Description	Parameter/Value	Unit
Solar radiation intensity (constant)	$J_s$	W/m <sup>2</sup>
Absorbance (black paint)	$a$	
Emissance (black paint)	$e$	
Internal power	$Q$	W
Fraction of sunlit orbit	$f_{in}$	
Planetary radiation intensity	$J_p$	W/m <sup>2</sup>
	$A_{s,surface}$	m <sup>2</sup>
	$A_{s,absorb}$	m <sup>2</sup>
	$A_{s,planetary}$	m <sup>2</sup>
	albedo	
	$J_a$	W/m <sup>2</sup>
	$B$	Wm <sup>-2</sup> K <sup>-4</sup>
	$T$	K
	$T(TC)$	C

Max Flux (HOT CASE): Beta angle versus Temperature Graph



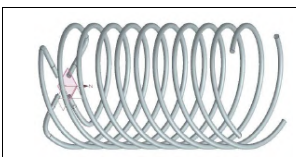
$$J_o = J_s \cdot d \cdot F^*$$

$$F_s = \frac{1}{160} \cos^{-1} \left[ \frac{(R + 283)^{1/2}}{(R + D) \cos \beta} \right] \cdot f$$

$$= 0 \text{ if } |\beta| \geq \beta^*$$

$$\beta^* = \sin^{-1} \left[ \frac{R}{R + D} \right] \quad 0^\circ \leq \beta^* \leq 90^\circ$$

$$\sigma = \text{Stefan-Boltzmann constant } (5.67 \times 10^{-8} \text{ W m}^{-2} \text{ K}^{-2})$$



Area Calculations:	Value
$f$	0.000955 m
$N$	0.9932 2.5
OD	0.04891 m
ID	0.04009
KOD	0.042
Calculated	0.035984
$L$	0.08996
LT	
Outer Surface Area:	0.01241 m <sup>2</sup>
+ Conn	0.048839 m <sup>2</sup>
$A_{s,absorb}$ and $A_{s,planetary}$	0.003
Albedo	0.02819
Helio and/or A	0.0015
Average of A's	0.01316 m <sup>2</sup>

$$T^{-4} = \frac{A_{planetary} T_p^4}{A_{sun} f_{acc} \sigma} + \frac{Q}{A_{sun} f_{acc} \sigma} + \frac{A_{solar} T_s^4}{A_{s}}$$

1. 24707637  
2. 0.509558860  
3.

Description	Parameter/Value	Unit
Solar radiation intensity (constant)	$J_s$	W/m <sup>2</sup>
Absorbance (black paint)	$a$	
Emissance (black paint)	$e$	
Internal power	$Q$	W
Fraction of sunlit orbit	$f_{in}$	
Planetary radiation intensity	$J_p$	W/m <sup>2</sup>
	$A_{s,surface}$	m <sup>2</sup>
	$A_{s,absorb}$	m <sup>2</sup>
	$A_{s,planetary}$	m <sup>2</sup>
	albedo	
	$J_a$	W/m <sup>2</sup>
	$B$	Wm <sup>-2</sup> K <sup>-4</sup>
	$T$	K
	$T(TC)$	C

$$| \beta | < \beta^*$$

$$K^{-1}$$

$$L_s = (2\pi r)^2 + p^2 \pi a^2$$

$$L_f = |L_s| \times N$$

$$A_{solar} = L_f \times \pi \times OD$$

$$\frac{A_{albedo} J_a \sigma(T)}{A_{s,acc} \sigma}$$

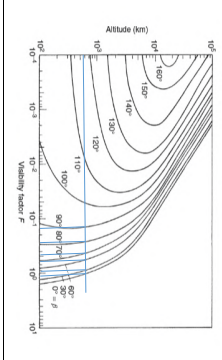
Parameters	Value	Unit
$J_s$	1414	W/m <sup>2</sup>
$f$	1.25	
$a$	0.8	
$e$	0.8	
$a/e$	1.12	
$Q$	0 W	
$f_{in}$	0.628	W/m <sup>2</sup>
$L_E$	550 km	
Orbit alt.	550 km	
$J_p$	232	W/m <sup>2</sup>
$A_{s,surface}$	0.048839	m <sup>2</sup>
$A_{s,absorb}$	0.031891	m <sup>2</sup>
$A_{s,planetary}$	0.00300211	m <sup>2</sup>
albedo	0.275	
$J_a$	568.8325	W/m <sup>2</sup>
$B$	0	Wm <sup>-2</sup> K <sup>-4</sup>
$B_0$	5.67E-08	Wm <sup>-2</sup> K <sup>-4</sup>
$T$	270258825	K
$T(TC)$	-2.891619758	C

Description	Parameter/Value	Unit
Solar radiation intensity (constant)	$J_s$	W/m <sup>2</sup>
Absorbance (black paint)	$a$	
Emissance (black paint)	$e$	
Internal power	$Q$	W
Fraction of sunlit orbit	$f_{in}$	
Planetary radiation intensity	$J_p$	W/m <sup>2</sup>
	$A_{s,surface}$	m <sup>2</sup>
	$A_{s,absorb}$	m <sup>2</sup>
	$A_{s,planetary}$	m <sup>2</sup>
	albedo	
	$J_a$	W/m <sup>2</sup>
	$B$	Wm <sup>-2</sup> K <sup>-4</sup>
	$T$	K
	$T(TC)$	C

NA: Very much an assumption



Parameters	Value	Unit	Description
$J_s$	1414	W/m <sup>2</sup>	Solar radiation intensity (constant)
$f_s$	1.15		Volatility factor
$e$	0.28		Emittance (black paint)
$a/e$	1.12		Emittance (black paint)
$Q$	0 W		Internal power
$f$	0.6277 %		Fraction of sunlight orbit
$J_{in}$	224	W/m <sup>2</sup>	Planetary radiation intensity
$J_p$	224	W/m <sup>2</sup>	
A, surface	0.048639	m <sup>2</sup>	
A, solar	0.01316	m <sup>2</sup>	
A, albedo	0.003	m <sup>2</sup>	
A, planeter	0.003	m <sup>2</sup>	
A, absor	500.335	W/m <sup>2</sup>	
$J_{in}$	5.67E-08	Wm <sup>-2</sup> K <sup>-4</sup>	
B	0 °		
58	269.413	K	
T	269.413	K	
T(C)	-3.7981	°C	



$$J_o = J_o A F$$

$$f_s = \frac{1}{180^\circ} \cos^{-1} \left[ \frac{(h_s + 2R_p)^{1/2}}{(R_s + h_s)^{1/2}} \right] f$$

$$= 0 \text{ if } |\beta| \geq \beta^*$$

$$\beta^* = \sin^{-1} \left[ \frac{R}{R+h_s} \right] \quad 0^\circ \leq \beta^* \leq 90^\circ$$

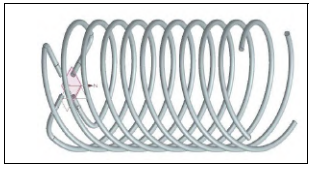
$$|\beta| < \beta^*$$

$$\left( \frac{R}{R+h_s} \right)^2 = \cos^2 \beta$$

$$\sigma = \text{Stefan-Boltzmann constant } (5.67 \times 10^{-8} \text{ W m}^{-2} \text{ K}^{-4})$$

$$J_{in} = \frac{A_{outer} J_o}{A_{sur}} + \frac{A_{outer} J_o}{A_{sur}} + \frac{A_{outer} J_o}{A_{sur}}$$

$$J_{in} = \frac{A_{outer} J_o}{A_{sur}} + \frac{A_{outer} J_o}{A_{sur}} + \frac{A_{outer} J_o}{A_{sur}}$$



Area Calculations:

$p$	0.003955 m
$N$	0.03548 m
$OD$	0.04391 m
$ID$	0.04009 m
$W$	0.042 m
$L$	0.035394 m
$L$	0.08996 m

Outer surface Area: 0.01241 m<sup>2</sup>  
 A, albedo and planet: 0.048639 m<sup>2</sup>  
 A, absor: 0.003 m<sup>2</sup>  
 A, planeter: 0.003 m<sup>2</sup>  
 A, solar: 0.01316 m<sup>2</sup>  
 Average of A's: 0.01316 m<sup>2</sup>

$$L_1 = (2\pi r)^2 + p^2 + v_{ax}^2$$

$$L_r = L_1 \times N$$

$$A_{outer} = L_r \times \pi \times OD$$

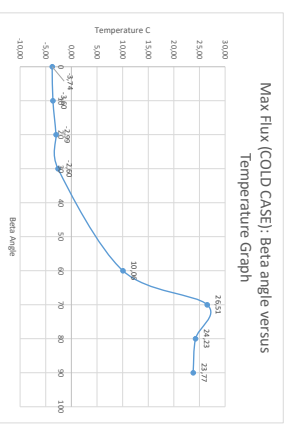
Parameters	Value	Unit	Description
$J_s$	1414	W/m <sup>2</sup>	Solar radiation intensity (constant)
$f_s$	1.15		Volatility factor
$e$	0.28		Emittance (black paint)
$a/e$	1.12		Emittance (black paint)
$Q$	0 W		Internal power
$f$	0.6277 %		Fraction of sunlight orbit
$J_{in}$	224	W/m <sup>2</sup>	Planetary radiation intensity
$J_p$	224	W/m <sup>2</sup>	
A, surface	0.048639	m <sup>2</sup>	
A, solar	0.01316	m <sup>2</sup>	
A, albedo	0.003	m <sup>2</sup>	
A, planeter	0.003	m <sup>2</sup>	
A, absor	500.335	W/m <sup>2</sup>	
$J_{in}$	5.67E-08	Wm <sup>-2</sup> K <sup>-4</sup>	
B	0 °		
58	269.413	K	
T	269.413	K	
T(C)	-3.7981	°C	

NB: Very much an assumption

Parameters	Value	Unit	Description
$J_s$	1414	W/m <sup>2</sup>	Solar radiation intensity (constant)
$f_s$	1.15		Volatility factor
$e$	0.28		Emittance (black paint)
$a/e$	1.12		Emittance (black paint)
$Q$	0 W		Internal power
$f$	0.6277 %		Fraction of sunlight orbit
$J_{in}$	224	W/m <sup>2</sup>	Planetary radiation intensity
$J_p$	224	W/m <sup>2</sup>	
A, surface	0.048639	m <sup>2</sup>	
A, solar	0.01316	m <sup>2</sup>	
A, albedo	0.003	m <sup>2</sup>	
A, planeter	0.003	m <sup>2</sup>	
A, absor	494.9	W/m <sup>2</sup>	
$J_{in}$	5.67E-08	Wm <sup>-2</sup> K <sup>-4</sup>	
B	0 °		
58	270.549	K	
T	270.549	K	
T(C)	-2.9879	°C	

Parameters	Value	Unit	Description
$J_s$	1414	W/m <sup>2</sup>	Solar radiation intensity (constant)
$f_s$	1.15		Volatility factor
$e$	0.28		Emittance (black paint)
$a/e$	1.12		Emittance (black paint)
$Q$	0 W		Internal power
$f$	0.6277 %		Fraction of sunlight orbit
$J_{in}$	224	W/m <sup>2</sup>	Planetary radiation intensity
$J_p$	224	W/m <sup>2</sup>	
A, surface	0.048639	m <sup>2</sup>	
A, solar	0.01316	m <sup>2</sup>	
A, albedo	0.003	m <sup>2</sup>	
A, planeter	0.003	m <sup>2</sup>	
A, absor	494.9	W/m <sup>2</sup>	
$J_{in}$	5.67E-08	Wm <sup>-2</sup> K <sup>-4</sup>	
B	0 °		
58	270.549	K	
T	270.549	K	
T(C)	-2.9879	°C	

Parameters	Value	Unit	Description
$J_s$	1414	W/m <sup>2</sup>	Solar radiation intensity (constant)
$f_s$	1.15		Volatility factor
$e$	0.28		Emittance (black paint)
$a/e$	1.12		Emittance (black paint)
$Q$	0 W		Internal power
$f$	0.6277 %		Fraction of sunlight orbit
$J_{in}$	224	W/m <sup>2</sup>	Planetary radiation intensity
$J_p$	224	W/m <sup>2</sup>	
A, surface	0.048639	m <sup>2</sup>	
A, solar	0.01316	m <sup>2</sup>	
A, albedo	0.003	m <sup>2</sup>	
A, planeter	0.003	m <sup>2</sup>	
A, absor	494.9	W/m <sup>2</sup>	
$J_{in}$	5.67E-08	Wm <sup>-2</sup> K <sup>-4</sup>	
B	0 °		
58	270.549	K	
T	270.549	K	
T(C)	-2.9879	°C	



Parameter/Value	Unit	Description
J <sub>s</sub>	1414 W/m <sup>2</sup>	Solar radiation intensity (constant)
F	0.9	Visibility factor
f	0.8	Frontal factor (Black paint)
e	0.8	Emissivity (Black paint)
a/e	1.12	Ratio of absorptance to emissivity
Q	0 W	Internal power
f	0.785 %	Fraction of sunlight orbit
J <sub>e</sub>	237 W/m <sup>2</sup>	Planetary radiation intensity
J <sub>o</sub>	224 W/m <sup>2</sup>	Planetary radiation intensity
A <sub>o</sub> surface	0.048639 m <sup>2</sup>	
A <sub>o</sub> solar	0.01316 m <sup>2</sup>	
A <sub>o</sub> albedo	0.003 m <sup>2</sup>	
A <sub>o</sub> planetar	0.003 m <sup>2</sup>	
A <sub>o</sub> photo	407232 W/m <sup>2</sup>	
J <sub>o</sub>	60 °	
B	5.67E-08 Wm <sup>-2</sup> K <sup>-4</sup>	
T	283.2868 K	
T (C)	10.05097 °C	

Parameter/Value	Unit	Description
J <sub>s</sub>	1414 W/m <sup>2</sup>	Solar radiation intensity (constant)
F	0.9	Visibility factor
f	0.8	Frontal factor (Black paint)
e	0.8	Emissivity (Black paint)
a/e	1.12	Ratio of absorptance to emissivity
Q	0 W	Internal power
f	1 %	Fraction of sunlight orbit
J <sub>e</sub>	237 W/m <sup>2</sup>	Planetary radiation intensity
J <sub>o</sub>	224 W/m <sup>2</sup>	Planetary radiation intensity
A <sub>o</sub> surface	0.048639 m <sup>2</sup>	
A <sub>o</sub> solar	0.01316 m <sup>2</sup>	
A <sub>o</sub> albedo	0.003 m <sup>2</sup>	
A <sub>o</sub> planetar	0.003 m <sup>2</sup>	
A <sub>o</sub> photo	3512316 W/m <sup>2</sup>	
J <sub>o</sub>	70 °	
B	5.67E-08 Wm <sup>-2</sup> K <sup>-4</sup>	
T	296.6537 K	
T (C)	23.50572 °C	

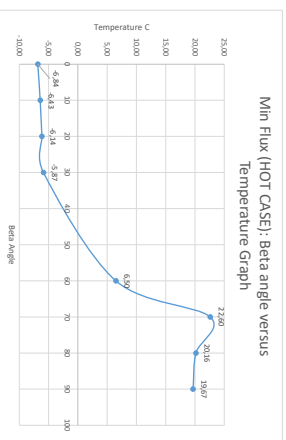
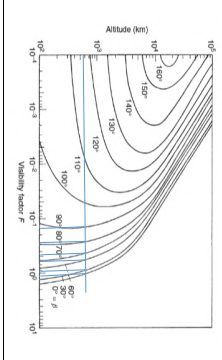
Parameter/Value	Unit	Description
J <sub>s</sub>	1414 W/m <sup>2</sup>	Solar radiation intensity (constant)
F	0.25	Visibility factor
f	0.8	Frontal factor (Black paint)
e	0.8	Emissivity (Black paint)
a/e	1.12	Ratio of absorptance to emissivity
Q	0 W	Internal power
f	1 %	Fraction of sunlight orbit
J <sub>e</sub>	237 W/m <sup>2</sup>	Planetary radiation intensity
J <sub>o</sub>	224 W/m <sup>2</sup>	Planetary radiation intensity
A <sub>o</sub> surface	0.048639 m <sup>2</sup>	
A <sub>o</sub> solar	0.01316 m <sup>2</sup>	
A <sub>o</sub> albedo	0.003 m <sup>2</sup>	
A <sub>o</sub> planetar	0.003 m <sup>2</sup>	
A <sub>o</sub> photo	148.47 W/m <sup>2</sup>	
J <sub>o</sub>	80 °	
B	5.67E-08 Wm <sup>-2</sup> K <sup>-4</sup>	
T	297.867 K	
T (C)	24.71588 °C	

Parameter/Value	Unit	Description
J <sub>s</sub>	1414 W/m <sup>2</sup>	Solar radiation intensity (constant)
F	0.9	Visibility factor
f	0.8	Frontal factor (Black paint)
e	0.8	Emissivity (Black paint)
a/e	1.12	Ratio of absorptance to emissivity
Q	0 W	Internal power
f	1 %	Fraction of sunlight orbit
J <sub>e</sub>	237 W/m <sup>2</sup>	Planetary radiation intensity
J <sub>o</sub>	224 W/m <sup>2</sup>	Planetary radiation intensity
A <sub>o</sub> surface	0.048639 m <sup>2</sup>	
A <sub>o</sub> solar	0.01316 m <sup>2</sup>	
A <sub>o</sub> albedo	0.003 m <sup>2</sup>	
A <sub>o</sub> planetar	0.003 m <sup>2</sup>	
A <sub>o</sub> photo	108.171 W/m <sup>2</sup>	
J <sub>o</sub>	90 °	
B	5.67E-08 Wm <sup>-2</sup> K <sup>-4</sup>	
T	286.6233 K	
T (C)	13.47228 °C	

Parameter/Value	Unit	Description
J <sub>s</sub>	1414 W/m <sup>2</sup>	Solar radiation intensity (constant)
F	0.9	Visibility factor
f	0.8	Frontal factor (Black paint)
e	0.8	Emissivity (Black paint)
a/e	1.12	Ratio of absorptance to emissivity
Q	0 W	Internal power
f	1 %	Fraction of sunlight orbit
J <sub>e</sub>	237 W/m <sup>2</sup>	Planetary radiation intensity
J <sub>o</sub>	224 W/m <sup>2</sup>	Planetary radiation intensity
A <sub>o</sub> surface	0.048639 m <sup>2</sup>	
A <sub>o</sub> solar	0.01316 m <sup>2</sup>	
A <sub>o</sub> albedo	0.003 m <sup>2</sup>	
A <sub>o</sub> planetar	0.003 m <sup>2</sup>	
A <sub>o</sub> photo	550 W/m <sup>2</sup>	
J <sub>o</sub>	90 °	
B	5.67E-08 Wm <sup>-2</sup> K <sup>-4</sup>	
T	296.6537 K	
T (C)	23.50572 °C	

Parameter/Value	Unit	Description
J <sub>s</sub>	1414 W/m <sup>2</sup>	Solar radiation intensity (constant)
F	0.9	Visibility factor
f	0.8	Frontal factor (Black paint)
e	0.8	Emissivity (Black paint)
a/e	1.12	Ratio of absorptance to emissivity
Q	0 W	Internal power
f	1 %	Fraction of sunlight orbit
J <sub>e</sub>	237 W/m <sup>2</sup>	Planetary radiation intensity
J <sub>o</sub>	224 W/m <sup>2</sup>	Planetary radiation intensity
A <sub>o</sub> surface	0.048639 m <sup>2</sup>	
A <sub>o</sub> solar	0.01316 m <sup>2</sup>	
A <sub>o</sub> albedo	0.003 m <sup>2</sup>	
A <sub>o</sub> planetar	0.003 m <sup>2</sup>	
A <sub>o</sub> photo	407232 W/m <sup>2</sup>	
J <sub>o</sub>	60 °	
B	5.67E-08 Wm <sup>-2</sup> K <sup>-4</sup>	
T	283.2868 K	
T (C)	10.05097 °C	

Parameters	Value	Unit	Description
$J_s$	1332	W/m <sup>2</sup>	Solar radiation intensity (constant)
$J_p$	1.15	W/m <sup>2</sup>	Planetary radiation intensity (constant)
$f$	0.23	W/m <sup>2</sup>	Volatility factor
$e$	0.8		Emittance (Black paint)
$a/e$	1.12		Emittance (Black paint)
$Q$	0 W		Internal power
$f$	0.6277 %		Fraction of sunlight
$J_{in}$	232	W/m <sup>2</sup>	Planetary radiation intensity
$J_{out}$	232	W/m <sup>2</sup>	Planetary radiation intensity
A, surface	0.048639	m <sup>2</sup>	
A, solar	0.01316	m <sup>2</sup>	
A, albedo	0.003	m <sup>2</sup>	
A, planetary	0.003	m <sup>2</sup>	
$J_{in}$	560.165	W/m <sup>2</sup>	
$J_{out}$	0		
B	5.67E-08	Wm <sup>-2</sup> K <sup>-4</sup>	
S8	10		
T	266.3239	K	
T(C)	-5.6899	°C	



Parameters	Value	Unit	Description
$J_s$	1332	W/m <sup>2</sup>	Solar radiation intensity (constant)
$J_p$	1.15	W/m <sup>2</sup>	Planetary radiation intensity (constant)
$f$	0.23	W/m <sup>2</sup>	Volatility factor
$e$	0.8		Emittance (Black paint)
$a/e$	1.12		Emittance (Black paint)
$Q$	0 W		Internal power
$f$	0.6277 %		Fraction of sunlight
$J_{in}$	232	W/m <sup>2</sup>	Planetary radiation intensity
$J_{out}$	232	W/m <sup>2</sup>	Planetary radiation intensity
A, surface	0.048639	m <sup>2</sup>	
A, solar	0.01316	m <sup>2</sup>	
A, albedo	0.003	m <sup>2</sup>	
A, planetary	0.003	m <sup>2</sup>	
$J_{in}$	522.144	W/m <sup>2</sup>	
$J_{out}$	0		
B	5.67E-08	Wm <sup>-2</sup> K <sup>-4</sup>	
S8	10		
T	267.0134	K	
T(C)	-5.1586	°C	

$$J_o = J_o A F$$

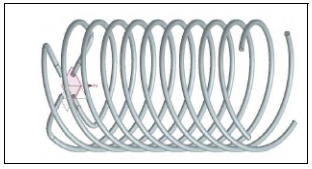
$$f = \frac{1}{180^\circ} \cos^{-1} \left[ \frac{(h^2 + 2Rb)^{1/2}}{(R + h) \cos \beta} \right] \quad \text{if } |\beta| < \beta^*$$

$$= 0 \quad \text{if } |\beta| \geq \beta^*$$

$$\beta^* = \sin^{-1} \left[ \frac{R}{R+h} \right] \quad 0^\circ \leq \beta^* \leq 90^\circ$$

$$\sigma = \text{Stefan-Boltzmann constant } (5.67 \times 10^{-8} \text{ W m}^{-2} \text{ K}^{-4})$$

$$J_{in} = A_{outer} J_o + A_{in} J_{atm} \sigma \epsilon + A_{in} J_{atm} \sigma \epsilon + A_{in} J_{atm} \sigma \epsilon$$



Area Calculations:	Value	Unit
$P$	0.003955	m
$N$	0.03548	m
$OD$	2.5	m
$ID$	0.04391	m
$W$	0.04009	m
$L$	0.042	m
$L_{in}$	0.035394	m
$L_{out}$	0.08986	m

$$L_1 = [(2\pi r)^2 + p^2]^{1/2}$$

$$L_r = L_1 \times N$$

$$A_{outer} = L_r \times \pi \times OD$$

Parameters	Value	Unit	Description
$J_s$	1332	W/m <sup>2</sup>	Solar radiation intensity (constant)
$J_p$	1.15	W/m <sup>2</sup>	Planetary radiation intensity (constant)
$f$	0.23	W/m <sup>2</sup>	Volatility factor
$e$	0.8		Emittance
$a/e$	1.12		Emittance
$Q$	0 W		Internal power
$f$	0.6277 %		Fraction of sunlight
$J_{in}$	232	W/m <sup>2</sup>	Planetary radiation intensity
$J_{out}$	232	W/m <sup>2</sup>	Planetary radiation intensity
A, surface	0.048639	m <sup>2</sup>	
A, solar	0.01316	m <sup>2</sup>	
A, albedo	0.003	m <sup>2</sup>	
A, planetary	0.003	m <sup>2</sup>	
$J_{in}$	560.165	W/m <sup>2</sup>	
$J_{out}$	0		
B	5.67E-08	Wm <sup>-2</sup> K <sup>-4</sup>	
S8	10		
T	266.7391	K	
T(C)	-5.4888	°C	

$$J_{in} = A_{outer} J_o + A_{in} J_{atm} \sigma \epsilon + A_{in} J_{atm} \sigma \epsilon + A_{in} J_{atm} \sigma \epsilon$$

Parameters	Value	Unit	Description
$J_s$	1332	W/m <sup>2</sup>	Solar radiation intensity (constant)
$J_p$	1.15	W/m <sup>2</sup>	Planetary radiation intensity (constant)
$f$	0.23	W/m <sup>2</sup>	Volatility factor
$e$	0.8		Emittance (Black paint)
$a/e$	1.12		Emittance (Black paint)
$Q$	0 W		Internal power
$f$	0.649 %		Fraction of sunlight
$J_{in}$	520	W/m <sup>2</sup>	Planetary radiation intensity
$J_{out}$	520	W/m <sup>2</sup>	Planetary radiation intensity
A, surface	0.048639	m <sup>2</sup>	
A, solar	0.01316	m <sup>2</sup>	
A, albedo	0.003	m <sup>2</sup>	
A, planetary	0.003	m <sup>2</sup>	
$J_{in}$	424.508	W/m <sup>2</sup>	
$J_{out}$	30		
B	5.67E-08	Wm <sup>-2</sup> K <sup>-4</sup>	
S8	10		
T	267.2898	K	
T(C)	-5.6899	°C	

Parameters	Value	Unit	Description
$J_s$	1332	W/m <sup>2</sup>	Solar radiation intensity (constant)
$J_p$	1.15	W/m <sup>2</sup>	Planetary radiation intensity (constant)
$f$	0.23	W/m <sup>2</sup>	Volatility factor
$e$	0.8		Emittance (Black paint)
$a/e$	1.12		Emittance (Black paint)
$Q$	0 W		Internal power
$f$	0.649 %		Fraction of sunlight
$J_{in}$	520	W/m <sup>2</sup>	Planetary radiation intensity
$J_{out}$	520	W/m <sup>2</sup>	Planetary radiation intensity
A, surface	0.048639	m <sup>2</sup>	
A, solar	0.01316	m <sup>2</sup>	
A, albedo	0.003	m <sup>2</sup>	
A, planetary	0.003	m <sup>2</sup>	
$J_{in}$	424.508	W/m <sup>2</sup>	
$J_{out}$	30		
B	5.67E-08	Wm <sup>-2</sup> K <sup>-4</sup>	
S8	10		
T	267.2898	K	
T(C)	-5.6899	°C	

NB: Very much an assumption

Parameter/Value	Unit	Description
J <sub>s</sub>	1332 W/m <sup>2</sup>	Solar radiation intensity (constant)
F	0.9	Visibility factor
f	0.25	Emittance (black paint)
e	0.8	Emittance (black paint)
a/e	1.12	Emittance (black paint)
Q	0 W	Internal power
f	0.7/85 %	Fraction of sunlight orbit
J <sub>e</sub>	237 W/m <sup>2</sup>	Orbit alt.
J <sub>p</sub>	232 W/m <sup>2</sup>	Orbit alt.
J <sub>o</sub>	0.048639 m <sup>2</sup>	Primary radiation intensity
A <sub>o</sub> surface	0.00316 m <sup>2</sup>	
A <sub>o</sub> solar	0.003 m <sup>2</sup>	
A <sub>o</sub> albedo	0.003 m <sup>2</sup>	
A <sub>o</sub> planet	0.003 m <sup>2</sup>	
A <sub>o</sub> bedo	419.58 W/m <sup>2</sup>	
J <sub>o</sub>	60 °	
B	5.67E-08 Wm <sup>-2</sup> K <sup>-4</sup>	
S <sub>B</sub>	279.8533 K	
T	279.8533 K	
T(C)	6.59418 °C	

Parameter/Value	Unit	Description
J <sub>s</sub>	1332 W/m <sup>2</sup>	Solar radiation intensity (constant)
F	0.9	Visibility factor
f	0.25	Emittance (black paint)
e	0.8	Emittance (black paint)
a/e	1.12	Emittance (black paint)
Q	0 W	Internal power
f	0.7/85 %	Fraction of sunlight orbit
J <sub>e</sub>	237 W/m <sup>2</sup>	Orbit alt.
J <sub>p</sub>	232 W/m <sup>2</sup>	Orbit alt.
J <sub>o</sub>	0.048639 m <sup>2</sup>	Primary radiation intensity
A <sub>o</sub> surface	0.00316 m <sup>2</sup>	
A <sub>o</sub> solar	0.003 m <sup>2</sup>	
A <sub>o</sub> albedo	0.003 m <sup>2</sup>	
A <sub>o</sub> planet	0.003 m <sup>2</sup>	
A <sub>o</sub> bedo	386.4432 W/m <sup>2</sup>	
J <sub>o</sub>	70 °	
B	5.67E-08 Wm <sup>-2</sup> K <sup>-4</sup>	
S <sub>B</sub>	295.2934 K	
T	295.2934 K	
T(C)	22.13937 °C	

Parameter/Value	Unit	Description
J <sub>s</sub>	1332 W/m <sup>2</sup>	Solar radiation intensity (constant)
F	0.25	Visibility factor
f	0.8	Emittance (black paint)
e	0.8	Emittance (black paint)
a/e	1.12	Emittance (black paint)
Q	0 W	Internal power
f	1 %	Fraction of sunlight orbit
J <sub>e</sub>	237 W/m <sup>2</sup>	Orbit alt.
J <sub>p</sub>	232 W/m <sup>2</sup>	Orbit alt.
J <sub>o</sub>	0.048639 m <sup>2</sup>	Primary radiation intensity
A <sub>o</sub> surface	0.00316 m <sup>2</sup>	
A <sub>o</sub> solar	0.003 m <sup>2</sup>	
A <sub>o</sub> albedo	0.003 m <sup>2</sup>	
A <sub>o</sub> planet	0.003 m <sup>2</sup>	
A <sub>o</sub> bedo	149.85 W/m <sup>2</sup>	
J <sub>o</sub>	80 °	
B	5.67E-08 Wm <sup>-2</sup> K <sup>-4</sup>	
S <sub>B</sub>	293.3127 K	
T	293.3127 K	
T(C)	20.1606 °C	

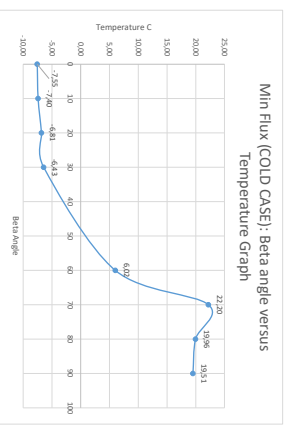
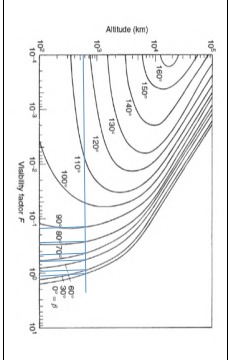
Parameter/Value	Unit	Description
J <sub>s</sub>	1332 W/m <sup>2</sup>	Solar radiation intensity (constant)
F	0.9	Visibility factor
f	0.25	Emittance (black paint)
e	0.8	Emittance (black paint)
a/e	1.12	Emittance (black paint)
Q	0 W	Internal power
f	0.7/85 %	Fraction of sunlight orbit
J <sub>e</sub>	237 W/m <sup>2</sup>	Orbit alt.
J <sub>p</sub>	232 W/m <sup>2</sup>	Orbit alt.
J <sub>o</sub>	0.048639 m <sup>2</sup>	Primary radiation intensity
A <sub>o</sub> surface	0.00316 m <sup>2</sup>	
A <sub>o</sub> solar	0.003 m <sup>2</sup>	
A <sub>o</sub> albedo	0.003 m <sup>2</sup>	
A <sub>o</sub> planet	0.003 m <sup>2</sup>	
A <sub>o</sub> bedo	550 W/m <sup>2</sup>	
J <sub>o</sub>	90 °	
B	5.67E-08 Wm <sup>-2</sup> K <sup>-4</sup>	
S <sub>B</sub>	320.3451 K	
T	320.3451 K	
T(C)	47.19181 °C	

Parameter/Value	Unit	Description
J <sub>s</sub>	1332 W/m <sup>2</sup>	Solar radiation intensity (constant)
F	0.9	Visibility factor
f	0.25	Emittance (black paint)
e	0.8	Emittance (black paint)
a/e	1.12	Emittance (black paint)
Q	0 W	Internal power
f	0.7/85 %	Fraction of sunlight orbit
J <sub>e</sub>	237 W/m <sup>2</sup>	Orbit alt.
J <sub>p</sub>	232 W/m <sup>2</sup>	Orbit alt.
J <sub>o</sub>	0.048639 m <sup>2</sup>	Primary radiation intensity
A <sub>o</sub> surface	0.00316 m <sup>2</sup>	
A <sub>o</sub> solar	0.003 m <sup>2</sup>	
A <sub>o</sub> albedo	0.003 m <sup>2</sup>	
A <sub>o</sub> planet	0.003 m <sup>2</sup>	
A <sub>o</sub> bedo	107.892 W/m <sup>2</sup>	
J <sub>o</sub>	90 °	
B	5.67E-08 Wm <sup>-2</sup> K <sup>-4</sup>	
S <sub>B</sub>	247E+08 K	
T	247E+08 K	
T(C)	247E+08 °C	

Parameter/Value	Unit	Description
J <sub>s</sub>	1332 W/m <sup>2</sup>	Solar radiation intensity (constant)
F	0.9	Visibility factor
f	0.25	Emittance (black paint)
e	0.8	Emittance (black paint)
a/e	1.12	Emittance (black paint)
Q	0 W	Internal power
f	0.7/85 %	Fraction of sunlight orbit
J <sub>e</sub>	237 W/m <sup>2</sup>	Orbit alt.
J <sub>p</sub>	232 W/m <sup>2</sup>	Orbit alt.
J <sub>o</sub>	0.048639 m <sup>2</sup>	Primary radiation intensity
A <sub>o</sub> surface	0.00316 m <sup>2</sup>	
A <sub>o</sub> solar	0.003 m <sup>2</sup>	
A <sub>o</sub> albedo	0.003 m <sup>2</sup>	
A <sub>o</sub> planet	0.003 m <sup>2</sup>	
A <sub>o</sub> bedo	247E+08 W/m <sup>2</sup>	
J <sub>o</sub>	247E+08 °	
B	5.67E-08 Wm <sup>-2</sup> K <sup>-4</sup>	
S <sub>B</sub>	247E+08 K	
T	247E+08 K	
T(C)	247E+08 °C	



Parameters	Value	Unit	Description
$J_s$	1332	W/m <sup>2</sup>	Solar radiation intensity (constant)
$F_p$	1.45	W/m <sup>2</sup>	Solar radiat
$f$	0.2	W/m <sup>2</sup>	Volubility factor
$e$	0.8	W/m <sup>2</sup>	Emittance (black paint)
$a/e$	1.12	W/m <sup>2</sup>	Emittance (black paint)
$Q$	0 W	W	Internal power
$f$	0.6277 %	%	Fraction of sunlight orbit
$J_e$	237	W/m <sup>2</sup>	Planetary radiation intensity
$J_p$	224	W/m <sup>2</sup>	Planetary radiation intensity
$J_{p,surface}$	0.048639	m <sup>2</sup>	A. surface
$A_solar$	0.01316	m <sup>2</sup>	A. solar
$A_{albedo}$	0.003	m <sup>2</sup>	A. albedo
$A_{planet}$	0.003	m <sup>2</sup>	A. planet
$J_{albedo}$	473.193	W/m <sup>2</sup>	A. albedo
$J_{planet}$	10	W/m <sup>2</sup>	A. planet
$B$	5.67E-08	Wm <sup>-2</sup> K <sup>-4</sup>	Stefan-Boltzmann constant
$T$	265.8205	K	Temperature
$T(TC)$	-7.35939	°C	Temperature



Parameters	Value	Unit	Description
$J_s$	1332	W/m <sup>2</sup>	Solar radiation intensity (constant)
$F_p$	1.45	W/m <sup>2</sup>	Solar radiat
$f$	0.2	W/m <sup>2</sup>	Volubility factor
$e$	0.8	W/m <sup>2</sup>	Emittance (black paint)
$a/e$	1.12	W/m <sup>2</sup>	Emittance (black paint)
$Q$	0 W	W	Internal power
$f$	0.6277 %	%	Fraction of sunlight orbit
$J_e$	237	W/m <sup>2</sup>	Planetary radiation intensity
$J_p$	224	W/m <sup>2</sup>	Planetary radiation intensity
$J_{p,surface}$	0.048639	m <sup>2</sup>	A. surface
$A_solar$	0.01316	m <sup>2</sup>	A. solar
$A_{albedo}$	0.003	m <sup>2</sup>	A. albedo
$A_{planet}$	0.003	m <sup>2</sup>	A. planet
$J_{albedo}$	473.193	W/m <sup>2</sup>	A. albedo
$J_{planet}$	10	W/m <sup>2</sup>	A. planet
$B$	5.67E-08	Wm <sup>-2</sup> K <sup>-4</sup>	Stefan-Boltzmann constant
$T$	265.8205	K	Temperature
$T(TC)$	-7.35939	°C	Temperature

$$J_e = J_e A_e$$

$$f_s = \frac{1}{180^\circ} \cos^{-1} \left[ \frac{(R^2 + 2RH)^{1/2}}{(R+H)\cos\beta} \right] \quad \text{if } |\beta| < \beta^*$$

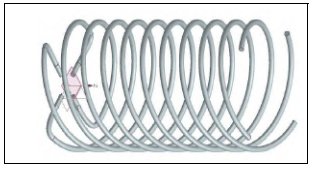
$$= 0 \quad \text{if } |\beta| \geq \beta^*$$

$$\beta^* = \sin^{-1} \left[ \frac{R}{R+H} \right] \quad 0^\circ \leq \beta^* \leq 90^\circ$$

$$\sigma = \text{Stefan-Boltzmann constant } (5.67 \times 10^{-8} \text{ W m}^{-2} \text{ K}^{-4})$$

$$1. \quad 237.7987 \quad 2. \quad 0.473782019$$

$$J_e = \frac{A_{albedo} J_{albedo}}{A_{surf} f_{albedo}} + \frac{A_{planet} J_{planet}}{A_{surf} f_{planet}} + \frac{A_{surface} J_{surface}}{A_{surf}}$$



Area Calculations:	Value	Unit
$P$	0.003955	m
$N$	0.03548	m
$OD$	2.5	m
$ID$	0.04391	m
$MD$	0.04009	m
$L_{albedo}$	0.042	m
$L_{planet}$	0.035394	m
$L_{t}$	0.08986	m

Outer surface Area:	0.01241	m <sup>2</sup>
A. albedo:	0.048639	m <sup>2</sup>
A. planet:	0.003	m <sup>2</sup>

$$|\beta| < \beta^*$$

$$K(4)$$

$$3. \quad \frac{A_{albedo} J_{albedo}}{A_{surf} f_{albedo}} + \frac{A_{planet} J_{planet}}{A_{surf} f_{planet}} + \frac{A_{surface} J_{surface}}{A_{surf}}$$

$$L_t = [(2\pi r)^2 + p^2]^{1/2}$$

$$L_r = [L_t \times N]$$

$$A_{outer} = L_r \times \pi \times OD$$

Parameters	Value	Unit	Description
$J_s$	1332	W/m <sup>2</sup>	Solar radiation intensity (constant)
$F_p$	1.45	W/m <sup>2</sup>	Solar radiat
$f$	0.2	W/m <sup>2</sup>	Volubility factor
$e$	0.8	W/m <sup>2</sup>	Emittance (black paint)
$a/e$	1.12	W/m <sup>2</sup>	Emittance (black paint)
$Q$	0 W	W	Internal power
$f$	0.6277 %	%	Fraction of sunlight orbit
$J_e$	237	W/m <sup>2</sup>	Planetary radiation intensity
$J_p$	224	W/m <sup>2</sup>	Planetary radiation intensity
$J_{p,surface}$	0.048639	m <sup>2</sup>	A. surface
$A_solar$	0.01316	m <sup>2</sup>	A. solar
$A_{albedo}$	0.003	m <sup>2</sup>	A. albedo
$A_{planet}$	0.003	m <sup>2</sup>	A. planet
$J_{albedo}$	473.193	W/m <sup>2</sup>	A. albedo
$J_{planet}$	10	W/m <sup>2</sup>	A. planet
$B$	5.67E-08	Wm <sup>-2</sup> K <sup>-4</sup>	Stefan-Boltzmann constant
$T$	265.7905	K	Temperature
$T(TC)$	-7.35939	°C	Temperature

Parameters	Value	Unit	Description
$J_s$	1332	W/m <sup>2</sup>	Solar radiation intensity (constant)
$F_p$	1.45	W/m <sup>2</sup>	Solar radiat
$f$	0.2	W/m <sup>2</sup>	Volubility factor
$e$	0.8	W/m <sup>2</sup>	Emittance (black paint)
$a/e$	1.12	W/m <sup>2</sup>	Emittance (black paint)
$Q$	0 W	W	Internal power
$f$	0.6277 %	%	Fraction of sunlight orbit
$J_e$	237	W/m <sup>2</sup>	Planetary radiation intensity
$J_p$	224	W/m <sup>2</sup>	Planetary radiation intensity
$J_{p,surface}$	0.048639	m <sup>2</sup>	A. surface
$A_solar$	0.01316	m <sup>2</sup>	A. solar
$A_{albedo}$	0.003	m <sup>2</sup>	A. albedo
$A_{planet}$	0.003	m <sup>2</sup>	A. planet
$J_{albedo}$	380.952	W/m <sup>2</sup>	A. albedo
$J_{planet}$	30	W/m <sup>2</sup>	A. planet
$B$	5.67E-08	Wm <sup>-2</sup> K <sup>-4</sup>	Stefan-Boltzmann constant
$T$	265.7915	K	Temperature
$T(TC)$	-6.9282	°C	Temperature

NB: Very much an assumption

Parameter/Value	Unit	Description
J <sub>s</sub>	1332 W/m <sup>2</sup>	Solar radiation intensity (constant)
F	0.9	Visibility factor
f	0.8	Emittance (black paint)
e	0.8	Emittance (black paint)
a/e	1.12	Ratio of absorptance to emittance
Q	0 W	Internal power
f	0.785 %	Fraction of sunlight orbit
J <sub>e</sub>	237 W/m <sup>2</sup>	Orbit alt.
J <sub>p</sub>	224 W/m <sup>2</sup>	Orbit alt.
J <sub>o</sub>	0.048639 m <sup>2</sup>	Primary radiation intensity
A <sub>o</sub> surface	0.048639 m <sup>2</sup>	
A <sub>o</sub> solar	0.01316 m <sup>2</sup>	
A <sub>o</sub> albedo	0.003 m <sup>2</sup>	
A <sub>o</sub> planetar	0.003 m <sup>2</sup>	
A <sub>o</sub> photo	388.615 W/m <sup>2</sup>	
J <sub>o</sub>	60 °	
B	5.67E-08 Wm <sup>-2</sup> K <sup>-4</sup>	
T	279.5895 K	
T(C)	67.5997 °C	

Parameter/Value	Unit	Description
J <sub>s</sub>	1332 W/m <sup>2</sup>	Solar radiation intensity (constant)
F	0.9	Visibility factor
f	0.8	Emittance (black paint)
e	0.8	Emittance (black paint)
a/e	1.12	Ratio of absorptance to emittance
Q	0 W	Internal power
f	1 %	Fraction of sunlight orbit
J <sub>e</sub>	237 W/m <sup>2</sup>	Orbit alt.
J <sub>p</sub>	224 W/m <sup>2</sup>	Orbit alt.
J <sub>o</sub>	0.048639 m <sup>2</sup>	Primary radiation intensity
A <sub>o</sub> surface	0.048639 m <sup>2</sup>	
A <sub>o</sub> solar	0.01316 m <sup>2</sup>	
A <sub>o</sub> albedo	0.003 m <sup>2</sup>	
A <sub>o</sub> planetar	0.003 m <sup>2</sup>	
A <sub>o</sub> photo	380.8688 W/m <sup>2</sup>	
J <sub>o</sub>	70 °	
B	5.67E-08 Wm <sup>-2</sup> K <sup>-4</sup>	
T	295.348 K	
T(C)	22.198 °C	

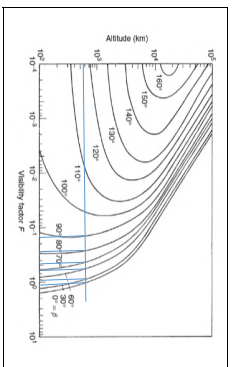
Parameter/Value	Unit	Description
J <sub>s</sub>	1332 W/m <sup>2</sup>	Solar radiation intensity (constant)
F	0.25	Visibility factor
f	0.8	Emittance (black paint)
e	0.8	Emittance (black paint)
a/e	1.12	Ratio of absorptance to emittance
Q	0 W	Internal power
f	1 %	Fraction of sunlight orbit
J <sub>e</sub>	237 W/m <sup>2</sup>	Orbit alt.
J <sub>p</sub>	224 W/m <sup>2</sup>	Orbit alt.
J <sub>o</sub>	0.048639 m <sup>2</sup>	Primary radiation intensity
A <sub>o</sub> surface	0.048639 m <sup>2</sup>	
A <sub>o</sub> solar	0.01316 m <sup>2</sup>	
A <sub>o</sub> albedo	0.003 m <sup>2</sup>	
A <sub>o</sub> planetar	0.003 m <sup>2</sup>	
A <sub>o</sub> photo	139.85 W/m <sup>2</sup>	
J <sub>o</sub>	80 °	
B	5.67E-08 Wm <sup>-2</sup> K <sup>-4</sup>	
T	293.038 K	
T(C)	19.898 °C	

Parameter/Value	Unit	Description
J <sub>s</sub>	1332 W/m <sup>2</sup>	Solar radiation intensity (constant)
F	0.9	Visibility factor
f	0.8	Emittance (black paint)
e	0.8	Emittance (black paint)
a/e	1.12	Ratio of absorptance to emittance
Q	0 W	Internal power
f	1 %	Fraction of sunlight orbit
J <sub>e</sub>	237 W/m <sup>2</sup>	Orbit alt.
J <sub>p</sub>	224 W/m <sup>2</sup>	Orbit alt.
J <sub>o</sub>	0.048639 m <sup>2</sup>	Primary radiation intensity
A <sub>o</sub> surface	0.048639 m <sup>2</sup>	
A <sub>o</sub> solar	0.01316 m <sup>2</sup>	
A <sub>o</sub> albedo	0.003 m <sup>2</sup>	
A <sub>o</sub> planetar	0.003 m <sup>2</sup>	
A <sub>o</sub> photo	101.2888 W/m <sup>2</sup>	
J <sub>o</sub>	90 °	
B	5.67E-08 Wm <sup>-2</sup> K <sup>-4</sup>	
T	303.6268 K	
T(C)	19.59881 °C	

Parameter/Value	Unit	Description
J <sub>s</sub>	1332 W/m <sup>2</sup>	Solar radiation intensity (constant)
F	0.9	Visibility factor
f	0.8	Emittance (black paint)
e	0.8	Emittance (black paint)
a/e	1.12	Ratio of absorptance to emittance
Q	0 W	Internal power
f	1 %	Fraction of sunlight orbit
J <sub>e</sub>	237 W/m <sup>2</sup>	Orbit alt.
J <sub>p</sub>	224 W/m <sup>2</sup>	Orbit alt.
J <sub>o</sub>	0.048639 m <sup>2</sup>	Primary radiation intensity
A <sub>o</sub> surface	0.048639 m <sup>2</sup>	
A <sub>o</sub> solar	0.01316 m <sup>2</sup>	
A <sub>o</sub> albedo	0.003 m <sup>2</sup>	
A <sub>o</sub> planetar	0.003 m <sup>2</sup>	
A <sub>o</sub> photo	101.2888 W/m <sup>2</sup>	
J <sub>o</sub>	90 °	
B	5.67E-08 Wm <sup>-2</sup> K <sup>-4</sup>	
T	303.6268 K	
T(C)	19.59881 °C	

Parameter/Value	Unit	Description
J <sub>s</sub>	1332 W/m <sup>2</sup>	Solar radiation intensity (constant)
F	0.9	Visibility factor
f	0.8	Emittance (black paint)
e	0.8	Emittance (black paint)
a/e	1.12	Ratio of absorptance to emittance
Q	0 W	Internal power
f	1 %	Fraction of sunlight orbit
J <sub>e</sub>	237 W/m <sup>2</sup>	Orbit alt.
J <sub>p</sub>	224 W/m <sup>2</sup>	Orbit alt.
J <sub>o</sub>	0.048639 m <sup>2</sup>	Primary radiation intensity
A <sub>o</sub> surface	0.048639 m <sup>2</sup>	
A <sub>o</sub> solar	0.01316 m <sup>2</sup>	
A <sub>o</sub> albedo	0.003 m <sup>2</sup>	
A <sub>o</sub> planetar	0.003 m <sup>2</sup>	
A <sub>o</sub> photo	101.2888 W/m <sup>2</sup>	
J <sub>o</sub>	90 °	
B	5.67E-08 Wm <sup>-2</sup> K <sup>-4</sup>	
T	303.6268 K	
T(C)	19.59881 °C	

Parameters	Value	Unit	Description
$J_s$	1414	W/m <sup>2</sup>	Solar radiation intensity (constant)
$\rho$	1.5		Voidage factor
$f$	0.28		Emittance (Black paint)
$e$	0.8		Emittance (Black paint)
$a/e$	1.12		Internal power
$Q$	1 W		Internal power
$Q_{int}$	0.628		Fraction of sunlight orbit
$L_E$	232	W/m <sup>2</sup>	
$L_{int}$	232	W/m <sup>2</sup>	Planetary radiation intensity
$J_p$	232	W/m <sup>2</sup>	
A, surface	0.048639	m <sup>2</sup>	
A, solar	0.01316	m <sup>2</sup>	
A, albedo	0.003	m <sup>2</sup>	
A, albedo	0.003	m <sup>2</sup>	
A, planetary	572.67	W/m <sup>2</sup>	
$J_a$	0		
B	5.67E-08	Wm <sup>-2</sup> K <sup>-4</sup>	
SB	0		
T	275.6212	K	
TTCQ	2471282	C	



$$J_a = J_s A F$$

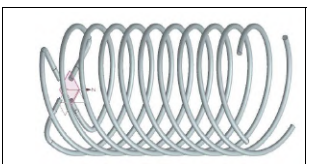
$$f_s = \frac{1}{180^\circ} \cos^{-1} \left[ \frac{(R+2RH)^2}{(R+H)^2} \right] \quad f_l = 0 \quad \text{if } |\beta| \geq 90^\circ$$

$$\beta^* = \sin^{-1} \left[ \frac{R}{R+H} \right] \quad 0^\circ \leq \beta^* \leq 90^\circ$$

$$\sigma = \text{Stefan-Boltzmann constant } (5.67 \times 10^{-8} \text{ W m}^{-2} \text{ K}^{-4})$$

- 24720767 1.44E+08 507958800
- 
- 

$$J^* = \frac{A_{\text{outer}} f_{\text{acc}} J_p}{A_{\text{sur}} f_{\text{acc}} \sigma} + \frac{Q}{A_{\text{sur}} f_{\text{acc}} \sigma} + \frac{A_{\text{outer}} J_a}{A_{\text{sur}}}$$



Area Calculations:

$\rho$	0.00955 m
N	0.01548 m
OD	2.5
ID	0.04391 m
MD	0.04709
L	0.242
L <sub>total</sub>	0.035394
L <sub>T</sub>	0.08986

Outer Surface Area:  
4.626 0.01241 m<sup>2</sup>

A. albedo and planet  
0.003

A. solar  
0.024819

A. surface A  
0.00316 m<sup>2</sup>

Average of A's  
0.01316 m<sup>2</sup>

$$r |\beta| < \beta^*$$

$$r \ll 1 \quad (4)$$

$$\frac{3}{A_{\text{sur}} f_{\text{acc}} \sigma} \left( \frac{\alpha}{\epsilon} \right) (f)$$

$$L_1 = [C(\pi r)^2 + p^2]^{1/2}$$

$$L_T = [L_1 \times N]$$

$$A_{\text{outer}} = L_T \times \pi \times OD$$

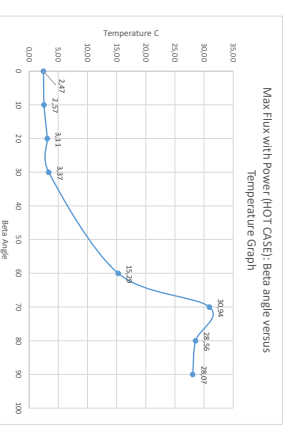
NB: Very much an assumption

Parameters	Value	Unit
$J_s$	1414	W/m <sup>2</sup>
$\rho$	1.5	
$f$	0.28	
$e$	0.8	
$a/e$	1.12	
$Q$	1 W	
$Q_{int}$	0.628	
$L_E$	232	W/m <sup>2</sup>
$L_{int}$	232	W/m <sup>2</sup>
$J_p$	232	W/m <sup>2</sup>
A, surface	0.048639	m <sup>2</sup>
A, solar	0.01316	m <sup>2</sup>
A, albedo	0.00300271	m <sup>2</sup>
A, albedo	0.00300271	m <sup>2</sup>
A, planetary	564.9315	W/m <sup>2</sup>
$J_a$	0	
B	5.67E-08	Wm <sup>-2</sup> K <sup>-4</sup>
SB	0	
T	275.215521	K
TTCQ	2.595082E2	C

Description	Parameter	Value	Unit
Solar radiation intensity (constant)	$J_s$	1414	W/m <sup>2</sup>
Voidage factor	$\rho$	1.5	
Emittance (Black paint)	$f$	0.28	
Emittance (Black paint)	$e$	0.8	
Internal power	$Q$	1 W	
Fraction of sunlight orbit	$Q_{int}$	0.628	
	$L_E$	232	W/m <sup>2</sup>
	$L_{int}$	232	W/m <sup>2</sup>
	$J_p$	232	W/m <sup>2</sup>
Planetary radiation intensity	A, surface	0.048639	m <sup>2</sup>
	A, solar	0.01316	m <sup>2</sup>
	A, albedo	0.003	m <sup>2</sup>
	A, albedo	0.003	m <sup>2</sup>
	A, planetary	554.288	W/m <sup>2</sup>
	$J_a$	0	
	B	5.67E-08	Wm <sup>-2</sup> K <sup>-4</sup>
	SB	0	
	T	275.21552	K
	TTCQ	3.133834	C

Description	Parameter	Value	Unit
Solar radiation intensity (constant)	$J_s$	1414	W/m <sup>2</sup>
Voidage factor	$\rho$	1.5	
Emittance (Black paint)	$f$	0.28	
Emittance (Black paint)	$e$	0.8	
Internal power	$Q$	1 W	
Fraction of sunlight orbit	$Q_{int}$	0.628	
	$L_E$	232	W/m <sup>2</sup>
	$L_{int}$	232	W/m <sup>2</sup>
	$J_p$	232	W/m <sup>2</sup>
Planetary radiation intensity	A, surface	0.048639	m <sup>2</sup>
	A, solar	0.01316	m <sup>2</sup>
	A, albedo	0.003	m <sup>2</sup>
	A, albedo	0.003	m <sup>2</sup>
	A, planetary	554.288	W/m <sup>2</sup>
	$J_a$	0	
	B	5.67E-08	Wm <sup>-2</sup> K <sup>-4</sup>
	SB	0	
	T	275.21552	K
	TTCQ	3.133834	C

Description	Parameter	Value	Unit
Solar radiation intensity (constant)	$J_s$	1414	W/m <sup>2</sup>
Voidage factor	$\rho$	1.5	
Emittance (Black paint)	$f$	0.28	
Emittance (Black paint)	$e$	0.8	
Internal power	$Q$	1 W	
Fraction of sunlight orbit	$Q_{int}$	0.628	
	$L_E$	232	W/m <sup>2</sup>
	$L_{int}$	232	W/m <sup>2</sup>
	$J_p$	232	W/m <sup>2</sup>
Planetary radiation intensity	A, surface	0.048639	m <sup>2</sup>
	A, solar	0.01316	m <sup>2</sup>
	A, albedo	0.003	m <sup>2</sup>
	A, albedo	0.003	m <sup>2</sup>
	A, planetary	451.066	W/m <sup>2</sup>
	$J_a$	0	
	B	5.67E-08	Wm <sup>-2</sup> K <sup>-4</sup>
	SB	0	
	T	276.5129	K
	TTCQ	3.398969	C



Description	Parameter	Value	Unit
Solar radiation intensity (constant)	$J_s$	1414	W/m <sup>2</sup>
Voidage factor	$\rho$	1.5	
Emittance (Black paint)	$f$	0.28	
Emittance (Black paint)	$e$	0.8	
Internal power	$Q$	1 W	
Fraction of sunlight orbit	$Q_{int}$	0.628	
	$L_E$	232	W/m <sup>2</sup>
	$L_{int}$	232	W/m <sup>2</sup>
	$J_p$	232	W/m <sup>2</sup>
Planetary radiation intensity	A, surface	0.048639	m <sup>2</sup>
	A, solar	0.01316	m <sup>2</sup>
	A, albedo	0.003	m <sup>2</sup>
	A, albedo	0.003	m <sup>2</sup>
	A, planetary	554.288	W/m <sup>2</sup>
	$J_a$	0	
	B	5.67E-08	Wm <sup>-2</sup> K <sup>-4</sup>
	SB	0	
	T	275.21552	K
	TTCQ	3.133834	C

Description	Parameter	Value	Unit
Solar radiation intensity (constant)	$J_s$	1414	W/m <sup>2</sup>
Voidage factor	$\rho$	1.5	
Emittance (Black paint)	$f$	0.28	
Emittance (Black paint)	$e$	0.8	
Internal power	$Q$	1 W	
Fraction of sunlight orbit	$Q_{int}$	0.628	
	$L_E$	232	W/m <sup>2</sup>
	$L_{int}$	232	W/m <sup>2</sup>
	$J_p$	232	W/m <sup>2</sup>
Planetary radiation intensity	A, surface	0.048639	m <sup>2</sup>
	A, solar	0.01316	m <sup>2</sup>
	A, albedo	0.003	m <sup>2</sup>
	A, albedo	0.003	m <sup>2</sup>
	A, planetary	451.066	W/m <sup>2</sup>
	$J_a$	0	
	B	5.67E-08	Wm <sup>-2</sup> K <sup>-4</sup>
	SB	0	
	T	276.5129	K
	TTCQ	3.398969	C

Parameter	Value	Unit	Description
J <sub>s</sub>	1414	W/m <sup>2</sup>	Solar radiation intensity (constant)
F	0.09		Visibility factor
e	0.8		Emittance (black panel)
a/e	1.12		Emittance (black panel)
Q	1 W		Internal power
L <sub>E</sub>	0.785 %		Fraction of sunlight
J <sub>e</sub>	232	W/m <sup>2</sup>	Primary radiation intensity
J <sub>0</sub>	232	W/m <sup>2</sup>	Primary radiation intensity
A <sub>surface</sub>	0.00639	m <sup>2</sup>	
A <sub>solár</sub>	0.01316	m <sup>2</sup>	
A <sub>albedo</sub>	0.003	m <sup>2</sup>	
A <sub>diameter</sub>	0.003	m <sup>2</sup>	
A <sub>albedo</sub>	445.1	W/m <sup>2</sup>	
J <sub>0</sub>	60		
B	5.67E-08	Wm <sup>-2</sup> K <sup>-4</sup>	
T	288.8316	K	
T (°C)	15.6779	°C	

Parameter	Value	Unit	Description
J <sub>s</sub>	1414	W/m <sup>2</sup>	Solar radiation intensity (constant)
F	0.09		Visibility factor
e	0.8		Emittance (black panel)
a/e	1.12		Emittance (black panel)
Q	1 W		Internal power
L <sub>E</sub>	1 %		Fraction of sunlight
J <sub>e</sub>	232	W/m <sup>2</sup>	Primary radiation intensity
J <sub>0</sub>	232	W/m <sup>2</sup>	Primary radiation intensity
A <sub>surface</sub>	0.00639	m <sup>2</sup>	
A <sub>solár</sub>	0.01316	m <sup>2</sup>	
A <sub>albedo</sub>	0.003	m <sup>2</sup>	
A <sub>diameter</sub>	0.003	m <sup>2</sup>	
A <sub>albedo</sub>	380.5074	W/m <sup>2</sup>	
J <sub>0</sub>	70		
B	5.67E-08	Wm <sup>-2</sup> K <sup>-4</sup>	
T	304.0888	K	
T (°C)	30.9588	°C	

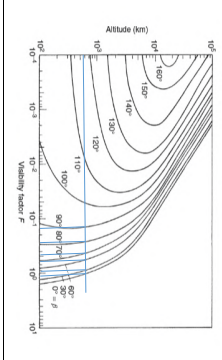
Parameter	Value	Unit	Description
J <sub>s</sub>	1414	W/m <sup>2</sup>	Solar radiation intensity (constant)
F	0.25		Visibility factor
e	0.8		Emittance (black panel)
a/e	1.12		Emittance (black panel)
Q	1 W		Internal power
L <sub>E</sub>	1		Fraction of sunlight
J <sub>e</sub>	237	W/m <sup>2</sup>	Primary radiation intensity
J <sub>0</sub>	232	W/m <sup>2</sup>	Primary radiation intensity
A <sub>surface</sub>	0.00639	m <sup>2</sup>	
A <sub>solár</sub>	0.01316	m <sup>2</sup>	
A <sub>albedo</sub>	0.003	m <sup>2</sup>	
A <sub>diameter</sub>	0.003	m <sup>2</sup>	
A <sub>albedo</sub>	159.075	W/m <sup>2</sup>	
J <sub>0</sub>	80		
B	5.67E-08	Wm <sup>-2</sup> K <sup>-4</sup>	
T	302.786	K	
T (°C)	29.5861	°C	

Parameter	Value	Unit	Description
J <sub>s</sub>	1414	W/m <sup>2</sup>	Solar radiation intensity (constant)
F	0.15		Visibility factor
e	0.8		Emittance (black panel)
a/e	1.12		Emittance (black panel)
Q	1 W		Internal power
L <sub>E</sub>	1 %		Fraction of sunlight
J <sub>e</sub>	232	W/m <sup>2</sup>	Primary radiation intensity
J <sub>0</sub>	232	W/m <sup>2</sup>	Primary radiation intensity
A <sub>surface</sub>	0.00639	m <sup>2</sup>	
A <sub>solár</sub>	0.01316	m <sup>2</sup>	
A <sub>albedo</sub>	0.003	m <sup>2</sup>	
A <sub>diameter</sub>	0.003	m <sup>2</sup>	
A <sub>albedo</sub>	114.534	W/m <sup>2</sup>	
J <sub>0</sub>	90		
B	5.67E-08	Wm <sup>-2</sup> K <sup>-4</sup>	
T	301.2314	K	
T (°C)	28.0738	°C	

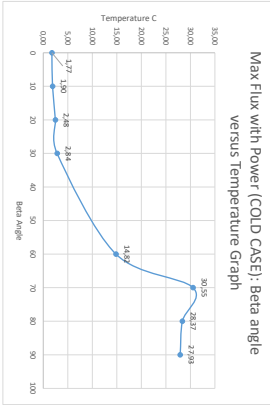
Parameter	Value	Unit	Description
J <sub>s</sub>	1414	W/m <sup>2</sup>	Solar radiation intensity (constant)
F	0.15		Visibility factor
e	0.8		Emittance (black panel)
a/e	1.12		Emittance (black panel)
Q	1 W		Internal power
L <sub>E</sub>	1 %		Fraction of sunlight
J <sub>e</sub>	232	W/m <sup>2</sup>	Primary radiation intensity
J <sub>0</sub>	232	W/m <sup>2</sup>	Primary radiation intensity
A <sub>surface</sub>	0.00639	m <sup>2</sup>	
A <sub>solár</sub>	0.01316	m <sup>2</sup>	
A <sub>albedo</sub>	0.003	m <sup>2</sup>	
A <sub>diameter</sub>	0.003	m <sup>2</sup>	
A <sub>albedo</sub>	114.534	W/m <sup>2</sup>	
J <sub>0</sub>	90		
B	5.67E-08	Wm <sup>-2</sup> K <sup>-4</sup>	
T	301.2314	K	
T (°C)	28.0738	°C	

Parameter	Value	Unit	Description
J <sub>s</sub>	1414	W/m <sup>2</sup>	Solar radiation intensity (constant)
F	0.15		Visibility factor
e	0.8		Emittance (black panel)
a/e	1.12		Emittance (black panel)
Q	1 W		Internal power
L <sub>E</sub>	1 %		Fraction of sunlight
J <sub>e</sub>	232	W/m <sup>2</sup>	Primary radiation intensity
J <sub>0</sub>	232	W/m <sup>2</sup>	Primary radiation intensity
A <sub>surface</sub>	0.00639	m <sup>2</sup>	
A <sub>solár</sub>	0.01316	m <sup>2</sup>	
A <sub>albedo</sub>	0.003	m <sup>2</sup>	
A <sub>diameter</sub>	0.003	m <sup>2</sup>	
A <sub>albedo</sub>	114.534	W/m <sup>2</sup>	
J <sub>0</sub>	90		
B	5.67E-08	Wm <sup>-2</sup> K <sup>-4</sup>	
T	301.2314	K	
T (°C)	28.0738	°C	

Parameters	Value	Unit	Description
J <sub>s</sub>	1414	W/m <sup>2</sup>	Solar radiation intensity (constant)
F	1.15		Visibility factor
e	0.28		Emittance (black paint)
a/e	1.12		Emittance (black paint)
Q	1 W		Internal power
f	0.6277 %		Fraction of sunlight orbit
J <sub>in</sub>	237	W/m <sup>2</sup>	
J <sub>out</sub>	224	W/m <sup>2</sup>	Planetary radiation intensity
A <sub>s</sub> surface	0.048639	m <sup>2</sup>	
A <sub>s</sub> solar	0.01316	m <sup>2</sup>	
A <sub>s</sub> albedo	0.003	m <sup>2</sup>	
A <sub>s</sub> planetary	0.003	m <sup>2</sup>	
A <sub>in</sub>	500.04	W/m <sup>2</sup>	
A <sub>out</sub>	0		
B	5.67E-08	Wm <sup>-2</sup> K <sup>-4</sup>	
T	274.9384	K	
T(C)	17.6972	°C	



Parameters	Value	Unit	Description
J <sub>s</sub>	1414	W/m <sup>2</sup>	Solar radiation intensity (constant)
F	1.15		Visibility factor
e	0.28		Emittance (black paint)
a/e	0.8		Emittance (black paint)
Q	1.12	W	Internal power
f	0.6364	%	Fraction of sunlight orbit
J <sub>in</sub>	550	W/m <sup>2</sup>	
J <sub>out</sub>	550	W/m <sup>2</sup>	Planetary radiation intensity
A <sub>s</sub> surface	0.048639	m <sup>2</sup>	
A <sub>s</sub> solar	0.01316	m <sup>2</sup>	
A <sub>s</sub> albedo	0.003	m <sup>2</sup>	
A <sub>s</sub> planetary	0.003	m <sup>2</sup>	
A <sub>in</sub>	494.9	W/m <sup>2</sup>	
A <sub>out</sub>	0		
B	5.67E-08	Wm <sup>-2</sup> K <sup>-4</sup>	
T	274.9384	K	
T(C)	24.9597	°C	



$$J_o = J_o A F$$

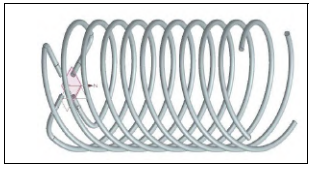
$$f = \frac{1}{180^\circ} \cos^{-1} \left[ \frac{(h^2 + 2Rb)^{1/2}}{(R + h) \cos \beta} \right] \quad \text{if } |b| < \beta$$

$$= 0 \quad \text{if } |b| \geq \beta$$

$$\beta^* = \sin^{-1} \left[ \frac{R}{R+h} \right] \quad 0^\circ \leq \beta^* \leq 90^\circ$$

$$\sigma = \text{Stefan-Boltzmann constant } (5.67 \times 10^{-8} \text{ W m}^{-2} \text{ K}^{-4})$$

$$J^* = \frac{1}{A_{\text{sur}}} \left( A_{\text{outer}} J_o + A_{\text{inner}} J_{\text{in}} \right)$$



Area Calculations:	Value	Unit
P	0.003955	m
N	0.03548	m
OD	0.04391	m
ID	0.04009	m
W0	0.042	m
L1	0.035394	m
L2	0.08986	m

Outer surface Area:	0.01241	m <sup>2</sup>
A <sub>in</sub> GDS:	0.048639	m <sup>2</sup>
A <sub>out</sub> Albedo panel:	0.003	
A <sub>out</sub> - Al:		
A <sub>total</sub> :	0.04819	
High surface A:	0.04819	
Low surface A:	0.04819	
Average of A's:	0.01316	m <sup>2</sup>

Parameters	Value	Unit	Description
J <sub>s</sub>	1414	W/m <sup>2</sup>	Solar radiation intensity (constant)
F	1.15		Visibility factor
e	0.28		Emittance (black paint)
a/e	0.8		Emittance (black paint)
Q	1.12	W	Internal power
f	0.648 %	%	Fraction of sunlight orbit
J <sub>in</sub>	550	W/m <sup>2</sup>	
J <sub>out</sub>	550	W/m <sup>2</sup>	Planetary radiation intensity
A <sub>s</sub> surface	0.048639	m <sup>2</sup>	
A <sub>s</sub> solar	0.01316	m <sup>2</sup>	
A <sub>s</sub> albedo	0.003	m <sup>2</sup>	
A <sub>s</sub> planetary	0.003	m <sup>2</sup>	
A <sub>in</sub>	494.9	W/m <sup>2</sup>	
A <sub>out</sub>	0		
B	5.67E-08	Wm <sup>-2</sup> K <sup>-4</sup>	
T	274.9384	K	
T(C)	24.9597	°C	

Parameters	Value	Unit	Description
J <sub>s</sub>	1414	W/m <sup>2</sup>	Solar radiation intensity (constant)
F	1.15		Visibility factor
e	0.28		Emittance (black paint)
a/e	0.8		Emittance (black paint)
Q	1.12	W	Internal power
f	0.648 %	%	Fraction of sunlight orbit
J <sub>in</sub>	550	W/m <sup>2</sup>	
J <sub>out</sub>	550	W/m <sup>2</sup>	Planetary radiation intensity
A <sub>s</sub> surface	0.048639	m <sup>2</sup>	
A <sub>s</sub> solar	0.01316	m <sup>2</sup>	
A <sub>s</sub> albedo	0.003	m <sup>2</sup>	
A <sub>s</sub> planetary	0.003	m <sup>2</sup>	
A <sub>in</sub>	494.9	W/m <sup>2</sup>	
A <sub>out</sub>	0		
B	5.67E-08	Wm <sup>-2</sup> K <sup>-4</sup>	
T	274.9384	K	
T(C)	24.9597	°C	

$$J^* = \frac{1}{A_{\text{sur}}} \left( A_{\text{outer}} J_o + A_{\text{inner}} J_{\text{in}} \right)$$

$$L_1 = (2\pi r)^2 + p^2 v_{\text{ax}}$$

$$L_2 = L_1 \times N$$

$$A_{\text{outer}} = L_2 \times \pi \times OD$$

Parameters	Value	Unit	Description
J <sub>s</sub>	1414	W/m <sup>2</sup>	Solar radiation intensity (constant)
F	1.15		Visibility factor
e	0.28		Emittance (black paint)
a/e	0.8		Emittance (black paint)
Q	1.12	W	Internal power
f	0.6397 %	%	Fraction of sunlight orbit
J <sub>in</sub>	237	W/m <sup>2</sup>	
J <sub>out</sub>	224	W/m <sup>2</sup>	Planetary radiation intensity
A <sub>s</sub> surface	0.048639	m <sup>2</sup>	
A <sub>s</sub> solar	0.01316	m <sup>2</sup>	
A <sub>s</sub> albedo	0.003	m <sup>2</sup>	
A <sub>s</sub> planetary	0.003	m <sup>2</sup>	
A <sub>in</sub>	502.3235	W/m <sup>2</sup>	
A <sub>out</sub>	0		
B	5.67E-08	Wm <sup>-2</sup> K <sup>-4</sup>	
T	275.0834	K	
T(C)	12.9032	°C	

NB: Very much an assumption

Parameter/Value	Unit	Description
J <sub>s</sub>	1414 W/m <sup>2</sup>	Solar radiation intensity (constant)
F	0.9	Visibility factor
f	0.8	Emittance (black paint)
e	0.8	Emittance (black paint)
a/e	1.12	Internal power
Q	1 W	Fraction of sunlight orbit
f	0.785 %	
J <sub>e</sub>	237 W/m <sup>2</sup>	Orbit alt.
J <sub>p</sub>	224 W/m <sup>2</sup>	Planetary radiation intensity
J <sub>o</sub>	0.048639 m <sup>2</sup>	
A <sub>o</sub> surface	0.00316 m <sup>2</sup>	
A <sub>o</sub> solar	0.003 m <sup>2</sup>	
A <sub>o</sub> albedo	0.003 m <sup>2</sup>	
A <sub>o</sub> planetar	0.003 m <sup>2</sup>	
A <sub>o</sub> photo	40233 W/m <sup>2</sup>	
J <sub>o</sub>	60 °	
B	5.67E-08 Wm <sup>-2</sup> K <sup>-4</sup>	
T	2873248 K	
T(C)	1458263 °C	

Parameter/Value	Unit	Description
J <sub>s</sub>	1414 W/m <sup>2</sup>	Solar radiation intensity (constant)
F	0.9	Visibility factor
f	0.8	Emittance (black paint)
e	0.8	Emittance (black paint)
a/e	1.12	Internal power
Q	1 W	Fraction of sunlight orbit
f	1 %	
J <sub>e</sub>	237 W/m <sup>2</sup>	Orbit alt.
J <sub>p</sub>	224 W/m <sup>2</sup>	Planetary radiation intensity
J <sub>o</sub>	0.048639 m <sup>2</sup>	
A <sub>o</sub> surface	0.00316 m <sup>2</sup>	
A <sub>o</sub> solar	0.003 m <sup>2</sup>	
A <sub>o</sub> albedo	0.003 m <sup>2</sup>	
A <sub>o</sub> planetar	0.003 m <sup>2</sup>	
A <sub>o</sub> photo	3512316 W/m <sup>2</sup>	
J <sub>o</sub>	70 °	
B	5.67E-08 Wm <sup>-2</sup> K <sup>-4</sup>	
T	3046986 K	
T(C)	3034959 °C	

Parameter/Value	Unit	Description
J <sub>s</sub>	1414 W/m <sup>2</sup>	Solar radiation intensity (constant)
F	0.25	Visibility factor
f	0.8	Emittance (black paint)
e	0.8	Emittance (black paint)
a/e	1.12	Internal power
Q	1 W	Fraction of sunlight orbit
f	1 %	
J <sub>e</sub>	237 W/m <sup>2</sup>	Orbit alt.
J <sub>p</sub>	224 W/m <sup>2</sup>	Planetary radiation intensity
J <sub>o</sub>	0.048639 m <sup>2</sup>	
A <sub>o</sub> surface	0.00316 m <sup>2</sup>	
A <sub>o</sub> solar	0.003 m <sup>2</sup>	
A <sub>o</sub> albedo	0.003 m <sup>2</sup>	
A <sub>o</sub> planetar	14847 W/m <sup>2</sup>	
A <sub>o</sub> photo	80 °	
B	5.67E-08 Wm <sup>-2</sup> K <sup>-4</sup>	
T	3015155 K	
T(C)	2893559 °C	

Parameter/Value	Unit	Description
J <sub>s</sub>	1414 W/m <sup>2</sup>	Solar radiation intensity (constant)
F	0.25	Visibility factor
f	0.8	Emittance (black paint)
e	0.8	Emittance (black paint)
a/e	1.12	Internal power
Q	1 W	Fraction of sunlight orbit
f	1 %	
J <sub>e</sub>	237 W/m <sup>2</sup>	Orbit alt.
J <sub>p</sub>	224 W/m <sup>2</sup>	Planetary radiation intensity
J <sub>o</sub>	0.048639 m <sup>2</sup>	
A <sub>o</sub> surface	0.00316 m <sup>2</sup>	
A <sub>o</sub> solar	0.003 m <sup>2</sup>	
A <sub>o</sub> albedo	0.003 m <sup>2</sup>	
A <sub>o</sub> planetar	14847 W/m <sup>2</sup>	
A <sub>o</sub> photo	80 °	
B	5.67E-08 Wm <sup>-2</sup> K <sup>-4</sup>	
T	3015155 K	
T(C)	2893559 °C	

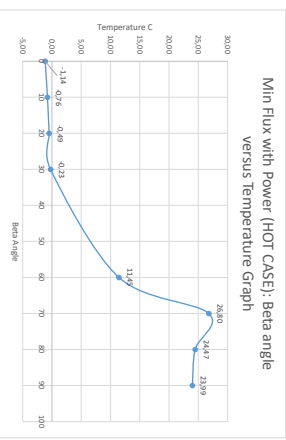
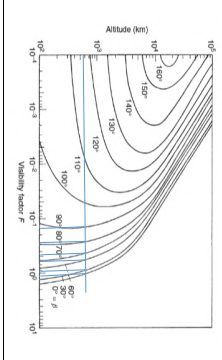
Parameter/Value	Unit	Description
J <sub>s</sub>	1414 W/m <sup>2</sup>	Solar radiation intensity (constant)
F	0.12	Visibility factor
f	0.8	Emittance (black paint)
e	0.8	Emittance (black paint)
a/e	1.12	Internal power
Q	1 W	Fraction of sunlight orbit
f	1 %	
J <sub>e</sub>	237 W/m <sup>2</sup>	Orbit alt.
J <sub>p</sub>	550 W/m <sup>2</sup>	Planetary radiation intensity
J <sub>o</sub>	0.048639 m <sup>2</sup>	
A <sub>o</sub> surface	0.00316 m <sup>2</sup>	
A <sub>o</sub> solar	0.003 m <sup>2</sup>	
A <sub>o</sub> albedo	0.003 m <sup>2</sup>	
A <sub>o</sub> planetar	1083171 W/m <sup>2</sup>	
A <sub>o</sub> photo	90 °	
B	5.67E-08 Wm <sup>-2</sup> K <sup>-4</sup>	
T	3012584 K	
T(C)	2729578 °C	

Parameter/Value	Unit	Description
J <sub>s</sub>	1414 W/m <sup>2</sup>	Solar radiation intensity (constant)
F	0.12	Visibility factor
f	0.8	Emittance (black paint)
e	0.8	Emittance (black paint)
a/e	1.12	Internal power
Q	1 W	Fraction of sunlight orbit
f	1 %	
J <sub>e</sub>	237 W/m <sup>2</sup>	Orbit alt.
J <sub>p</sub>	224 W/m <sup>2</sup>	Planetary radiation intensity
J <sub>o</sub>	0.048639 m <sup>2</sup>	
A <sub>o</sub> surface	0.00316 m <sup>2</sup>	
A <sub>o</sub> solar	0.003 m <sup>2</sup>	
A <sub>o</sub> albedo	0.003 m <sup>2</sup>	
A <sub>o</sub> planetar	1083171 W/m <sup>2</sup>	
A <sub>o</sub> photo	90 °	
B	5.67E-08 Wm <sup>-2</sup> K <sup>-4</sup>	
T	3012584 K	
T(C)	2729578 °C	

Parameter/Value	Unit	Description
J <sub>s</sub>	1414 W/m <sup>2</sup>	Solar radiation intensity (constant)
F	0.12	Visibility factor
f	0.8	Emittance (black paint)
e	0.8	Emittance (black paint)
a/e	1.12	Internal power
Q	1 W	Fraction of sunlight orbit
f	1 %	
J <sub>e</sub>	237 W/m <sup>2</sup>	Orbit alt.
J <sub>p</sub>	224 W/m <sup>2</sup>	Planetary radiation intensity
J <sub>o</sub>	0.048639 m <sup>2</sup>	
A <sub>o</sub> surface	0.00316 m <sup>2</sup>	
A <sub>o</sub> solar	0.003 m <sup>2</sup>	
A <sub>o</sub> albedo	0.003 m <sup>2</sup>	
A <sub>o</sub> planetar	1083171 W/m <sup>2</sup>	
A <sub>o</sub> photo	90 °	
B	5.67E-08 Wm <sup>-2</sup> K <sup>-4</sup>	
T	3012584 K	
T(C)	2729578 °C	

Parameter/Value	Unit	Description
J <sub>s</sub>	1414 W/m <sup>2</sup>	Solar radiation intensity (constant)
F	0.12	Visibility factor
f	0.8	Emittance (black paint)
e	0.8	Emittance (black paint)
a/e	1.12	Internal power
Q	1 W	Fraction of sunlight orbit
f	1 %	
J <sub>e</sub>	237 W/m <sup>2</sup>	Orbit alt.
J <sub>p</sub>	224 W/m <sup>2</sup>	Planetary radiation intensity
J <sub>o</sub>	0.048639 m <sup>2</sup>	
A <sub>o</sub> surface	0.00316 m <sup>2</sup>	
A <sub>o</sub> solar	0.003 m <sup>2</sup>	
A <sub>o</sub> albedo	0.003 m <sup>2</sup>	
A <sub>o</sub> planetar	1083171 W/m <sup>2</sup>	
A <sub>o</sub> photo	90 °	
B	5.67E-08 Wm <sup>-2</sup> K <sup>-4</sup>	
T	3012584 K	
T(C)	2729578 °C	

Parameters	Value	Unit	Description
$J_s$	1332	W/m <sup>2</sup>	Solar radiation intensity (constant)
$f$	1.15		Velocity factor
$e$	0.2		Emissivity (black paint)
$a/e$	1.12		Emissivity (black paint)
$Q$	1 W		Internal power
$f$	0.6277 %		Fraction of sunlit orbit
$J_p$	232	W/m <sup>2</sup>	Planetary radiation intensity
$J_p$	232	W/m <sup>2</sup>	Planetary radiation intensity
A, surface	0.048639	m <sup>2</sup>	
A, solar	0.0316	m <sup>2</sup>	
A, albedo	0.003	m <sup>2</sup>	
A, planetary	0.003	m <sup>2</sup>	
$J_p$	560.166	W/m <sup>2</sup>	
B	10 <sup>-7</sup>		
S8	5.67E-08	Wm <sup>-2</sup> K <sup>-4</sup>	
T	272.2876	K	
T(C)	-0.2385	°C	



Parameters	Value	Unit	Description
$J_s$	1332	W/m <sup>2</sup>	Solar radiation intensity (constant)
$f$	1.15		Velocity factor
$e$	0.2		Emissivity (black paint)
$a/e$	0.8		Emissivity (black paint)
$Q$	1 W		Internal power
$f$	0.6277 %		Fraction of sunlit orbit
$J_p$	232	W/m <sup>2</sup>	Planetary radiation intensity
$J_p$	232	W/m <sup>2</sup>	Planetary radiation intensity
A, surface	0.048639	m <sup>2</sup>	
A, solar	0.0316	m <sup>2</sup>	
A, albedo	0.003	m <sup>2</sup>	
A, planetary	0.003	m <sup>2</sup>	
$J_p$	522.144	W/m <sup>2</sup>	
B	2.0		
S8	5.67E-08	Wm <sup>-2</sup> K <sup>-4</sup>	
T	272.2876	K	
T(C)	-0.2385	°C	

$$J_o = J_o A F$$

$$f = \frac{1}{180^\circ} \cos^{-1} \left[ \frac{(h_s + 2Rb)^{1/2}}{(R + h_s) \cos \beta} \right] \quad \text{if } |\beta| < \beta^*$$

$$= 0 \quad \text{if } |\beta| \geq \beta^*$$

$$\beta^* = \sin^{-1} \left[ \frac{R}{R + h_s} \right] \quad 0^\circ \leq \beta^* \leq 90^\circ$$

$\sigma = \text{Stefan-Boltzmann constant } (5.67 \times 10^{-8} \text{ W m}^{-2} \text{ K}^{-2})$

1. 24720757 2. 444E+08 3. 482701576

$$J^* = \frac{A_{\text{outer}} J_p}{A_{\text{sur}} f_{\text{acc}} \sigma} + \frac{Q}{A_{\text{sur}} f_{\text{acc}} \sigma} + \frac{A_{\text{outer}} J_o}{A_{\text{sur}}}$$

Area Calculations:

$\rho$	0.003955 m
$N$	0.03548 m
OD	2.5
ID	0.04391 m
WD	0.04009
$L_{\text{inlet}}$	0.042
$L_{\text{outlet}}$	0.035394
LT	0.08996

Outer surface Area: 0.01241 m<sup>2</sup>  
A, OD: 0.048639 m<sup>2</sup>  
A, albedo and planet: 0.003  
A, inlet: 0.024819  
A, outlet: 0.024819  
Average of A's: 0.01316 m<sup>2</sup>

$$J^* = \frac{A_{\text{outer}} J_o}{A_{\text{sur}} f_{\text{acc}} \sigma} + \frac{Q}{A_{\text{sur}} f_{\text{acc}} \sigma} + \frac{A_{\text{outer}} J_o}{A_{\text{sur}}}$$

$$L_1 = (2\pi r)^2 + p^2 v_{\text{ax}}$$

$$L_r = L_1 \times N$$

$$A_{\text{outer}} = L_r \times \pi \times OD$$

Parameters	Value	Unit	Description
$J_s$	1332	W/m <sup>2</sup>	Solar radiation intensity (constant)
$f$	1.15		Velocity factor
$e$	0.2		Emissivity (black paint)
$a/e$	1.12		Emissivity (black paint)
$Q$	1 W		Internal power
$f$	0.6277 %		Fraction of sunlit orbit
$J_p$	232	W/m <sup>2</sup>	Planetary radiation intensity
$J_p$	232	W/m <sup>2</sup>	Planetary radiation intensity
A, surface	0.048639	m <sup>2</sup>	
A, solar	0.0316	m <sup>2</sup>	
A, albedo	0.003	m <sup>2</sup>	
A, planetary	0.003	m <sup>2</sup>	
$J_p$	424.508	W/m <sup>2</sup>	
B	30 <sup>-7</sup>		
S8	5.67E-08	Wm <sup>-2</sup> K <sup>-4</sup>	
T	272.2876	K	
T(C)	-0.2385	°C	

Parameters	Value	Unit	Description
$J_s$	1332	W/m <sup>2</sup>	Solar radiation intensity (constant)
$f$	1.15		Velocity factor
$e$	0.2		Emissivity (black paint)
$a/e$	0.8		Emissivity (black paint)
$Q$	1 W		Internal power
$f$	0.6277 %		Fraction of sunlit orbit
$J_p$	232	W/m <sup>2</sup>	Planetary radiation intensity
$J_p$	232	W/m <sup>2</sup>	Planetary radiation intensity
A, surface	0.048639	m <sup>2</sup>	
A, solar	0.0316	m <sup>2</sup>	
A, albedo	0.003	m <sup>2</sup>	
A, planetary	0.003	m <sup>2</sup>	
$J_p$	424.508	W/m <sup>2</sup>	
B	30 <sup>-7</sup>		
S8	5.67E-08	Wm <sup>-2</sup> K <sup>-4</sup>	
T	272.2876	K	
T(C)	-0.2385	°C	

NB: Very much an assumption

Parameter/Value	Unit	Description
J <sub>s</sub>	1332 W/m <sup>2</sup>	Solar radiation intensity (constant)
F	0.9	Visibility factor
f	0.8	Emittance (Black paint)
e	0.8	Emittance (Black paint)
a/e	1.12	Internal power
Q	1 W	Fraction of sunlight orbit
f	0.7/85 %	
J <sub>e</sub>	237 W/m <sup>2</sup>	
J <sub>o</sub> Orbit alt.	232 W/m <sup>2</sup>	Planetary radiation intensity
J <sub>o</sub> Surface	0.048639 m <sup>2</sup>	
A <sub>o</sub> Solar	0.01316 m <sup>2</sup>	
A <sub>o</sub> Albedo	0.003 m <sup>2</sup>	
A <sub>o</sub> Planetar	0.003 m <sup>2</sup>	
A <sub>o</sub> bedo	419.58 W/m <sup>2</sup>	
J <sub>o</sub> B	60 °	
J <sub>o</sub> SB	5.67E-08 Wm <sup>-2</sup> K <sup>-4</sup>	
T	288.5978 K	
T(C)	15.49755 °C	

Parameter/Value	Unit	Description
J <sub>s</sub>	1332 W/m <sup>2</sup>	Solar radiation intensity (constant)
F	0.9	Visibility factor
f	0.8	Emittance (Black paint)
e	0.8	Emittance (Black paint)
a/e	1.12	Internal power
Q	1 W	Fraction of sunlight orbit
f	1 %	
J <sub>e</sub>	237 W/m <sup>2</sup>	
J <sub>o</sub> Orbit alt.	232 W/m <sup>2</sup>	Planetary radiation intensity
J <sub>o</sub> Surface	0.048639 m <sup>2</sup>	
A <sub>o</sub> Solar	0.01316 m <sup>2</sup>	
A <sub>o</sub> Albedo	0.003 m <sup>2</sup>	
A <sub>o</sub> Planetar	0.003 m <sup>2</sup>	
A <sub>o</sub> bedo	388.4412 W/m <sup>2</sup>	
J <sub>o</sub> B	70 °	
J <sub>o</sub> SB	5.67E-08 Wm <sup>-2</sup> K <sup>-4</sup>	
T	298.5911 K	
T(C)	26.09112 °C	

Parameter/Value	Unit	Description
J <sub>s</sub>	1332 W/m <sup>2</sup>	Solar radiation intensity (constant)
F	0.25	Visibility factor
f	0.8	Emittance (Black paint)
e	0.8	Emittance (Black paint)
a/e	1.12	Internal power
Q	1 W	Fraction of sunlight orbit
f	1 %	
J <sub>e</sub>	237 W/m <sup>2</sup>	
J <sub>o</sub> Orbit alt.	232 W/m <sup>2</sup>	Planetary radiation intensity
J <sub>o</sub> Surface	0.048639 m <sup>2</sup>	
A <sub>o</sub> Solar	0.01316 m <sup>2</sup>	
A <sub>o</sub> Albedo	0.003 m <sup>2</sup>	
A <sub>o</sub> Planetar	0.003 m <sup>2</sup>	
A <sub>o</sub> bedo	140.85 W/m <sup>2</sup>	
J <sub>o</sub> B	80 °	
J <sub>o</sub> SB	5.67E-08 Wm <sup>-2</sup> K <sup>-4</sup>	
T	293.517 K	
T(C)	20.4659 °C	

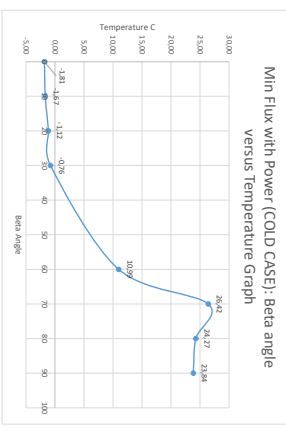
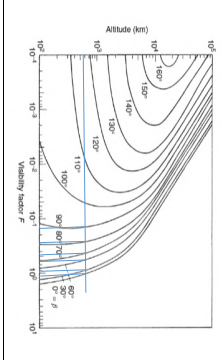
Parameter/Value	Unit	Description
J <sub>s</sub>	1332 W/m <sup>2</sup>	Solar radiation intensity (constant)
F	0.12	Visibility factor
f	0.8	Emittance (Black paint)
e	0.8	Emittance (Black paint)
a/e	1.12	Internal power
Q	1 W	Fraction of sunlight orbit
f	1 %	
J <sub>e</sub>	237 W/m <sup>2</sup>	
J <sub>o</sub> Orbit alt.	550 W/m <sup>2</sup>	Planetary radiation intensity
J <sub>o</sub> Surface	232 W/m <sup>2</sup>	
A <sub>o</sub> Solar	0.048639 m <sup>2</sup>	
A <sub>o</sub> Albedo	0.01316 m <sup>2</sup>	
A <sub>o</sub> Planetar	0.003 m <sup>2</sup>	
A <sub>o</sub> bedo	0.04 m <sup>2</sup>	
J <sub>o</sub> B	90 °	
J <sub>o</sub> SB	5.67E-08 Wm <sup>-2</sup> K <sup>-4</sup>	
T	301.408 K	
T(C)	23.29799 °C	

Parameter/Value	Unit	Description
J <sub>s</sub>	1332 W/m <sup>2</sup>	Solar radiation intensity (constant)
F	0.12	Visibility factor
f	0.8	Emittance (Black paint)
e	0.8	Emittance (Black paint)
a/e	1.12	Internal power
Q	1 W	Fraction of sunlight orbit
f	1 %	
J <sub>e</sub>	237 W/m <sup>2</sup>	
J <sub>o</sub> Orbit alt.	550 W/m <sup>2</sup>	Planetary radiation intensity
J <sub>o</sub> Surface	232 W/m <sup>2</sup>	
A <sub>o</sub> Solar	0.048639 m <sup>2</sup>	
A <sub>o</sub> Albedo	0.01316 m <sup>2</sup>	
A <sub>o</sub> Planetar	0.003 m <sup>2</sup>	
A <sub>o</sub> bedo	0.04 m <sup>2</sup>	
J <sub>o</sub> B	90 °	
J <sub>o</sub> SB	5.67E-08 Wm <sup>-2</sup> K <sup>-4</sup>	
T	301.408 K	
T(C)	23.29799 °C	

Parameter/Value	Unit	Description
J <sub>s</sub>	1332 W/m <sup>2</sup>	Solar radiation intensity (constant)
F	0.12	Visibility factor
f	0.8	Emittance (Black paint)
e	0.8	Emittance (Black paint)
a/e	1.12	Internal power
Q	1 W	Fraction of sunlight orbit
f	1 %	
J <sub>e</sub>	237 W/m <sup>2</sup>	
J <sub>o</sub> Orbit alt.	550 W/m <sup>2</sup>	Planetary radiation intensity
J <sub>o</sub> Surface	232 W/m <sup>2</sup>	
A <sub>o</sub> Solar	0.048639 m <sup>2</sup>	
A <sub>o</sub> Albedo	0.01316 m <sup>2</sup>	
A <sub>o</sub> Planetar	0.003 m <sup>2</sup>	
A <sub>o</sub> bedo	0.04 m <sup>2</sup>	
J <sub>o</sub> B	90 °	
J <sub>o</sub> SB	5.67E-08 Wm <sup>-2</sup> K <sup>-4</sup>	
T	301.408 K	
T(C)	23.29799 °C	



Parameters	Value	Unit	Description
$J_s$	1332	W/m <sup>2</sup>	Solar radiation intensity (constant)
$F$	1.45		Solar radiat
$f$	0.8		Visibility factor
$e$	0.8		Emittance (black paint)
$a/e$	1.12		Emittance (black paint)
$Q$	1 W		Internal power
$f$	0.6277 %		Fraction of sunlight
$J_e$	237	W/m <sup>2</sup>	Planetary radiation intensity
$J_p$	224	W/m <sup>2</sup>	Planetary radiation intensity
A, surface	0.048639	m <sup>2</sup>	
A, solar	0.01316	m <sup>2</sup>	
A, albedo	0.003	m <sup>2</sup>	
A, planetar	0.003	m <sup>2</sup>	
A, absorp	0.295	m <sup>2</sup>	
$J_a$	473.52	W/m <sup>2</sup>	
B	0 °		
5B	5.67E-08	Wm <sup>-2</sup> K <sup>-4</sup>	
T	271.3999	K	
T(C)	-1.60004	°C	



Parameter	Value	Unit	Description
$J_s$	1332	W/m <sup>2</sup>	Solar radiation intensity (constant)
$F$	1.45		Solar radiat
$f$	0.8		Visibility factor
$e$	0.8		Emittance (black paint)
$a/e$	1.12		Emittance (black paint)
$Q$	1 W		Internal power
$f$	0.6277 %		Fraction of sunlight
$J_e$	237	W/m <sup>2</sup>	Planetary radiation intensity
$J_p$	224	W/m <sup>2</sup>	Planetary radiation intensity
A, surface	0.048639	m <sup>2</sup>	
A, solar	0.01316	m <sup>2</sup>	
A, albedo	0.003	m <sup>2</sup>	
A, planetar	0.003	m <sup>2</sup>	
A, absorp	0.295	m <sup>2</sup>	
$J_a$	473.52	W/m <sup>2</sup>	
B	0 °		
5B	5.67E-08	Wm <sup>-2</sup> K <sup>-4</sup>	
T	271.3999	K	
T(C)	-1.60004	°C	

$$J_a = J_e A_f$$

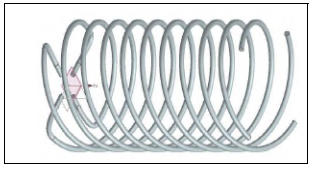
$$f_s = \frac{1}{180^\circ} \cos^{-1} \left[ \frac{(R^2 + 2RH)^{1/2}}{(R + H)\cos\beta} \right] \quad \text{if } |\beta| < \beta^*$$

$$= 0 \quad \text{if } |\beta| \geq \beta^*$$

$$\beta^* = \sin^{-1} \left[ \frac{R}{R + H} \right] \quad 0^\circ \leq \beta^* \leq 90^\circ$$

$\sigma =$  Stefan-Boltzmann constant ( $5.67 \times 10^{-8} \text{ W m}^{-2} \text{ K}^{-4}$ )

$$J^* = \frac{A_{\text{outer}} J_e}{A_{\text{sur}} f_{\text{acc}} \sigma} + \frac{Q}{A_{\text{sur}} f_{\text{acc}} \sigma} + \frac{A_{\text{outer}} J_a}{A_{\text{sur}}}$$



Area Calculations:	Value	Unit
$P$	0.003955	m
$N$	0.03548	m
$OD$	2.5	m
$ID$	0.04391	m
$MD$	0.04009	m
$L$	0.242	m
$L_{\text{heliofield}}$	0.035394	m
$LT$	0.08996	m

Outer surface Area:	0.01241	m <sup>2</sup>
A, heliofield:	0.048639	m <sup>2</sup>
A, heliofield planet:	0.003	
A, heliofield:	0.02489	
A, heliofield:	0.02489	
Average of A's:	0.01316	m <sup>2</sup>

$$J^* = \frac{A_{\text{outer}} J_e}{A_{\text{sur}} f_{\text{acc}} \sigma} + \frac{Q}{A_{\text{sur}} f_{\text{acc}} \sigma} + \frac{A_{\text{outer}} J_a}{A_{\text{sur}}}$$

$$L_1 = [(2\pi r)^2 + p^2]^{1/2}$$

$$L_r = [L_1 \times N]$$

$$A_{\text{outer}} = L_r \times \pi \times OD$$

Parameter	Value	Unit	Description
$J_s$	1332	W/m <sup>2</sup>	Solar radiation intensity (constant)
$F$	1.45		Solar radiat
$f$	0.8		Visibility factor
$e$	0.8		Emittance (black paint)
$a/e$	1.12		Emittance (black paint)
$Q$	1 W		Internal power
$f$	0.6277 %		Fraction of sunlight
$J_e$	237	W/m <sup>2</sup>	Planetary radiation intensity
$J_p$	224	W/m <sup>2</sup>	Planetary radiation intensity
A, surface	0.048639	m <sup>2</sup>	
A, solar	0.01316	m <sup>2</sup>	
A, albedo	0.003	m <sup>2</sup>	
A, planetar	0.003	m <sup>2</sup>	
A, absorp	0.295	m <sup>2</sup>	
$J_a$	473.52	W/m <sup>2</sup>	
B	0 °		
5B	5.67E-08	Wm <sup>-2</sup> K <sup>-4</sup>	
T	271.4286	K	
T(C)	-1.67912	°C	

Parameter	Value	Unit	Description
$J_s$	1332	W/m <sup>2</sup>	Solar radiation intensity (constant)
$F$	1.45		Solar radiat
$f$	0.8		Visibility factor
$e$	0.8		Emittance (black paint)
$a/e$	1.12		Emittance (black paint)
$Q$	1 W		Internal power
$f$	0.6277 %		Fraction of sunlight
$J_e$	237	W/m <sup>2</sup>	Planetary radiation intensity
$J_p$	224	W/m <sup>2</sup>	Planetary radiation intensity
A, surface	0.048639	m <sup>2</sup>	
A, solar	0.01316	m <sup>2</sup>	
A, albedo	0.003	m <sup>2</sup>	
A, planetar	0.003	m <sup>2</sup>	
A, absorp	0.295	m <sup>2</sup>	
$J_a$	380.952	W/m <sup>2</sup>	
B	30 °		
5B	5.67E-08	Wm <sup>-2</sup> K <sup>-4</sup>	
T	272.2489	K	
T(C)	-0.79033	°C	

NB: Very much an assumption

Parameter/Value	Unit	Description
J <sub>s</sub>	1332 W/m <sup>2</sup>	Solar radiation intensity (constant)
F	0.9	Visibility factor
f	0.8	Emittance (black paint)
e	0.8	Emittance (black paint)
a/e	1.12	Internal power
Q	1 W	Fraction of sunlight orbit
f	0.7/85 %	
J <sub>p</sub>	237 W/m <sup>2</sup>	Planetary radiation intensity
J <sub>p</sub> orbit alt.	224 W/m <sup>2</sup>	
J <sub>p</sub> surface	0.048639 m <sup>2</sup>	
A <sub>p</sub> solar	0.01316 m <sup>2</sup>	
A <sub>p</sub> Jibido	0.003 m <sup>2</sup>	
A <sub>p</sub> Jibeter	0.003 m <sup>2</sup>	
A <sub>p</sub> Jibeto	0.003 m <sup>2</sup>	
J <sub>p</sub> Jibeto	388.615 W/m <sup>2</sup>	
J <sub>p</sub> B	60 °	
J <sub>p</sub> SB	5.67E-08 Wm <sup>-2</sup> K <sup>-4</sup>	
T	284.1384 K	
T(C)	10.9841 °C	

Parameter/Value	Unit	Description
J <sub>s</sub>	1332 W/m <sup>2</sup>	Solar radiation intensity (constant)
F	0.9	Visibility factor
f	0.8	Emittance (black paint)
e	0.8	Emittance (black paint)
a/e	1.12	Internal power
Q	1 W	Fraction of sunlight orbit
f	1 %	
J <sub>p</sub>	237 W/m <sup>2</sup>	Planetary radiation intensity
J <sub>p</sub> orbit alt.	224 W/m <sup>2</sup>	
J <sub>p</sub> surface	0.048639 m <sup>2</sup>	
A <sub>p</sub> solar	0.01316 m <sup>2</sup>	
A <sub>p</sub> Jibido	0.003 m <sup>2</sup>	
A <sub>p</sub> Jibeter	0.003 m <sup>2</sup>	
A <sub>p</sub> Jibeto	0.003 m <sup>2</sup>	
J <sub>p</sub> Jibeto	380.8688 W/m <sup>2</sup>	
J <sub>p</sub> B	70 °	
J <sub>p</sub> SB	5.67E-08 Wm <sup>-2</sup> K <sup>-4</sup>	
T	295.5654 K	
T(C)	20.4189 °C	

Parameter/Value	Unit	Description
J <sub>s</sub>	1332 W/m <sup>2</sup>	Solar radiation intensity (constant)
F	0.25	Visibility factor
f	0.8	Emittance (black paint)
e	0.8	Emittance (black paint)
a/e	1.12	Internal power
Q	1 W	Fraction of sunlight orbit
f	1 %	
J <sub>p</sub>	237 W/m <sup>2</sup>	Planetary radiation intensity
J <sub>p</sub> orbit alt.	224 W/m <sup>2</sup>	
J <sub>p</sub> surface	0.048639 m <sup>2</sup>	
A <sub>p</sub> solar	0.01316 m <sup>2</sup>	
A <sub>p</sub> Jibido	0.003 m <sup>2</sup>	
A <sub>p</sub> Jibeter	0.003 m <sup>2</sup>	
A <sub>p</sub> Jibeto	0.003 m <sup>2</sup>	
J <sub>p</sub> Jibeto	139.86 W/m <sup>2</sup>	
J <sub>p</sub> B	80 °	
J <sub>p</sub> SB	5.67E-08 Wm <sup>-2</sup> K <sup>-4</sup>	
T	297.2128 K	
T(C)	24.2788 °C	

Parameter/Value	Unit	Description
J <sub>s</sub>	1332 W/m <sup>2</sup>	Solar radiation intensity (constant)
F	0.12	Visibility factor
f	0.8	Emittance (black paint)
e	0.8	Emittance (black paint)
a/e	1.12	Internal power
Q	1 W	Fraction of sunlight orbit
f	1 %	
J <sub>p</sub>	237 W/m <sup>2</sup>	Planetary radiation intensity
J <sub>p</sub> orbit alt.	550 W/m <sup>2</sup>	
J <sub>p</sub> surface	0.048639 m <sup>2</sup>	
A <sub>p</sub> solar	0.01316 m <sup>2</sup>	
A <sub>p</sub> Jibido	0.003 m <sup>2</sup>	
A <sub>p</sub> Jibeter	0.003 m <sup>2</sup>	
A <sub>p</sub> Jibeto	0.003 m <sup>2</sup>	
J <sub>p</sub> Jibeto	101.2888 W/m <sup>2</sup>	
J <sub>p</sub> B	90 °	
J <sub>p</sub> SB	5.67E-08 Wm <sup>-2</sup> K <sup>-4</sup>	
T	286.6013 K	
T(C)	23.9422 °C	

Parameter/Value	Unit	Description
J <sub>s</sub>	1332 W/m <sup>2</sup>	Solar radiation intensity (constant)
F	0.12	Visibility factor
f	0.8	Emittance (black paint)
e	0.8	Emittance (black paint)
a/e	1.12	Internal power
Q	1 W	Fraction of sunlight orbit
f	1 %	
J <sub>p</sub>	237 W/m <sup>2</sup>	Planetary radiation intensity
J <sub>p</sub> orbit alt.	550 W/m <sup>2</sup>	
J <sub>p</sub> surface	0.048639 m <sup>2</sup>	
A <sub>p</sub> solar	0.01316 m <sup>2</sup>	
A <sub>p</sub> Jibido	0.003 m <sup>2</sup>	
A <sub>p</sub> Jibeter	0.003 m <sup>2</sup>	
A <sub>p</sub> Jibeto	0.003 m <sup>2</sup>	
J <sub>p</sub> Jibeto	101.2888 W/m <sup>2</sup>	
J <sub>p</sub> B	90 °	
J <sub>p</sub> SB	5.67E-08 Wm <sup>-2</sup> K <sup>-4</sup>	
T	286.6013 K	
T(C)	23.9422 °C	

Parameter/Value	Unit	Description
J <sub>s</sub>	1332 W/m <sup>2</sup>	Solar radiation intensity (constant)
F	0.12	Visibility factor
f	0.8	Emittance (black paint)
e	0.8	Emittance (black paint)
a/e	1.12	Internal power
Q	1 W	Fraction of sunlight orbit
f	1 %	
J <sub>p</sub>	237 W/m <sup>2</sup>	Planetary radiation intensity
J <sub>p</sub> orbit alt.	550 W/m <sup>2</sup>	
J <sub>p</sub> surface	0.048639 m <sup>2</sup>	
A <sub>p</sub> solar	0.01316 m <sup>2</sup>	
A <sub>p</sub> Jibido	0.003 m <sup>2</sup>	
A <sub>p</sub> Jibeter	0.003 m <sup>2</sup>	
A <sub>p</sub> Jibeto	0.003 m <sup>2</sup>	
J <sub>p</sub> Jibeto	101.2888 W/m <sup>2</sup>	
J <sub>p</sub> B	90 °	
J <sub>p</sub> SB	5.67E-08 Wm <sup>-2</sup> K <sup>-4</sup>	
T	286.6013 K	
T(C)	23.9422 °C	

## F.2 Traditional Spring Calculations

Shigly (Machine Design)		Original Design	
Material Name:	ASTM A228 STEEL	Unit:	For 4 Springs:
Yield Stress for 1mm diameter:	242,500,000 Pa	Pa	-
Shear Modulus (G):	80000,000,000 Pa	Pa	-
Mean diameter (D):	0.0093 m	m	-
Wire diameter (d):	0.0005 m	m	-
Spring Index 'C':	18.6	-	-
No. total coils (Nt):	3	-	-
No. active coils (Na):	3	-	-
Solid Height (Ls) (Plain):	0.008 m	0.008	-
Solid Height (Ls) (Ground):	0.0015 m	0.006	-
Free Length (FL):	0.25 m	-	-
Types of Ends:	Plain	-	-
Deflection based on Ls:	-	-	-
Pitch (p):	0.003333333 m	-	-
OD @ Solid Length:	0.02608433 m	-	-
Spring Rate(k):	29,908,645 N/m	1095,02423	-
Force required @ clearance SL:	62,874,653 N	250,71,861.2	-
Work Correction Factor (WCF):	1.072865372	-	-
Torsion Stress (T) (Nw):	26,883,72,043 Pa	510952,66906	(Ratios set out, accounts for bending stress and curvature of spring)
Buckling (F) (D):	0.963	-	(If greater than 4 buckling may occur, see figure 24.8)
Buckling (F) (FL):	109,250,000 Pa	-	(Table 24.6, here its worked off of yield stress, therefore greater FDS included)
Max allowable torsional stress:	31,082,662.26 Pa	-	(If there's a negative value, spring wont work)

Design Limitations	
Will design for spring index max of 1.0.	
Solid height of spring will not exceed 28mm	
Minimum deployed height of 50mm	
Nt = Na	

Formulas:	
$L_s = (N_t + 1)d$	$K_{w1} = \frac{4C-1}{4C-4} + \frac{0.615}{C}$
$L_s = N_t d$	$K_{w2} = 1 + \frac{0.5}{C}$
$OD_{at\ solid} = \sqrt{D^2 + \frac{p^2 - d^2}{\pi^2}} + d$	$S = \frac{8K_w P D}{\pi d^3}$
$k = \frac{P}{f} = \frac{Gd^4}{8D^3 N_t}$	

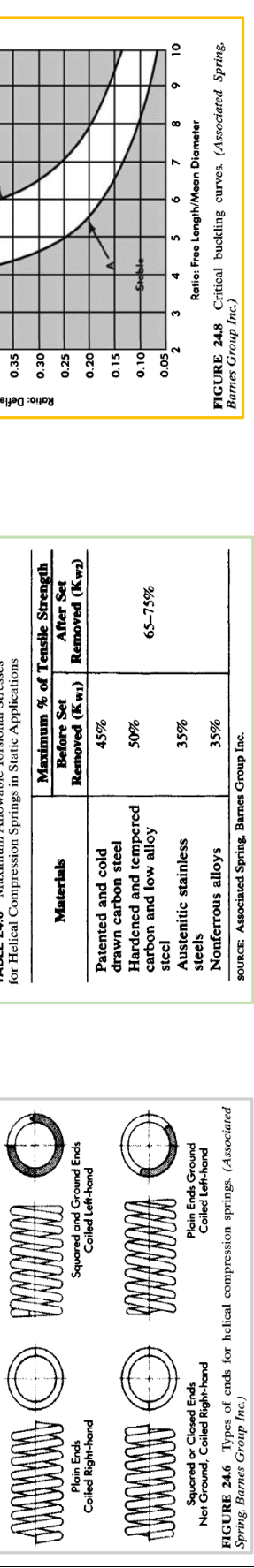


TABLE 24.6 Maximum Allowable Torsional Stresses for Helical Compression Springs in Static Applications		
Materials	Maximum % of Tensile Strength Before Set Removed (Kw1)	Maximum % of Tensile Strength After Set Removed (Kw2)
Patented and cold drawn carbon steel	45%	65-75%
Hardened and tempered carbon and low alloy steel	50%	
Austenitic stainless steels	35%	
Nonferrous alloys	35%	

SOURCE: Associated Spring, Barnes Group Inc.



Antenna Iteration 2: 1,91mm Wire; 42mm Helix Diameter; 88.7 mm Height		ASTM A228 STEEL		Unit: For 4 Springs:	
Material Name:	ASTM A228 STEEL	Pa	-	Pa	-
Yield Stress for 1,91mm diameter:	1970000000	Pa	-	Pa	-
Shear Modulus (G):	8000000000	Pa	-	Pa	-
Mean diameter (D):	0.042	m	-	m	-
Wire diameter (d):	0.00191	m	-	m	-
Spring Index 'C':	21.9895288	-	-	-	-
No. total coils (N):	2.5	-	-	-	-
No. active coils (Na):	2.5	-	-	-	-
Solid Height (Ls) (Plain)	0.006685	m	0.02674	0.05348	
Solid Height (Ls) (Ground)	0.004775	m	0.0191	0.0382	
Free Length (FL)	0.0887	m	-	-	
Types of Ends	Plain	-	-	-	
Deflection based on LS	0.03548	m	-	-	
Pitch (p)	0.03548	m	-	-	
OD @ (Solid Length)	0.04539766	m	-	-	
Spring Rate (R)	78.9314311	N/m	3874.124524	-	
Force required @ clearance SL	50.02978902	N	200.0358669	-	
Wahl Correction Factor (Kw)	1.25131802	-	-	-	
Torsion Stress (S) (with Kw)	84543321.3	Pa	326695285	-	
Buckling (F) (D)	2.111904762	-	-	-	
Buckling (D) (d)	0.794662418	-	-	-	
Max Allowable Torsional Stress	886500000	Pa	-	-	
MATS - Tors. Stress	68986278.74	Pa	-	-	
Comments:					
Buckling will not occur.					
Spring index is fairly, but still below 25					

Antenna Iteration 2: 1,6mm Wire; 42mm Helix Diameter; 88.7 mm Height		ASTM A228 STEEL		Unit: For 4 Springs:	
Material Name:	ASTM A228 STEEL	Pa	-	Pa	-
Yield Stress for 1,6mm diameter:	2020000000	Pa	-	Pa	-
Shear Modulus (G):	8000000000	Pa	-	Pa	-
Mean diameter (D):	0.042	m	-	m	-
Wire diameter (d):	0.0016	m	-	m	-
Spring Index 'C':	26.25	-	-	-	-
No. total coils (N):	2.5	-	-	-	-
No. active coils (Na):	2.5	-	-	-	-
Solid Height (Ls) (Plain)	0.0056	m	0.0224	0.0448	
Solid Height (Ls) (Ground)	0.004	m	0.016	0.032	
Free Length (FL)	0.0887	m	-	-	
Types of Ends	Plain	-	-	-	
Deflection based on LS	0.03548	m	-	-	
Pitch (p)	0.03548	m	-	-	
OD @ (Solid Length)	0.04508937	m	-	-	
Spring Rate (R)	359.8278824	N/m	1415.311531	-	
Force required @ clearance SL	125.131802	N	102.8912475	-	
Wahl Correction Factor (Kw)	1.25131802	-	-	-	
Torsion Stress (S) (with Kw)	702365899.3	Pa	2829427237	-	
Buckling (F) (D)	2.111904762	-	-	-	
Buckling (D) (d)	0.818616685	-	-	-	
Max Allowable Torsional Stress	909000000	Pa	-	-	
MATS - Tors. Stress	201643180.7	Pa	-	-	
Comments:					
Buckling will not occur.					
Spring index is above 25, achieving tolerances may be difficult					

Antenna Iteration 2: 1,6mm Wire; 42mm Helix Diameter; 88.7 mm Height		ASTM A228 STEEL		Unit: For 4 Springs:	
Material Name:	ASTM A228 STEEL	Pa	-	Pa	-
Yield Stress for 1,6mm diameter:	2170000000	Pa	-	Pa	-
Shear Modulus (G):	8000000000	Pa	-	Pa	-
Mean diameter (D):	0.042	m	-	m	-
Wire diameter (d):	0.0021	m	-	m	-
Spring Index 'C':	38.18181818	-	-	-	-
No. total coils (N):	2.5	-	-	-	-
No. active coils (Na):	2.5	-	-	-	-
Solid Height (Ls) (Plain)	0.00385	m	0.0154	0.0308	
Solid Height (Ls) (Ground)	0.00275	m	0.011	0.022	
Free Length (FL)	0.0887	m	-	-	
Types of Ends	Plain	-	-	-	
Deflection based on LS	0.03548	m	-	-	
Pitch (p)	0.03548	m	-	-	
OD @ (Solid Length)	0.0445905	m	-	-	
Spring Rate (R)	79.04883925	N/m	316.186157	-	
Force required @ clearance SL	6.1419101	N	24.1676644	-	
Wahl Correction Factor (Kw)	1.03828282	-	-	-	
Torsion Stress (S) (with Kw)	2.111904762	Pa	2045745576	-	
Buckling (F) (D)	2.111904762	-	-	-	
Buckling (D) (d)	0.871696421	-	-	-	
Max Allowable Torsional Stress	976500000	Pa	-	-	
MATS - Tors. Stress	469083686.3	Pa	-	-	
Comments:					
Buckling will not occur.					
Spring index is very high, achieving tolerances may be difficult/impossible to achieve.					

Antenna Iteration 2: 1,68mm Wire; 42mm Helix Diameter; 88.7 mm Height		ASTM A228 STEEL		Unit: For 4 Springs:	
Material Name:	ASTM A228 STEEL	Pa	-	Pa	-
Yield Stress for 1,68mm diameter:	2020000000	Pa	-	Pa	-
Shear Modulus (G):	8000000000	Pa	-	Pa	-
Mean diameter (D):	0.042	m	-	m	-
Wire diameter (d):	0.00168	m	-	m	-
Spring Index 'C':	25	-	-	-	-
No. total coils (N):	2.5	-	-	-	-
No. active coils (Na):	2.5	-	-	-	-
Solid Height (Ls) (Plain)	0.00588	m	0.02352	0.04704	
Solid Height (Ls) (Ground)	0.0042	m	0.0168	0.0336	
Free Length (FL)	0.0887	m	-	-	
Types of Ends	Plain	-	-	-	
Deflection based on LS	0.03548	m	-	-	
Pitch (p)	0.03548	m	-	-	
OD @ (Solid Length)	0.045188622	m	-	-	
Spring Rate (R)	430.08	N/m	1720.32	-	
Force required @ clearance SL	30.9272752	N	123.6911008	-	
Wahl Correction Factor (Kw)	1.09585	-	-	-	
Torsion Stress (S) (with Kw)	786478762	Pa	2945790875	-	
Buckling (F) (D)	2.111904762	-	-	-	
Buckling (D) (d)	0.81090752	-	-	-	
Max Allowable Torsional Stress	909000000	Pa	-	-	
MATS - Tors. Stress	1724152983.3	Pa	-	-	
Comments:					
Buckling will not occur.					
Spring index is exactly 25, tolerances may be difficult to achieve.					

# Appendix G

## Top Brace Iterations

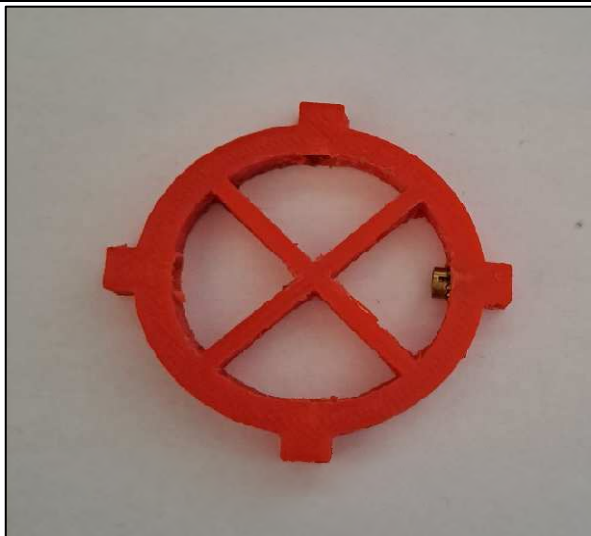
Top Brace Rev1



Top Brace Rev2



Top Brace Rev3



Top Brace Rev4



Top Brace Rev 5





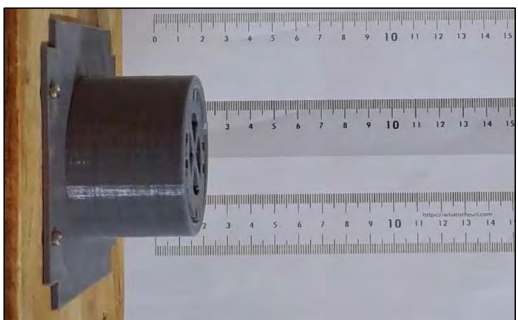
# Appendix H

## Deployment Test Results

1.91 mm Deployment Test

Test 1:

Stowed Antenna:



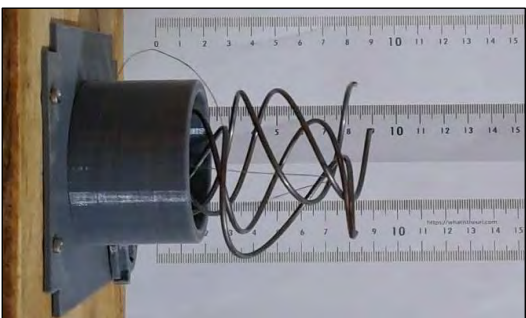
Deploy Action Shot 1:



Deploy Action Shot 2:



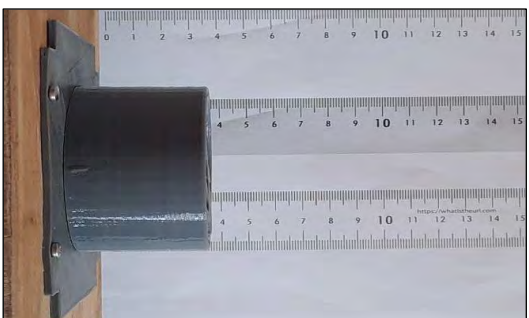
Deployed:



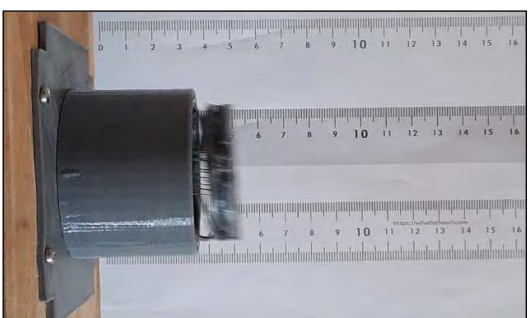
1.91 mm Deployment Test

Test 2:

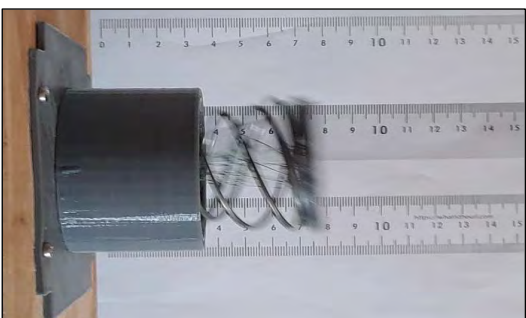
Stowed Antenna:



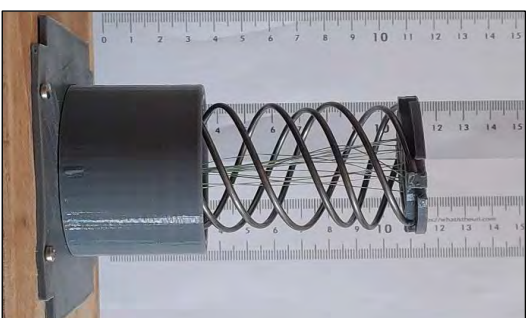
Deploy Action Shot 1:



Deploy Action Shot 2:



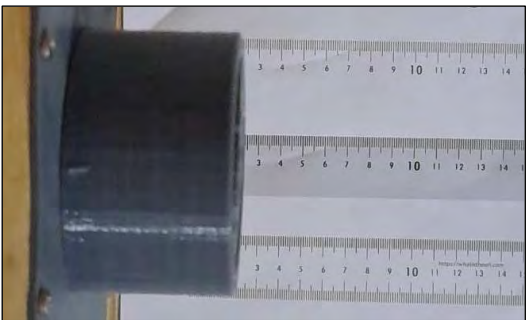
Deployed:



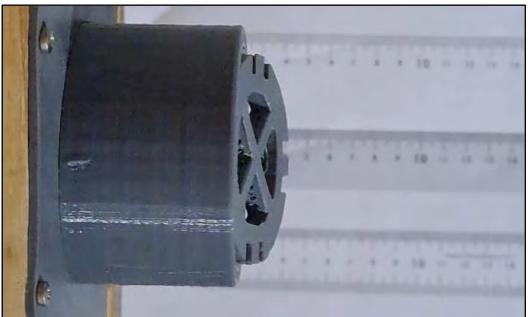
1.91 mm Deployment Test

Test 3:

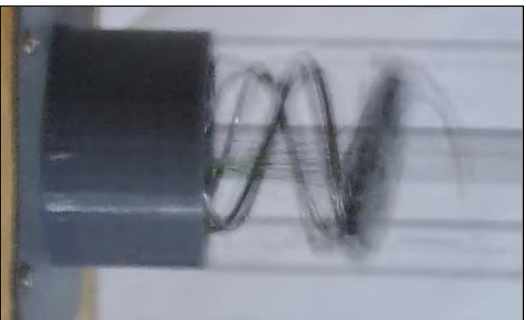
Stowed Antenna:



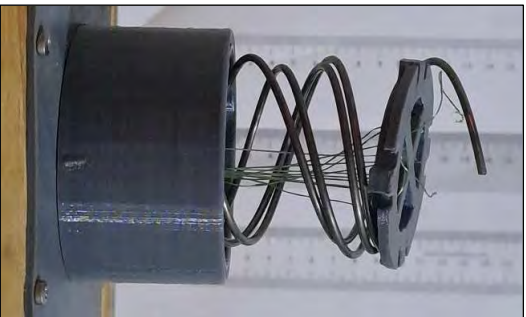
Deploy Action Shot 1:



Deploy Action Shot 2:



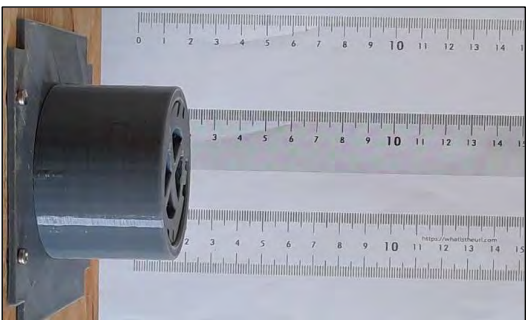
Deployed:



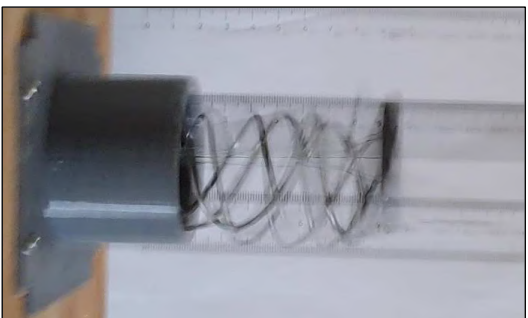
1.91 mm Deployment Test

Test 4:

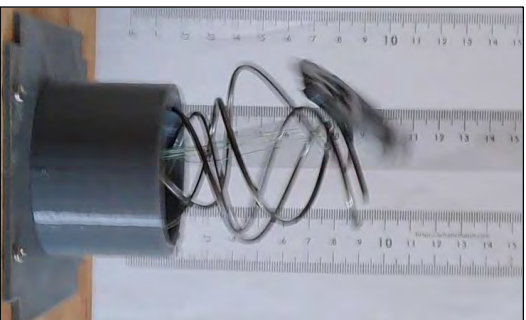
Stowed Antenna:



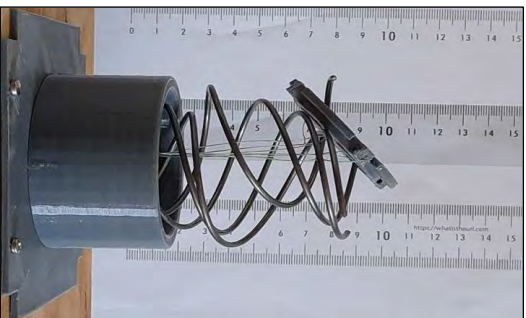
Deploy Action Shot 1:



Deploy Action Shot 2:



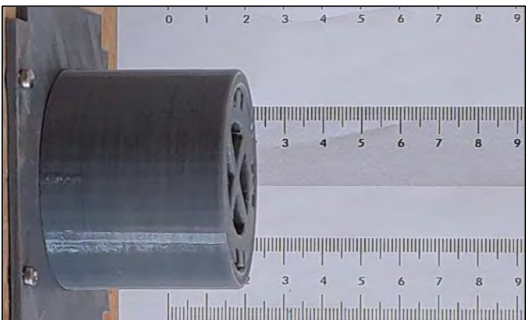
Deployed:



1.91 mm Deployment Test

Test 5:

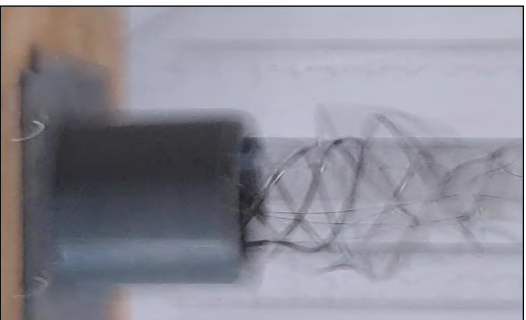
Stowed Antenna:



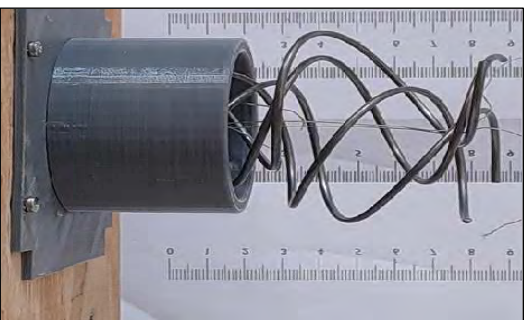
Deploy Action Shot 1:



Deploy Action Shot 2:



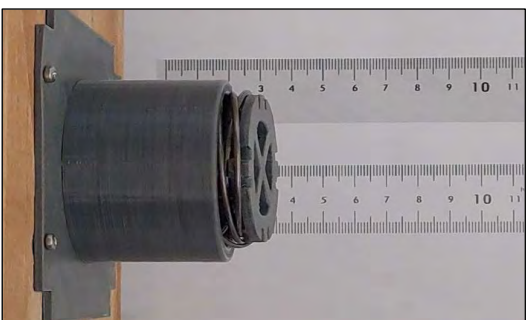
Deployed:



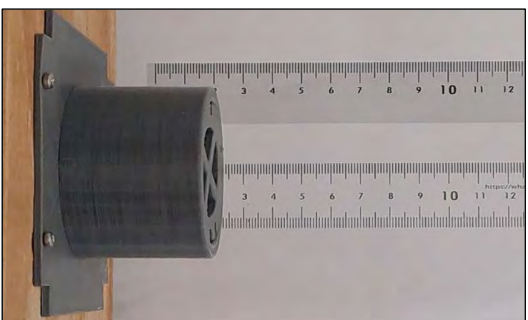
1.6 mm Deployment Test

Test 1:

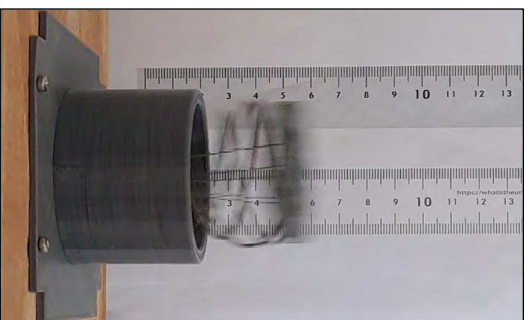
Stowing Antenna:



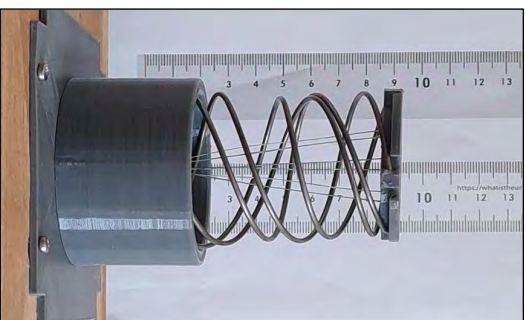
Stowed Antenna:



Deploy Action Shot:



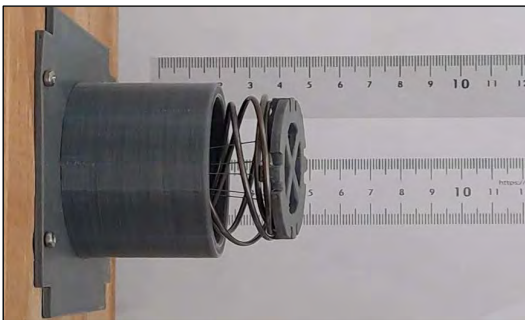
Deployed:



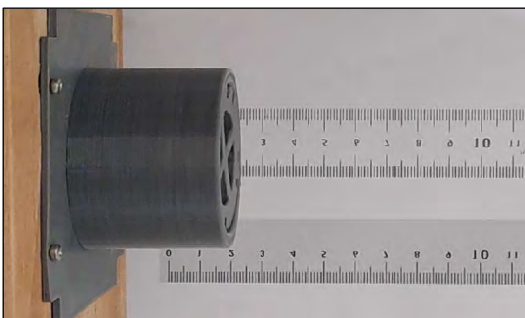
1.6 mm Deployment Test

Test 2:

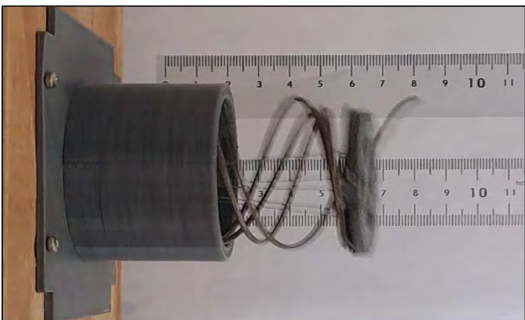
Stowing Antenna:



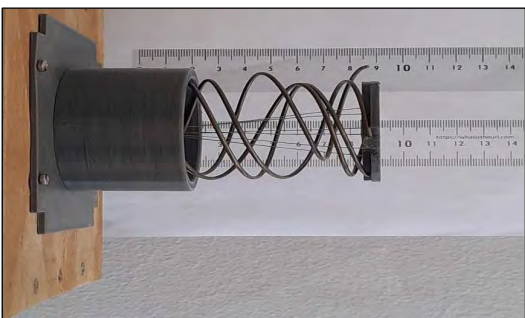
Stowed Antenna:



Deploy Action Shot:



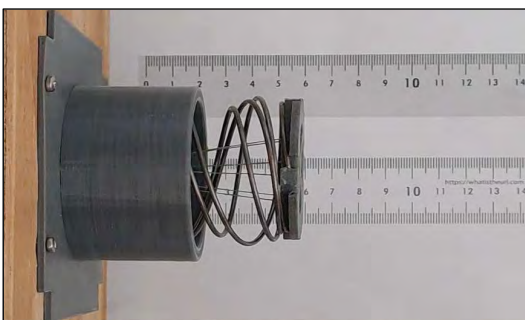
Deployed:



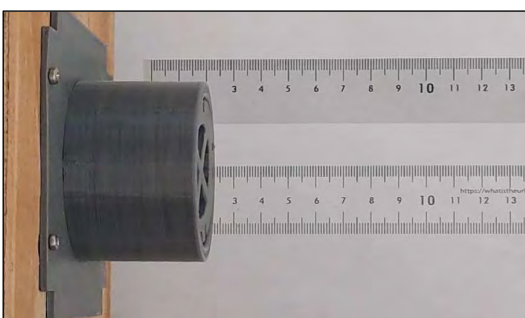
1.6 mm Deployment Test

Test 3:

Stowing Antenna:



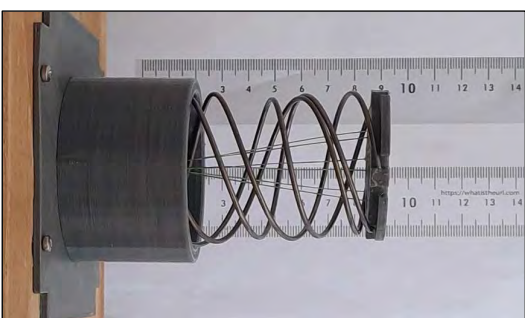
Stowed Antenna:



Deploy Action Shot:



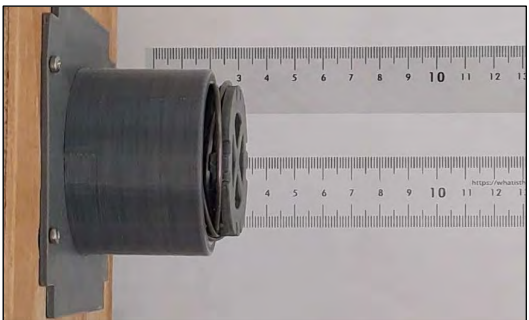
Deployed:



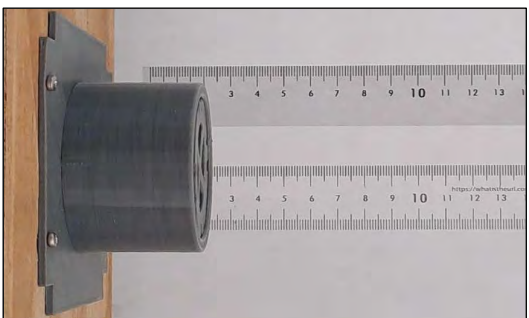
1.6 mm Deployment Test

Test 4:

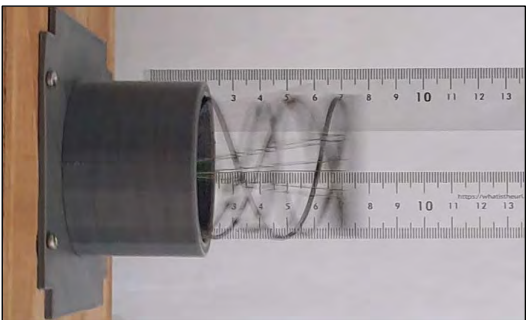
Stowing Antenna:



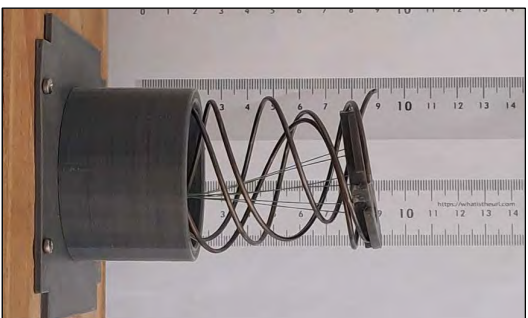
Stowed Antenna:



Deploy Action Shot:



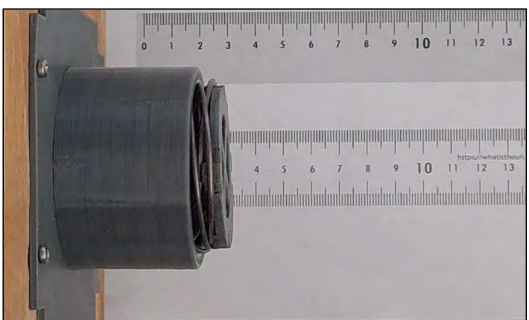
Deployed:



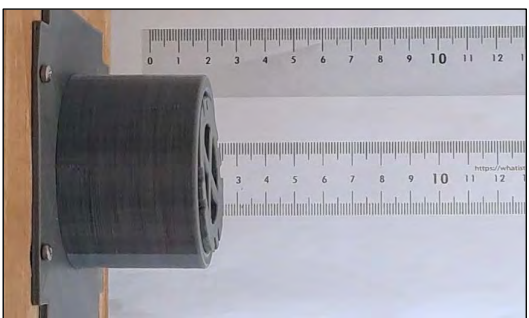
1.6 mm Deployment Test

Test 5:

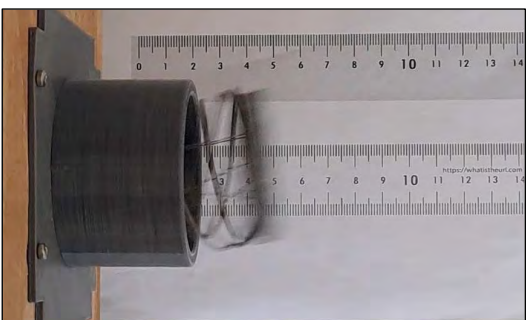
Stowing Antenna:



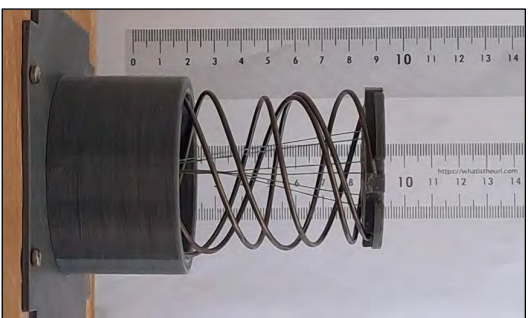
Stowed Antenna:



Deploy Action Shot:



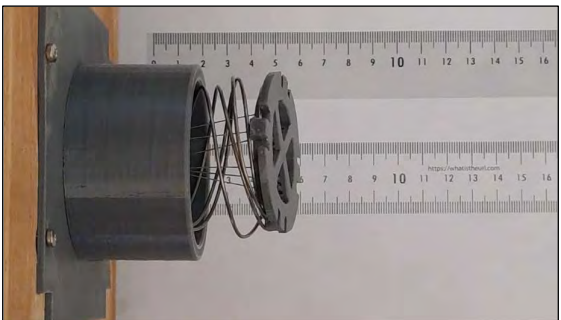
Deployed:



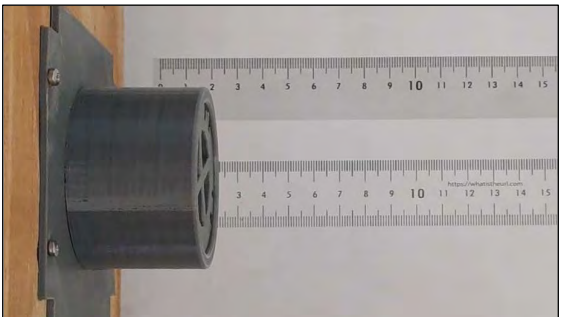
1.1 mm Deployment Test

Test 1:

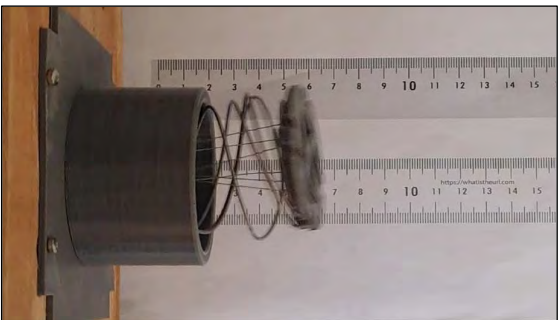
Stowing Antenna:



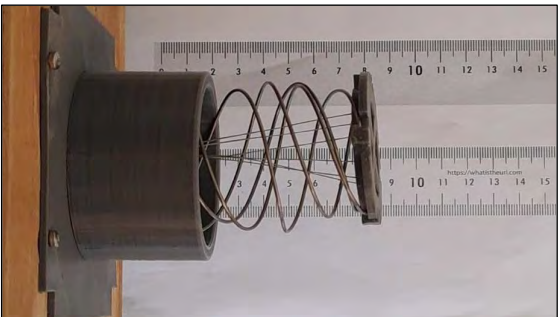
Stowed Antenna:



Deploy Action Shot:



Deployed:



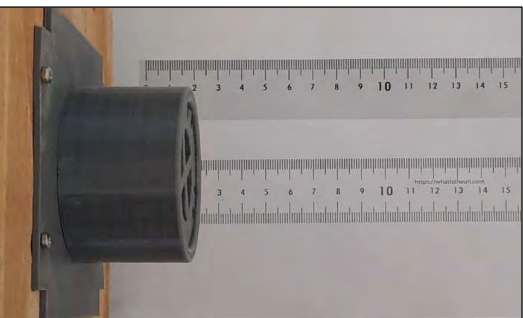
1.1 mm Deployment Test

Test 2:

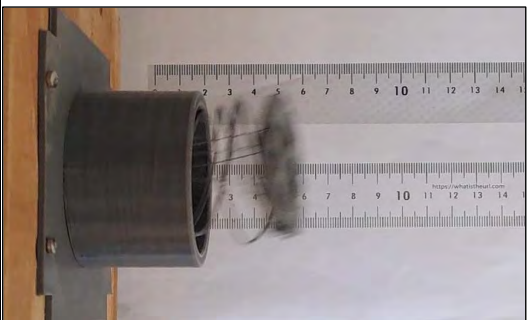
Stowing Antenna:



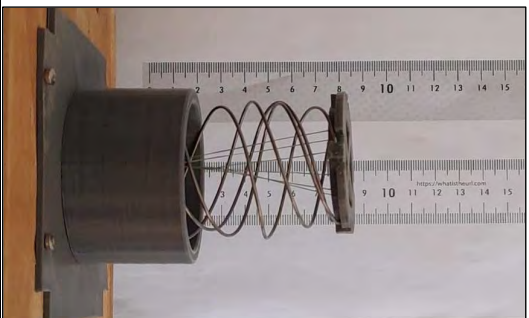
Stowed Antenna:



Deploy Action Shot:



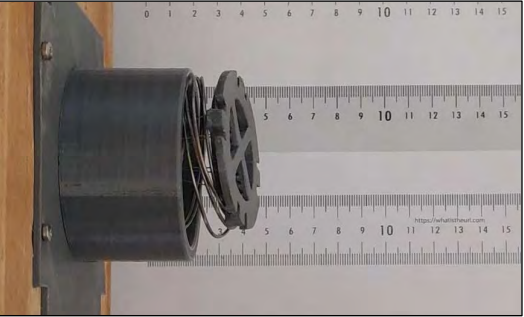
Deployed:



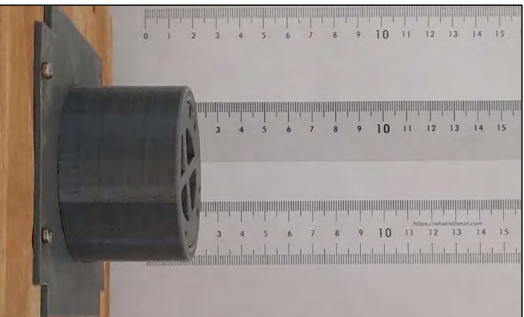
1.1 mm Deployment Test

Test 3:

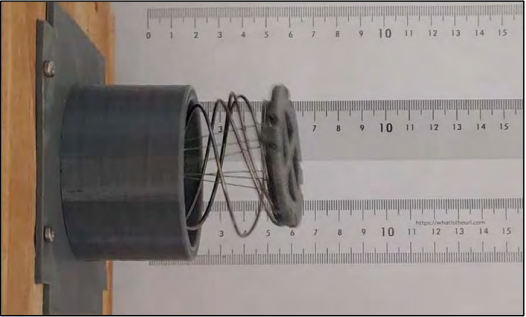
Stowing Antenna:



Stowed Antenna:



Deploy Action Shot:



Deployed:



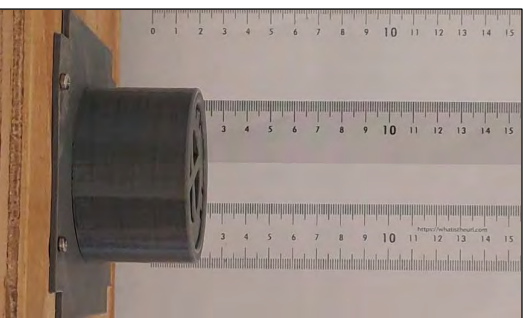
1.1 mm Deployment Test

Test 4:

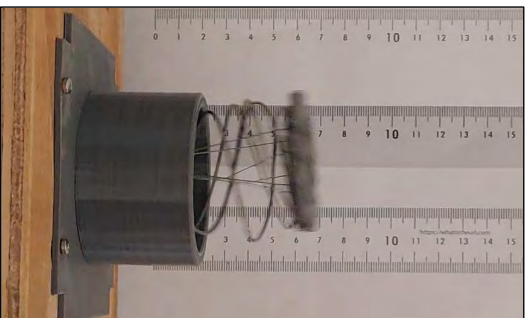
Stowing Antenna:



Stowed Antenna:



Deploy Action Shot:



Deployed:

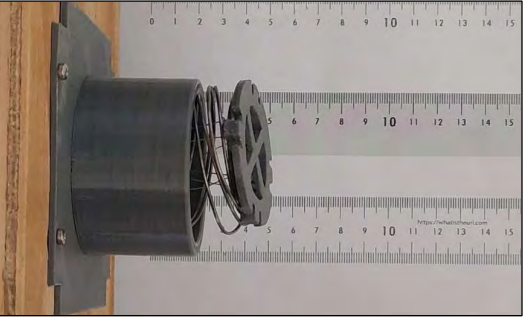




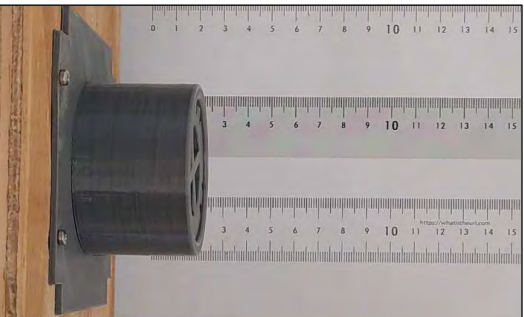
1.1 mm Deployment Test

Test 5:

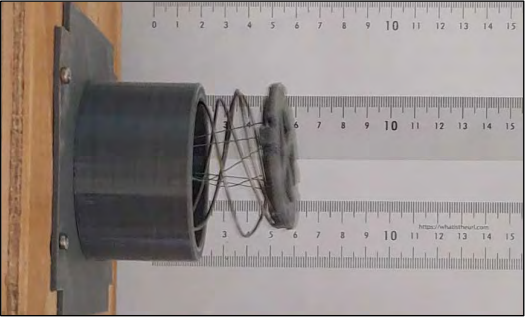
Stowing Antenna:



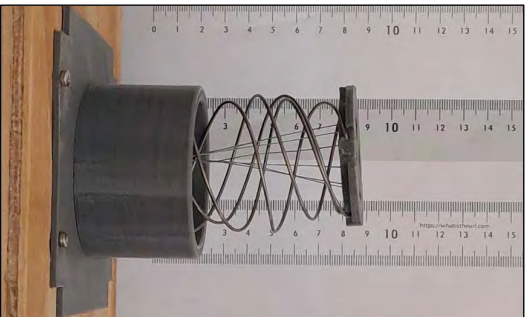
Stowed Antenna:



Deploy Action Shot:



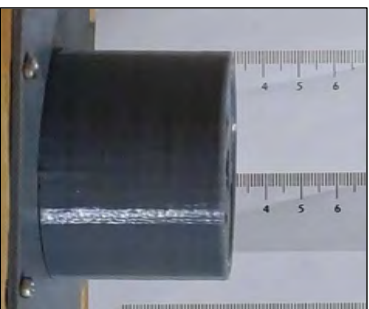
Deployed:



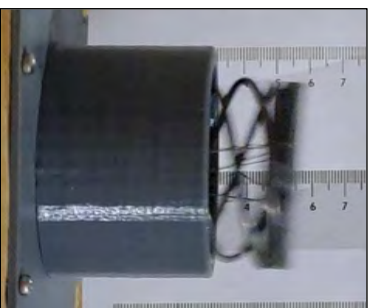
1.91 mm Staged Deployment Test

Test 1:

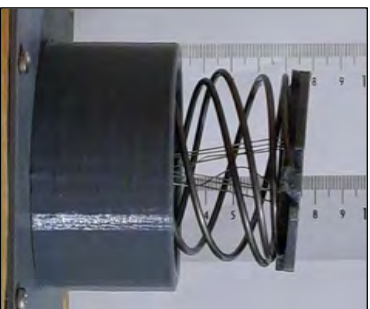
Stowed Antenna (Stage 1):



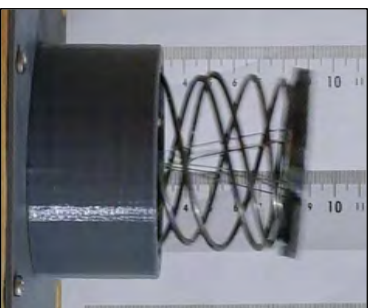
Deploying Action Shot 1:



Stage 2:



Deploying Action Shot 2:



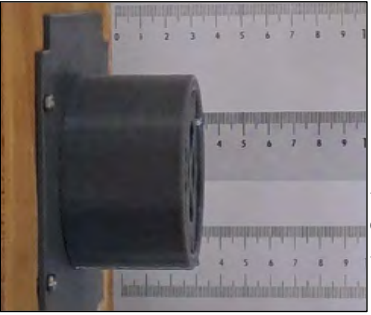
Deployed (Stage 3):



1.91 mm Staged Deployment Test

Test 2:

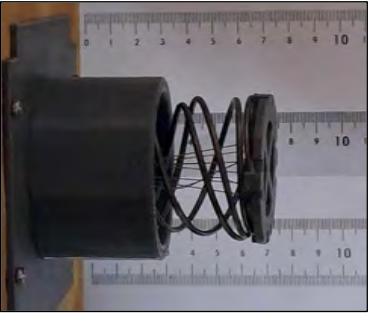
Stowed Antenna (Stage 1):



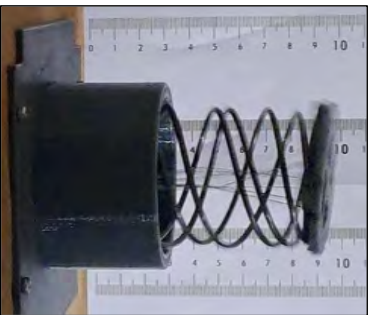
Deploying Action Shot 1:



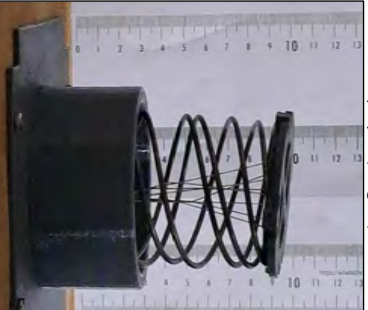
Stage 2:



Deploying Action Shot 2:



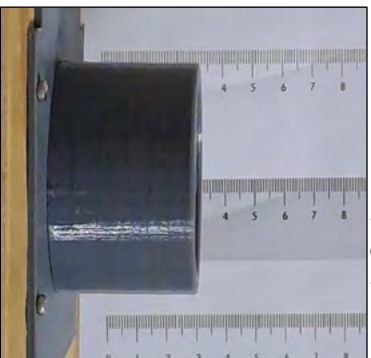
Deployed (Stage 3):



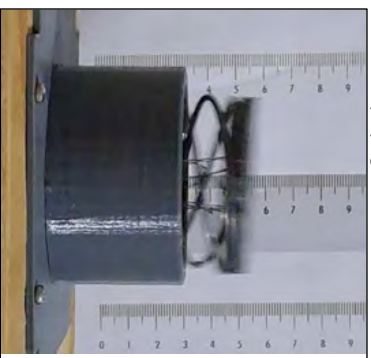
1.91 mm Staged Deployment Test

Test 3:

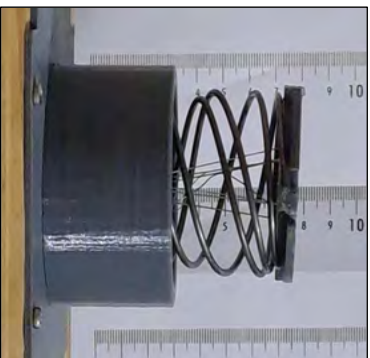
Stowed Antenna (Stage 1):



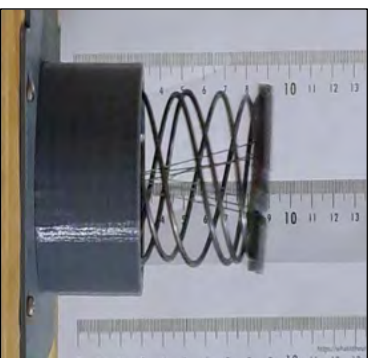
Deploying Action Shot 1:



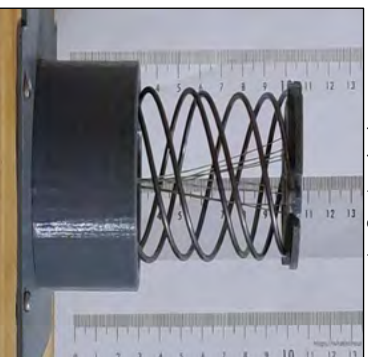
Stage 2:



Deploying Action Shot 2:



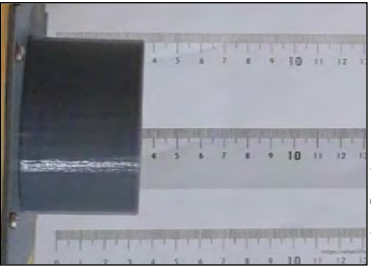
Deployed (Stage 3):



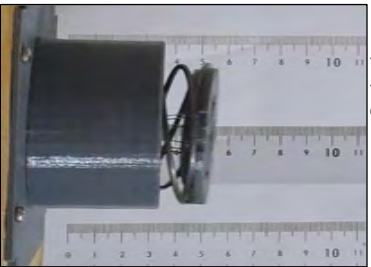
1.91 mm Staged Deployment Test

Test 4:

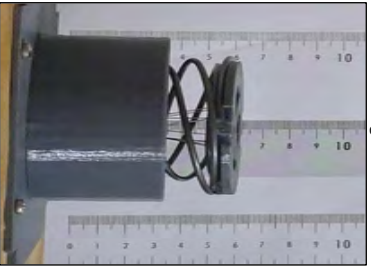
Stowed Antenna (Stage 1):



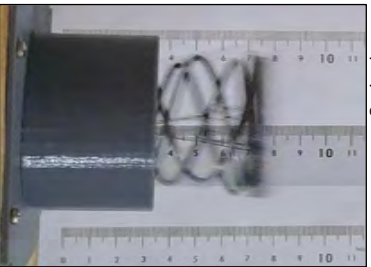
Deploying Action Shot 1:



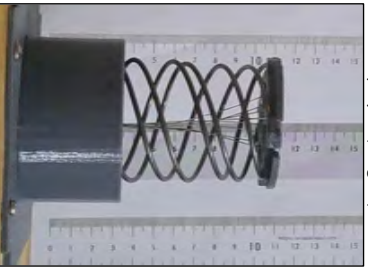
Stage 2:



Deploying Action Shot 2:



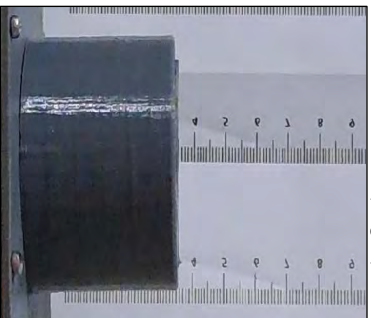
Deployed (Stage 3):



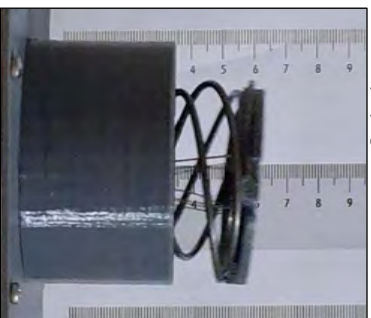
1.91 mm Staged Deployment Test

Test 5:

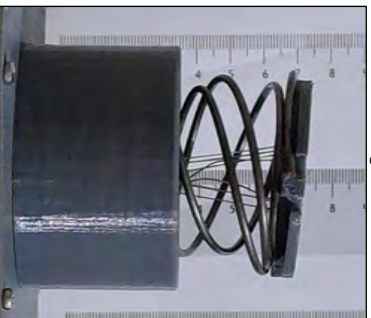
Stowed Antenna (Stage 1):



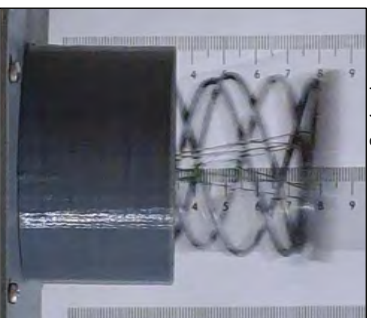
Deploying Action Shot 1:



Stage 2:



Deploying Action Shot 2:



Deployed (Stage 3):

